Magnetic order and spin dynamics in the extended kagome system $CaBaCo_2Fe_2O_7$

Johannes Reim

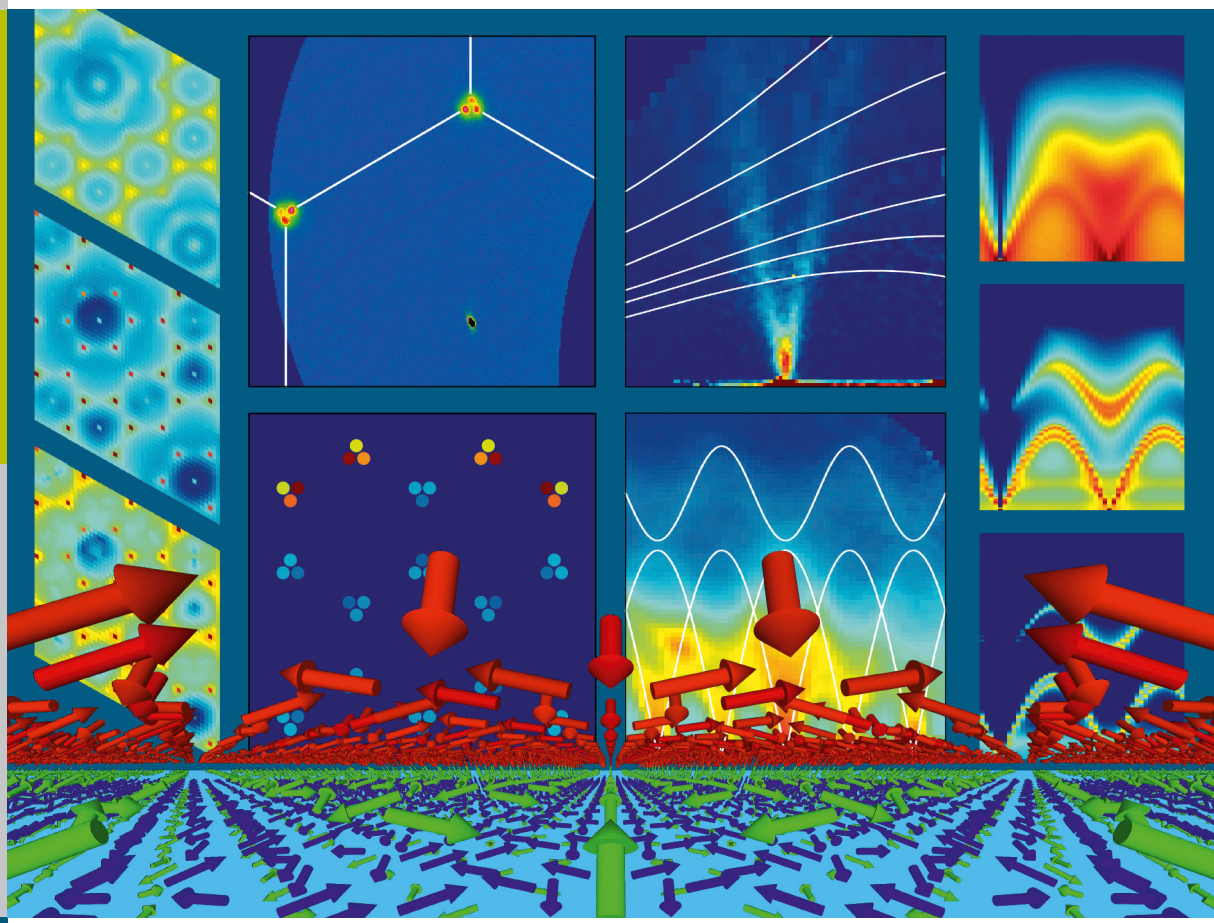

Schlüsseltechnologien / Key Technologies
Band / Volume 115
ISBN 978-3-95806-097-5

JÜLICH FORSCHUNGSZENTRUM

Schriften des Forschungszentrums Jülich
Reihe Schlüsseltechnologien / Key Technologies Band / Volume 115

Forschungszentrum Jülich GmbH
Peter Grünberg Institute (PGI)
Scattering Methods (PGI-4 / JCNS-2)

Magnetic order and spin dynamics in the extended kagome system $CaBaCo_2Fe_2O_7$

Johannes Reim

Schriften des Forschungszentrums Jülich
Reihe Schlüsseltechnologien / Key Technologies Band / Volume 115

ISSN 1866-1807 ISBN 978-3-95806-097-5

Bibliographic information published by the Deutsche Nationalbibliothek.
The Deutsche Nationalbibliothek lists this publication in the Deutsche Nationalbibliografie; detailed bibliographic data are available in the Internet at http://dnb.d-nb.de.

Publisher and Distributor: Forschungszentrum Jülich GmbH
Zentralbibliothek
52425 Jülich
Tel: +49 2461 61-5368
Fax: +49 2461 61-6103
Email: zb-publikation@fz-juelich.de
www.fz-juelich.de/zb

Cover Design: Grafische Medien, Forschungszentrum Jülich GmbH

Printer: Grafische Medien, Forschungszentrum Jülich GmbH

Schriften des Forschungszentrums Jülich
Reihe Schlüsseltechnologien / Key Technologies, Band / Volume 115

D 82 (Diss. RWTH Aachen University, 2015)

ISSN 1866-1807
ISBN 978-3-95806-097-5

The complete volume is freely available on the Internet on the Jülicher Open Access Server (JuSER) at www.fz-juelich.de/zb/openaccess.

Zusammenfassung

Das erweiterte Kagomesystem in der hexagonalen Schwedenborgitstruktur zeigt ähnlich zu den Pyrochloren ein hochfrustriertes Netzwerk von tetraedrisch koordinierten magnetischen Ionen. Diese formen geschichtete Kagome- und Dreiecksgitter, was wiederum Doppeltetraedersäulen senkrecht zu eben diesen Schichten ergibt. Die gebrochene Inversionssymmetrie erhöht die Komplexität der magnetischen Ordnung durch die nicht verschwindende Dzyaloshinskii-Moriya Wechselwirkung. Kürzlich untersuchte Materialien dieser Klasse zeigen mannigfaltige Zeichen von ungewöhnlicher geometrischer Frustration und ungeordneten Grundzuständen trotz der typischerweise starken antiferromagnetischen Wechselwirkung. In der vorliegenden Arbeit wird die magnetische Ordnung und Spindynamik im antiferromagnetisch gekoppelten Material $CaBaCo_2Fe_2O_7$, eine Verbindung dieser Materialklasse, im Detail untersucht.
Als primäre experimentelle Methode werden verschiedene Arten von Neutronenstreuinstrumenten eingesetzt. Diese Experimente werden von der theoretischen Seite mit Monte Carlo Simulationen für die Modellierung der magnetischen Ordnung und Simulationen der Spindynamik zur Bestimmung der Anregungen ergänzt. Beide Methoden basieren auf dem gleichen Nächste-Nachbar Heisenberg-Modell. In diesem Model wird zwischen der Wechselwirkung innerhalb der Gitter J_{in} und zwischen den Gittern J_{out} unterschieden. In dem Phasendiagramm basierend auf diesem Model wurde eine antiferromagnetisch geordnete Phase für Verhältnisse $\tau = J_{\text{out}}/J_{\text{in}} \geq 1.5$ und eine 3D Spinflüssigkeit für kleinere Verhältnisse gefunden. Der Doppeltetraeder ist aus dem Dreieck des Kagomegitters und zwei Plätzen von verschiedenen Dreiecksgittern aufgebaut und bildet den grundlegenden Baustein der magnetischen Struktur. Aus der Energieminimierung des Doppeltetraeders ergibt sich eine sogenannte Summenregel, die besagt, dass die Spins auf den trigonalen Plätzen parallel orientiert sind und die Summe über die Kagomespins die mit dem Verhältnis τ gewichteten trigonalen Spins kompensiert. Innerhalb der Spinflüssigkeitsphase folgt daraus für die Kagomespins eine Verkippung gegenüber der antiferromagnetisch geordneten Spinstruktur abhängig vom Verhältnis der Austauschwechselwirkungen. In den meisten Materialien dieser Klasse ist die Abweichung so hoch, dass nur eine kurzreichweitige Ordnung vorhanden ist. Bisher ist $CaBaCo_2Fe_2O_7$ das einzige bekannte Material mit einer langreichweitige dreidimensionale Ordnung ohne einen strukturellen Phasenübergang zur orthorhombischen Symmetrie. Das macht das vorliegende Material einzigartig und interessant als Modelsystem für die Untersuchung der Wechselwirkungen im Zusammenspiel mit der geometrischen Frustration. Es wurde zuvor berichtet, dass unterhalb von 160 K eine kommensurable magnetische Ordnung mit einer $\sqrt{3}\times\sqrt{3}$ mal größeren Einheitszelle auftritt. In der vorliegenden Arbeit wurde mit hochauflösenden Pulver- und Einkristalldiffraktometern eine langperiodische Ordnung zusätzlich zur kommensurablen Ordnung beobachtet. Die langperiodische Modulation ist nur entlang den Kagome- und Dreiecksschichten vorhanden und die Ordnung entlang der senkrechten Richtung bleibt kommensurabel. Es wurde festgestellt, dass die Periode der Modulation temperaturunabhängig ist und die Größe der Aufspaltung einer Periode von $370\,\text{Å}$, bzw. 58 kristallographischen Einheitszellen und einem Ausbreitungsvektor $\mathbf{k} \approx (0.342,\, 0.342,\, 0)$ entspricht. Das mit Einkristallneutronenstreuung beobachtete Streumuster deckt sich mit einer antiferromagnetischen multi-q Ordnung mit dem Propagationsvektor $\mathbf{k}$ und den dazugehörigen symmetrisch äquivalenten. Um die Spinstruktur der langperiodischen Ordnung zu untersuchen, wurden Neutronenstreuexperimente mit Polarisationsanalyse durchgeführt. Von den Polarisationkanälen können die Streubeiträge von Momenten parallel und senkrecht zur Streuebene und die chirale magnetische Streuung, ein Streubeitrag sensitiv für die vektorielle Chiralität, separiert werden. Diese offenbaren, dass die lang periodische Spinstruk-

tur (bezüglich der Intensität dominant unterhalb von 20 K) stärker gekantet ist im Vergleich zu der eher koplanaren Spinstruktur der kommensurablen Ordnung (bezüglich der Intensität dominant oberhalb von 80 K). Zwischen den beiden Temperaturen zeigen die Ergebnisse der Neutronenstreuung und Messungen der Magnetisierung eine kontinuierliche Umorientierung der Spins. Durch die gebrochene Inversionssymmetrie können Dzyaloshinskii-Moriya (DM) Wechselwirkungen vorhanden sein. Es konnte gezeigt werden, dass, wenn man die Energie der Spinkonfiguration gegen den reziproken Raum aufträgt, eine geschickte Wahl von DM Vektoren Energieminima an den Positionen der Satellitenpeaks erzeugen kann. Diese DM Vektoren bevorzugen gekantete Kagomespins in Übereinstimmung mit den Streubeiträgen. Somit ist dies ein geeigneter Mechanismus verantwortlich für die Umorientierung und die Erzeugung einer langperiodischen Ordnung. Bei einem System innerhalb der Spinflüssigkeitsphase können die Kagomespins innerhalb bestimmter Grenzen frei variieren, deshalb sind schon kleine DM Wechselwirkungen ausreichend. Des Weiteren weist die Symmetrie der chiralen magnetischen Streuung daraufhin, dass die langperiodische Spinstruktur aus zykloidal angeordneten Spins besteht. Die Vorschrift zur Erzeugung einer passenden Struktur basierend auf den experimentellen Ergebnissen kann die gemessenen Streubeiträge angemessen gut beschreiben. Zudem ähnelt die berechnete Spinstruktur der in der Skyrmionphase in MnSi beobachteten Struktur mit der Ausnahme, dass es sich hier um eine Art von Skyrmiongitter mit einer antiferromagnetischen Modulation handelt.

Darüber hinaus lassen sich noch weitere Erkenntnisse aus der Spindynamik ableiten. Da jedoch die Auflösung der verfügbaren inelastischen Instrumente unzureichend ist, um die langperiodische Ordnung aufzulösen, wurde das kommensurable Model für die theoretische Beschreibung verwendet. Ein deutlicher Unterschied wurde zwischen den Spinwellen, die sich parallel zu den Kagome- und Dreiecksgittern, und denen, die sich entlang der Doppeltetraedersäulen ausbreiten, sowohl in der linearen Spinwellenrechnung (LSWT) als auch in den Neutronenstreuexperimenten gefunden. Experimentelle Beobachtungen und theoretische Modellierung zeigen eher flache Dispersionen in den Schichten aber steile entlang der c-Achse und linear Steigung entlang allen Richtungen nahe des Γ-Punktes. Da die LSWT auf die antiferromagnetisch geordnete Phase limitiert ist, werden in der vorliegenden Arbeit die Anregungen mit Spindynamiksimulationen bei endlichen Temperaturen und innerhalb der Spinflüssigkeitsphase bestimmt. Die gemessenen Anregungen entlang Richtung $[0\,0\,1]$ lassen sich erfolgreich mit den aus den Simulationen abgeleiteten Dispersionen beschreiben. Die daraus hergeleiteten Spinlängen und Wechselwirkungen sind vergleichbar mit den Werten, die in anderen Experimenten bestimmt wurden.

Die experimentellen Methoden, im Besonderen die für die Untersuchung der langperiodischen Ordnung verwendeten, sind an der Grenze der heutigen Möglichkeit. Um die Auflösung der Neutronen-Einkristalldiffraktometer BioDiff und MIRA optimal ausnutzen zu können, mussten neue Auswerteroutinen entwickelt werden. Außerdem mussten die Instrumente Morpheus und MIRA um die XYZ-Polarisationsanalyse erweitert werden, die die notwendigen Einblicke in die Spinstruktur ermöglicht. Trotz der beobachteten Komplexität konnte sowohl die kommensurable magnetische Ordnung als auch die Spindynamik in $CaBaCo_2Fe_2O_7$ mit dem Nächste-Nachbar Heisenberg-Modell konsistent erklärt werden. Es wurde gezeigt, dass die DM Wechselwirkung ein geeigneter Mechanismus für die Etablierung der langperiodischen Ordnung ist und die dazugehörige Spinstruktur dem Skyrmiongitter ähnelt. Die dargelegte Theorie ist über die Auswertung zu $CaBaCo_2Fe_2O_7$ hinaus für die gesamte Materialklasse gültig.

Abstract

The extended kagome system in the hexagonal Swedenborgite structure displays similarly to the pyrochlores a highly frustrated network of tetrahedrally coordinated magnetic ions. These ions form stacked kagome and triangular layers resulting in double tetrahedra columns perpendicular to said layers. However, its broken inversion symmetry raises further the complexity of ordering due to non-vanishing Dzyaloshinskii-Moriya interactions. Recently investigated compounds of this family show various signs for unusual geometric frustration and disordered ground states despite of the typically strong antiferromagnetic exchange. In the present thesis, the magnetic order and the spin dynamics observed on the antiferromagnetically coupled material $CaBaCo_2Fe_2O_7$ a Swedenborgite are studied in detail.
As a primary tool for the experimental investigation, different types of neutron scattering instruments have been used. The experiments are complemented from the theoretical side with Monte Carlo simulations for the modelling of the magnetic order and spin dynamics simulations for the determination of the excitations. Both methods are based on the same Heisenberg nearest neighbour model, in which the in-plane J_{in} and out-of-plane J_{out} exchange interactions are distinguished. In the phase diagram determined using this model an antiferromagnetically ordered phase was found for ratios $\tau = J_{\text{out}}/J_{\text{in}} \geq 1.5$ and a 3D spin liquid at lower ratios. The double tetrahedron formed by a triangle of the kagome and two sites of different triangular lattices was found to be the essential building block for the magnetic structure. From the so-called sum rule for the building block derived from the energy minimization follows, that the triangular spins align parallel and the sum of the kagome spins compensates the triangular spins weighted with ratio τ. Thus, in the spin liquid phase the kagome spins tilt with regard to the antiferromagnetically ordered spin structure depending on the ratio of the interactions. In most materials of this compound family, the deviation is so high that only short range order is present. So far, $CaBaCo_2Fe_2O_7$ is the only known compound of this family, which exhibits a long-range three dimensional order, without a structural transition to an orthorhombic symmetry. This alone already makes the present material unique and interesting as a model system for understanding the interactions and the influence of geometric frustration. A commensurate magnetic order with a $\sqrt{3} \times \sqrt{3}$ larger unit cell was reported to arise below 160 K. Using high-resolution powder as well as single crystal diffractometers, a long-periodic modulation was observed in addition to the commensurate magnetic order. The long periodic modulation is only present within the kagome and triangular layers, with the order remaining commensurate perpendicular to the layers. The period of the modulation found to be temperature-independent corresponds to a periodicity of about 370 Å or 58 crystallographic unit cells and a propagation vector $\mathbf{k} \approx (0.342, 0.342, 0)$. The scattering pattern observed in neutron single crystal measurements is related to a multi-q antiferromagnetic structure with $\mathbf{k}$ and its symmetrically equivalents. In order to investigate the spin structure related to the long periodic order, neutron scattering experiments with polarization analysis were performed. From the polarization channels, the scattering contributions from moments parallel and perpendicular to the scattering plane as well as the chiral magnetic scattering, a scattering contribution sensitive to vectorial chirality, have been separated. These reveal that the long periodic spin structure (prominent in intensity below 20 K) is canted more strongly in comparison to the more coplanar spin structure in the case of the commensurate order (prominent in intensity above 80 K). A continuous reorientation between the two spin structures is visible in neutron scattering as well as magnetisation data. With the broken inversion symmetry the Dzyaloshinskii-Moriya (DM) interactions can be present. A suitable choice of DM vectors was shown to create energy minima in the energy-vs-

reciprocal space landscape at the satellite peak positions. These DM vectors favour a canting of the kagome spins, which is therefore a suitable mechanism to cause this reorientation and to establish the long-periodic order. In the spin liquid phase the kagome spins are able to tilt freely within a certain range, thus even a small DM interaction is sufficient. Furthermore, the symmetry of the chiral magnetic scattering indicates that the long periodic spin structure consists solely of spin cycloids. The instruction to create an appropriate spin structure derived from this information describes the measured scattering contributions reasonably well. The resulting spin structure is similar to the one observed in the skyrmion phase of MnSi. The only exception in this case is, this is a skyrmion-like lattice with an antiferromagnetic modulation.
Further insight has been gained from the spin dynamics, yet the available resolution of current inelastic instruments is insufficient to resolve the long periodic order. Therefore in this case, the commensurate model was used for a theoretical description. A distinct deviation had been found for the spin waves propagating parallel to the kagome and triangular layers and those propagating along the double tetrahedra columns or rather the c-axis in both linear spin wave theory (LSWT) and neutron scattering experiments. Both experimental observation and theoretical modelling reveal rather flat dispersions within the layers, steep ones along the c-axis and a linear slope along all directions close to the Γ-point. Since LSWT is limited to the antiferromagnetically ordered phase, in the present thesis the excitations have been determined using spin dynamics calculations at finite temperatures and in the spin liquid phase. With the dispersions derived from the simulation results, the excitations measured along $[0\,0\,1]$-direction have been described successfully. The extracted moment lengths and interactions are comparable with those determined from magnetometry and spin structure refinement.
The experimental methods, especially those used for the investigation of the long periodic order, have been at the boundary of the feasibility of current instrumentation. In order to make optimal use of the instrumental resolution of the neutron single crystal diffractometers BioDiff and MIRA, new evaluation methods had to be developed. Furthermore, the instruments Morpheus and MIRA had to be expanded in order to allow for XYZ-polarization analysis providing necessary insight to the spin structure. Despite the observed complexity a consistent explanation has been found describing the commensurate magnetic order and spin dynamics of $CaBaCo_2Fe_2O_7$ with the Heisenberg nearest neighbour model. The introduction of the DM interaction was shown to be a suitable mechanism for establishing a long periodic order, with the corresponding spin structure resembling a skyrmion lattice. Beyond the evaluation on $CaBaCo_2Fe_2O_7$, the theoretical arguments are relevant for the whole compound family.

Contents

1 Introduction **1**

2 Neutron scattering principles **5**
2.1 Scattering from crystal structure 5
2.2 Scattering from magnetic order 8
2.3 Polarisation analysis 12
2.4 Inelastic scattering 14

3 Methodology for neutron scattering experiments **17**
3.1 Sample description 18
3.2 Exploring the **Q**-space with high resolution 19
3.3 Combining polarisation analysis with four-circle geometry 21
3.4 Time-of-flight spectroscopy and data preparation 25

4 Magnetic frustration in the Swedenborgite structure **27**
4.1 Model description of the magnetic order 28
4.2 Spin wave dispersions with LSWT 30
4.3 Beyond the harmonic approximation using spin dynamics simulation 31
4.3.1 Elastic scattering 32
4.3.2 Inelastic scattering 35
4.3.3 Nematic phase 37

5 Structural and magnetic properties of $CaBaCo_2Fe_2O_7$ **41**
5.1 Relevant results from previous studies 41
5.1.1 Crystal structure 41
5.1.2 Magnetic order 42
5.2 Transitions in magnetometry 44
5.3 Magnetic structure determination 46
5.3.1 Commensurate and long-periodic order distinguished by powder diffraction 46
5.3.2 Refinement of the commensurate magnetic structure 50
5.4 Resolving the magnetic order in **Q**-space 59
5.5 Magnetic peak structure at the resolution limit 61
5.6 Spin dynamics 68
5.6.1 The overall spin wave excitation spectrum 68
5.6.2 Investigating spin wave excitations with resolution adapted cuts 71

6 Discussion **75**
6.1 Average and commensurate magnetic order 75
6.2 Long-periodic order due to a spin spiral state 77

6.3 Cycloidal spin structure and skyrmion lattice 81
6.4 Spin dynamics under strong frustration 86

7 Summary and Outlook **93**

A Bibliography **99**

B Additional Figures **105**

C List of Figures **115**

D Single crystal refinement results **123**

E Source code for creating a skyrmion-like lattice **133**

1 Introduction

The research on strongly correlated electron systems covers unusual electronic and magnetic properties, e.g. metal-insulator transition, superconductivity, orbital as well as charge ordering or mixed valence states. Possible materials include the d-electron based transition metal oxides and f-electron based heavy fermion intermetallics. To understand the rich physical phenomena, new theoretical models had to be derived. Though investigations on such compounds have been conducted since early 1960s until today, the understanding is still incomplete [ABY11]. Of all these within in present thesis, geometric frustration and complex ordering phenomena are of major relevance. The corresponding research is introduced shortly.

There is a strong and growing research interest in geometrically frustrated spin systems [Ram94, MR06]. Geometric frustration is defined as a phenomenon, where not all interactions can be fulfilled at the same time due to the lattice geometry (cf. Fig. 2.6). Especially, the triangular and kagome lattices have been studied in the context of geometric frustration [Sac92, CHS92, MGN$^+$06, CZ09]. In frustrated systems, the macroscopic manifold of competing ground states may lead to the emergence of new, sometimes exotic phenomena, such as topological magnetic monopoles, and in view of applications to a functional link for multiferroic behaviour, which can be exploited in spintronics. As a result of frustrated interactions, a long periodic structure was found in the antiferromagnetically coupled compound $BiFeO_3$ [LCF$^+$08], which has been of notable interest, since it is a magnetic ferroelectric at room-temperature. The small splitting of the commensurate magnetic peaks observed in neutron scattering corresponds to a periodicity of 64 nm. From the structure refinement the structure was determined to be a circular cycloid.

Recently, the concept of topologically protected spin textures was introduced and has been met with great interest in condensed matter physics. The stability of such structures can be derived from topological arguments. One such texture is the magnetic skyrmion, which is a non-trivial swirling spin structure carrying a topological quantum number [NT12] and results in a long periodic magnetic structure. The finite scalar spin chirality generates a fictitious magnetic field giving rise to the non-trivial topological Hall effect in electron transport phenomena [KOA$^+$11]. Skyrmions have attracted interest because of their possible application in new technologies such as magnetic information storage and processing devices. Detailed investigations have already been performed, exploring the H-T phase diagram of promising compounds. The skyrmion lattice has been found in several materials in a small phase pocket at low magnetic fields. The skyrmion lattice is a large scale structure of spins observed by neutron scattering in reciprocal space and microscopy techniques in real space. Such triangular lattices of skyrmions have been observed in small-q helimagnets, for example MnSi [MBJ$^+$09], (Fe,Co)Si [YOK$^+$10] and

Cu_2OSeO_3 [SKI$^+$12, ACW$^+$12], upon application of a weak external magnetic field.
The investigation of strongly correlated electron systems requires various experimental methods to reveal the complex nature. Aside from the macroscopic methods e.g. measuring the specific heat, conductivity or magnetic moment, microscopic methods, in particular scattering experiments have been very insightful. Different types of scattering methods exist using probes like photons, electrons or neutrons. Each probe has certain advantages and the suitable probe has to be chosen adopted to the study. Within the present thesis X-ray diffraction experiments have been used to determine the crystal structure of the material and neutron scattering for the investigation of the magnetic order and spin wave excitations. Long periodic magnetic order or skyrmions may emerge in ferromagnetically coupled spin structures, therefore small-angle neutron scattering is the adequate choice as it provides sufficient resolution for the small splitting of the commensurate magnetic peaks. Yet this is only true for ferromagnetically coupled systems, where the split peaks can be observed close to the origin of the reciprocal lattice. In antiferromagnetically coupled systems like $BiFeO_3$ [LCF$^+$08] the peaks arise far away from the origin, which requires a more careful instrumentation. Furthermore, polarization analysis is an established method in neutron scattering, which is mainly used to separate the magnetic from the nuclear scattering. Here a more advanced XYZ-difference method [SC93, Sch10] is used. This method allows to obtain a more comprehensive picture of complex spin structure, since it reveals the vector properties of spin correlations, in addition to the separation of magnetic from nuclear scattering (cf. Sec. 2.3).

In the present thesis the compound $CaBaCo_2Fe_2O_7$ is investigated, which belongs to the class of strongly correlated materials. $CaBaCo_2Fe_2O_7$ is part of a family of compounds called Swedenborgites [Val04b]. The Swedenborgite structure derived from the original mineral $NaBe_4SbO_7$ (cf. Fig. 4.1) features a hexagonal symmetry, space group $P6_3mc$, and stacked triangular and kagome layers resulting in double tetrahedra columns of beryllium ions [PKW35]. Recently compounds have been synthesized replacing the beryllium ions on these sites with magnetic ones [VA02], which has attracted interest due to the possibility to study the phenomenon of geometric frustration. The magnetic pyrochlore oxides, another type of structure with magnetic triangular and kagome lattices, are studied extensively [GGG10]. However, in the case of the pyrochlores this results in a network of corner-sharing tetrahedra. Here, the broken inversion symmetry in the Swedenborgites allows for Dzyaloshinskii-Moriya interaction to be present, which can add an interesting complexity to the magnetic order and is prohibited for the undistorted structure of the pyrochlores. The present compound exhibits strong antiferromagnetic exchange interactions and shows an antiferromagnetic order below $T_N \approx 160\,\mathrm{K}$ [Ros11] without a distortion of the lattice [RRS$^+$14], thus it is an ideal system to study. In neutron scattering experiments polarization analysis was used to separate different scattering contributions like the scattering from moments out-of plane and in plane as well as chiral magnetic scattering. This allowed for a deeper insight into the magnetic order and revealed a spin reorientation between 80 and 4 K [Ros11], which would have been invisible otherwise. Despite the additional complexity the magnetic order has been modelled to some extend using a Heisenberg nearest neighbour model distinguishing between the intra- and inter-lattice interactions proposed in [MCR$^+$09, KMMC10]. This model was used to investigate the magnetic order depending on both the ratio of exchange interactions and temperature and also to calculate the dispersions of magnetic excitations using linear spin wave theory (LSWT) [Rei11].
Still, in the previous investigations important questions like the magnetic structure have remained unsolved, thus, here the magnetic order is studied in further detail using high resolution neutron diffraction and the spin dynamics using a multi-incident time-of-flight spectrometer.

Since polarization analysis was proven to be quite useful, it will be applied extensively in the study of the magnetic order. Furthermore, the observed spin wave excitations and the spin reorientation could not be explained with the Heisenberg model. For an improved agreement the introduction of Dzyaloshinskii-Moriya interactions will be discussed. Since the Heisenberg model allows for a huge variety of energetically equivalent ground states, LSWT is rather limited. Thus, here a numerical simulation is used to simulate the spin wave excitations. These results are not limited to the case of $CaBaCo_2Fe_2O_7$, but are relevant for the whole compound family, as both the structure of the magnetic order as well as the excitations can be related back to the frustrated building blocks of the extended kagome lattice.
In Chapter 2 the relevant theory is discussed based around the relevant neutron scattering methods covering magnetic order, the according space groups and spin wave dispersions for simple spin structures. With the need to conduct specific experiments necessary for the investigation of $CaBaCo_2Fe_2O_7$, e.g. polarisation analysis, additional experimental methods have been introduced to existing instruments during this thesis, in these cases the modifications are described in Chapter 3. Following, in Chapter 4 the compound family Swedenborgites is introduced together with the relevant previous results and our spin dynamics simulations, which apply to the whole family. Then we will focus on the material of interest $CaBaCo_2Fe_2O_7$ in Chapter 5. Initially the results from previous studies are stated and followed by the new ones discovered in the present thesis. All results will be combined in the discussions in Chapter 6, where we will elaborate on the main findings in $CaBaCo_2Fe_2O_7$: the commensurate magnetic spin structure, the mechanism leading to the formation of the long periodic order, the corresponding spin structure and modelling the spin dynamics. In Chapter 7 the results are summarised including an outlook covering possible future investigations.

2

Neutron scattering principles

The main experimental method of investigation used in the present thesis is neutron scattering. In contrast to other particle or scattering methods, neutrons have significant advantages in regards to the investigation of magnetism, as they have a spin, are heavier than electrons and electrically neutral. As a result they are not diffracted by the charge of the electrons and protons of the investigated material. This leads to a higher penetration depth. The incident neutrons can only interact with the material's magnetic moments or the nuclear potential. Both possibilities are comparable in regards to their scattering probability. The de Broglie wavelength λ of a neutron with wave number k, mass m_n and velocity v can be calculated using

$$\lambda(\text{Å}) = \frac{2\pi}{k} = \frac{h}{m_n v} = \frac{0.286}{\sqrt{E(\text{eV})}}. \tag{2.1}$$

Here $h = 2\pi\hbar$ denotes the Planck constant. With typical wavelengths between 40 Å and 0.9 Å the energy E of the neutron can be tuned to the energy for the excitation of magnons. Therefore, neutron scattering is the preferred method of investigation for spin wave excitations. Two different sources for neutrons are mainly used, fission reactors or spallation sources. The first one is a continuous source and the latter one a pulsed source, both of them have their individual advantages and instruments located at each of these sources are used in the present study.

2.1 Scattering from crystal structure

The elastic scattering is defined as a scattering without a change in energy between the incident and scattered neutron. If a change in energy is present this is called inelastic scattering (cf. Subsection 2.4). The sample size can be assumed as small in regards to the distance between source and sample as well as sample and detector. Thus the Fraunhofer approximation can be applied, which allows us to consider both the incident (i) neutron radiation as well as the scattered (f) radiation as planar waves with wavevectors $\mathbf{k}_i$ and $\mathbf{k}_f$. In the following, the scattering will be calculated for monochromatic neutrons for simplicity, but scattering with a white[1] neutron beam also follows the same principles.

[1] Contains a wide range of wavelengths.

In the case of elastic scattering there is no change in energy of the neutrons. Thus, for the wave vectors it follows:

$$k_i = |\mathbf{k}_i| = |\mathbf{k}_f| = k_f = \frac{2\pi}{\lambda} \tag{2.2}$$

with λ as the corresponding wave length. Then the scattering vector $\mathbf{Q}$ is defined as:

$$\mathbf{Q} = \mathbf{k}_f - \mathbf{k}_i \quad \Rightarrow \quad \mathrm{Q} = |\mathbf{Q}| = \frac{4\pi}{\lambda} \sin\theta, \tag{2.3}$$

with the scattering angle θ. Since the momentum $\mathbf{p}$ is conserved according to Eq. 2.1 it follows:

$$\hbar\mathbf{Q} = \hbar(\mathbf{k}_f - \mathbf{k}_i) = \mathbf{p}_f - \mathbf{p}_i. \tag{2.4}$$

In a scattering experiment the intensity I is measured in dependence of the scattering vector. This is proportional to the scattering cross section $\frac{\mathrm{d}\sigma}{\mathrm{d}\Omega}$, which is defined as the number of particles scattered into the solid angle $\mathrm{d}\Omega$. For its determination the Born approximation is used, which states that an incident planar wave will yield a spherical wave upon scattering with a point-sized target. The intensity of the scattered wave at point $\mathbf{r}'$ is proportional to the interaction potential $V(\mathbf{r}')$. For an incident wave function ψ^0 and the Green function $G(\mathbf{r}, \mathbf{r}') = \frac{e^{ik|\mathbf{r}-\mathbf{r}'|}}{4\pi|\mathbf{r}-\mathbf{r}'|}$ this can be written as:

$$\Psi(\mathbf{r}) = \psi^0(\mathbf{r}) + \frac{2m_n}{\hbar^2} \int G(\mathbf{r}, \mathbf{r}') V(\mathbf{r}') \Psi(\mathbf{r}') \, \mathrm{d}^3 r' = \psi^0 + \mathbf{G} V \psi. \tag{2.5}$$

If the interaction potential is neglected, the scattered wave and the incident wave are the same. But if the potential is approximated regarding its strength, in a way that for a weaker potential it is scattered once and for a stronger potential it is scattered twice, this results in the so called Born series:

$$\Psi^0 = \psi^0 \qquad \text{no scattering} \tag{2.6}$$

$$\Psi^1 = \psi^0 + \mathbf{G} V \psi^0 \qquad \text{scattered once} \tag{2.7}$$

$$\Psi^2 = \psi^0 + \mathbf{G} V \psi^0 + \mathbf{G} V \mathbf{G} V \psi^0 \qquad \text{scattered twice} \tag{2.8}$$

$$\vdots$$

In the case of neutron scattering the potential can be described as a weak potential in a first approximation. This leads to the differential scattering cross section, which is defined as an element of a transition matrix for the interaction potential from the state of the incident wave to the one of a scattered wave:

$$\frac{\mathrm{d}\sigma}{\mathrm{d}\Omega} = \left(\frac{m_n}{2\pi\hbar^2} \right)^2 | \langle \mathbf{k}_f | V | \mathbf{k}_i \rangle |^2. \tag{2.9}$$

Considering the scattering by an atom located at $\mathbf{R}$ the interaction potential can modelled with a Fermi pseudo potential:

$$V(\mathbf{r}) = \frac{2\pi\hbar^2}{m_n} b \cdot \delta(\mathbf{r} - \mathbf{R}). \tag{2.10}$$

The scattering length b is a measure for the scattering intensity and varies for different elements as well as their isotopes. For this potential the scattering cross section is calculated to

$$\frac{\mathrm{d}\sigma}{\mathrm{d}\Omega} = \left| \sum_j \sum_i \sigma_i b_i e^{i\mathbf{Q}\cdot\mathbf{R}_j} \right|^2, \tag{2.11}$$

with σ_i denoting the share of an ion in the compound and b_i the scattering length of this ion. In this context it is to be mentioned, that the scattering can be differentiated into two kinds: coherent (*coh*) and incoherent (*incoh*) scattering. Thus the scattering cross section can be written as:

$$\frac{\mathrm{d}\sigma}{\mathrm{d}\Omega} = \left(\frac{\mathrm{d}\sigma}{\mathrm{d}\Omega}\right)_{coh} + \left(\frac{\mathrm{d}\sigma}{\mathrm{d}\Omega}\right)_{incoh}. \tag{2.12}$$

The incoherent scattering stems from the deviations in the regularity of the lattice and is independent from the scattering vector or the structure of the investigated compound. Incoherent scattering results in an increased scattering background. The coherent scattering describes the interference of the scattering of the system's periodic lattice with an average scattering length. The coherent scattering is the one relevant for the study of the material structure and the incoherent scattering will be disregarded in the following.
The scattering intensity for a scattering vector $\mathbf{Q}$ depends on its relation to the lattice in real space. The relation is defined by a discrete Fourier transformation, which creates a reciprocal lattice from the periodic lattice in real space. The scattering triangle defined in Equation 2.3 allows for a very helpful geometric construction called the Ewald sphere (cf. Fig. 2.1). The vector $\mathbf{k}_i$ points from the origin of the real space to the origin of the reciprocal space. A sphere with a radius of k_i is drawn around the origin of the real space and accordingly the position of the sample. The vector $\mathbf{k}_f$ is of the same length as $\mathbf{k}_i$ and is starting at the origin of the real space as well. The scattering triangle is closed by the vector $\mathbf{Q}$ with both the starting and the end point limited to the surface of the sphere. Considering the underlying reciprocal space, only the points on the surface of the Ewald sphere can be measured for the specified incident wave vector $\mathbf{k}_i$. In real space this sphere is located at the position of the sample and is projected to the detector.

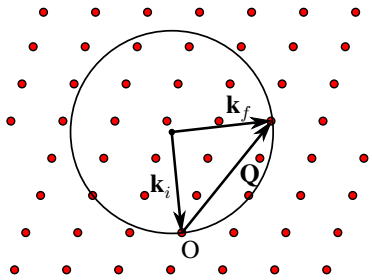

Figure 2.1: Construction of the Ewald sphere in two dimensions. Bragg reflections are marked in red.

Considering the construction of the Ewald sphere and the differential cross-section for the nuclear coherent scattering it is apparent that the positions of atoms $\mathbf{R}_j$ and also their periodicity play an important role for the nuclear scattering. In order to describe the periodicity of a crystal lattice the idea of a unit cell was introduced as a volume consisting of atoms from which the whole crystal lattice can be created through translation symmetry. Then, 14 different types of unit cells have been identified which are called the Bravais lattices. Furthermore, the lattice symmetry can be described using the 32 point groups. As groups these are closed under their symmetry operations and keep at least one point invariant, this is why e.g. translation symmetry is excluded. Combining both and additionally the symmetry operations of screw axes and glide

planes a more comprehensive description of the symmetry has been derived in the form of 230 space groups, which are listed in the *International Tables for Crystallography* [Hah06]. In this thesis, the space groups will be noted with their international symbol also known as Hermann-Mauguin notation. These are based on the centering of the Bravais lattice and the symmetry operations along the high symmetry directions. In the case of $CaBaCo_2Fe_2O_7$ the space group is $P6_3mc$, which means it is a primitive unit cell, along the highest symmetry direction there is a six-fold screw axis (here the c-axis), along the $a+b$ direction there is a mirror plane with a normal vector parallel to $a+b$ and, along the a or b-axis, there is a glide plane with a normal vector parallel to c-axis.

2.2 Scattering from magnetic order

The magnetic scattering is based on the interaction between the spin of the neutron with magnetic field created by the unpaired electrons of the scattering atoms. In contrast to the nuclear scattering the spin of the neutron $\boldsymbol{\mu}_N$ as well as the magnetic field exhibited by the moment of the electrons $\mathbf{B} = \mathbf{B}_{\text{spin}} + \mathbf{B}_{\text{orbit}}$ has a direction, where the scattering depends on the orientation to one another. This is described by the Zeeman potential:

$$\mathbf{V}_m = -\boldsymbol{\mu}_N \cdot \mathbf{B} = -\gamma_n \mu_N \boldsymbol{\sigma} \cdot \mathbf{B}, \tag{2.13}$$

with γ_n the gyromagnetic factor of the neutrons, μ_N the nuclear magneton and $\boldsymbol{\sigma}$ its spin operator. Assuming the quantization axis along z without loss of generality and scattering changes the state of the neutron spin, the differential cross section can be calculated by:

$$\frac{\mathrm{d}\sigma}{\mathrm{d}\Omega} = \left(\frac{m_n}{2\pi\hbar^2}\right)^2 \left|\langle \mathbf{k}_f \sigma_f^z | \mathbf{V}_m | \mathbf{k}_i \sigma_i^z \rangle\right|^2 \tag{2.14}$$

$$= (\gamma_n r_0)^2 \left| -\frac{1}{2\mu_B} \left\langle \sigma_f^z | \boldsymbol{\sigma} \cdot \mathbf{M}_\perp(\mathbf{Q}) | \sigma_i^z \right\rangle \right|^2 . \tag{2.15}$$

The detailed calculation can be found in [Squ78]. $\mathbf{M}(\mathbf{Q})$ is the Fourier transformed magnetization of the sample

$$\mathbf{M}(\mathbf{Q}) = \int \mathbf{M}(\mathbf{r}) e^{i\mathbf{Q}\cdot\mathbf{r}} \, \mathrm{d}^3 r, \tag{2.16}$$

but here only the part of the magnetization, which is perpendicular to $\mathbf{Q}$ can be observed. The parallel term of the magnetic dipole field cancel out due to destructive interference and only the perpendicular term remains, which is defined as

$$\mathbf{M}_\perp(\mathbf{Q}) = \hat{\mathbf{e}}_\mathrm{Q} \times \mathbf{M}(\mathbf{Q}) \times \hat{\mathbf{e}}_\mathrm{Q}, \tag{2.17}$$

with the unit vector $\hat{\mathbf{e}}_\mathrm{Q} = \frac{\mathbf{Q}}{\mathrm{Q}}$. Two important results can be derived from Equation 2.15. On the one hand only the magnetisation perpendicular to the scattering vector contributes to the scattering and on the other hand the scattering depends on the orientation of the neutron spin. The latter one allows for a method called polarization analysis, which uses the orientation of the neutron spin to be sensitive to specific scattering contributions (cf. Section 2.3).
In contrast to the nuclear scattering the magnetic scattering takes place at the free electrons of an atom, which as a whole cannot be considered as a point scatterer. This leads to a magnetic

form factor $f_m(\mathrm{Q})$ of radial symmetry. It describes the decrease in intensity for a deviation from the forward scattering and is material specific, as it is determined by the Fourier transform of the atomic spin density. This reduces the intensity of the magnetic scattering observed at $\mathbf{Q}$ with increasing Q. The differential cross section for the magnetic scattering is then given by:

$$\frac{\mathrm{d}\sigma}{\mathrm{d}\Omega}_{\mathrm{mag}} = (\gamma_n r_0)^2 \left| f_m(\mathrm{Q}) \sum_i \langle \mathbf{S}_{i\perp} \rangle \, e^{i\mathbf{Q}\cdot\mathbf{R}_i} \right|^2 , \tag{2.18}$$

with $\langle \mathbf{S}_{i\perp} \rangle$ denoting the expectation value of the perpendicular component of the spin moment $\mathbf{S}_i$ of atom i. The relevant part for the magnetic order is just the sum and is also known as the structure factor $S(\mathbf{Q})$. The total scattering $F_\mathbf{Q}$ is combined from the crystal structure factor ($N_\mathbf{Q}$) and the magnetic contribution:

$$F_\mathbf{Q} = N_\mathbf{Q} + \boldsymbol{\sigma} \cdot \mathbf{M}_\perp(\mathbf{Q}) \tag{2.19}$$

with a differential cross section of

$$\frac{\mathrm{d}\sigma}{\mathrm{d}\Omega} = |F_\mathbf{Q}|^2. \tag{2.20}$$

In contrast to the nuclear scattering here apart from their positions and periodicity also the direction of the spins is relevant, which is basically described by the magnetic order. The order arises based on the exchange interaction J_{ex} between two spins, which is defined by the energy difference between the antisymmetric and symmetric case $J_{\mathrm{ex}} = E_- - E_+$. These energies are in turn defined via the overlap integrals of the orbitals. Among the materials with a magnetic feature different kinds of interactions have been discovered. They have been categorized into paramagnetic, ferromagnetic, antiferromagnetic and ferrimagnetic ones. Macroscopically the categorization depends on the materials behaviour under varying an external field and temperature. However, specifying each material's category is more difficult as materials undergo transitions with temperature which changes its characteristics from one kind to another. Furthermore, materials usually exhibit contributions from several kinds at the same temperature. These transitions can lead to the arise of a magnetic order, which depends on the interplay of interactions minimizing the energy. Considering a linear chain of ions and spins, here four different kinds of order relevant for this thesis will be discussed shortly regarding their spin structure as well as the resulting neutron scattering. As the exchange interaction decreases with distance between the spins, in many cases considering only the interactions between nearest neighbours is already sufficient. In the following a Heisenberg nearest neighbour model $H = -J_{\mathrm{ex}} \sum_i \mathbf{S}_i \cdot \mathbf{S}_{i+1}$ is assumed. In the corresponding figures the crystal structure contributions are marked in red and the magnetic ones in blue. The upper row displays the ions and spins and in the lower row the resulting scattering.

Ferromagnetic order In a ferromagnetic order the exchange interaction between neighbouring spins is positive $J_{\mathrm{ex}} > 0$, which means a parallel alignment of the spins is favoured. The lattice parameter, for both the magnetic order and crystal structure, is equal. Thus in the scattering the peaks from the nuclear and the ones from the magnetic scattering are superimposed.

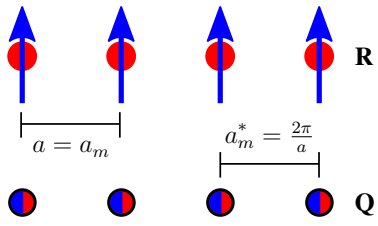

Figure 2.2: Illustration of a ferromagnetic order on a linear chain of ions.

Antiferromagnetic order In case of an antiferromagnetic order the exchange interaction between neighbouring spins is negative $J_{ex} < 0$ favouring an antiparallel alignment of the spins. Here the lattice parameter for the magnetic order is doubled in regards to the lattice parameter of the crystal structure. Due to the structure factor the intensity at the crystal Bragg peaks vanishes. This leads to separated magnetic and crystal structure peaks in the scattering.

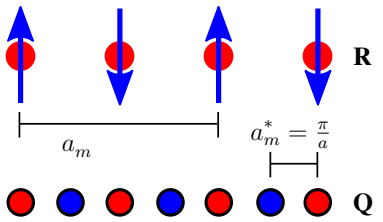

Figure 2.3: Illustration of an antiferromagnetic order on a linear chain of ions.

Ferrimagnetic order In principle the antiferromagnetic order is a special case of the ferrimagnetic one. Here the exchange interaction between neighbouring spins is negative $J_{ex} < 0$ as well, but every second spin has a different length e.g. due to mixed valence states or ions. Still an antiparallel alignment of the spins is favoured. The lattice parameter for the magnetic order remains doubled. But here magnetic peaks arise at the crystal Bragg peak positions in addition to the peaks from antiferromagnetic order.

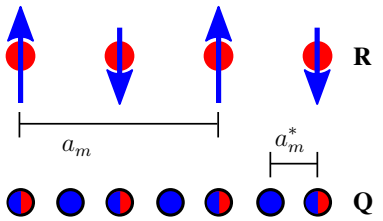

Figure 2.4: Illustration of an ferrimagnetic order on a linear chain of ions.

Long-periodic order The previous cases have been commensurate magnetic orders as the magnetic lattice parameters deviates from the crystal one only by a small integer. However, if more complex interactions are present a magnetic order can arise with a long periodicity and several times larger lattice parameter. Such a long-periodic order can arise from additional interactions aside from the main coupling. The scattering peaks corresponding to the long-periodic order are located close to the original peaks considering the magnetic order for the main coupling alone.

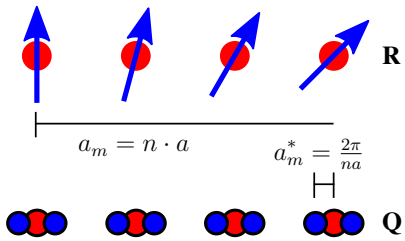

Figure 2.5: Illustration of a long periodic order with a period of n unit cells for a prominent ferromagnetic coupling on a linear chain of ions .

In the context of magnetic order another concept is relevant for the present thesis called frustration [Wan50, Tou77], which describes the fact that not all interactions can be fulfilled at the same time. This occurs due to competing interactions or geometric frustration [Ram94] and typically leads to complex and canted spin structures. Such a spin structure is displayed in Fig. 2.5 as an example for the long periodic order, which can for example arise from a Dzyaloshinskii-Moriya-vector **D** oriented along the viewing direction. The Dzyaloshinskii-Moriya exchange interaction introduces the additional term $H_{DM} = \mathbf{D}_{ij} \cdot (\mathbf{S}_i \times \mathbf{S}_j)$ to the energy minimization. Since the rotation vector is perpendicular to the propagation vector, the resulting spin structure is of cycloidal type. Up to now only the interactions have been considered as relevant for the magnetic order, but depending on its geometry the arrangement of spins in two or three dimensions can have a significant impact as well. The arrangement of antiferromagnetically coupled spins on the corner of an equilateral triangle is geometrically frustrated as not all couplings

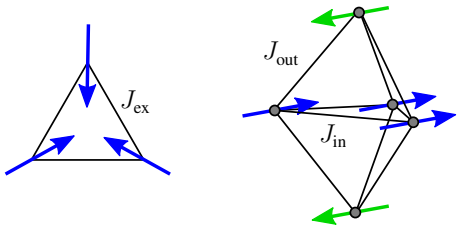

Figure 2.6: Cases of frustration in two and three dimensions relevant for the present study, with exchange interactions $J_{ex},\ J_{in},\ J_{out} < 0$.
(a) Antiferromagnetically coupled spins order in a 120° structure due to geometric frustration. **(b)** The interaction J_{in} connecting neighbouring blue spins and J_{out} connecting blue and green spins compete with each other. For a ratio of $J_{out}/J_{in} \geq 1.5$ the interaction J_{out} forces the blue spins to align parallel. For lower ratios the order on the double tetrahedron becomes more complex.

can be fulfilled at the same time (cf. Fig. 2.6a). Thus, the spins make a compromise, which in the case of the triangle results in the spins to be rotated 120° to one another. There is no unique best solution in energy, but a manifold of solutions with the same energy. This is why such states are called degenerate. Geometries or rather lattices, which are prone to geometric frustration are ones which consist of triangles, like the triangular or kagome lattice and in three dimensions a tetrahedron. Here, the double tetrahedron is an important building block (cf. Fig. 2.6b). Depending on the ratio of the exchange interactions, this results in a rather complex order (cf. Section 4.1 and [MCR$^+$09, KMMC10]). If the structure is incompletely ordered, the degeneracy provides a lot of freedom to the order of the magnetic structure and interesting types of order have been found in materials featuring these structures.

Of course this is only a very simplified description of possible spin structures. For a comprehensive categorization the so-called magnetic space groups have been derived from the crystal space groups using the concept of magnetic superfamily resulting in 1651 different types [Ope86]. A complete list can be found in [Lit13] with a short introduction found in [Lit08]. As the spins are axial vectors this usually reduces the symmetry, when changing from the crystal to magnetic structure. The other important characteristic, which follows from the axial vector, is that the spin direction is inverted under a mirror symmetry operation. Furthermore, every symmetry operation can be subsequently inverted in time, which is indicated by the notation of the operator with $'$. This leads to the significant increase in possible magnetic space groups. Still the basic concepts of the crystal space groups remain the same.

2.3 Polarisation analysis

Polarization is defined as the average of the neutron spin operator over the whole beam $\mathbf{P} = \overline{\boldsymbol{\sigma}}$. The first comprehensive study of polarized neutron scattering for simple magnetic structures was published by Halpern and Johnson in 1939 [HJ39]. In 1963 the formalism was extended in order to allow the investigation of more complex magnetic structures containing for example spin spirals by Blume [Blu63] and Maleev [MBS63]. In contrast to the previously discussed type of neutron scattering, which is called unpolarised $\mathbf{P} = 0$ accordingly, here the orientation of the incoming neutrons is aligned using a polariser. There are different methods used for polarization, but basically the dependence of the scattering or absorption length on the spin orientation is used to get rid of the neutrons with undesired orientation. Additional devices called flipper are used to change the orientation of the neutrons. They basically consist of two coils creating a crossed magnetic field, which can be tuned to apply a field inside the flipper which rotates the neutron spins through the Larmor precession. In order to maintain the polarization throughout the instrument an external guide field is applied along the polarization axis. If a polarization setup contains only these components it is called half-polarized as the scattered neutrons are summed regarding their final state. For a full-polarized setup an analyser is added between sample and detector, which works in the same manner as the polariser. Assuming a guide field along the z-direction four different scattering combinations exist: up-up, up-down, down-up and down-down. The first denotes the orientation of the incoming neutrons regarding $\hat{\mathbf{e}}_z$ and second of the scattered neutrons. In this sense the up-up and down-down channels are called the non spin-flip and the up-down and down-up channels the spin-flip ones. A spin-flip process takes place if a neutron is scattered by the magnetic field of a spin of the sample and the neutron spin is not collinear with the magnetic field. In general the nuclear scattering is always measured in the non spin-flip channels and depending on the orientation of the moments in the material magnetic scattering is observed in the spin-flip and non spin-flip channel. Until 1969, when Moon, Riste and Koehler published their work on polarized neutron scattering [MRK69], the method of polarization analysis referred to measurements of the difference in the polarization between the polarization of the incoming $\mathbf{P}_i$ and scattered beam and $\mathbf{P}_f$, which occurs due to spin-flip scattering. Here, the different polarization channels allow access to measure the different cross sections, which in turn are used for further evaluation via a difference method in order to extract specific scattering contributions. They already noted a special case where the neutron polarization at the sample is parallel to the scattering vector $\mathbf{Q}$. Since only the magnetic scattering contribution from moments perpendicular to $\mathbf{Q}$ can be measured (cf. Eq. 2.15) and in this case the neutron spin is perpendicular to these moments, the magnetic scattering is just observed in the spin-flip channel. This offers a nice separation between the nuclear and magnetic scattering. But in order to change the orientation of polarization the orientation of the guide field must vary smoothly in order to allow for an adiabatic spin rotation, otherwise this leads to a depolarisation of the neutron beam. The idea (using polarizations along $\mathbf{Q}$ and $\hat{\mathbf{e}}_z$) was extended by Schärpf and Capellmann in 1993 introducing the XYZ-difference method [SC93], which makes use of different neutron polarizations at the sample position specifically along $\hat{\mathbf{e}}_x$, $\hat{\mathbf{e}}_y$ and $\hat{\mathbf{e}}_z$. The coordinate system is defined as follows. In general the polarization of the incident neutrons is perpendicular to the instrument floor, which is $\hat{\mathbf{e}}_z$. Then the direction of the scattering vector is defined as $\hat{\mathbf{e}}_x$ and $\hat{\mathbf{e}}_y$ for an orthogonal right-handed coordinate system. In this publication they addressed the problem, that in this coordinate system the polarization is only valid for specific lines in $\mathbf{Q}$. This prevented effective use of detector arrays, which would allow for higher intensity. They successfully derived the equations for powder and sin-

gle crystal diffraction experiments, which allow for a correction of the polarization in detector arrays located in the $\hat{\mathbf{e}}_x$-$\hat{\mathbf{e}}_y$ plane using a parameter called Schärpf angle α. In the work from Schweika [Sch10] this was elaborated further. Based on the 12 polarization channels available from positive and negative fields along $\hat{\mathbf{e}}_x$, $\hat{\mathbf{e}}_y$ and $\hat{\mathbf{e}}_z$ as well as distinguishing the spin-flip and non-spin-flip scattering it was shown that some major scattering contributions can be separated for single crystals using a difference method. In the present thesis, the polarization analysis is used only in combination with point detectors or in the case of area detectors the corrections can be neglected due to the distance between sample and detector in comparison to the area of the detector. In [Blu63, MBS63] formula for the intensity I and the intensity of the final polarisation $P_f I$ were derived. With the reduced formalism introduced in [Mal02] and the notation from [Sch10] ($N(\mathbf{Q}) = N$ and $\mathbf{M}_\perp(\mathbf{Q}) = \mathbf{M}_\perp$) this can be written as

$$I = N^\dagger N + \mathbf{M}_\perp^\dagger \mathbf{M}_\perp + \mathbf{P}_i * \mathbf{M}_\perp^\dagger N + \mathbf{P}_i * \mathbf{M}_\perp N^\dagger + i\mathbf{P}_i(\mathbf{M}_\perp^\dagger \times \mathbf{M}_\perp) \tag{2.21}$$

and

$$\begin{aligned}\mathbf{P}_f I = {} & \mathbf{P}_i N^\dagger N + (\mathbf{P}_i * \mathbf{M}_\perp^\dagger)\mathbf{M}_\perp + (\mathbf{P}_i * \mathbf{M}_\perp)\mathbf{M}_\perp - \mathbf{P}_i(\mathbf{M}_\perp^\dagger \mathbf{M}_\perp) \\ & + iN(\mathbf{P}_i \times \mathbf{M}_\perp^\dagger) - iN^\dagger(\mathbf{P}_i \times \mathbf{M}_\perp) + N\mathbf{M}_\perp^\dagger + N^\dagger \mathbf{M}_\perp - i(\mathbf{M}_\perp^\dagger \times \mathbf{M}_\perp).\end{aligned} \tag{2.22}$$

With $\nu \in x, y, z$ and $\overline{\nu} \in \overline{x}, \overline{y}, \overline{z}$, $I_{\nu\nu}$ denotes the measured intensity for a non spin-flip channel and $I_{\nu\overline{\nu}}$ the measured intensity for a spin-flip channel. Here the entries on the diagonal of the matrix are sufficient for the scattering contributions of interest. For these channels the spin-flip and the non spin-flip scattering intensity adds up to the scattering intensity without polarization:

$$I = I_{\nu\nu} + I_{\nu\overline{\nu}} \tag{2.23}$$

and the final polarization decreases by the amount of the spin-flip scattering:

$$\mathbf{P}_f I = I_{\nu\nu} - I_{\nu\overline{\nu}}. \tag{2.24}$$

From the Equations 2.23 and 2.24 it follows

$$I_{\nu\nu} = \frac{1}{2}(I + \mathbf{P}_f I) \;\text{ and }\; I_{\nu\overline{\nu}} = \frac{1}{2}(I - \mathbf{P}_f I). \tag{2.25}$$

With the polarization along ν this results in

$$I_{\nu\nu} = N^\dagger N + N\mathbf{M}_{\perp,\nu}^\dagger + N^\dagger \mathbf{M}_{\perp,\nu} + \mathbf{M}_{\perp,\nu}^\dagger \mathbf{M}_{\perp,\nu} \tag{2.26}$$

and

$$I_{\nu\overline{\nu}} = \mathbf{M}_\perp^\dagger \mathbf{M}_\perp - \mathbf{M}_{\perp,\nu}^\dagger \mathbf{M}_{\perp,\nu} + i(\mathbf{M}_\perp^\dagger \times \mathbf{M}_\perp)_\nu. \tag{2.27}$$

Analogue also the scattering channels

$$I_{\overline{\nu}\overline{\nu}} = N^\dagger N - N\mathbf{M}_{\perp,\nu} - N^\dagger \mathbf{M}_{\perp,\nu} + \mathbf{M}_{\perp,\nu}^\dagger \mathbf{M}_{\perp,\nu} \tag{2.28}$$

and

$$I_{\overline{\nu}\nu} = \mathbf{M}_\perp^\dagger \mathbf{M}_\perp - \mathbf{M}_{\perp,\nu}^\dagger \mathbf{M}_{\perp,\nu} - i(\mathbf{M}_\perp^\dagger \times \mathbf{M}_\perp)_\nu \tag{2.29}$$

can be calculated. Using the Equations (2.26–2.29) the scattering contributions can be separated from the polarization channels. Since only the magnetic moment perpendicular to $\mathbf{Q}$

is contributing in neutron scattering and $\hat{\mathbf{e}}_x$ is along $\mathbf{Q}$, the total magnetic scattering can be determined using

$$|\mathbf{M}_\perp|^2 = \frac{1}{2}(I_{x\overline{x}} + I_{\overline{x}x}) = \mathbf{M}^\dagger_{\perp,y}\mathbf{M}_{\perp,y} + \mathbf{M}^\dagger_{\perp,z}\mathbf{M}_{\perp,z}. \tag{2.30}$$

On the other hand, subtracting these channels leads to the chiral magnetic scattering

$$I_{\text{chiral}} = I_{x\overline{x}} - I_{\overline{x}x} = 2i(\mathbf{M}^\dagger_\perp \times \mathbf{M}_\perp)_x. \tag{2.31}$$

In order to determine the scattering contributions from moments parallel to $\hat{\mathbf{e}}_y$ e.g. the spin-flip channels of the polarization along $\hat{\mathbf{e}}_z$ can be used

$$M^\dagger_{\perp,y}M_{\perp,y} = \frac{1}{2}(I_{z\overline{z}} + I_{\overline{z}z}) = (M_y)^2. \tag{2.32}$$

and for the scattering contribution from moments parallel to $\hat{\mathbf{e}}_z$ the non spin-flip channels

$$M^\dagger_{\perp,z}M_{\perp,z} \approx \frac{1}{2}(I_{zz} + I_{\overline{z}\overline{z}}) = M^\dagger_{\perp,z}M_{\perp,z} + N^\dagger N \approx (M_z)^2. \tag{2.33}$$

under the assumption of vanishing nuclear scattering at the same $\mathbf{Q}$-vector. In the case of an antiferromagnetically ordered compound this can be valid. The polarization channels along $\hat{\mathbf{e}}_z$ are experimentally advantageous as they usually can be set up the most easiest. There are other interesting scattering contributions, which can be separated [Sch10], however only the presented ones are used in the present study.

2.4 Inelastic scattering

Up to now it was assumed, that the energy of the neutron is conserved under scattering. In the case of inelastic scattering this constraint is removed. Therefore not only the momentum conservation but also the energy conservation has to be considered:

$$\frac{\hbar^2}{2m_n}(k_i^2 - k_f^2) = \hbar\omega_{\mathbf{q}} \tag{2.34}$$

$$\mathbf{k}_i - \mathbf{k}_f = \boldsymbol{\tau} \pm \mathbf{q} = \mathbf{Q}, \tag{2.35}$$

with the energy for exciting a spin wave or rather a magnon $\hbar\omega_{\mathbf{q}}$, a reciprocal lattice vector $\boldsymbol{\tau}$ and the reduced wave vector $\mathbf{q}$. In general this is worked out considering the spin states of the neutron σ and using the double differential cross section:

$$\frac{d^2\sigma}{d\Omega dE_f} = \frac{k_f}{k_i}\left(\frac{m_n}{2\pi\hbar^2}\right)^2 \left|\langle \mathbf{k}_f, \sigma_f, \lambda_f | V | \mathbf{k}_i, \sigma_i, \lambda_i \rangle\right|^2 \delta(\hbar\omega + E_{\lambda_i} - E_{\lambda_f}). \tag{2.36}$$

For single magnon processes the linear spin wave theory can be applied. Then this can be further evaluated using the formula for energy (Eq. 2.34) and momentum conservation (Eq. 2.35) and

the scattering cross section of a magnon is derived as (an extensive derivation can be found in [Squ78]):

$$\begin{aligned}\frac{d^2\sigma}{d\Omega dE_f} &= (\gamma r_0)^2 \frac{k_f}{k_i}\frac{1}{2\pi\hbar}\frac{1}{2}S(1+\hat{\mathbf{Q}}_z^2)(\frac{1}{2}gf_m(\mathbf{Q}))^2 e^{-2W} \\ &\times \sum_{\boldsymbol{\tau},\mathbf{q}} (\delta(\mathbf{Q}-\mathbf{q}-\boldsymbol{\tau})\delta(\hbar\omega_{\mathbf{q}}-\hbar\omega)\left\langle n_{\mathbf{q}}+1\right\rangle \\ &+\delta(\mathbf{Q}+\mathbf{q}-\boldsymbol{\tau})\delta(\hbar\omega_{\mathbf{q}}+\hbar\omega)\left\langle n_{\mathbf{q}}\right\rangle),\end{aligned} \tag{2.37}$$

with the g-factor g and Debye-Waller factor e^{-W}. The thermal average of the number of magnons is given at $\boldsymbol{q}$ by the Bose-Einstein statistics:

$$\langle n_{\mathbf{q}}\rangle = \frac{1}{e^{\frac{\hbar\omega_{\mathbf{q}}}{k_B T}}-1} \tag{2.38}$$

with the Boltzmann constant k_B and at a temperature T. In the double differential cross section the sum is calculated over two different summands. The first one describes the creation and second the annihilation of a magnon. In the inelastic experiments conducted in the present study, only the excitation of magnons was investigated. Then it follows for the momentum conservation:

$$\mathbf{k}_i - \mathbf{k}_f = \boldsymbol{\tau} + \mathbf{q} = \mathbf{Q}. \tag{2.39}$$

For an experiment this has the following consequences. The energy of the incident neutrons E_i is selected, which also defines the incident wave vector $\mathbf{k}_i$. With fixed $\mathbf{k}_i$ the energy of the excited magnon $\hbar\omega_{\mathbf{q}}$ only depends on the wave vector of the scattered neutron $\mathbf{k}_f$. At the same time the scattering vector $\mathbf{Q}$ depends solely on $\mathbf{k}_f$ for constant $\mathbf{k}_i$. Combining both functions this results in a paraboloid in energy with its maximum at $E_i > 0$ and $\mathbf{k}_i$. Only the points on its surface can be measured for a fixed parameter set. Depending on the flexibility of an instrument this directly limits the accessible points in $\mathbf{Q}$ and energy.
The elastic structure factor $S(\mathbf{Q})$ can be generalized to the dynamic structure factor [Hov54], defined as:

$$S(\mathbf{Q},\omega) = \frac{N}{2\pi}\iint e^{i(\mathbf{Q}*\mathbf{r}-\omega t)}\cdot G(\mathbf{r},t)\,\mathbf{d}\mathbf{r}\mathrm{d}t, \tag{2.40}$$

which is basically the Fourier transformation of the pair distribution function $G(\mathbf{r},t)$ of the system's spins in time and space.

Dispersions of linear spin chains In Subsection 2.2 the magnetic order for different coupling types on a linear spin chain was discussed. Exemplary the spin dispersions for the commensurate ordered spin structures can be calculated semi classically (see [Hel88] for the calculations). The possible number of dispersions depends on the spins per unit cell, which is a single one in the case of the ferromagnetic spin chain and two in the antiferromagnetic and ferrimagnetic case (considering only magnon excitations). With spin lengths S, S_A and S_B, and the reciprocal lattice parameter a_m^*, the dispersions are defined as follows:
Ferromagnetic spin chain

$$\hbar\omega(q) = 4|J_{\text{ex}}|S\left(1-\cos\frac{2\pi q}{a_m^*}\right), \tag{2.41}$$

antiferromagnetic spin chain

$$\hbar\omega(q) = 4S \left| J_{\text{ex}} \cdot \sin\left(\frac{\pi q}{a_m^*}\right) \right| \tag{2.42}$$

and ferrimagnetic spin chain assuming $S_A \geq S_B > 0$ for the two different spins

$$\hbar\omega(q) = 2|J_{\text{ex}}| \left[\sqrt{(S_A - S_B)^2 + 4S_A S_B \sin^2\left(\frac{\pi q}{a_m^*}\right)} \pm (S_A - S_B) \right]. \tag{2.43}$$

The resulting dispersion are displayed in Figure 2.7. Comparing the dispersions for the ferro-

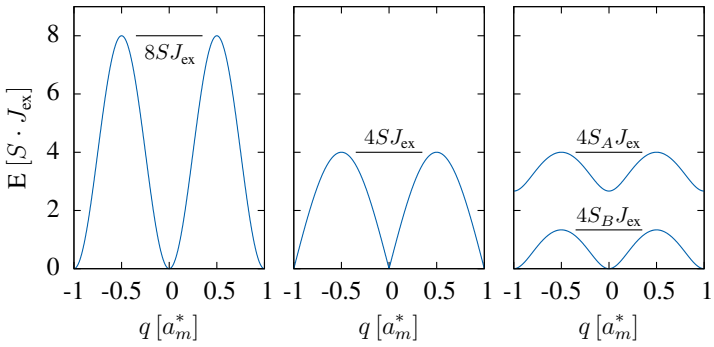

Figure 2.7: Dispersions calculated for linear spin chains, for ferromagnetically (left), antiferromagnetically (middle) and ferrimagnetically coupled spins (right). In the case of the ferrimagnetic spin chain $S_B = 1/3 \cdot S$ and $S_A = S$.

magnetic and antiferromagnetic spin chain, both are basically trigonometric functions, but in the first case close to $q = 0$ there is a continuous quadratic dependence of energy on q, while in the antiferromagnetic case there is a linear dependence. Despite the same absolute spin length and exchange interaction the dispersions for the antiferromagnetic chain stretch only half the range in energy. Even with the close connection between the antiferromagnetic and the ferrimagnetic spin chain their dispersions are quite different. Of course a lower and upper excitation band exists in the ferrimagnetic case, which are separated for $S_A > 2S_B$, but also the dependence of dispersions close to $q = 0$ is quadratic instead of linear. Yet the energy dependence close to the respective maxima is the same as for the antiferromagnetic chain.

3

Methodology for neutron scattering experiments

The goal of the present study is to understand the magnetic order and spin dynamics exhibited by $CaBaCo_2Fe_2O_7$ and how this relates to the other isostructural compounds of the Swedenborgite family. The crystal structure of $CaBaCo_2Fe_2O_7$ has already been solved using X-ray scattering [Val04b] and refined using neutron scattering [RRS$^+$14]. Its magnetic properties have been investigated in magnetization measurements and single crystal neutron diffraction experiments [Ros11]. However, a determination of the magnetic structure has yet to be performed and some results especially a spin reorientation (cf. Fig. 5.3) cannot be explained with a simple Heisenberg nearest neighbour model (cf. Section 4.1). This will be discussed in Subsection 5.1.2. In order to address these open questions, instruments with high resolution are necessary. At the same time in the case of $CaBaCo_2Fe_2O_7$ the use of XYZ-polarization analysis gave a better insight to the magnetic ordering amongst others revealing a spin reorientation not visible in the total magnetic scattering [Ros11]. Therefore, the usage of instruments providing both polarization analysis as well as high resolution is advised. Yet both methods come along with a significant decrease in neutron flux. That is why they are not widely available and experiments will take more time for the same statistics compared to experiments, which do not use these options. In this study we have been challenged to add new methods to existing instruments to suit our needs or use suitable ones in new ways if they are designed for different tasks. If the way, a specific instrument is usually used, was not sufficient for our studies, a detailed description is presented in the following. However, it is also important to back the new methods up with established ones, so the results can be cross-checked with tested setups. Where the instrument has been used in its usual way and comprehensive descriptions are available they will be referenced where used in Chapter 5.

The strategy we have utilized in the course of the study was to start with a widespread investigation of the compound and then to focus on specific observations of interest. Therefore, we have started with the investigation of the magnetic order using a neutron powder diffractometer with a high resolution, POWGEN at SNS, Oak Ridge (USA). This way it was assured, that no magnetic features were missed. However, in powder diffractograms the actual peak structure is not visible due to the powder average. Previously the magnetic structure has been refined successfully for similar compounds from powder data [SYM$^+$06, CRZM06, CPH$^+$10]. Yet, in the case of a more complex type of magnetic order, powder diffraction might be insufficient. In order to solve this issue a four-circle single crystal diffractometer was used next, Morpheus

(PSI, Villigen, Switzerland). With the help of a four-circle setup a larger set of peaks distinct from the background can be measured separately (cf. Tables D.1 and D.3). Here, the integrated intensities have been determined to solve the magnetic structure. These first measurements already indicate a more complex magnetic structure, which in order to understand required to resolve the peaks in **Q** as well as a large coverage in reciprocal space to ascertain that this structure is repeated regularly. The ideal instrument of choice has been the single crystal neutron diffractometer BioDiff (MLZ, Garching, Germany) [SOL$^+$11] (cf. Section 3.2). Following this, the structure of the magnetic ordering is investigated by mapping few peaks in **Q**. For this purpose experiments have been conducted on two different single crystal diffractometers, Morpheus and MIRA (MLZ, Garching, Germany), mapping a smaller set of magnetic Bragg peaks. In order to investigate the underlying spin structure in detail, polarization analysis has been applied, which allows to measure the vector properties of the scattering, distinguishing in-plane and out-of plane moments as well as chiral properties (cf. Section 3.3). Combining the results from the different experiments allowed for a reliable solution. Still, further insight can be gained from the spin dynamics present in the compound. Previous studies already revealed a rather complex structure [Rei11]. Therefore an adopted resolution is required to resolve the excitations in **Q** and energy. A good resolution is provided at triple axis spectrometers, but such instruments only allow for measuring the excitations along certain axes and is either suited for excitations at low energies (can reach only up to 15 to 20 meV with cold neutrons depending on instrument and **Q**) or at higher energies with hot neutrons, again at the drawback of decreased resolution. Thus different instruments have to be used to cover the whole range in excitations. A new instrument type has been developed recently, which is a time-of-flight spectrometer using several incident energies simultaneously. Depending on which part in **Q** and energy is of interest the data set from the incident energy providing the best resolution still reaching this part can be used.

3.1 Sample description

In total three different single crystals and a powder sample grounded from a single crystal of $CaBaCo_2Fe_2O_7$ have been used for the experiments. All single crystals have been synthesized using the same floating zone method (M. Valldor). The synthesis is described in detail in [RRS$^+$14]. Two large single crystals have been grown from a preoriented seed (cf. Fig. 3.1a). The orientations have been chosen in a way, that if the crystal is mounted with the main rotation axis parallel to the growth direction, the horizontal scattering plane corresponds to the $(h\,k\,0)$ ($\sim 3\,\mathrm{cm}^3$ and $\sim 5\,\mathrm{g}$) and $(h\,h\,l)$ ($\sim 2\,\mathrm{cm}^3$ and $\sim 3\,\mathrm{g}$) scattering planes, respectively, to about 2°. These scattering planes have been chosen as they are the most interesting in hexagonal symmetry in combination with antiferromagnetic order. A crystal with a $(h\,0\,l)$ orientation was available as well, but not used in the thesis at hand. The third single crystal is of smaller size ($2 \cdot 2 \cdot 2\,\mathrm{mm}^3$ and 37.5 mg) with its top and bottom planes perpendicular to the c-axis (cf. Fig. 3.1b).

At the start of the study mainly the larger single crystals have been used as they offer a higher flux of scattered neutrons. On the one hand this allows for better statistics or shorter measurement times, on the other hand some experiments are not reasonable on small crystals due to insufficient statistics e.g. inelastic neutron scattering experiments. After determining the general magnetic order using the larger crystals and figuring out what might be of specific in-

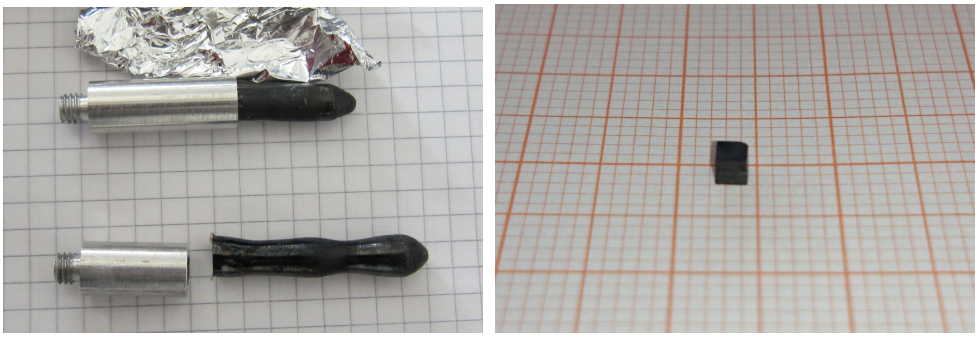

(a) **(b)**

Figure 3.1: Shape and size differences of the single crystals used in the experiments relevant for the present thesis.
(a) Large single crystals with $(h\,h\,l)$- and $(h\,k\,0)$-orientation and aluminium sample holders. **(b)** Small crystal with its c-axis oriented parallel to the normal vector of the paper.

terest the smaller crystal was used because of the enhanced resolution. This way the magnetic structure can be investigated in detail.

3.2 Exploring the Q-space with high resolution

The single-crystal neutron diffractometer BioDiff is situated at the FRM II in Garching (Germany). It is designed with a high resolution intended for resolving structures of large biological macromolecules. In contrast to most single crystal diffractometers, which use small area detectors or even point detectors, here a large cylindrical shaped area detector is used covering about 3.02π sr [SOL$^+$11]. The small sample was mounted on a aluminium rod and covered with the aluminium container of the cryostat (cf. Fig. 3.2). Then the sample position is adjusted in x, y and z regarding the incident beam. Instead of the image detector a CCD camera was used as a detector, which allows for a faster recording and reading. In fact this measurement was the first one of a solid state crystal with a small (relative to the usually measured protein crystals) unit cell and at temperatures down to 4 K. Due to the antiferromagnetic order, the magnetic unit cell of $CaBaCo_2Fe_2O_7$ is enlarged, but still only up to eight peaks are visible on the same detector image instead of a several hundred peaks. This renders the usual methods to determine the orientation and structure from a single frame impossible and the development of a new software, which uses the whole set of measurements for the evaluation, was required. As discussed in Section 2.1 the Ewald sphere is projected onto the area detector. Due to the cylindrical shape of the detector only the top and bottom part of the Ewald sphere are not covered (see Fig. 3.3a). Knowing the dimensions of the area detector each pixel position p is calculated to spherical coordinates of the Ewald sphere, with the incoming beam at $\varphi_p = 0$, $\theta_p = 0$. Then the sample rotation ω_n for each step n and the incoming wavelength $\lambda_i = \frac{2\pi}{k_i}$ are used to convert the

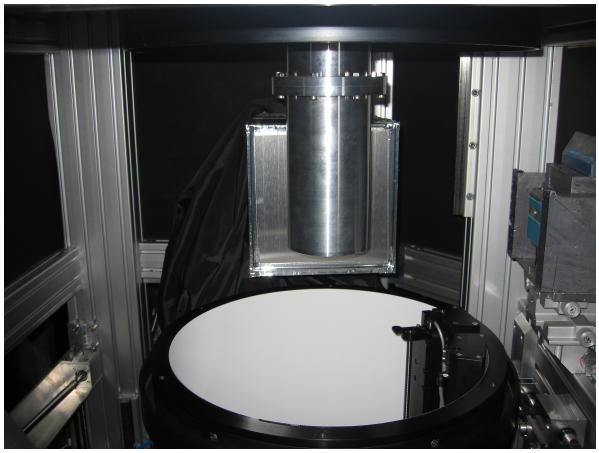

Figure 3.2: Instrumental setup at Biodiff. Sample is mounted inside an aluminium can. The cylindrical image plate was moved to the bottom for mounting the can. The CCD camera is to the back and the incident beam to the right.

detector pixel positions into **Q**-space:

$$\mathbf{Q}_p = k_i \cdot \begin{pmatrix} \cos\omega_n & -\sin\omega_n & 0 \\ \sin\omega_n & \cos\omega_n & 0 \\ 0 & 0 & 1 \end{pmatrix} \cdot \begin{pmatrix} \cos\theta_p \cdot \cos\varphi_p + 1 \\ -\cos\theta_p \cdot \sin\varphi_p \\ \sin\theta_p \end{pmatrix}. \tag{3.1}$$

It is preferable to determine the orientation matrix of the crystal, which can be used to correct for a misalignment. Yet this was not possible using the available software. In case of the investigated single crystal this is a few degrees only, which will not yield huge deviations for single scattering planes. After the conversion the detector images can be sorted in a three dimensional rectangular regular grid, while normalizing by the amount of pixels per volume element. Afterwards a volume of the grid can be selected and summed up along one of the directions, which will yield a two dimensional image with the colour code related to the measured intensity. In the specific case of this experiment the step width for the sample rotation has been chosen in relation to the instrument resolution, meaning the addition of intermediate steps will not result in additional information. Still the shape of the Ewald sphere yields a non-regular grid with a lower density in certain volumes. In order to prevent empty elements in these volumes of the measured **Q**-space, while keeping a high resolution of the regular grid, the detector images have been interpolated. Let the geometry of two Ewald spheres related to two detector images D_n and D_{n+1} of neighbouring sample rotation steps n and $n+1$ differ in rotation by $\Delta_n = \omega_{n+1} - \omega_n$ (cf. Fig. 3.3b). Then the intensity $I_{n,i,p}$ for pixel p of each interpolated detector image will be calculated weighing the pixels' intensity of the neighbouring detector images according to its intermediate rotation ω_i, with $\omega_n < \omega_i < \omega_{n+1}$:

$$I_{n,\omega_i,p} = I_{n,\omega_{n+1},p} \cdot \frac{\omega_i - \omega_n}{\Delta_n} + I_{n,\omega_n,p} \cdot \frac{\omega_{n+1} - \omega_i}{\Delta_n}. \tag{3.2}$$

The resulting detector images will be sorted into the regular grid in the same manner. The interpolation takes place along the segment of a circle, which is physically questionable. But considering the already small rotation steps, this is a justifiable approximation and allows for a

significantly faster computation.
Lastly, it is important to mention, that all detector images feature a similar periodic intensity pattern as systematic background, which stems from the photoelectric reading mechanism. This results in a relatively high uniform background in the extracted cuts. That is why scattering of lower intensity might not be observable.

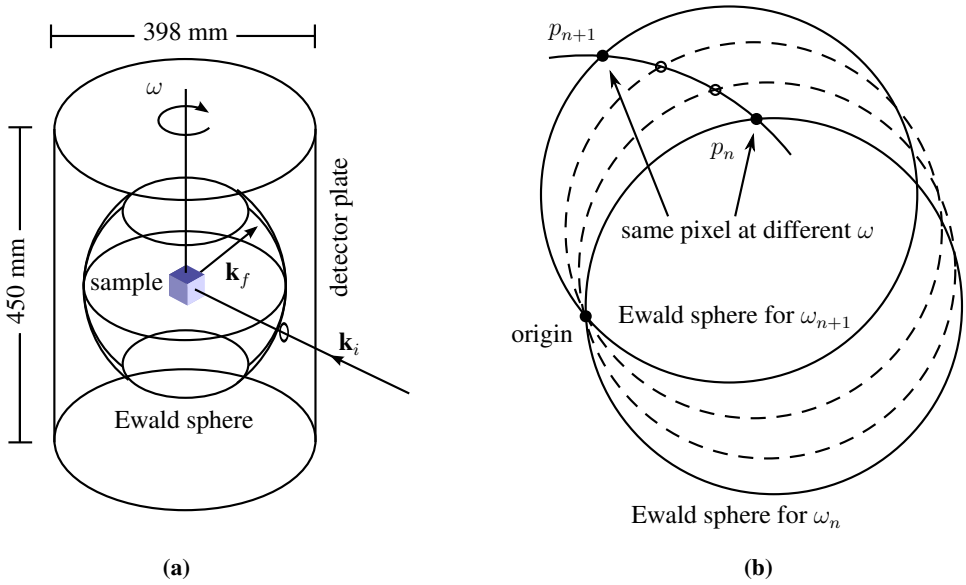

Figure 3.3: Schematics regarding the evaluation of the detector images taken at BioDiff. **(a)** The Ewald sphere of the scattered beam is projected onto the cylindrically shaped detector plate. **(b)** Horizontal cut through the Ewald sphere displaying the method of interpolation between two detector images of neighbouring rotation steps.

3.3 Combining polarisation analysis with four-circle geometry

The combination of a polarization analysis with a four-circle geometry is very helpful as it combines two advantages. On the one hand a four-circle diffractometer provides the versatility to access a lot of peaks of different scattering planes using the same sample. Therefore, this geometry is not only used for neutron scattering experiments but also widely spread for X-ray scattering experiments as well. On the other hand the polarization analysis offers a more comprehensive insight into the spin structure of the material's magnetic order. Still this combination especially considering the more advanced XYZ-polarization analysis is quite unusual and, to our knowledge, there are no experiments providing it. Therefore, it was necessary to construct additional parts, which allow the magnetic field at the sample position to be tuned, in order to complete the setup. In the following, two different approaches will be presented, first using a cage of permanent magnets at Morpheus and second using hand-wound coils at

MIRA. However it is essential to provide a short introduction in to the geometry of the four-circle diffractometer.
The name of the geometry stems from the four different angles which are used to rotate the crystal as well as the detector to measure at each desired point in **Q**-space. Theoretically, three angles should be sufficient, namely an angle χ to cant the horizontal scattering plane, an angle ϕ, which is on the circle of χ, to rotate the sample round itself and an angle 2θ for the rotation of the detector arm along the instrument floor. However, in regards of the actual instrumentation the dimensions of a setup put constraints on the range of these angles. In order to compensate for that four angles have been found to be ideal. The additional angle ω is used to rotate the sample around the normal vector of the horizontal scattering plane. This also allows access to the same points in **Q**-space using different combinations of angles, which is helpful in the case of further equipment being introduced to the setup. Apart from the polarisation analysis also the cryostat, required for temperature dependent measurements, puts additional constraints on the movability.

The neutron scattering instrument Morpheus is located at the spallation source of the Paul Scherrer institute in Villigen (Switzerland) and is a multi-purpose instrument as the single parts can be interchanged according to the specific needs. Thus for every new experiment the user can and has to adjust the instrument. This allows for a wide range of possibilities covering elastic diffraction as well as reflectometer geometry. Here two different setups have been used. The first one was optimized in order to measure the integrated intensities on as many magnetic Bragg peaks as possible on the large crystal with hhl-orientation, whereas the other setup is intended to map several magnetic Bragg peaks with polarization analysis on the large crystal with hk0-orientation. In both cases we are interested in accessing the magnetic scattering of different scattering planes, which is why the instrument was setup consistently as a single crystal four-circle diffractometer. The first three circles are provided by mounting the sample in a Eulerian cradle and the last one is the detector arm. At the end of the detector arm a point detector is mounted. For the first experiment this is already sufficient and provides the widest possible range for the angles. But for the second one the setup was extended to provide polarization analysis (cf. Fig. 3.4). The necessary parts have been described in Section 2.3. Here polarizing supermirrors and a Mezei-type flipper have been used. The guide field has been created using permanent magnets. The polarization was setup in a so-called *crossed* way. Such that the analyser scatters the neutrons which have not been flipped by the scattering with the sample. The spin flipped neutrons are measured by a point detector. Using the flipper both channels are accessible. The magnetic field responsible for the neutron orientation at the sample position is created with a small cage built from permanent magnets and metal plates (cf. inset of Fig. 3.4). Thus, a manual reassembling of the cage is necessary for the measurement of polarization channels with a different magnetic field. Due to the construction with metal plates and permanent magnets this was most practical for magnetic fields parallel to $\hat{\mathbf{e}}_x$ direction. The metal plates normal vector points perpendicular to the area normal vector of the Eulerian cradle and parallel to **Q**. Yet, keeping the magnetic field (anti)parallel to the scattering vector as desired for the polarization analysis requires a fixed relation between the ω and 2θ angles, which reduces the accessible **Q**-space. Introducing the magnetic cage into the Eulerian cradle strongly restricts the accessible angle range on the one hand due to the cryostat hitting the cage or the cage blocking the incident and scattered neutron beam.

The neutron scattering instrument MIRA located at the FRM II in Garching (Germany) is another multi-purpose instrument, which has been used successfully among others as a reflectome-

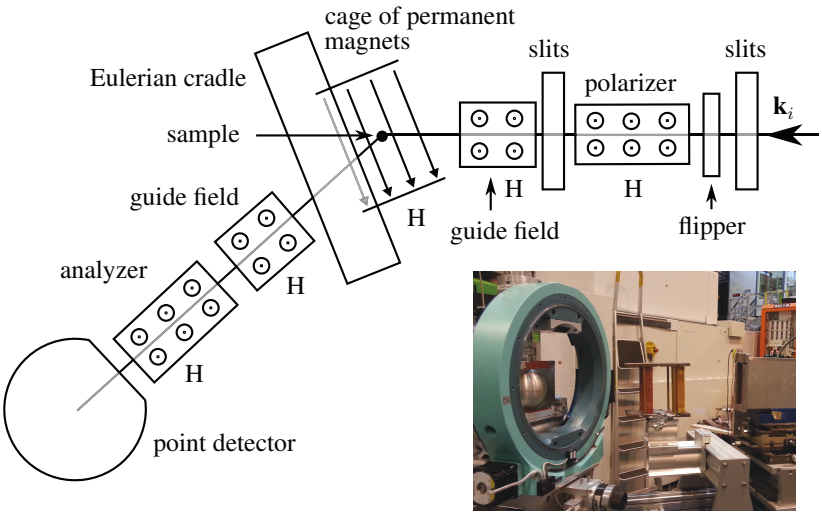

Figure 3.4: Schematic drawing of the polarization analysis setup at the neutron diffractometer Morpheus for the polarization channel H parallel to **Q**. The inset shows the Eulerian cradle and inside the metal plates held together with the permanent magnets, as well as in the middle the permanent magnets for the guide field and to the right the analyser.

ter or even a triple axis spectrometer [GBJ$^+$07]. Similar to the setup for Morpheus a four-circle geometry is used together with a full polarization option including a flipper and an analyser. But here a $20 \times 20\,\mathrm{cm}^2$ position sensitive detector (PSD) with a $1 \times 2\,\mathrm{mm}^2$ resolution is available, which allows one to resolve the magnetic peaks along the horizontal and vertical direction at the same time. The large crystal with $(h\,k\,0)$-orientation and the small crystal have been measured. Both crystals have been oriented with their c-axis parallel to the rotation axis for angle ω. This allows for measurements in the $(h\,k\,0)$-scattering plane without rotating around other angles. From the experiment at BioDiff it has been found, that the magnetic peaks are broad within the scattering plane but sharp along the perpendicular direction. Thus the supermirror was mounted with the mirrors horizontal to prevent discontinuity in the magnetic peaks' detector image stemming from the wedge formed by two mirrors. Provided by the instrument a fully polarized option was available [GBP03], consisting of polariser, analyser and guide fields (see Figs. 3.5a and 3.6). But the XYZ-polarization analysis has been found necessary in our case. Thus around the sample position a cage formed by electromagnetic coils has been created (see Fig. 3.5b), allowing for a tuning of the magnetic field at the sample position along $\pm x$ and $+z$ direction. In comparison to the setup at Morpheus this one allows for easier change of the magnetic field, reproducibility and even wider rotations of the Eulerian cradle. Also, using a combination of coil currents other field contributions at the sample position can be compensated. The circle of the detector arm has been linked to the ω-angle in a way that the conditions for XYZ-polarization analysis are fulfilled ($\mathbf{H}_{\pm x} \parallel \mathbf{Q}$). The general setup of the magnetic guide fields was optimized to allow for an adiabatic spin reorientation in combination with the hand-wound coils using a magnetic probe. Then the coil currents were calibrated using the spin-flip ratio observed on a crystal structure peak. As the flipper is far away from the sample, its magnetic field has only a minor influence compared to the coils for the neutron spin orientation at

the sample position and also vice-versa. Thus, the flipper currents were optimized independently.
From previous experiments using the instrument as a triple axis spectrometer (TAS) the methods for evaluating the detector images for measurements, which keep to TAS geometry, have been readily available and the equations for the XYZ-polarization analysis could be added to the evaluation. In this geometry the measured detector images are summed perpendicular to the horizontal scattering plane increasing the statistics, which is a valid simplification considering the distance between sample and detector. Yet here the magnetic peaks in other scattering planes ($(h\,k\,1)$ and $(h\,k\,2)$) were measured as well, at this point the vertical arrays of the detector plate are no longer perpendicular to these scattering planes. In this case, summing the detector vertically contributes intensities to the false positions. Thus, the evaluation methods had to be improved by converting each detector pixel into three dimensional **Q**-space based on the instrument geometry. Afterwards the points in **Q** of each set of detector images are sorted into a regular rectangular grid, similar to the method used for BioDiff. The density of the measured pixels is increased using the same interpolation between neighbouring detector images as described for BioDiff (cf. Section 3.2). Due to the size of the analyser and its distance to the detector, only part of the area detector is effectively covered by the analyser. Also the casing of the analyser is visible as a significant drop in intensity on the detector images, obstructing the scattered neutrons. For each sample and experimental setup, the pixel array detecting neutrons, which have passed through the analyser, is selected and the rest is masked in the software in order to decrease the background and contributions from other channels. In cases where no analyser was installed the whole detector image is used in the software.

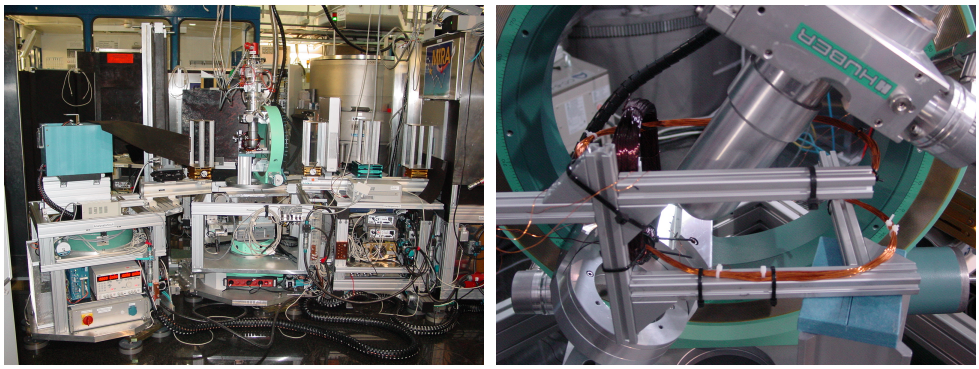

(a) **(b)**

Figure 3.5: Polarization setup on the neutron diffractometer MIRA.
(a) Overall setup with the incoming beam from the right. **(b)** Close up of the cage of hand-wound coils at the sample position.

In both cases the polarization setups allow to measure the polarization channels $I_{x\bar{x}}$ and $I_{\bar{x}x}$, because the crystal and magnetic Bragg peaks are separated in **Q** for K-type antiferromagnetic ordered compounds like $CaBaCo_2Fe_2O_7$. Thus the Equations 2.30 and 2.31 can be used to calculate the scattering contributions total magnetic scattering and chiral magnetic scattering. The two other polarization channels give insight into the orientation of the moments regarding the scattering plane. The channel $I_{z\bar{z}}$ is proportional to the scattering from moments parallel to the scattering plane (cf. Eq. 2.32) and I_{zz} is proportional to the scattering from moments

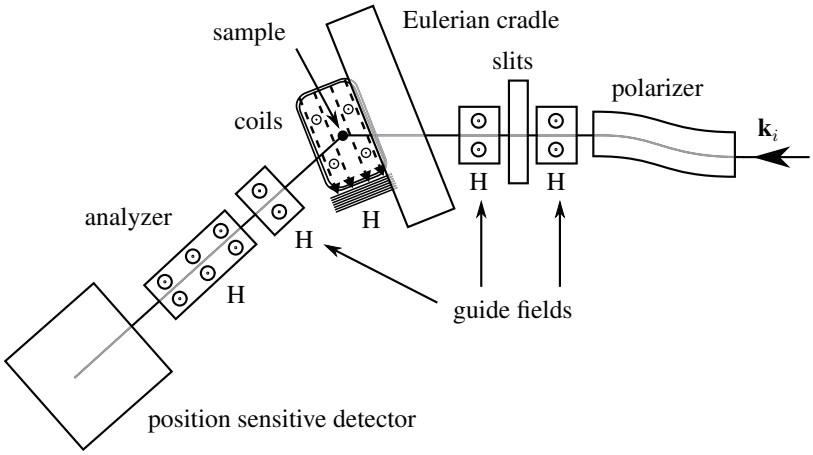

Figure 3.6: Schematic of the configuration for the polarization channel H parallel to **Q** setup at the neutron diffractometer MIRA (cf. Fig. 3.5).

perpendicular to the scattering plane (cf. Eq. 2.33).

3.4 Time-of-flight spectroscopy and data preparation

4Seasons is one of two neutron time-of-flight spectrometers found at the spallation source of the MLF facility of J-Parc in Tokai (Japan) [KNN+09, KNI+13]. It provides an angular detector coverage of 90° of position sensitive He^3 coils along the horizontal plane, and also a vertical angular coverage of 52°. The incoming neutron flux is highest in the thermal regime at up to 300 meV. It stands out from other experiments like e.g. ARCS at the SNS in Oak Ridge (USA), because it supports multi-incident-energy measurements. The unused detector time in the distance vs. time diagram stemming from the time between two pulses can be filled with the scattering from neutrons of different incident energies [LSM08]. At 4Seasons one can measure the excitations with up to four different incident energies at the same time. This allows for adopted resolution in energy and **Q**-space at the different energy levels as well as measuring different parts of the **Q**-space at the same time. As the inelastic scattering usually suffers from the low statistics or longer measurement times, this is a significant improvement. Depending on the choice of energies this comes at the drawback of the higher energies in spin wave excitation being contaminated from the excited neutrons scattered at an earlier time in the distance vs. time diagram.

As this kind of instruments covers a huge part of **Q**-space, in principle, only a rough orientation of the sample is necessary, which is done beforehand. Here the instrument itself did not offer a possibility to improve the orientation. The data is collected in coordinates of scattering angles and time-of-flight, and need to be transformed to **Q** and energy-space. The transformed data as

received shows a small misalignment of the sample (cf. Fig. 3.7a) and a correction was needed to make best use of the data. In order to correct the remaining misalignment by software the orientation of the crystal has to be determined during the experiment. This can be achieved by performing a so-called Laue diffraction using a white neutron beam with dephasing the chopper. Due to the band of wavelengths the Bragg condition is fulfilled for a huge set of Bragg peaks at the same time, which can be in turn used to determine the crystal orientation. Such a method is applied at ARCS, but was not available here. Thus, the orientation has to be determined from the measured data set. One possibility is to use the regular grid of the Bragg reflections. If one can rotate the data set in a way that the Bragg reflections are superimposed along different viewing directions, the orientation of the crystal can be easily extract. Technically the reorientation is trivial, but these data sets can become quite large ($\approx 100\,\mathrm{GB}$), which is computational challenging. Together with the IT department of the JCNS/PGI of the Forschungszentrum Jülich a new software was developed which allows for displaying these huge datasets and real-time rotation at the same time [Rhi14]. The determined orientation will be used for the data evaluation in Subsection 5.6.2. The benefit of a corrected sample misalignment, even if it is only slightly (here about 2°), is, that the reciprocal lattice is set up for the evaluation allowing for cuts based on this lattice. Also integration along the axes of this lattice will add up the measured excitations without blurring these further. Otherwise hardly any evaluation can be performed. Here the large single crystal with $(h\,h\,l)$-orientation has been measured. The impact of the misalignment can be seen in Figure 3.7a especially in comparison with the reoriented dataset (see Fig. 3.7b).

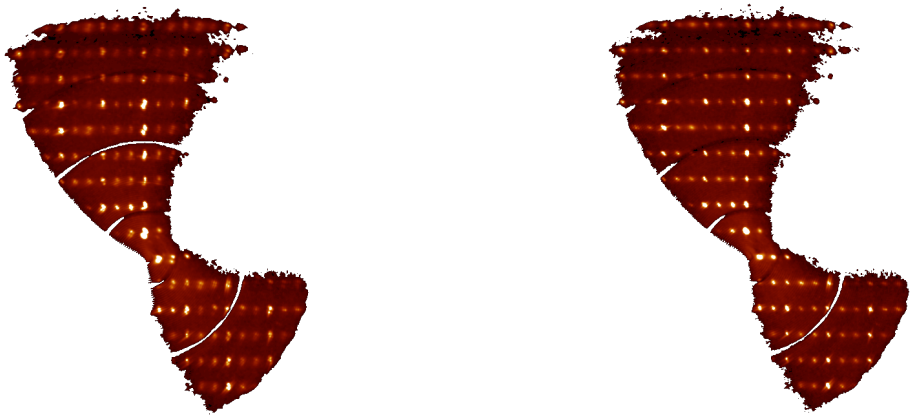

(a) **(b)**

Figure 3.7: Correction of the misalignment present in the hhl-oriented single crystal measured at 4Seasons. Here the measurement at 4 K with an incident energy of 90 meV is shown.
(a) In case of the misaligned crystal the $\{h\,h\,l\}$-scattering planes show a doubling of peaks. **(b)** After applying a slight reorientation the magnetic and crystal structure peaks of the $\{h\,h\,l\}$-scattering planes superimpose perfectly.

4

Magnetic frustration in the layered kagome system of the Swedenborgite structure

During the last few years, the study of compounds exhibiting unusual magnetic order due to geometric frustration has attracted major interest. They offer opportunities to observe novel ordering phenomena. Some material classes such as the pyrochlores have been investigated quite intensively. Another class, the Swedenborgites, have been discovered just recently. The compound family is named after the original mineral $NaBe_4SbO_7$ [AB33]. The hexagonal structure was determined to be of the $P6_3mc$ crystallographic space group. This material features triangular and kagome layers of Beryllium ions stacked along the c-direction parallel to the six fold screw axis (cf. Fig. 4.1).

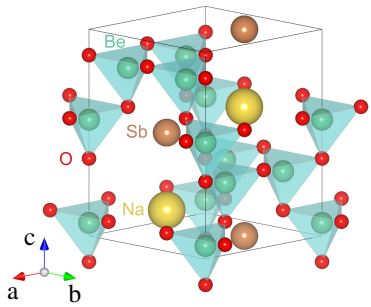

Figure 4.1: Crystal structure of the mineral $NaBe_4SbO_7$ called Swedenborgite [PKW35].

These two dimensional lattices are of great interest, because they are prone to geometric frustration. If the lattices are formed by magnetic ions and antiferromagnetic interactions are present, it can result in a huge manifold of spin states equivalent in energy. In [VA02] it was shown, that the Beryllium ions can be substituted with magnetic ions by synthesizing the compound $YBaCo_4O_7$. Here the cobalt ions form magnetic triangular and kagome layers, which results in columns of double tetrahedra along the c-axis on a triangular layer [VSS09]. In the following years various other isostructural compounds have been successfully synthesized with purely magnetic ions on the Beryllium sites like $YBaCo_3FeO_7$, $CaBaCo_3FeO_7$ and $CaBaCo_2Fe_2O_7$ and

also with partially non magnetic ions like $CaBaCo_3AlO_7$ and $YBaCoZn_4O_7$ [Val04b]. Already in magnetisation and susceptibility measurements they displayed complex magnetic properties, e.g. spin-glass-like in $YBaCo_{4-x}Zn_xO_7$ [Val04a] and (Ca,Y)Ba(Co,Fe,Al,Zn)$_4$O$_7$ [Val05a] or disordered antiferromagnets for $CaBaCo_{4-x-y}Zn_xAl_yO_7$ [Val05b]. Further studies reveal a large variety of ordering phenomena in various experiments as well, e.g. short-range order, 1d order, 2d order, spin glass or spin liquids [SYM$^+$06, SVL07, MCR$^+$09, CRZM06, RPCM11, HMZ$^+$06]. Up to now the only materials observed to exhibit a 3D magnetic order undergo a structural transition from the hexagonal space group to an orthorhombic one, which takes place at a higher temperature [HMZ$^+$06, KCR$^+$09, VSS09]. Therefore, these compounds are not suitable for the study of the magnetic order in the Swedenborgite structure.

4.1 Model description of the magnetic order

In [MCR$^+$09, KMMC10] a Heisenberg nearest neighbour model has been developed to model the scattering observed in $YBaCo_4O_7$ belonging to the Swedenborgites. But as all Swedenborgites share the same magnetic structure the model is useful for other compounds as well. The magnetic ions form both kagome and triangular layers, which are stacked along the c-direction. While the triangular layer can be mirrored at the kagome layers, the latter are rotated by 60° against each other. Regarding a- and b-axes the triangular sites are located in the centre of kagome triangles. This leads to columns of double tetrahedra along the c-axis. Four bonds can be distinguished: 1. inter-column kagome-kagome, 2. intra-column kagome-kagome, 3. kagome to upper triangular site, 4. kagome to lower triangular site. Thus, four different exchange interactions can exist. In [KMMC10] the reduction to two interactions has been discussed. It has been found, that with small deviations one interaction for the in-plane bonds J_{in} and one for the out-of-plane bonds J_{out} is sufficient. This results in the Heisenberg nearest neighbour model:

$$H = -\sum_{i,j \in \text{ same layer}} J_{\text{in}} \cdot \mathbf{S}_i \cdot \mathbf{S}_j - \sum_{i,j \in \text{ diff. layer}} J_{\text{out}} \cdot \mathbf{S}_i \cdot \mathbf{S}_j. \tag{4.1}$$

with $J_{\text{in}}, J_{\text{out}} < 0$ and spins $\mathbf{S}_i$ of unity length. The double tetrahedron is the essential building block for the whole spin structure, where the model for each one can be written as:

$$H_{DT} = -\frac{J_{\text{in}}}{2}\left[(\mathbf{S}_1 + \mathbf{S}_2 + \mathbf{S}_3 + \tau\mathbf{S}_4 + \tau\mathbf{S}_5)^2 - 2\tau^2\mathbf{S}_4 \cdot \mathbf{S}_5 - C\right] \tag{4.2}$$

with ratio $\tau = J_{\text{out}}/J_{\text{in}}$, kagome spins $\mathbf{S}_1, \mathbf{S}_2, \mathbf{S}_3$, triangular spins $\mathbf{S}_4, \mathbf{S}_5$ and constant $C = \mathbf{S}_1^2 + \mathbf{S}_2^2 + \mathbf{S}_3^2 + J_{\text{out}}\mathbf{S}_4^2 + J_{\text{out}}\mathbf{S}_5^2$. Minimizing the energy for the double tetrahedron results in two constraints

$$\max(\mathbf{S}_4 \cdot \mathbf{S}_5) \tag{4.3}$$

and the so-called sum rule:

$$\min(\mathbf{S}_1 + \mathbf{S}_2 + \mathbf{S}_3 + \tau\mathbf{S}_4 + \tau\mathbf{S}_5)^2. \tag{4.4}$$

The constraint 4.3 can only be maximized by orienting the triangular spins parallel, which is independent from the interactions or kagome spins. The minimization of Equation 4.4 includes both triangular and kagome spins. It also depends on a weighing factor τ, which is the ratio

between the exchange interactions J_{out} and J_{in}. Taking the constraint 4.3 into account, this can only be minimized if the triangular spins $\mathbf{S}_{\text{tri}}$ are compensated by the kagome spins $\mathbf{S}_{\text{kag}}$:

$$2\tau\mathbf{S}_{\text{tri}} = -\sum_{i\,\in\,\text{kag}} \mathbf{S}_i = -\mathbf{S}_{\text{kag, eff}}. \tag{4.5}$$

The three kagome spins add up to the effective spin $\mathbf{S}_{\text{kag, eff}}$ antiparallel to $\mathbf{S}_{\text{tri}}$. For $\tau \geq 1.5$ the best solution is to orient each kagome spin antiparallel. For $\tau < 1.5$ the kagome spins must not align parallel and thus a manifold of best solutions exists. In this sense the frustration inherent to the system increases the number of possible states and the entropy. Using Monte Carlo simulations (MCS) a ratio close to $\tau = 1.0$ was found to best model the observed scattering in $YBaCo_4O_7$ [MCR$^+$09].
Calculating the specific heat from MCS, a phase diagram for temperature T/J_{in} versus ratio

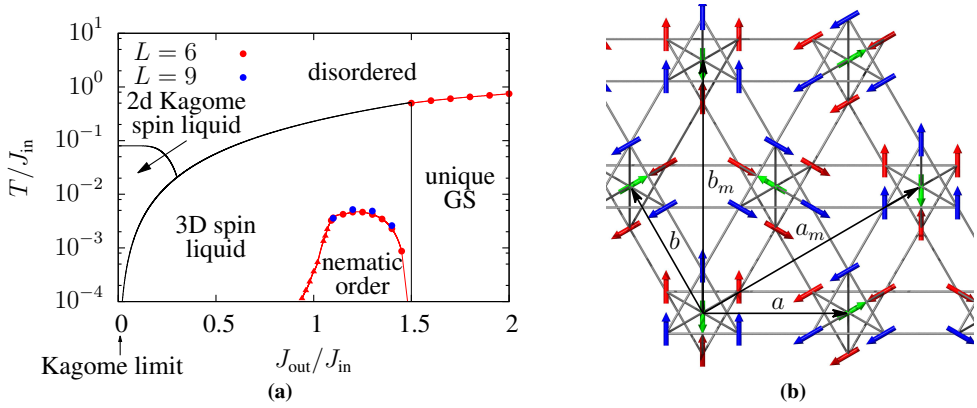

Figure 4.2: Results from Monte Carlo simulation based on the Heisenberg nearest neighbour model. **(a)** Phase diagram with T/J_{in} vs. ratio $\tau = J_{\text{out}}/J_{\text{in}}$. Figure adapted from [BF14]. **(b)** Ground state in the antiferromagnetically ordered phase [KMMC10, Ros11, BF14], view along c-axis. Triangular spins in green and kagome spins in red/blue. Figure adapted from [Rei11]. Kagome spins with the same colour are of the same layer.

τ has been determined in cooperation with our group [BF14] (cf. Fig. 4.2a). It displays a disordered regime at $T \gtrsim 0.5 \cdot J_{\text{in}}$. Depending on τ a phase transition to either an antiferromagnetically ordered state ($\tau \geq 1.5$) or a 3D spin liquid regime exists. For ratios $0.9 < \tau < 1.5$ a nematic phase has been found at even lower temperatures and was postulated for ratios down to $\tau = 0$. According to the the sum rule in the antiferromagnetically ordered phase for $\tau \geq 1.5$ a unique solution exists for each double tetrahedra. Thus a unique solution follows for the whole spin structure (cf. Fig. 4.2b) as no freedom is left for the spins to vary. Decreasing the ratio below $\tau = 1.5$ a manifold of solutions exist for each double tetrahedra, but the triangular spins of the same column stay parallel due to Eq. 4.3. In MCS, periodic boundary conditions are used, as these spin structures become unstable without. But this also leads to neighbouring columns following the periodicity, which results in a spin structure similar to the unique ground state with canted kagome spins. The strength of canting depends on the freedom provided by the sum rule. Within this state the energy can be minimized for each kagome layer separately. Thus this ordering can be considered a 3D spin liquid. With decreasing ratio τ the exchange

interaction J_{out} becomes of less importance and the spin structure deviates more strongly from the unique ground state, which ultimately resolves in the kagome limit for $J_{\text{out}} = 0$.

4.2 Spin wave dispersions with LSWT

Using MCS a unique ground state has been found for $\tau \geq 1.5$. This enabled us to calculate the spin wave dispersions based on the Heisenberg nearest neighbour model using linear spin wave theory [Rei11]. For ratios $\tau < 1.5$, the system is in the spin liquid phase, which does not order in a specific ground state. Therefore, only the dispersions for ratios $\tau \geq 1.5$ can be calculated with LSWT based on this ground state.
The dispersions strongly vary for the different symmetry directions within the magnetic Bril-

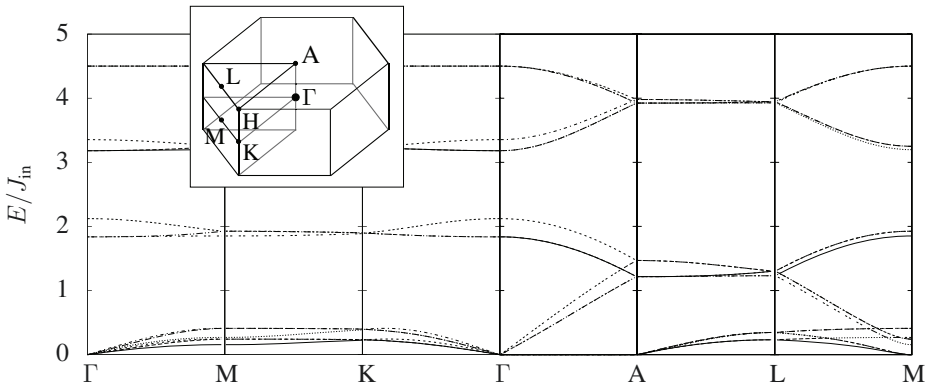

Figure 4.3: Spin wave dispersions determined with LSWT for $J_{\text{out}}/J_{\text{in}} = 1.5$, based on the Heisenberg nearest neighbour model [Rei11]. The inset shows the high symmetry points of the hexagonal Brillouin zone. The dispersion in $\{h\,k\,0\}$-scattering planes are rather flat, compared to the steep dispersions along $\langle 0\,0\,1\rangle$-directions. Furthermore, a large gap in energy is present.

louin zone (BZ). Along the directions within the $\{h\,k\,0\}$-scattering planes the dispersions are rather flat or even constant in energy, while the dispersions along $\langle 0\,0\,1\rangle$ show a steep slope from the high symmetry point Γ to A and M to L. This means the spin wave propagates at a higher velocity along the c-axis direction compared to the spin waves in the ab-plane. The dispersions appear to be folded back at the BZ boundary to the next magnetic BZ in c^*-direction. This means that the magnetic unit cell could be viewed as half its size. This would resolve in the upper limit of the dispersions to be at the A-point. Furthermore, it is apparent that two different excitation bands exist, which are separated in energy. The lower one goes from the elastic line up to $E \approx 2 \cdot J_{\text{in}}$, where the upper one spans from $E \approx 3.2 \cdot J_{\text{in}}$ to $E \approx 4.5 \cdot J_{\text{in}}$ leaving an excitation gap of about $\Delta E \gtrsim 1 \cdot J_{\text{in}}$. In this sense the dispersions are similar to the ones of ferrimagnetic linear spin chain (cf. Fig. 2.7), but there are also very distinct deviations. For instance here the lower dispersions show a linear energy dependence close to the Γ-point and therefore, more closely related to the dispersions of an antiferromagnetic spin chain. Only at the M-point a quadratic energy dependence is present with an energy gap of $E = 0.2 J_{\text{in}}$. Furthermore, the lower and upper excitation band span over a different range in energy. These deviations stem

from the difference between a simple spin chain and the coupled double tetrahedra columns. In both cases all spins are assumed to be of the same length, still an upper band is present. Similar dispersions are found considering just the double tetrahedra, which is why the influence of the coupling is relative small. This leads to the conclusion of two different spin wave types. For the lower excitation band the antiferromagnetic spin chain spanned by the single kagome and triangular spins is relevant, but in the case of the upper excitation band a ferrimagnetic spin chain formed by the triangular spins and the effective spin of the kagome spins has to be considered (cf. Eq. 4.5).

4.3 Beyond the harmonic approximation using spin dynamics simulation

The spin wave dispersions determined using linear spin wave theory (cf. Section 4.2) are limited to ratios $\tau \geq 1.5$ and the linear terms. But especially for ratios $\tau < 1.5$, rich physical observations can be expected according to the phase diagram (cf. Fig. 4.2a). Furthermore, since strong frustration is present in the Swedenborgite compounds, the higher order terms might play an important role in the excitations. In order to calculate the spin wave excitations for models without a unique or even unknown ground state, other methods have been developed. For example Monte Carlo simulation can be used to relax the spin system into a local ground state, which does not have to be the global energy minimum. Then linear spin wave calculations can be used to determine the dispersions based on this ground state. Averaging of the dispersions from several local ground states will yield the excitation spectrum. This is a useful method, but as linear spin wave theory is limited to the linear term, the excitation spectrum will not contain higher order contributions, which can be significant especially in frustrated systems.
In the present thesis, a completely numerical approach is taken, which has been developed by Julien Robert [Rob07]. Monte Carlo simulation is used to anneal the spin system at a specific temperature. Starting in this state, the equations of motion are used to change the direction of each spin within a mean field of the neighbouring spins in time:

$$\frac{\mathrm{d}\mathbf{S}_i}{\mathrm{d}t} = \mathbf{S}_i \times \sum_j \mathbf{S}_j = \mathbf{S}_i \times \mathbf{H}_{\mathrm{MF},i}. \tag{4.6}$$

After the desired number of steps in time MCS is used again exploring the phase space and determining a new starting state for the development in time. This will be repeated several times. The time development of all these states are attached and convoluted with a Gaussian window function [PTVF92] for continuous spin change. Using a Fourier transform in space and time, the dynamic structure factor $S(\mathbf{Q}, \omega)$ (cf. Eq. 2.40) is calculated. A detailed description can be found in [Rob07, RCSB08, TRH$^+$14]. The magnetic form factor according to the magnetic ions present in the compound is not applied, because this study is not intended to describe the measurements in detail. But it should give insight to the structure of excitations yielded by the model. The radial decrease in intensity by the magnetic form factor would not help in this task. Thus, instead of actual scattering the intensity maps are cuts taken from the dynamic structure factor $S(\mathbf{Q}, \omega)$ (cf. Eq. 2.40). The width of the cuts are defined by the resolution of the perpendicular directions and thus depends on the simulated range of the real-space dimension. Consequently, the width in $\mathbf{Q}$ is given by the Fourier transform of the dimensions of the simulated lattice and the width in energy by the Fourier transform of the range in time. In Section

6.4 the results will be compared to the experimental data.
In [Rei11] I have developed a similar algorithm based on the information found in [Rob07]. But in this thesis the simulations have been performed in cooperation with Julien Robert, as his program was already tested thoroughly and readily available. For every parameter set 500 different spin states have been used as starting configurations for the development in time. Using the software Mathematica [Wol14] the set of dynamic structure factors has been evaluated on a local server. The parameters like the ratio of $J_{\text{out}}/J_{\text{in}}$ have been selected based on previous studies and the phase diagram on temperature vs. ratio (cf. Fig. 4.2a). In [RRS$^+$14] we have already reported that a magnetic order arises in the compound $CaBaCo_2Fe_2O_7$, which is particularly studied in the present thesis. The magnetic peaks visible in powder data clearly deviate from the diffuse scattering observed for $YBaCo_4O_7$ [MCR$^+$09]. Thus, a ratio $\tau > 1.0$ is expected to describe the magnetic order in $CaBaCo_2Fe_2O_7$ best. Furthermore, the phase diagram shows an additional nematic phase at low temperatures for $1.0 < J_{\text{out}}/J_{\text{in}} < 1.5$, which is of peculiar interest in understanding the complexity of the model. Moreover, the phase diagram has been explored at ratios ranging from $\tau = 0.5$ to 1.6. As temperatures $T/J_{\text{in}} = 0.5,\ 0.1,\ 0.01$ and $T/J_{\text{in}} = 0.001$ have been chosen, as they give insight into the excitations for all different phases. At $T/J_{\text{in}} = 0.5$ the system is at the transition to either the spin liquid state, the antiferromagnetically ordered phase or slightly above the respective phase, while $T/J_{\text{in}} = 0.01$ is far away from any boundary. For a ratio of $J_{\text{out}}/J_{\text{in}} = 1.3$ the system is within the nematic phase for $T/J_{\text{in}} = 0.001$. All simulations have been performed for a time period of $t \approx 150 J_{\text{in}}^{-1}$ resulting in an energy resolution of $\delta E \approx 0.021 J_{\text{in}}$. The size of the spin structure has been varied between 12 and 24 unit cells along all three directions, which results in a reciprocal spatial resolution between $\delta Q \approx 0.083$ [rlu] and $\delta Q \approx 0.042$ [rlu] (reciprocal lattice unit). In the following $(\delta Q)^3$ denotes the volume in **Q**-space defined by the resolution along all three reciprocal lattice vectors.

4.3.1 Elastic scattering

In principle the simulation is performed to explore the spin wave excitations, but of course the elastic structure factor is part of the data as well, allowing for investigation of the magnetic order. The displayed scattering maps show a clear dependence on ratio τ and temperature. At $T/J_{\text{in}} = 0.5$ even for the ratio $\tau = 0.5$, an arising structure can be observed (cf. Fig. 4.4 top row). For ratios $\tau > 1.3$, intensity is strongest at the K-points of the crystal structure Brillouin zone (BZ)[1] indicating an order close to a $\sqrt{3} \times \sqrt{3}$ antiferromagnetic one in the ab-plane. The possible peaks are surrounded by diffuse scattering of triangular shape, where the corners point along the BZ boundary forming a bow tie shaped pattern. Apart from the high intensity on the BZ boundary low intensity can be found at some of the crystal Bragg peak positions, which is related to a small antiferromagnetic contribution from so called $q = 0$ structures. This means that the magnetic unit cell for these contributions is the same as the crystal unit cell.
With decreasing temperature the intensity at the K-points increases, accompanied by the triangular shaped diffuse scattering for all ratios (cf. Fig. 4.4 middle row). Between $T/J_{\text{in}} = 0.5$ and 0.1 the overall diffuse scattering decreases for ratios $\tau \geq 1.3$. This trend is even more pronounced for the higher ratios. In addition, the diffuse scattering forms structures similar to pinch-points at some crystal Bragg Peak positions (e.g. $(1\,1\,0)$), best visible for ratios $1.0 \leq \tau \leq 1.4$ at $T/J_{\text{in}} = 0.01$. Pinch point singularities seen in spin-ices are also found in

[1] In the following the abbreviation BZ will always refer to the Brillouin zone of the crystal structure.

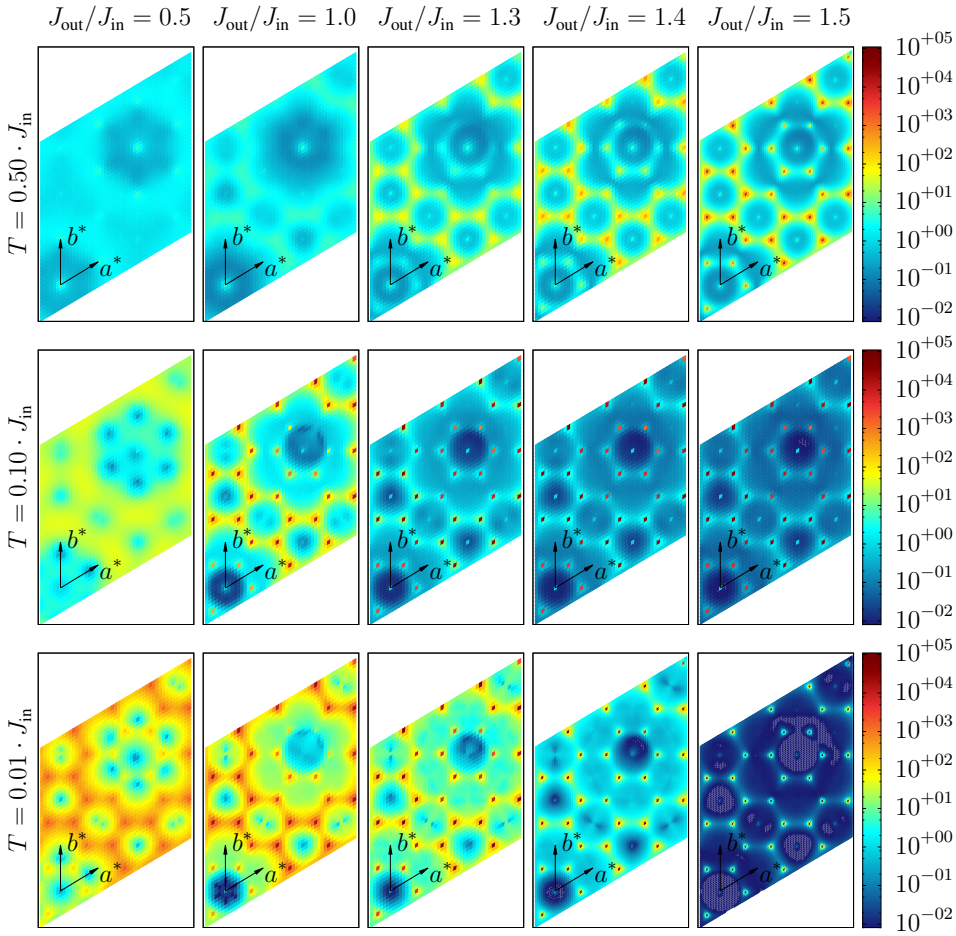

Figure 4.4: Extracted $(h\,k\,0)$ scattering plane from the dynamic structure factor for $-0.021J_{in} < E < 0.021J_{in}$, calculated using the spin dynamics simulation. The magnetic order increases with increasing ratio and decreasing temperature, while the diffuse scattering is mostly localized along the crystal stucture Brillouin zone boundary. The colour scale denotes the value of $S(\mathbf{Q},\omega)$ per $(\delta Q)^3 \cdot \delta E$.

the 2D kagome antiferromagnet at the same positions [Zhi08], which corresponds to the case $J_{\text{out}}/J_{\text{in}} = 0$. The pinch points denote a long correlation length along one and a short one along the other direction, compared to the 2d kagome antiferromagnet here these directions are switched. With finite J_{out} such features tend to smear out, however, relics can still be seen. Still the diffuse scattering remains strongest along the BZ boundary.
Cooling down to $T/J_{\text{in}} = 0.01$, the intensity of the diffuse scattering is significantly increased for ratios below $\tau = 1.5$ (cf. Fig. 4.4 bottom row). For $\tau \geq 1.5$, where the diffuse scattering vanishes almost completely at the benefit of the intensity at the K-points. At the same time the intensity at the crystal Bragg peak positions also decreases. For the ratios $\tau \leq 1.45$ the pinch points become more distinct. The intensity of the structure factor along and close to the BZ increases for ratios $\tau \leq 1.3$. Since the total intensity is conserved as $I_{\text{total}} = \iint S(\mathbf{Q}, \omega)\, \mathrm{d}\mathbf{Q}\mathrm{d}\omega$, this overall increase has to lead to a decrease of spectral weight on the excitations (cf. Fig. 4.5). In general, the structure factor for ratios $1.0 \leq \tau < 1.5$ reveals prominent peaks at the K-points of the BZ, related to an antiferromagnetic order despite being in the spin liquid regime. Additionally, two different kinds of diffuse scattering are visible. The first one is of triangular shape around the K-point also spread along the BZ boundary and the other one is covering most of the inner BZ at two orders of magnitude lower intensity. For the ratios $\tau \geq 1.5$ the ratio between the Bragg peaks at the K-point and the surrounding diffuse scattering is more pronounced, but the latter one is still not negligible and shows the same triangular shape. The overall background intensity drops about several magnitudes.

Cuts along the other high symmetry directions $(h\,h\,l)$ (cf. Fig. B.6) and $(h\,0\,l)$ (cf. Fig. B.7) were taken. The cuts of the $(h\,h\,l)$ scattering planes show magnetic Bragg peaks at the $(1/3\ 1/3\ l)$ positions. For all ratios except $\tau = 1.0$, only peaks with $\{l = 2n \,|\, n \in \mathbb{Z}\}$ are visible, indicating that the magnetic unit cell could be reduced to its half along the c-direction. Offside this symmetry plane magnetic Bragg peaks are also present for $\{l = 2n + 1 \,|\, n \in \mathbb{Z}\}$. The ratio $\tau = 1.0$ appears to be a special case, where magnetic peaks are present for all $\{l = n \,|\, n \in \mathbb{Z}\}$. Bragg peaks at these positions despite being very low in intensity are already visible for $\tau = 1.1$. Apart from the Bragg peaks, diffuse scattering connecting the $\{h\,k\,0\}$-scattering planes is prominent for all ratios and temperatures, but its intensity relative to the intensity of the Bragg peaks diminishes with decreasing temperature and increasing ratio and almost vanishes for $\tau = 1.5$ and $T/J_{\text{in}} = 0.01$. Since the kagome layers along the c-axis are only loosely coupled with each other for $\tau < 1.5$, the spin configuration of different kagome layers can vary basically freely from each other within a certain range. This range of variation decreases with decreasing temperature fluctuations and with increasing ratio, therefore this observation is to be expected. Due to the symmetry of the magnetic order, no magnetic Bragg peaks are visible in the $(h\,0\,l)$ scattering plane. The remaining diffuse scattering is also of low intensity but of rather complex structure. Here the $\{h\,k\,0\}$ scattering planes are connected by lines of diffuse scattering most prominent at $\{h = 2n+1 \,|\, n \in \mathbb{Z}\}$. This shows that the variation of spin configurations between the kagome layers is far from arbitrary but allowed only within a certain range provided by the sum rule (Eq. 4.4) around the antiferromagnetically ordered spin structure.

4.3.2 Inelastic scattering

In frustrated systems a broad excitation response is typically expected, which is why the spin dynamics simulation is better suited than linear spin wave theory. Upon cooling, the broad response develops continuously towards clearer defined spin wave dispersions. From the simulated dynamic structure factor, cuts along the energy axis and an axis in **Q** can be extracted. The most interesting axes in **Q** are the high symmetry directions of the magnetic Brillouin zone. In measurements the most distinct excitations have been observed along the $\langle 0\,0\,1\rangle$-directions [Rei11], and will therefore be of main focus here. The results for the directions $[1\,1\,0]$ and $[1\,0\,0]$ are shown in the Appendix (cf. Figs. B.8 and B.9).
At the temperature $T/J_{\text{in}} = 0.5$, dispersions along $[0\,0\,1]$-direction are visible for ratios $\tau \geq 1.1$

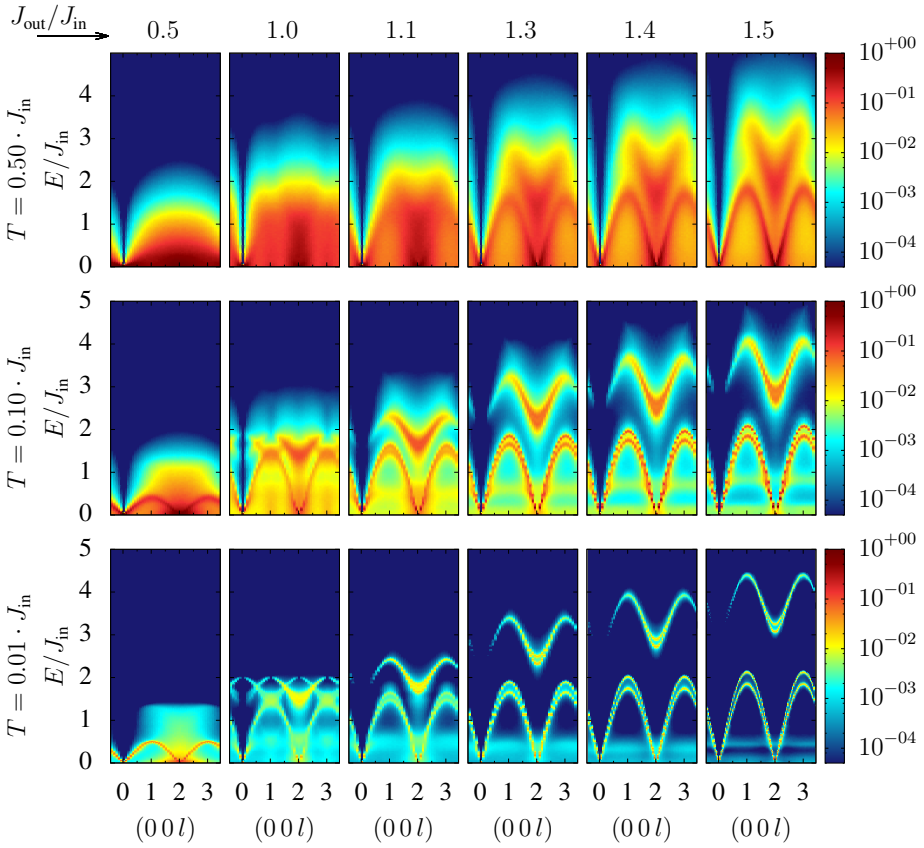

Figure 4.5: Excitations along $[0\,0\,1]$-direction. Cuts are taken from the dynamic structure factor of the spin dynamics calculations. Two excitation bands are present. The lower excitation band appears to be only loosely related with the ratio of the exchange interactions and temperature, while the upper one raises significantly with decreasing temperature and increasing ratio. The colour scale denotes the value of $S(\mathbf{Q},\omega)$ per $(\delta Q)^3 \cdot \delta E$.

within the excitation spectrum (cf. Fig. 4.5 top row). These dispersions correspond to the

dispersion of a linear antiferromagnetic spin chain

$$D(q_z) \propto \tau \cdot \sin\left(\frac{\pi l}{2}\right). \tag{4.7}$$

Along the $[0\,0\,1]$-direction a Goldstone mode exists only at $\{(0\,0\,l)\,|\,l = 2n, n \in \mathbb{Z}\}$, which indicates that the magnetic unit cell can be reduced to its half regarding the interactions in the model without loss of generality. At this temperature the dispersions are filled to the elastic line with an excitation continuum. In addition, between two dispersions further v-shaped broad excitations arise, which shift to higher energies with increasing ratio τ. At ratios below $\tau \leq 1.0$ only a very broad excitation spectrum is visible, which appears to scale with ratio τ. Along the other symmetry directions the excitation spectra are similarly broad for all ratios (cf. Figs. B.6 and B.7 top row). This means that at this temperature the spins are best ordered along the c-direction. However, peaks have still been observed in the $(h\,k\,0)$ scattering plane of the elastic partition of the structure factor (cf. Fig. 4.4 top row), which shows that the order along the c-axis induces also an order in the ab-plane. From Monte Carlo simulation it is known that the triangular spins order first upon decreasing temperature and the kagome spins will follow. Taking the rules derived from energy minimization into account, these dispersions along $[0\,0\,1]$ direction must be related to the triangular spins aligning parallel forming a linear chain. Yet, as the observed dispersions are similar to dispersions of an antiferromagnetic chain, the intermediate kagome spins have to form an effective spin of similar length antiparallel to the triangular spin (cf. Eq. 4.5). As all spins are of unity length, this is only possible due to higher disorder for the kagome sites at this temperature.

Upon cooling the spin system to $T/J_{\text{in}} = 0.1$ for ratios $\tau \geq 1.1$, the excitation continuum beneath the dispersions decreases in intensity, with a horizontal soft-mode at one third of the maximum energy of the dispersions (cf. Fig. 4.5 middle row). Furthermore, instead of one here two distinct dispersions are visible with slightly different slopes at Γ and different maximal energies. The area between these two dispersions is filled with an excitation continuum of similar intensity as the horizontal mode. The previous v-shaped excitations have risen in energy and are separated from the dispersions at lower energy. At the Γ-points $\{(0\,,\,0\,,\,4\,n\,+\,2)\,|\,n \in \mathbb{Z}\}$ with spectral weight on these excitations, two dispersions can be told apart as the upper and lower limits of the upper excitation band. The area between these two dispersions is also filled with an excitation continuum. At the **Q**-positions of the upper band's minimum the excitations of the lower band go down to the elastic line. Still with some simplifications the spectrum resembles one of a linear ferrimagnetically coupled spin chain (cf. Fig. 2.7), featuring an acoustic and optical excitation band. At $T/J_{\text{in}} = 0.1$ the fluctuations due to temperature are mostly suppressed due to the magnetic order. Thus, the effective spin of the three kagome spins of a double tetrahedron can be calculated according to the sum rule (cf. Eq. 4.4), which is larger than the triangular spin for ratios $\tau > 0.5$. Analogue to the discussion for the results from LSWT, along the c-axis the double tetrahedra columns can be viewed as two effective spins of different length, which is basically a linear ferrimagnetic coupled spin chain. This also explains the reason for the upper band shifting more strongly to higher energies than at $T/J_{\text{in}} = 0.5$ for the same increase in ratio, because the effective kagome spin increases proportionally to ratio τ. As the optical excitation band rises proportional to the ratio, for $\tau = 1.0$, its lower dispersion overlaps with the acoustic branch at its maximum.
As discussed previously the four stacked layers along c-axis can be reduced to two, considering just the magnetic interactions. Viewing the three kagome spins as an effective spin would yield two spins per unit cell. This would allow for two magnon dispersions. However, apparently

this assumption is only correct in a first approximation, because the acoustic and optical branch display a splitting into two separate dispersions. The complexity added by viewing the three kagome spins independently and the resulting four spins per unit cell is in correspondence with the four dispersions along $[0\,0\,1]$.

Further cooling does not change the general structure of the excitations (cf. Fig. 4.5 bottom row). The upper band raises stronger in energy than the lower band due the decreased temperature fluctuations of the kagome spins. The intensities for the dispersions mostly decrease according to the Bose-Einstein statistics. Nevertheless, they become more pronounced, as the background of the excitation spectrum decrease by an additional magnitude. The area between the dispersion duads for the acoustic and optical excitation spectrum is still filled with an excitation continuum, but its intensity decreases with increasing ratio and is hardly observable for $\tau = 1.6$. In addition, the non-zero energy soft-mode recedes to lower energies. Surprisingly, for the ratio $\tau = 0.5$, a case characterised by highest disorder and entropy, the dispersions of the linear antiferromagnetic chain are rather thin and exhibit high intensities. They are clearly distinguishable from a broad magnetic response in the background with the highest intensity at $(0\,0\,2)$.

4.3.3 Nematic phase

For ratios of $1.0 \leq \tau < 1.5$, a second ordered phase has been observed at $T < 0.005$ [BF14] (cf. Fig. 4.2a). The spins have been found to favour a coplanar state and the phase is therefore called nematic. Apart from the decrease in diffuse scattering, additional peaks have been found at the former pinch points, indicating a significant share in $q = 0$ structure.

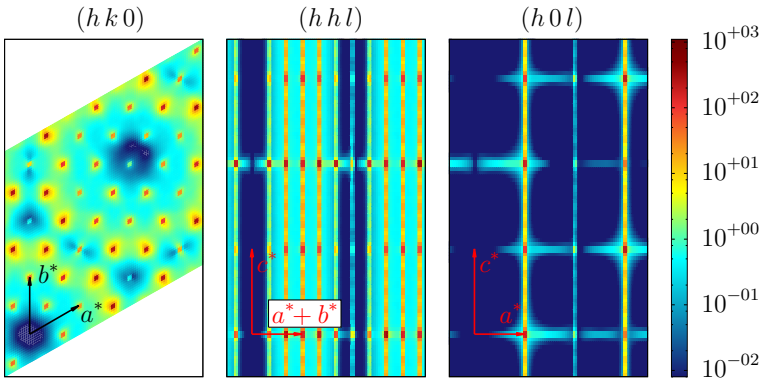

Figure 4.6: Cuts of the high symmetry scattering planes for $-0.021 J_{\text{in}} < E < 0.021 J_{\text{in}}$ through the dynamic structure factor simulated at $T/J_{\text{in}} = 0.001$ for a ratio of $J_{\text{out}}/J_{\text{in}} = 1.3$. In the nematic phase the diffuse scattering is located close to the K-points in the $(h\,k\,0)$ scattering plane. The scattering planes $(h\,h\,l)$ and $(h\,0\,l)$ show a significant decrease of the intensity variation along $\langle 0\,0\,1 \rangle$ indicating a shorter correlation length along c. The colour scale denotes the value of $S(\mathbf{Q}, \omega)$ per $(\delta Q)^3 \cdot \delta E$.

The same pattern is visible here as well (cf. Fig. 4.6 left). Furthermore, the shape of the diffuse scattering surrounding the peaks at the K-points changed to a hexagon with a slightly stronger intensity towards the BZ centre. Overall, the diffuse scattering in the $(h\,k\,0)$ scattering

plane is enhanced near the K-point extending further in ridges along the BZ boundary. In the perpendicular scattering planes, $(h\,h\,l)$ as well as $(h\,0\,l)$, the diffuse scattering becomes much more pronounced and exhibits only little intensity variation along the $[0\,0\,1]$ direction indicating a shorter correlation length along the c-axis. At the same time the intensity variation in the diffuse scattering increases along the directions $[1\,1\,0]$ and $[1\,0\,0]$. This is in vast difference to the scattering observed in the 3D spin liquid state at $T/J_{\text{in}} = 0.01$ both within this study (cf. Figs. B.6 and B.7) and in [KMMC10], where the lowest variation in scattering intensity is observed along the direction $[1\,1\,0]$. Assuming a mostly coplanar spin state, which at the same time has a symmetry similar to the spin structure of the antiferromagnetic ground state, a freedom for the spins on the kagome layers opens up, resulting in a spin structure less coupled along c-direction. This effectively yields a short-range order along this direction evidenced in the increased diffuse scattering. Here the triangular spins have been found to vary from the antiferromagnetic ground state by only $\pm 3°$. Whereas the kagome spins vary in the ab-plane by $\sim \pm 45°$ and out of plane by $\pm 10°$ from the antiferromagnetic ground state. The distribution of the kagome spins' orientation shows maxima close to the aforementioned limits of the angular variation in the ab-plane. Still this is in correspondence with the sum rule, as the kagome spins

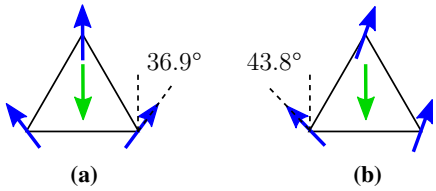

Figure 4.7: Possible spin configurations on a double tetrahedron for $J_{\text{out}}/J_{\text{in}} = 1.3$ in the nematic phase with kagome spins in blue and triangular spins in green. View is along c-axis. Due to the coplanarity, the kagome spins deviate more strongly from the antiferromagnetic ground state according to the sum rule. **(a)** Symmetrically tilted kagome spins. **(b)** Antisymmetrically tilted kagome spins.

have to vary by a higher angle if being confined to the ab-plane in order to fulfil the rule (cf. Fig. 4.7). Assuming coplanar spins with one kagome spin oriented antiparallel to the triangular spins, the other two kagome spins will tilt antisymmetrically compensating the perpendicular component. Using the sum rule (cf. Eq. 4.4) the tilting angle is $36.9°$. The highest tilting angle for a single spin takes place if two kagome spins tilt parallel away from the collinear orientation, at which point the third spin tilts by an angle of $43.8°$. These angles fit very nicely with the maxima observed in the distribution. This strong deviation from the antiferromagnetic ground state results in the share in $q = 0$ structure and thus the peaks at the crystal Bragg peak positions.

Not only does the spin structure within this phase differ from the one in the others phases, but the excitation spectrum changes as well. The excitations become more distinct and similar to the ones observed for a ratio of $\tau = 1.5$ at $T/J_{\text{in}} = 0.01$. Along the direction $[0\,0\,1]$ the upper excitation band still ranges from $E/J_{\text{in}} = 2.5$ to 3.5 while the soft-mode at non-zero energy vanishes completely. More significant changes can be observed along the other directions $[1\,1\,0]$ and $[1\,0\,0]$. At the low energies, instead of a broad response in energy, clear dispersions are visible, which indicates clearly that the spin system in the nematic phase is better ordered, allowing for better defined spin waves.

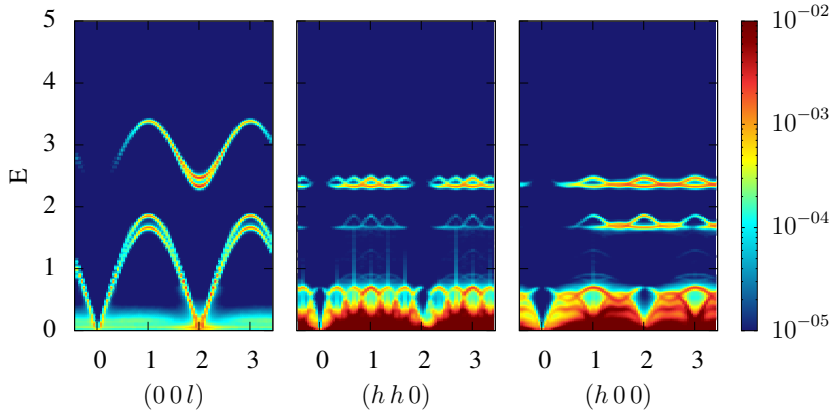

Figure 4.8: Cuts in energy and along the high symmetry directions through the dynamic structure factor simulated at $T/J_{\text{in}} = 0.001$ for a ratio of $J_{\text{out}}/J_{\text{in}} = 1.3$. In the nematic phase the dispersions become more distinct along all directions. The colour scale denotes the value of $S(\mathbf{Q}, \omega)$ per $(\delta Q)^3 \cdot \delta E$.

5

Structural and magnetic properties of $CaBaCo_2Fe_2O_7$

In the previous chapter the results, which apply to the whole Swedenborgite compound family, have been presented. The following chapter focuses on the specific properties of $CaBaCo_2Fe_2O_7$ and why this compound is of particular interest.

5.1 Relevant results from previous studies

The thesis at hand is based on the studies from other groups presented in Chapter 4, which are necessary for an understanding of the observations. The compound $CaBaCo_2Fe_2O_7$ has already been investigated in the Diploma thesis of Erik Rosén [Ros11] as well as my own [Rei11]. Our findings regarding the crystal structure and macroscopic measurements have been published in [RRS$^+$14]. In order to paint a complete picture, the most relevant findings will be introduced shortly.

5.1.1 Crystal structure

The crystal structure of $CaBaCo_2Fe_2O_7$ has been previously investigated using powder X-ray diffraction, reporting a $P6_3mc$ space group symmetry [Val04b]. Recent measurements confirmed the same symmetry, but with slightly different cell parameters of $a = b \approx 6.360$ Å and $c \approx 10.276$ Å [RRS$^+$14]. The internal structure has been refined using the powder diffraction data, but in X-ray scattering the scattering length density for Co and Fe is too similar to distinguish these. Therefore, single crystal neutron scattering has been performed at 190 K and 2.5 K, which could be refined using the $P6_3mc$ space group. Here, the scattering length density is significantly different for Co and Fe, which allows a refinement of their site distribution. Within the crystallographic unit cell the magnetic sites contain two triangular and two kagome lattice planes. It was found, that the sites are statistically occupied by Co and Fe ions, whereby mostly Fe (85%) on the triangular sites and mostly Co (60%) on the kagome sites. The oxidation states of Co^{2+} and Fe^{3+} have been determined from the X-ray absorption spectrum. In the refinement of the crystal structure model the atomic displacement factor was enlarged for oxygen ions on two of the three symmetrical positions. Introducing split positions for both of

these greatly improved the refinement. The resulting crystal structure is displayed in Figure 5.1. Descending to a lower symmetry ($P31c$) was tested but could not improve the structural description [RRS$^+$14]. The same model has been applied to the data at 2.5 K. No movement of the ions could be determined within the resolution limit. As a result the positions of the oxygen ions regarding the bonds between nearest neighbour magnetic sites break the inversion symmetry, which allows for the presence of Dzyaloshinskii-Moriya interactions.

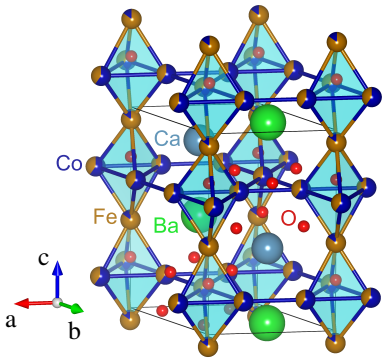

Figure 5.1: Crystal structure of $CaBaCo_2Fe_2O_7$ [RRS$^+$14]. The statistical distribution of Co and Fe over the magnetic sites is displayed as pie charts. The bonds show nearest neighbour connections between magnetic sites. The double tetrahedra forming columns along c are highlighted in cyan.

5.1.2 Magnetic order

In [Ros11], the specific heat and magnetisation have been measured on single crystal samples of $CaBaCo_2Fe_2O_7$ both showing an anomaly at around 160 K. From the temperature dependence in the magnetometry data an antiferromagnetically ordered phase is evidenced below the transition temperature T_N. A Weiss temperature of $\theta_W \approx -1500$ K was extracted from the gradient of the reciprocal specific heat in the paramagnetic regime above 760 K, according to the Curie-Weiss-law. This results in a ratio of $\frac{-\theta}{T_N} \approx 10$, which characterizes a strongly frustrated magnetic structure [FTS$^+$06]. The diffuse neutron scattering diffractometer DNS has been used to investigate the magnetic ordering in the $(h\,k\,0)$ and $(h\,h\,l)$ scattering plane at 4 K [Ros11]. DNS offers an XYZ-polarization analysis option for separation of the different scattering contributions in combination with an array of detectors according to [Sch10]. Separating the total magnetic scattering, both individual scattering planes show Bragg peaks at the K-points of the BZ (cf. Fig. 5.2), which indicates a long-range $\sqrt{3} \times \sqrt{3}$ antiferromagnetic order along all directions with the propagation vector $(1/3\ 1/3\ 0)$. Diffuse scattering of low intensity is visible close to the magnetic peaks, slightly elongated along the BZ boundary. At the crystal Bragg peak positions, magnetic peaks of low intensity can be observed, which can either be related to a small ferromagnetic contribution or a remaining intensity from the separation. The other separated scattering contributions namely the spin-incoherent scattering, nuclear magnetic scattering from moments parallel to y and nuclear magnetic scattering from moments parallel to z do not exhibit significant intensity in comparison to the intensity of the total magnetic scattering. The absence of nuclear magnetic scattering indicates the atomic occupation and spin

orientation to be uncorrelated.

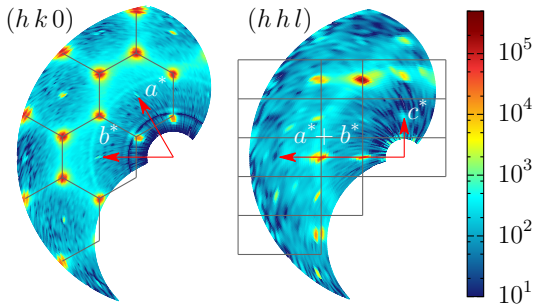

Figure 5.2: The $(h\,k\,0)$ and $(h\,h\,l)$ scattering plane measured at DNS at 4 K on the large single crystals, from [Ros11]. The BZ is marked in grey. Only at the K-points magnetic peaks are observed indicating a commensurate antiferromagnetic order. The corresponding spin structure is similar to the antiferromagnetic ground state (cf. Fig. 4.2b).

Furthermore, four selected peaks have been measured with temperature dependence [Ros11]. The measurement for the magnetic peak $(4/3\ 1/3\ 0)$ is displayed in Fig. 5.3. Calculating the integrated intensities for the separation channels allows for further insight in the temperature development of the magnetic ordering. The integrated intensity for the chiral scattering has been calculated taking the absolute value. While all scattering contributions show a phase transition around $T_N \approx 160\,K$, two different trends in temperature are visible within the antiferromagnetic phase. The magnitude of the scattering intensity from moments parallel to the ab-plane $(M_y)^2$ increases faster than the intensity from other scattering contributions until it reaches a maximum at around 80 K, and then drops upon cooling further. At this temperature the scattering intensity from moments parallel to the c-axis $(M_z)^2$ as well as the chiral magnetic scattering increases. At around 20 K the variation in intensity converges to a saddle point for all contributions, with $(M_y)^2$ still slightly higher in intensity than the others. Overall, the temperature trend of the chiral scattering is similar to $(M_z)^2$, indicating a strong correlation. Considering the direction of the spins contributing the respective scattering $(M_y)^2$ and $(M_z)^2$, a spin reorientation exists from a more coplanar spin structure in ab-plane at 80 K to a spin structure canted more strongly out of this plane at 4 K. Such a behaviour is not expected from the simple Heisenberg nearest neighbour model (cf. Eq. 4.1). Furthermore, the reorientation appears to be continuous without an intermediate phase transition. It has to be noted, that the temperature dependence of the total magnetic scattering is somewhat unusual. Down to 80 K it resembles the power law of a second order magnetic phase transition, but the drop below 80 K implies that the magnetic order decreases or changes into a significantly different structure. On the other hand this could be due to an error in the integration itself.
Based on the model introduced in Section 4.1, Monte Carlo simulations (MCS) have been performed. In [KMMC10] the scattering intensities are calculated for the $(h\,k\,0)$ and $(h\,h\,l)$ scattering plane. The comparison between these results and the measurements performed at DNS requires a ratio of $\tau > 1.0$. In the measurement no diffuse scattering has been observed close to the magnetic Bragg peaks, which might even indicate a ratio close to $\tau = 1.5$ or higher. The triangular spins of the corresponding spin structure are almost collinearly aligned, while the kagome spins display a higher disorder. This is a direct result from the constraints in the

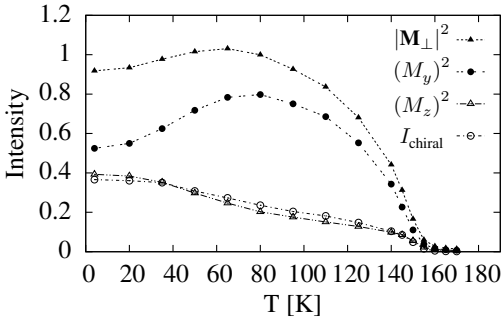

Figure 5.3: Temperature dependence of the different scattering contributions for the magnetic peak $(4/3\ 1/3\ 0)$ measured at DNS and normalized to the total magnetic scattering at 80 K, from [Ros11]. Integrated intensity was calculated from the absolute of the intensity map at the peak position. Below the phase transition at 160 K, between 80 K and 4 K a spin reorientation is visible.

Equations 4.3 and 4.4. In [Rei11], the exchange interactions have been calculated by linking the transition temperature observed in measurements with the one determined by MCS, based on the assumption of a ratio $\tau = 1.5$ to be $J_{\text{in}} \approx -28$ meV and $J_{\text{out}} \approx -41$ meV. This also fits to the effective exchange interaction $J_{\text{eff}} \approx -35$ meV determined from the Curie-Weiss temperature.

5.2 Transitions in magnetometry

A physcial property measurement system (PPMS) named Dynacool from Quantum Design [Qua] has been used to measure the magnetisation with the vibrating sample magnetometer option depending on temperature and externally applied magnetic field. Both field cooled (FC) and zero field curves (ZFC) have been measured. For the FC curve the field was applied at 350 K then the sample was cooled down. Upon heating the magnetic moment has been measured. The observed magnetic moment $m(\text{emu})$ has been calculated to the magnetic moment (μ_B) per magnetic ion using:

$$\mu_{\text{ion}}(\mu_B) = \frac{m(\text{emu})}{m(\text{g})} \cdot \frac{M_R}{N} \cdot \frac{1}{N_A \cdot \mu_B}. \tag{5.1}$$

with the Avogadro constant N_A, the molecular weight M_R and divided by the $N = 4$ magnetic ions per chemical formula. Similar measurements have been performed before on a different crystal of the same compound [Ros11], but here the small crystal (cf. Section 3.1) is investigated, which has also been measured with neutron scattering. This allows for a direct correlation between the two methods.

Orienting the c-axis perpendicular to the applied field, a clear antiferromagnetic transition can be observed near 160 K (cf. Fig. 5.4). In addition, this transition exhibits an increase of the magnetic moment with decreasing temperature above the transition followed by a decrease below the transition. In the paramagnetic regime the external field can rotate the spins more parallel

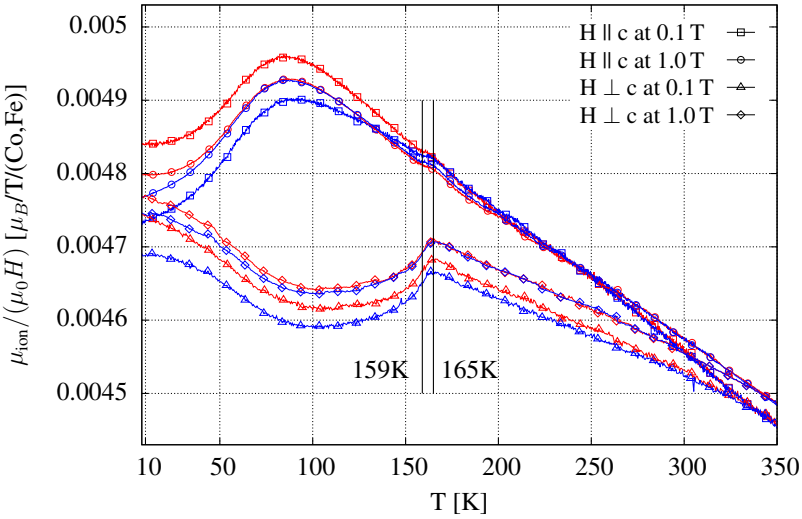

Figure 5.4: Magnetic moment from FC (red curves) and ZFC (blue curves) measurements converted to moment in μ_B per ion (cf. Eq. 5.1). For easier viewing each curve is divided by the external field. Below the phase transition a reorientation is visible between the states at 80 K and 10 K.

for decreasing temperature fluctuations. But when an antiferromagnetic order arises this works against the external field, which results in a decrease in the magnetisation. Here the order in the ab-plane is known to have a 120° character (cf. Fig. 4.2b), which is expected to cancel any magnetic moment with strengthening order. This also explains the very small overall magnetisation per ion. Furthermore, the transition temperature appears to be field independent within the accessible range. Before the paramagnetic contribution, not stemming from the sample, is dominant below 10 K, already at 80 K the magnetic moment increases upon cooling again. This increase is visible down to the paramagnetic contribution. From this it follows that the spin structure changes again starting at 80 K in a way that the spins can be aligned to the magnetic field more easily. This change continues till 10 K.
The Néel transition is visible only slightly in the FC/ZFC curves with the magnetic field parallel to the c-axis. This is the easy axis, as the magnetic order results only in a small increase in energy for the spins to vary along this direction. That is why the magnetisation increases further after a small kink. Around 80 K it reaches a broad maximum. At this temperature the magnetic order overcomes the temperature fluctuations and the spins can follow the external field less and less. This trend continues until the paramagnetic contribution arises at around 10 K.
Especially when both field directions are considered at the same time the magnetometry data paints a very intriguing picture of two competing contributions. The first one arises upon cooling below the Néel temperature, which is clearly visible for the magnetic field perpendicular to c. While the magnetic order develops in the ab-plane the component of the moments along c-axis still exhibits a behaviour similar to a paramagnet. Slightly below 100 K where this component is finally constrained by the magnetic order, the component in ab-plane is able to vary more freely. The overall degeneracy present in the system cannot be removed upon cooling, only the component of the moments, which is more constrained, changes.
In principle the results are similar to the ones obtained in [Ros11]. The general dependence on

the direction of the external field as well as the main transition at 160 K are the same in both. But in contrast to the previous measurement, no additional peaks are visible here, but continuous spin structure reorientations within the antiferromagnetic phase. One takes place between 160 till 80 K and the other between 80 and 4 K.

5.3 Magnetic structure determination

In order to determine the spin structure in a magnetic compound, usually two different experiments are possible. In both cases a model is applied for refinement to the measured data. The first one is to measure the magnetic order using neutron powder diffraction, which allows for faster measuring times and therefore to measure at several temperatures. This way the change of the spin structure with temperature can be followed. But usually this only allows for a refinement of simpler structures, as information is lost due to the powder average. The other option is to measure the integrated intensities on a single crystal, which takes several times longer, but each peak can be measured separately. The gain in information allows for a more precise refinement or a refinement of a more complex spin structure. Here, both methods have been applied.

5.3.1 Commensurate and long-periodic order distinguished by powder diffraction

The powder diffractometer POWGEN [HHGH11] at the spallation source SNS in Oak Ridge (USA) uses a double chopper setup to select a wavelength band from the incoming neutron pulse. Here two different wavelength bands have been used to cover the Q-ranges from 2.04 to 9.54 $Å^{-1}$ and 0.61 to 2.73 $Å^{-1}$. The diffractograms at lower Q features a higher resolution. Powder diffractograms have been taken at several temperatures between 190 and 12 K[1]. Due to the available time the measurement of the lower-Q wavelength band has been prioritized over the other. As a polarization option is not available, the powder diffractograms show the temperature dependence of the superposition of the crystal and magnetic structure (cf. Fig. 5.5). However, no magnetic peaks are observed in the data at 190 K, above the Néel-transition at around 160 K. The crystal structure for $CaBaCo_2Fe_2O_7$ has been already solved from single crystal data and published in [RRS+14]. Using this structural model in the software FullProf [RC93] the diffractogram can be fitted convincingly, just refining the lattice parameters (cf. Fig. 5.6). Furthermore, the crystal structure peaks do not change upon the magnetic phase transition (cf. Fig. 5.5) revealing a structural invariance. Below 160 K the diffractograms show additional peaks, which can be attributed to the magnetic order. Due to the magnetic form factor, the magnetic peaks are most prominent in the lower-Q diffractograms. The model for the crystal structure has been applied to all diffractograms refining just the lattice parameters. Since the magnetic peaks are of similar intensity to the crystal structure peaks, the goodness of the fit decreases significantly. As the crystal and magnetic peaks are overlapping in Q, excluding the latter will not be sufficient for a good refinement. Still, an assessment by eye proves the crystallographic model to be valid within this instrumental resolution over the whole temperature range (cf. Fig. 5.6). This is to be stressed as it shows that $CaBaCo_2Fe_2O_7$ is a system

[1] Further cooling was time inefficient using the available cryostat.

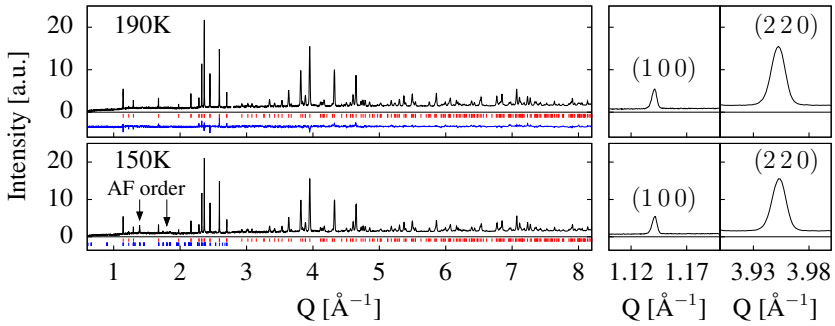

Figure 5.5: Powder diffractograms measured above and below the magnetic phase transition at 160 K at the time-of-flight diffractometer Powgen. The pattern at 190 K is fitted with the structural model (cf. Fig. 5.1), difference between fit and data as blue line. Indicators for crystal structure peaks in red and magnetic ones in blue. The shape of the crystal structure peaks does not change upon transitioning, indicating a structural invariance. Figure adapted from [RRS$^+$14].

of the Swedenborgite compound family, which does not undergo a structural phase transition, at least not within the instrumental resolution and the accessible temperature range. For the isostructural compound $YBaCo_4O_7$ a structural transition to an orthorhombic phase was found [HMZ$^+$06].

Looking more closely into the structure of the magnetic peaks, their shape evidences, that the magnetic order is more complex and the structure changes with temperature. Especially at 4 K the diffractogram reveals additional peaks close to the commensurate peak towards higher as well as lower Q. Such satellites can arise from a long-periodic or even incommensurate magnetic order. If such an order exists, it is most likely closely related to the antiferromagnetic order, since the deviation from the commensurate position is relatively small. If this additional structure still obeys the symmetry of the commensurate order, the observed peaks are most likely related to a splitting along the high symmetry directions:

- parallel to $(h\,k\,0)$-scattering plane on top of on the crystal structure $\rightarrow$ three satellites,
- parallel to $(h\,k\,0)$-scattering plane on top of the antiferromagnetic order $\rightarrow$ six satellites,
- parallel to $[0\,0\,1]$-direction $\rightarrow$ two satellites.

Looking at the powder diffactrograms, the satellite peaks are well pronounced at temperatures below 80 K (cf. Fig. 5.6), but only two satellite peaks are visible per magnetic Bragg reflection, as a possible third one overlaps either with another satellite or with the main peak due to the powder average. There are no indications for more than three peaks, which excludes the splitting on top of the antiferromagnetic order. The splitting parallel to the $[0\,0\,1]$-direction can also be excluded, as it would result in a single satellite for the magnetic peaks in the $(h\,k\,0)$-scattering plane. Judging from the peak shape of the magnetic peak $(1/3\ 1/3\ 2)$ at 1.4 Å^{-1} (cf. Fig. 5.6), which shows higher intensity to higher Q, the satellite peaks are located on the BZ boundary instead of being shifted towards the crystal Bragg peaks. In order to extract the intensity for each satellite, the model displayed in Fig. 5.7a is applied. Fitting the model to the powder data is most reliable at low temperatures as the intensities of the satellite peaks increase with decreasing temperature. Assuming the symmetry of commensurate order, there are two different kinds of satellite triplets. The ones close to magnetic peaks $(h\,k\,l)$ with $h = k$ and those with $h \neq k$. In

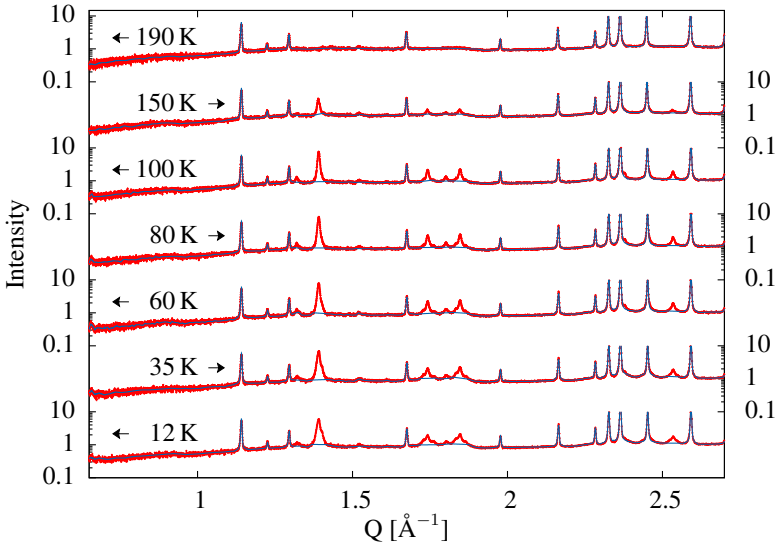

Figure 5.6: Powder diffraction pattern measured at Powgen (SNS) with the low-Q wavelength band. The refinement of the crystal structure using FullProf is marked as blue lines. The difference can be attributed to the magnetic contribution, but the single peaks show a more complex structure.

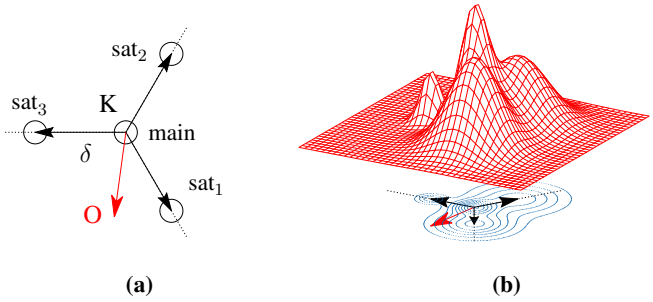

Figure 5.7: Model used for the extraction of the integrated intensities from powder diffraction data. **(a)** The three satellites are assumed to be shifted away from the K-point along the BZ boundary by the distance δ. **(b)** Visualization of the fit results in two dimensions of the peak $(4/3\ 1/3\ 0)$ at 4 K.

the first case the splitting is symmetrical in regards to **Q**, which constrains the satellites shifted transverse to **Q** to exhibit the same intensity. For the latter case all three satellites can exhibit a different intensity. In this case the fit function for a main peak including its satellites is written as:

$$f(\mathrm{Q}) = I_{\mathrm{main}} \cdot \phi(\mathrm{Q}, \mathrm{Q}_{0,\mathrm{main}}, \sigma_{\mathrm{main}}) + \sum_{\mathrm{sat}} I_{\mathrm{sat}} \cdot \phi(\mathrm{Q}, \mathrm{Q}_{0,\mathrm{sat}}, \sigma_{\mathrm{sat}}) \tag{5.2}$$

with the normal function

$$\phi(\mathrm{Q}, \mathrm{Q}_0, \sigma) = \frac{1}{\sqrt{2\pi} \cdot \sigma} \cdot e^{-0.5 \cdot (\frac{\mathrm{Q}-\mathrm{Q}_0}{\sigma})^2}. \tag{5.3}$$

The position for the main peaks $Q_{0,\text{main}}$ is calculated from the lattice parameters, whereas the

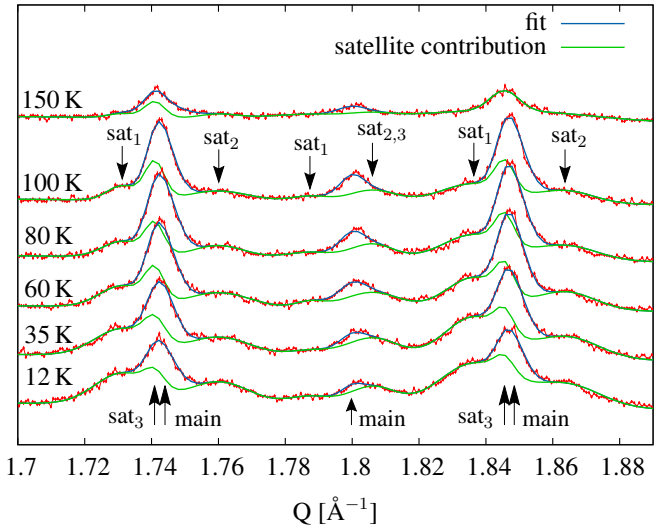

Figure 5.8: Fit (blue line) of the diffraction pattern around the magnetic peaks $\{4/3\ 1/3\ 0\}$, $\{2/3\ 2/3\ 2\}$ and $\{4/3\ 1/3\ 1\}$ with a main and three satellite peaks each (cf. Fig. 5.7a). The splitting δ is kept constant and was refined initially from the data at 12 K. The contribution from the satellite peaks (green line) includes the fitted background.

position for each satellite peak $Q_{0,\text{sat}}$ is calculated in $\mathbf{Q}$ using $Q_{0,\text{main}}$ and the parameter of the shift δ, which is also a parameter of the fit, and then projected to Q. The normal distributions are used to fit the peak shape using σ and intensity I. The diffractograms will be fit in the range $1.7\,\text{Å}^{-1} \leq Q \leq 1.9\,\text{Å}^{-1}$, containing three magnetic peaks $\{4/3\ 1/3\ 0\}$, $\{2/3\ 2/3\ 2\}$ and $\{4/3\ 1/3\ 1\}$ but no crystal structure peaks. This part of the powder pattern can be fitted convincingly at all temperatures with the described model (cf. Fig. 5.8). First a linear background was fitted to the boundaries of the range. Since no indications for a shift of the propagation vector have been observed, the magnitude of the splitting $\delta \approx 0.017 \pm 0.002\,\text{Å}^{-1}$ was determined from the fit at 4 K and kept temperature-independent, besides the general temperature expansion. This indicates that the satellite peaks might relate to a stable long-periodic ordering instead of an incommensurate one, yet this cannot be discerned using the data at hand. The determined splitting relates to a magnetic order with a periodicity of about 370 Å or rather 58 crystallographic unit cells and a propagation vector of $\mathbf{k} \approx (0.342(1),\ 0.342(1),\ 0)$ noted in the crystallographic unit cell. If a satellite peak overlaps with the main peak, as it does for $(4/3\ 1/3\ 0)$, the fit cannot yield a unique solution for these two peaks as their intensity can be substituted within a wide range. This leads to relatively large error bars on the intensity of both peaks. In order to compensate for this effect the intensities of both peaks have been added up, resulting in a continuous temperature dependence with relative smaller error bars (cf. Fig. 5.9).

On the one hand, a model that assumes one main peak and only the two satellite peaks sat_1 and sat_2 shows a decrease in the goodness-of-fit for temperatures below 150 K. Therefore, the intensity of the third satellite peak can be considered significant, which means that the actual intensity of the main peak plummets further. On the other hand, using a model with three satellite peaks but no main peak will yield a much poorer fit, even at 12 K. From these results the

existence of a main peak can be presumed down to 12 K and at the same time the existence of three satellite peaks up to 100 K and thus both types of order.

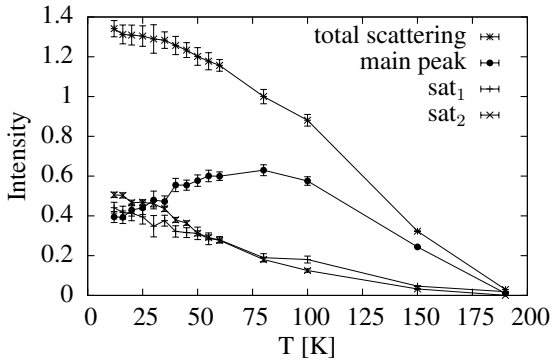

Figure 5.9: Temperature dependence of extracted intensities from the magnetic peak $\{4/3\ 1/3\ 0\}$ and its satellite peaks from powder diffraction data measured at POWGEN. The main peak includes the satellite peak. Intensities have been normalized to the total magnetic scattering at 80 K. A trade of in intensity between the main peak and the satellite peaks are visible with the main peak most prominent at 80 K.

Spin reorientation The scattering intensity for all peaks arises between 190 K and 150 K according to the Néel transition at 160 K (cf. Fig. 5.9). The total magnetic scattering, which is the sum over the intensities of the main peak as well as the satellite peaks increases considerably until 60 K and then converges to a maximum at around 20 K. The summed intensity of the main peak and the third satellite increases until 80 K and decreases furtheron. At 12 K their intensity is reduced to 2/3 of its maximum. The temperature dependence of the intensity of both satellite peaks sat_1 and sat_2 show a flattish slope close to the phase transition which increases more quickly below 80 K. Here the trend appears to converge to an intensity maximum at 12 K, which is however higher than the one for the intensity of the main peak and the third satellite. Apparently two different structures exist related to the main and the satellite peaks, which reveal a different temperature dependence of opposing trend in some sense. This means that the structure related to main peak changes continuously into the structure of the satellite peaks with decreasing temperature without a second phase transition. This reorientation is similar to the one observed at DNS in the different scattering contributions (cf. Fig. 5.3).

5.3.2 Refinement of the commensurate magnetic structure

As presented in Subsection 2.2 the possibilities of the magnetic structure are resticted to some degree by the symmetry of the crystal structure, which is recommended to be solved first. At least the position of the magnetic sites and the crystal space group are essential for the refinement of the magnetic structure using symmetry analysis. The results from the crystal structure refinement show a hexagonal space group $P6_3mc$ above and below the magnetic ordering transition [RRS+14]. A detailed description of the refined crystal structure of $CaBaCo_2Fe_2O_7$ can be found in Subsection 5.1.1, which was confirmed to be suitable at all temperatures using the powder data in the previous subsection. The magnetic sites span two triangular and kagome

layers stacked along the c-axis. The sites are statistically occupied by Co and Fe ions, whereby there is mostly Fe (85%) on the triangular sites and mostly Co (60%) on the kagome sites. The oxidation states Co^{2+} and Fe^{3+} have been determined using X-ray spectroscopy. The measurements at DNS have revealed a K-type antiferromagnetic order. The following refinement is based on this model and the integrated intensities measured at Morpheus using 4-circle geometry (cf. Tables D.1 and D.2).
The software MAXMAGN from the Bilbao crystallographic server [APMO$^+$11, TFO$^+$12] uses the crystal space group, the position of magnetic ions and the propagation vector of the magnetic order to calculate possible magnetic space groups (cf. Section 2.2). Within each solution only a limited list of independent magnetic sites/moments exist (cf. Tables D.6 and D.7), as the other sites and also corresponding moments are created from symmetry relations. Six different magnetic space groups have been suggested as possible solutions using a large unit cell $(3a, 3b, c)$: $P6_3c'm'$, $P6'_3cm'$, $P6'_3c'm$, $P6_3cm$, $P31m'$ and $P31m$. In Tables D.8 and D.9 the resulting independent sites and the free parameters are stated. In the case of the space groups with hexagonal symmetry $P6_3$, a six-fold screw axis exists along the c-axis, where the normal vector of the mirror planes are in the ab-plane. Descending to the trigonal space groups $P3$, relaxes the six-fold screw axis to a three-fold rotation symmetry. A symmetry operation noted with $'$ indicates a time inversion of the spin subsequent to the usual operation. Due to the spin's nature as an axial vector applying a mirror operation also inverts the spin. In the following the different solutions are discussed. The adjacent pictures (view along c-axis) are examples from the refinement at 80 K, but the general structure applies at other temperatures as well. The ordered moments of the same kagome layer are displayed in red and blue respectively and the triangular moments in green.

Solution in space group $P6_3c'm'$ (#185.201)
There are four independent magnetic sites two triangular and two kagome ones. The moments on the triangular sites are fixed antiparallel along c-axis due to the six-fold rotation symmetry with only their spin lengths to be refined. Depending on the symmetry position, there are two types of columns: triangular moments which are oriented parallel to the c-axis and triangular moments antiparallel to c-axis. The kagome moments surrounding the triangular moments parallel to the c-axis are fixed in regards to their angle in the ab-plane, pointing radially away. They are refined to rotate slightly out of plane in a way such that they compensate the inner triangular spin. The other kagome moments despite having the freedom to rotate freely, are refined to a similar structure, with an opposite canting out of plane.

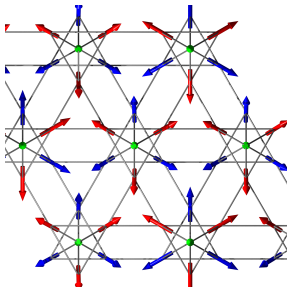

Figure 5.10: Spin structure refined in magnetic space group $P6_3c'm'$.

Solution in space group $P6'_3cm'$ (#185.200) The same magnetic sites are linked via symmetry as in the previous solution. Even the restrictions to the magnetic moments are kept the same. But as different symmetry relations are applied, the refinement results in a different spin structure. Here triangular moments of the same column alternate between parallel and antiparallel to the c-axis. This results in the kagome moments with the fixed in plane angle to alternate in their orientation as well. One kagome layer is pointing towards the center at an out of plane angle and the moments of the other layer point along the opposite direction. The other kagome moments are refined to orient circularly around the triangular spin, while the rotation sense changes between columns.

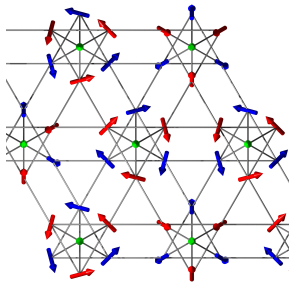

Figure 5.11: Spin structure refined in magnetic space group $P6'_3cm'$.

Solution in space group $P6'_3c'm$ (#185.199) Here one of the moments on the triangular sites is set to length zero (indicated by a grey ball in the figure), while the other is still confined along c-axis and its orientation alternates between the columns. The moments on the kagome sites surrounding the triangular site without a moment are fixed, in a way that the moments are oriented circular in ab-plane around the axis of triangular moments. The orientation alternates between different kagome layers. The other kagome moments can rotate freely, but the refined structure is similar to the fixed kagome moments.

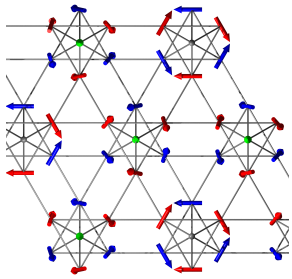

Figure 5.12: Spin structure refined in magnetic space group $P6'_3c'm$.

Solution in space group $P6_3cm$ (#185.197) The magnetic sites as well as the restrictions to the magnetic moment are the same as in the previous solution. However, since different symmetry relations are applied, the refined spin structure is different. The orientation of the non-zero moments on the triangular sites alternate from one layer to another on the same column, but nonetheless the effective length of the moment is refined to be close to zero. Here the moments on the kagome sites orient circular with the same sense of rotation for both layers of a column and is opposite between the columns with zero and non-zero moment on triangular sites.

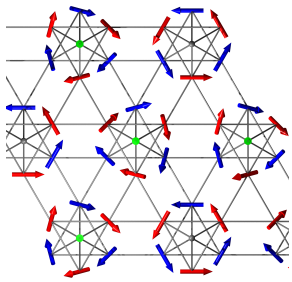

Figure 5.13: Spin structure refined in magnetic space group $P6_3cm$.

Solution in space group $P31m'$ (#157.55) The prior solutions all featured symmetry relations connecting the moments of the two triangular and kagome layers, respectively. Yet the symmetry relations for the solutions in the triangular symmetry only connect the moments within the same layer. Therefore, there are now six independent magnetic sites, two triangular and four kagome ones for the two solutions with trigonal symmetry. On the triangular sites the moments may tilt out of plane, but they are fixed concerning their orientation in ab-plane. This also applies for the two kagome moments on the mirror plane, while the other moments can rotate freely. Due to the symmetry three different columns exist, which are rotated 120° to one another. The moments on neighbouring kagome sites of different columns tend to be rotated by 120° to one another as well.

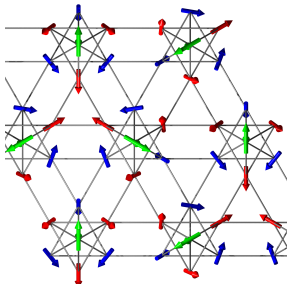

Figure 5.14: Spin structure refined in magnetic space group $P31m'$.

Solution in space group $P31m$ (#157.53) In contrast to the previous solution, here the orientation of the moments on the triangular sites is fixed completely to the ab-plane. One moment of each kagome layer of the same column is oriented antiparallel to the triangular moment. The remaining moments on kagome sites can rotate freely. From the refinement these moments, also tend to align antiparallel to the moments on the triangular sites, which yields an almost 120° rotation between moments on neighbouring kagome sites of different columns. Of course the pattern of 120° rotated columns is preserved.

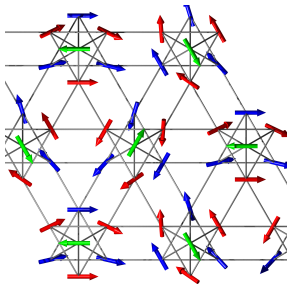

Figure 5.15: Spin structure refined in magnetic space group $P31m$.

FullProf refinement

Firstly, the crystallographic model (cf. Subsection 5.1.1) has been applied for a refinement of the integrated crystal structure peaks in order to determine the scale-factor. Only a few crystal structure peaks unique in the space group $P6_3mc$ could be measured (cf. Table D.2), therefore the parameters of the model have been fixed. With the use of this scale-factor, the length of the moments is defined in μ_B in the refinement of the magnetic structure. Following the proposed solutions above, magnetic CIF files were exported as control files for refinements using the FullProf suite [RC93]. The definition of the magnetic moments has been changed from Cartesian to spherical coordinates, as these allow for an easier linking of the parameters. This way the moments' length can be directly linked for both the triangular and kagome site, respectively. The scale factor from the crystal refinement has to be adjusted due to the use of a larger unit cell. The magnetic unit cell is 9 times larger than the structural unit cell, which leads to a decrease of the scale factor by a factor 81 [RC11]. As described before the Co and Fe ions are statistically distributed over the magnetic sites, which have been included by adjusting the occupations according to the percentages. This will change the refinement results because

of the different magnetic form factors for Co^{2+} and Fe^{3+}. The aim now, is to determine the solution, which can best describe the measured set of integrated intensities.
The integrated intensities (cf. Table D.3) have been measured on the single crystal with $(h\,h\,l)$-

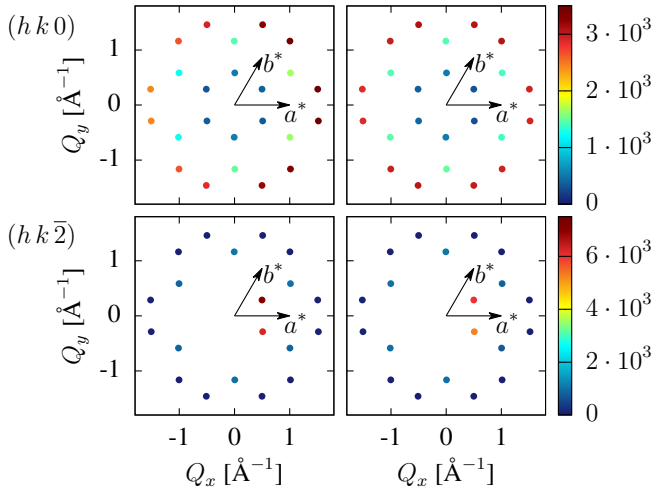

Figure 5.16: Integrated intensities of the scattering planes $(h\,k\,0)$ and $(h\,k\,\overline{2})$ measured on Morpheus at 80 K, plotted in the respective scattering plane. Left: Original intensities show a deviation between symmetrically equivalent peaks. Right: The deviation has been corrected by applying an angular dependent factor f_{angular} (cf. Equation 5.4).

orientation, which is quite large for this type of experiment. Usually a smaller more evenly shaped crystal is used in order to minimize multi-scattering, extinction or shape effects. Plotting the intensities at their respective positions in **Q** reveals that an angular dependence is present. Due to the shape of the crystal the illuminated sample volume varies under the sample rotation. This can be corrected by applying a factor f_{angular}

$$f_{\text{angular}} = 1 - w \cdot \cos\varphi, \tag{5.4}$$

where φ is the angle in $\{h\,k\,0\}$ regarding the vector a^* and the constant w as a weighing factor of the angular dependence. A good correction was determined for $w \approx 18\%$ (cf. Fig. 5.16). In preparation for the refinement, the set of all integrated intensities are reduced within each desired solution (cf. Tables D.4 and D.5), as the condition of peaks being symmetrically equivalent depends on the used magnetic space group. Here, only hexagonal or trigonal space groups are of interest. In both cases the average over the equivalent peaks will automatically correct the found angular dependence in intensity while increasing the error in comparison. This is still reasonable as a bigger error is a natural consequence for a measurement on a larger crystal.
Despite using the symmetry information from the magnetic space group, the parameter phase space is still too large for an immediate Rietveld refinement. So at first, simulated annealing is used to determine a starting configuration and if possible decrease the parameters set by linking more parameters.

Simulated annealing FullProf provides an option to use simulated annealing to refine the model according to the data. Simulated annealing is a method based on Monte Carlo simulation, where parameters and therefore the moments are changed at random, and the corresponding structure factors are compared to the data. If the agreement is decreasing with the change, the change is only accepted with a specific chance, depending on the temperature. With decreasing temperature the chance also decreases, which leads the spin structure to anneal [RC93]. However, due to its structure, the method is not useful to determine the parameter error.
From the temperature dependence observed at DNS (cf. Fig. 5.3) the spin structures at 4 and 80 K are the most interesting, because they are at the extremes of the spin reorientation. Thus the integrated intensities for the sample have been measured at these temperatures. The temperature dependence also indicates a more complex structure at low temperatures, as the peak shapes of the integrated intensities measured at 80 K show a more commensurate order. This results in overall larger relative errors for the integrated intensities at 4 K (cf. Table D.3). The proposed commensurate space groups are probably better applicable to the data set at 80 K. Therefore, this measurement will be refined at first and its result applied to the intensities measured at 4 K. From the refinement of the crystal structure it was determined, that all triangular and kagome sites have the same average occupations of ions, respectively (cf. Subsection 5.1.1). Thus the same is likely for the moments on these sites, which can be realized in the model by linking the corresponding parameter of the moments on the respective sites. From the results of the refinement using simulated annealing, it can be concluded that two peaks cannot be reproduced well by any of the space groups. These peaks have been at the limit of the accessible range of the instrument, which might have led to the intensities not being correctly determined. Calculating the structure factor for the resulting spin structures reveals that the space groups $P6_3c'm'$ and $P31m'$ yield significant intensity at the crystal Bragg peak positions. In this experiment the four-circle setup could not be combined with polarization analysis without restricting oneself to a small set of magnetic peaks. Therefore, the magnetic contribution at the crystal Bragg peak positions could not be separated. However, from polarization analysis at DNS the magnetic scattering at the crystal Bragg peak position is known to be close to zero. Thus, peaks with zero intensity can be added at the crystal Bragg peak positions for the refinement. In order to use these space groups for the Rietveld refinement, the number of parameters must still be decreased. From iterations of the refinements and the correlation matrix, one can conclude which parameters can be linked, without reducing the refinement's goodness-of-fit (see Table 5.1 and D.9). This leads to the following 5 different configurations:

A Parameters are only constraint by the definition of the magnetic space group.

B Link the moments length of the kagome and triangular sites, respectively.

C Add peaks with zero intensity at the crystal Bragg peak positions.

D Remove the two magnetic peaks from the refinement.

E Link further parameters (depends on the used space group).

While the latter models always include the constraints of their previous ones. These configurations are submodels to the magnetic space groups. The resulting spin configuration will remain in the superior magnetic space group and thus only change slightly. In addition, the magnetisation can be calculated, which reveals an important deviation between the magnetic space groups. The refined spin structures with non-zero intensities at the crystal Bragg peak

positions also exhibit a non-zero magnetisation along c-direction, which can be used as an indication for the ferromagnetic part. The different models are compared using the agreement factors calculated by FullProf. Since integrated intensities have been refined the R_{Bragg} factor is a suitable choice, which is defined as

$$R_{Bragg} = 100 \cdot \frac{\sum_{hkl} |I_{hkl,obs} - I_{hkl,calc}|}{\sum_{hkl} |I_{hkl,obs}|} \tag{5.5}$$

with $I_{hkl,obs}$ the observed intensity for the peak at $(h\,k\,l)$ and $I_{hkl,calc}$ the calculated intensity for the same peak [RC11].

	$P6_3c'm'$		$P6'_3cm'$		$P6'_3c'm$		$P6_3cm$		$P31m'$		$P31m$	
Conf.	R_{Bragg}	**M**	R_{Bragg}	**M**	R_{Bragg}	**M**	R_{Bragg}	**M**	R_{Bragg}	**M**	R_{Bragg}	**M**
A	42.2	-5.25	71.0	0	42.2	0	71.0	0	18.1	5.11	18.5	0
B	42.2	2.26	71.1	0	58.4	0	77.4	0	18.2	4.45	21.2	0
C	46.9	-1.35	74.5	0	71.0	0	77.2	0	22.0	-3.36	22.0	0
D	46.4	-1.11	80.8	0	70.1	0	80.5	0	17.4	0.03	17.2	0
E	-	-	-	-	-	-	-	-	17.6	0.00	17.3	0

Table 5.1: Goodness-of-fit for the different solutions and configurations (Conf.) from the refinement of the data at 80 K using simulated annealing. Net magnetisation **M** per crystallographic unit cell in μ_B is oriented along $\hat{\mathbf{e}}_z$.

In the case of the magnetic space groups $P6_3c'm'$, $P6'_3c'm$ and $P31m'$, the model **C** leads to more than a 10% decrease of the refinements' goodness-of-fit. With the introduction of model **D**, the net magnetisation vanishes for the magnetic space group $P31m'$. Regarding all different models the goodness-of-fit of the refinement for the solutions in the hexagonal symmetry are significantly reduced, compared to the solutions in trigonal symmetry. Therefore, further analysis is only needed for the latter ones.
The same procedure has been applied to the data measured at 4 K. The obvious difference is a decrease in the goodness-of-fit of the refinement for the trigonal solutions (see table 5.2). Thus it can be deduced that the spin structure at 4 K is not only more complex, but also differs from the commensurate model. Still the trigonal solutions give the best refinements.
The results for the refinement of the spin structure at both temperatures and the links between

	$P6_3c'm'$		$P6'_3cm'$		$P6'_3c'm$		$P6_3cm$		$P31m'$		$P31m$	
Conf.	R_{Bragg}	**M**	R_{Bragg}	**M**	R_{Bragg}	**M**	R_{Bragg}	**M**	R_{Bragg}	**M**	R_{Bragg}	**M**
A	38.2	-0.21	68.0	0	38.1	0	68.3	0	24.3	16.8	23.0	0
B	38.3	1.83	68.2	0	55.8	0	75.6	0	24.4	15.2	27.0	0
C	43.0	-1.04	71.8	0	69.3	0	75.5	0	28.1	-0.03	28.5	0
D	41.1	-1.04	79.8	0	67.5	0	78.6	0	22.8	0.00	22.7	0
E	-	-	-	-	-	-	-	-	23.2	0.00	22.9	0

Table 5.2: Goodness-of-fit for the different solutions and configurations (Conf.) from the refinement of the data at 4 K using simulated annealing. Net magnetisation **M** per crystallographic unit cell in μ_B is oriented along $\hat{\mathbf{e}}_z$.

the parameters are listed for the hexagonal space groups in Table D.8 and for the trigonal space groups in Table D.9.

Rietveld refinement The refinement using the Rietveld method is based on the configuration **E** with the peaks of zero intensity added at the crystal Bragg positions, with the two peaks removed and additional linking between the refinement parameters, which was determined using simulated annealing. This configuration has the least number of parameters and most constraints, while exhibiting still a good refinement in comparison with the other configurations. The refined spin structure from the simulated annealing is used as a starting configuration. However, the Rietveld refinement cannot yield a result with a decent goodness-of-fit (cf. Table 5.3). From the simulated annealing it is known, that a parameter configuration with a better agreement exists. Yet, due to the geometric frustration and the degeneracy found in the model it is very likely that several configurations of similar goodness-of-fit exist. This is why the Rietveld refinement is unable to converge to a single solution and results in a worse agreement. Nevertheless the errors determined with this method depict the possible variation of the parameters. The results of the Rietveld refinement including the linking of parameters and errors are given in Table D.10.

	$P31m'$		$P31m$	
Temperature	R_{Bragg}	**M**	R_{Bragg}	**M**
80 K	67.3	0	91.0	0
4 K	67.9	0	76.6	0

Table 5.3: Results of the refinement of the data at 80 K using Rietveld for the configuration **E**.

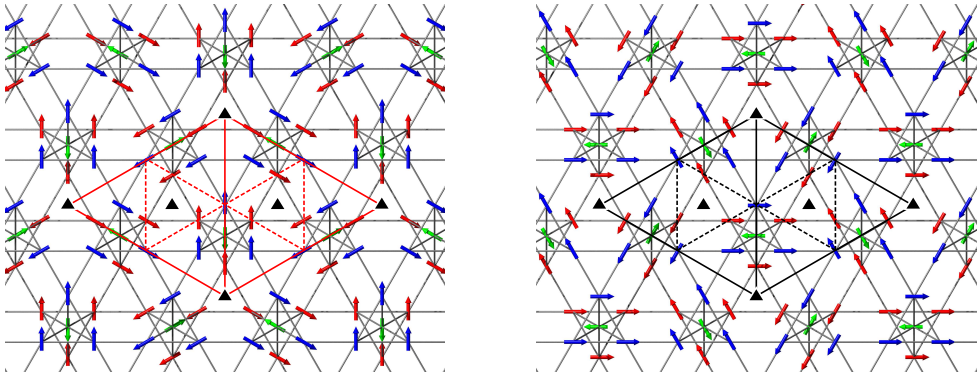

(a) **(b)**

Figure 5.17: Investigation of the symmetry of the ground state from the Monte Carlo simulation. Symmetry operations are marked according to the notation in [Lit08] with time inverted operations in red. **(a)** Comparison with magnetic space group $P31m'$. **(b)** Spin structure was rotated by 90° around the c-axis and comparing it with magnetic space group $P31m$.

The refinement of the spin structure in the magnetic space group $P31m$ yields a better fit to the measured integrated intensities than the one in $P31m'$. However, the difference is not that significant especially compared to the absolute goodness-of-fit of the refinement. Therefore, it is of interest to compare the solutions to the ground state found using the Heisenberg nearest neighbour model (cf. Section 4.1 and Fig. 4.2b). The three-fold rotation axes are found to be located in between the columns, in the centre of triangles spanned by three red kagome spins (cf.

Fig. 5.17). In the case of $P31m'$ the mirror planes, which usually invert the spin, are inverted in time again, which basically leads to common mirror planes. Thus, the mirror planes can be located on the spins, if the spin is oriented parallel to the mirror plane. Furthermore, according to the magnetic group tables (cf. [Lit13] p. 5233), the mirror planes are parallel to the c-axis and intersect along the three fold rotation axes. Such mirror planes can be found for the spin structure in Fig. 5.17a. The mirror glide planes are a direct result from the other symmetry operations. This leads to a construction of symmetry operators which is in correspondence with the definition of $P31m'$. This spin structure does not fulfil the symmetry operations defined by $P31m$. Yet, in the Heisenberg nearest neighbour model there is no special axis defined in the ab-plane. Therefore, the selection of the spin structure in Fig. 5.17a is arbitrary and each other solution created by a rotation of each spin around the c-axis by the same angle also minimizes the energy. Yet, in regards to the symmetry operators special axes exist. Thus for a rotation by 90° the resulting spin structure (cf. Fig. 5.17b) shows the symmetry operations required for the $P31m$ space group (cf. [Lit13] p. 5229). The next step is to compare the results of the Heisenberg model with the refined spin structure. The two constraints (Eqs. 4.3 and 4.4) have been found to play a major role in the ordering observed in the model. In the case of the spin structure in $P31m$ (cf. Fig. 5.15) the triangular spins are confined in ab-plane and thus parallel to one another fulfilling Equation 4.3. The symmetry operations for the kagome spins cancel any effective moment along the c-axis and the kagome spins allowed to rotate freely cant significantly out of the ab-plane. This not only results in the vanishing net magnetisation, but also matches the influence of the sum rule (Eq. 4.4). The spin structure refined in $P31m'$ (cf. Fig. 5.14) shows triangular spins, which cant significantly out of the ab-plane in the same sense, but also canted to one another. Furthermore, the kagome spins of the same layer of each column cant if allowed out of plane. The symmetry relations allow for the structure to exhibit an effective moment along the c-axis, which was observed to possibly vanish. This does not fit with the derived constraints of the Heisenberg nearest neighbour model. Still the model is only a simple approach to reproduce the observed ordering. The solution in $P31m'$ cannot be ruled out from this alone, as other mechanisms can be present leading to a structure like this one. One such important mechanism could be the Dzyaloshinskii-Moriya interaction, which is allowed for $CaBaCo_2Fe_2O_7$, but has not been included to the model due to the huge increase in parameter space. But an adapt choice can possibly support a canting out of plane and yield a net magnetisation. This will be discussed further in combination with the complex part of the structure in Section 6.2.

The spin structures from the refinement can be evaluated further for comparison with results from other measurements. The solutions in the magnetic space groups $P31m'$ and $P31m$ have been most viable and are comparable to the spin structures determined with Monte Carlo simulation. In Tables 5.4, D.9 and D.10 the results based on the refinements with configuration **E** are presented. With changing temperature from 80 to 4 K a decrease in the ordered moment and an increase of the moments' angle with regards to the a-b plane is present. The moment as a parameter itself is a direct result from the refinement, while the average angle out-of-plane is calculated averaging over all spins in the large unit cell.

This is actually opposite to what is observed usually in a magnetic order. It is expected, that with decreasing temperature the fluctuations decrease, which then leads to higher ordered moments and less canted spins. Here this indicates an unusual behaviour related to the temperature dependence observed on DNS (cf. Fig. 5.3). Regarding the refinements, it has to be noted

		$P31m'$				$P31m$			
		moment [μ_B]		oop a. [°]		moment [μ_B]		oop a. [°]	
		tri	kag	tri	kag	tri	kag	tri	kag
SA	80 K	2.73	2.23	0.36	22.7	2.95	2.41	0.00	20.2
Ri	80 K	2.15 ±0.44	1.18 ±0.34	0.00	16.5	1.96 ±0.76	1.37 ±0.65	0.00	20.7
SA	4 K	2.57	2.24	0.03	23.4	2.88	2.39	0.00	21.0
Ri	4 K	2.11 ±0.28	1.11 ±0.20	0.08	21.9	1.85 ±0.38	0.91 ±0.21	0.00	23.4

Table 5.4: Spin structure evaluation of the refinement with the final model using both methods simulated annealing (SA) as well as Rietveld (Ri). The average of the absolute angle between the respective spins and the a-b plane is noted as out-of-plane angle (oop a.).

that the results from simulated annealing and Rietveld are, even though they show a similar behaviour, inconsistent. The reduced ordered moments for the kagome and triangular sites in both solutions and at each of the two temperatures indicates that the method did not converge to a reliable spin structure, in conjunction with the decreased goodness-of-fit for the Rietveld refinements. Still the determined errors appear to be reasonable. Assuming that the phase space in the simulated annealing is ergodic, the results are actually quite reliable. From the oxidation states for Co and Fe and the tetrahedral coordination [RRS$^+$14] in the high spin state this yields spins $S_{\text{Co}} = 3/2$ and $S_{\text{Fe}} = 5/2$. This results in total ordered moments of $m_{S,\text{Co}} \approx 3\,\mu_B$ and $m_{S,\text{Fe}} \approx 5\,\mu_B$. From the refinement of the crystal structure (cf. Subsection 5.1.1) considering the distribution of magnetic ions the average spin magnetic moment on the triangular sites for fully ordered spins is $m_{\text{tri}} \approx 4.7\,\mu_B$ and on the kagome sites $m_{\text{kag}} \approx 3.78\,\mu_B$. This shows that the moments are not that strongly ordered. The lower spin state only exists for the Fe-ions, due to the tetrahedral coordination. But the refined ordered moment is higher than the resulting ordered spin moment even considering the occupations and thus the low spin state can be excluded for both ions.

5.4 Resolving the magnetic order in Q-space

From the temperature dependence observed on DNS and Powgen the magnetic structure at two different temperatures is most interesting: 80 and 4 K. These were selected for the experiment conducted at BioDiff. The wavelength for the incoming neutrons was set to $\lambda_n = 4.4\,\text{Å}$, which allows for measuring up to $Q = 2.7\,\text{Å}^{-1}$. In order to make use of the good resolution of the detector in the horizontal and vertical direction, the small crystal was used. The sample has been pre-oriented to about 2° with its c-axis parallel to the rotation axis of the sample table (cf. Fig. 3.3a). At both temperatures an angular segment of around 60° has been measured in 0.5° steps and an intermediate segment of around 20° in 0.25° steps, covering the high intense magnetic peak $(4/3,\ 1/3,\ 0)$. With these segments at least two of each magnetic equivalent peaks have been measured, which were accessible with the selected wavelength. At each rotation step the sample was measured for two minutes. After each measurement the image plate was read at the medium resolution setting. For the evaluation, the method described in Section 3.3 has been used. Due to the slight misalignment of the sample, the range for integration has been increased up to $0.2\,\text{Å}^{-1}$ along the perpendicular direction in order to integrate over all peaks of the same scattering plane. This also enhances the background of the scattering.

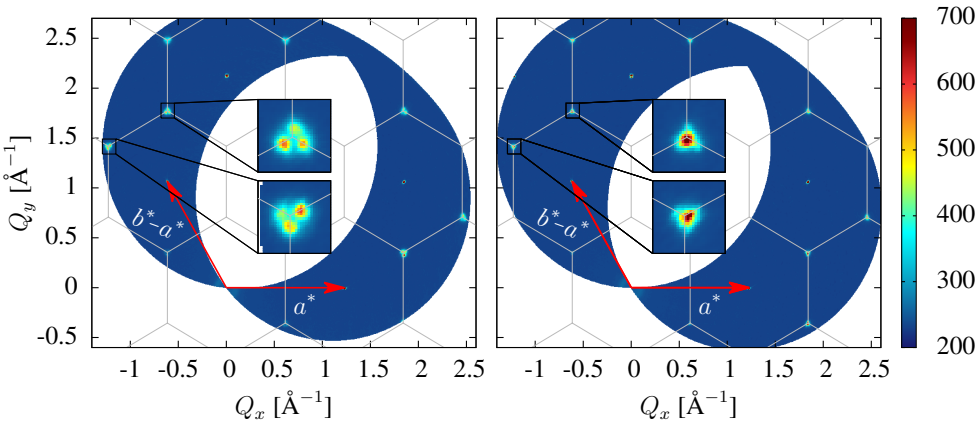

Figure 5.18: Extracted cuts of the hk0 scattering plane from the measurements at Biodiff at 4 K (left) and 80 K (right). The BZ boundary is marked in grey. The magnetic Bragg peaks $(\overline{5/3},\ 4/3,\ 0)$ and $(\overline{4/3},\ 5/3,\ 0)$ (symmetrical equivalents to $(4/3,\ 1/3,\ 0)$) are highlighted in insets. The commensurate magnetic peaks at 80 K vanish upon cooling to 4 K with only split peaks remaining. The splitting corresponds to the model in Fig. 5.7 for $\delta \approx 0.017$ Å^{-1}.

From the measurements, the $(h\,k\,0)$, $(h\,k\,1)$ and $(h\,k\,\overline{1})$ scattering planes could be extracted for both temperatures. The peaks with the highest intensities belong to the crystal structure. They feature a very sharp structure, which demonstrates the high resolution of the instrument in combination with the used sample. As expected these do not change with temperature. The remaining peaks can be attributed to the magnetic structure. It is also important to note, that apart from these expected peaks, no further Bragg intensities or diffuse scattering has been observed at neither temperature within the explored **Q**-space. This excludes the existence of further structures exhibiting scattering above the background limit (cf. Section 3.2).
At 80 K the magnetic peaks in all scattering planes can be found at the K-points of the BZ (cf. Figs. 5.18 and B.2 right), which fits with the data observed at DNS (cf. Fig. 5.2). Here these peaks of high intensity appear to be slightly smeared ($\Delta\mathbf{Q} \approx 0.015$ Å^{-1}) along the BZ boundary to the M-points of the BZ, forming a somewhat triangular shape. This means, that the spin structure in the ab-plane is in principle long-range ordered commensurably, with a $\sqrt{3}\times\sqrt{3}$ unit cell. Additionally, structures of shorter range order are present, yielding the diffuse scattering observed close to the commensurate peaks. Cuts perpendicular to $(h\,k\,0)$ reveal a smaller peak width along $[0\,0\,1]$, which means that the spin structure has a longer correlation length along the c-axis.
Decreasing the temperature to 4 K, a significant change can be observed (cf. Figs. 5.18 and B.2 left). Instead of the previous smearing, three peaks with decreased intensity have been measured at the corners of the previous triangle. At the same time the peak at the K-point has vanished completely. Furthermore, some of the triplet peaks show a variation in intensity within each triplet. Comparing the satellite peaks of symmetrical equivalent magnetic peaks, the variation obeys the six-fold symmetry around $[0\,0\,1]$ as well as the mirror planes spanned by $[0\,1\,0]$ and $[0\,0\,1]$. This means the intensity variation over all three is only allowed for satellite triplets, where the magnetic peak can be written as $(h\,k\,l)$, with $h \neq k$. For triplets with $h = k$ the satellite peaks next to the mirror plane exhibit the same intensity. The width of each satellite peak appears to be resolution limited, which is true along $\langle 0\,0\,1\rangle$ as well (cf. Fig. 5.19). Thus,

the associated magnetic structure is of a long-range order type.

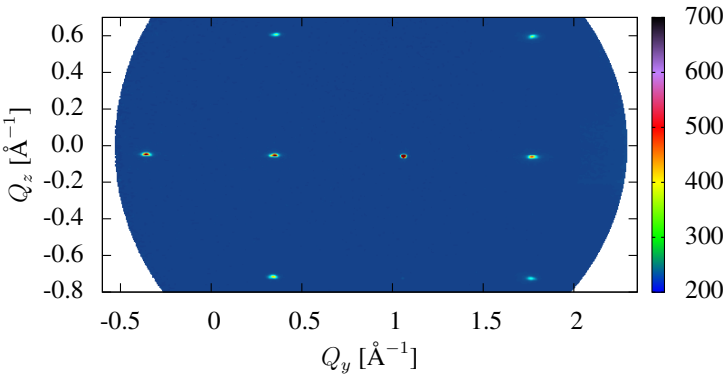

Figure 5.19: A cut through the magnetic peak $(\overline{4/3}\ 5/3\ 0)$ along $\hat{\mathbf{e}}_x$ as defined in Fig. 5.18, extracted from the data set measured on BiodDiff at 80 K. Shift in Q_z stems from a misalignment of the sample. Judging from the peak width the spin structure has a long correlation length along $\langle 0\,0\,1\rangle$-direction.

5.5 Magnetic peak structure at the resolution limit

The structure of the magnetic peaks could be resolved using powder diffraction as well as single crystal diffractometer, but as the revealed structure is rather complex and further information is needed to determine the spin structure which the observed scattering is related to. Here polarization analysis is used to distinguish the scattering contributions (cf. Section 2.3). Therefore, selected magnetic peaks are mapped with high resolution. The setups have been described in Section 3.3.

Apart from the integrated intensities, which have been determined on the neutron scattering instrument Morpheus, some of the magnetic peaks have been mapped in the $(h\,k\,0)$-scattering plane on the large crystal. This has been done using polarization analysis allowing for the calculation of the total and chiral magnetic scattering from the polarization channels $I_{x\bar{x}}$ and $I_{\bar{x}x}$. At 4 K in the total magnetic scattering the highest intensity is observed at the K-point of the BZ for all magnetic peaks (cf. Fig. 5.20 upper row). But significant scattering is visible close by the K-point as well. This diffuse scattering is shaped like triangles with corners oriented along the BZ boundary. In the case of the magnetic peak $(1/3\ 1/3\ 0)$, the scattering maps show an additional structure. On the one hand, the central peak appears to be slightly split transverse to the **Q**-vector and on the other hand the diffuse scattering does not continuously decrease with increasing distance from the K-point, but local maxima are present at the corners (cf. Fig. 5.20 upper row left). This structure is not so obvious for the other peaks. The chiral scattering is anti-symmetrical transverse to the **Q**-vector with the same direction for all peaks (cf. Fig 5.20 lower row). Heating the sample to 80 K results in the diffuse scattering to be localized closer to the K-point showing no additional structure.
For the peak $(4/3\ 1/3\ 0)$ the polarization channels I_{zz} and $I_{z\bar{z}}$ have been measured at 4 K. The scattering map for $I_{z\bar{z}}$ shows higher intensity close to the K-point with a slight elongation towards the magnetic peak $(2/3\ 2/3\ 0)$, while the scattering for I_{zz} shows no specific maximum but

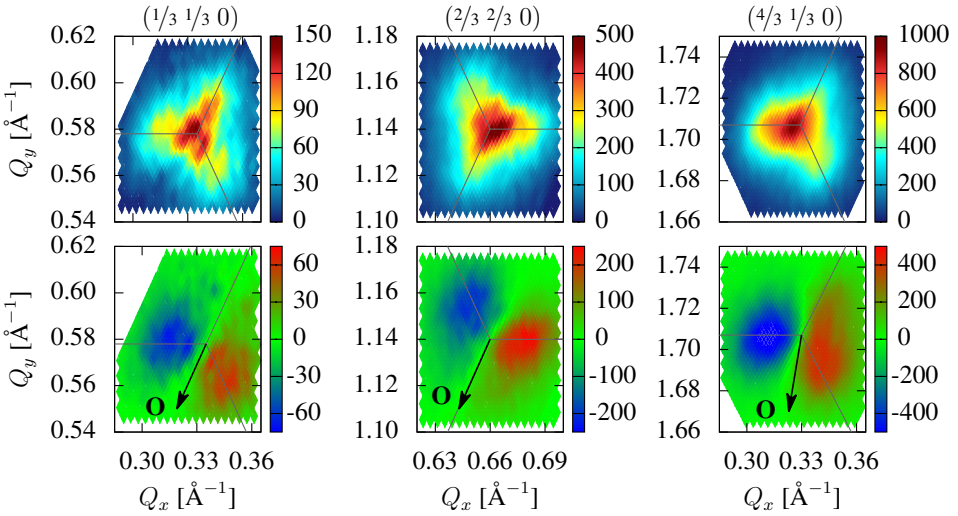

Figure 5.20: Structure of selected magnetic peaks calculated from polarization channels measured at 4 K on Morpheus. In the total magnetic scattering (upper row) the peaks reveal additional structure along the Brillouin zone boundary (grey). The chiral scattering (lower row) is anti-symmetrical transverse to the **Q**-vector for all peaks.

is of the same intensity at the corners as well as the centre (cf. Fig. B.1). The change between 80 and 4 K is not that prominent compared to the one observed at BioDiff, even considering the difference in resolution. This can be attributed to a slight material variation between the different measured crystals which leads to a difference of the magnetic order.

Similar measurements have been performed on the neutron scattering instrument MIRA. The setup for this instrument was specially created for this experiment and described in Section 3.3. Both the small crystal and the large crystal with $(h\,k\,0)$ orientation were measured. The polarization analysis option has been installed allowing further insight into the complex magnetic order observed in the previously presented experiment on BioDiff. MIRA features a high resolution while allowing the mapping of small volumes of **Q**-space, using a position sensitive detector performing rocking scans. As the general structure has been investigated on the instruments Powgen and BioDiff, in this experiment we focus on the specific magnetic peaks and their development under temperature. Again at 80 and 4 K larger sets of peaks have been measured, as these temperatures proved to be most interesting. Using a setup with electromagnetic coils and setting the wavelength of the incoming neutrons to 4.75 Å, we were able to measure peaks in the $(h\,k\,0)$, $(h\,k\,1)$ and $(h\,k\,2)$ scattering plane. From the sets, three peaks featuring comparably higher intensity have been selected and measured at several temperatures between 150 and 4 K. Depending on the measured polarization channels, different scattering contributions can be separated.
For every peak the polarization channels with **H** parallel and antiparallel to **Q** in the spin-flip configuration have been measured, allowing us calculate the total magnetic scattering as well as the chiral magnetic scattering. The additional polarization channels, which have been measured, are **H** parallel z with spin-flip and non spin-flip configuration, related to the scattering from moments both in-plane and out-of-plane (cf. Section 2.3). In order to access the $(h\,k\,2)$ scattering plane the ϕ angle of the four-circle geometry is used to rotate the crystal around the

normal vector of the Eulerian cradle. This effectively tilts the before mentioned scattering plane against the instrument floor. Thus, the performed rocking scans cut through the $(h\,k\,2)$ plane instead of measuring along it, which results in scattering intensity to be blocked by the analyser cavity. Due to the K-type antiferromagnetic order only negligible nuclear scattering intensity has been observed at the magnetic Bragg peak positions. Thus removing the cavity still allows for measuring the two channels $I_{x\overline{x}}$ and $I_{\overline{x}x}$. From these channels the total magnetic scattering and the chiral magnetic scattering can still be calculated.
Judging from the shape of the crystal Bragg peaks, the resolution ellipsoid is primarily elon-

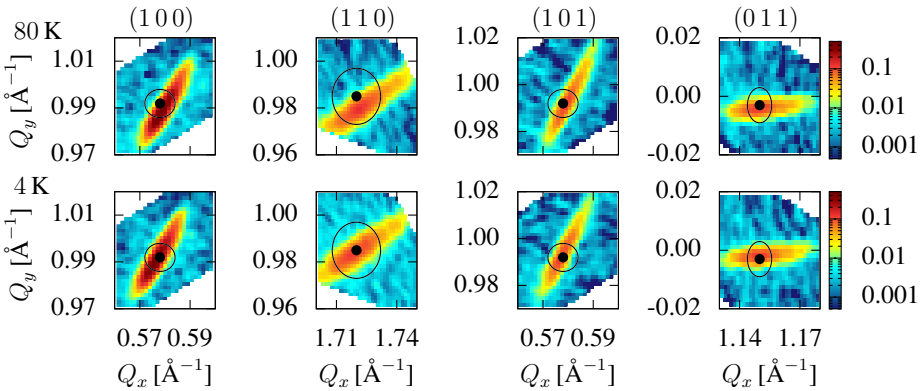

Figure 5.21: Selected crystal peak structure measured at MIRA on the small crystal show structural invariance between 80 and 4 K and an elongation of the resolution ellipsoid along **Q**. Black dots mark the BZ centre, which was defined during the experiment to a precision of $\Delta Q \approx 0.012\,\text{Å}^{-1} \cdot (|h| + |k|)$, indicated by the black circle.

gated along **Q** and in the case of the small crystal, sharp along the perpendicular directions. This means the same elongation observed for the magnetic peaks can be attributed to the instrument and therefore not inherent to the structure. The elongation of the peaks can lead to an overlapping of the main peak and its satellite peaks, which depends on their arrangement relative to **Q** and complicates the evaluation.

Since the two different crystals of $CaBaCo_2Fe_2O_7$ differ in the observed magnetic order, where the effect is more pronounced in the smaller one, this will be discussed first. Additional to the magnetic peaks a few crystal structure peaks have also been measured at both temperatures, which show no variation under temperature apart from the expected thermal expansion. Thus, the crystal structure remains the same within the temperature range. At 80 K in the total magnetic scattering, the main peak is the most prominent one for each magnetic peak, but noticeable intensity has been measured at the satellite peak positions as well (cf. Fig. 5.22 upper row). Furthermore, the main peak appears to hold some structure aside from the elongation due to the resolution ellipsoid, but this cannot be resolved clearly with the resolution and statistics at hand. Looking into the chiral magnetic scattering it is anti-symmetrical transverse to the **Q**-vector, while it is more pronounced at the satellite peak positions, it extends close to the K-points of the BZ (cf. Fig. B.3 upper row). If one of the satellite peaks is located on the **Q**-vector to the K-point, the chiral scattering vanishes for this satellite peak.
The total magnetic scattering extracted from the measurements at 4 K show the disappearing of the main peak and an increase of the satellites' intensity at the same time (cf. Fig. 5.22 lower row), as observed on BioDiff. Also, the intensity variation is present for the satellite triplets,

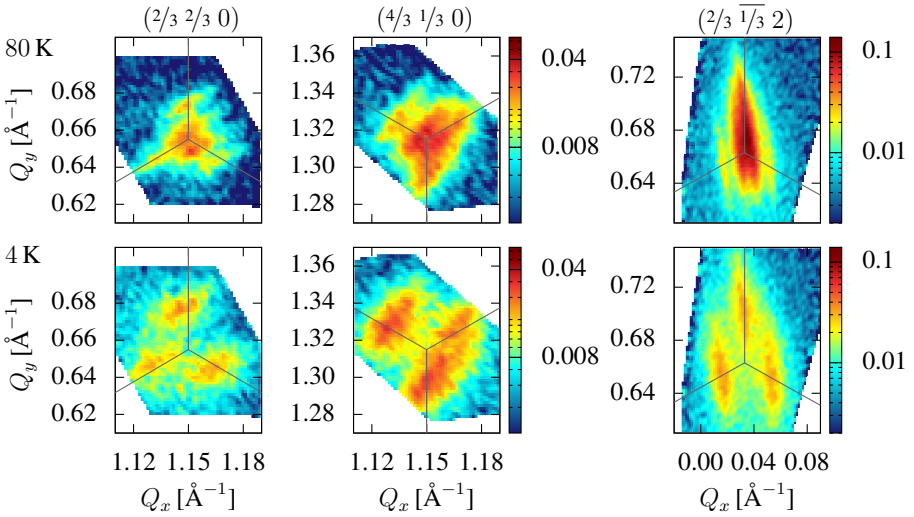

Figure 5.22: Peak structure close to the K-point of the BZ in the total magnetic scattering measured at MIRA on the small crystal. Satellite peaks with the same splitting are observable at 80 and 4 K, while the intensity at the K-point vanishes completely at 4 K.

where it is not prohibited by symmetry. Accordingly, the chiral scattering is only present at satellite positions, anti-symmetrical transverse to **Q** and vanishing for satellites on the **Q**-vector (cf. Fig. B.3 lower row). In the case of the magnetic peaks in the $(h\,k\,2)$ scattering plane, only 2 satellite peaks have been observed due to the third one being obstructed by the analyser cavity. Thus, the maps of peak $(2/3\ \overline{1/3}\ 2)$ in Fig. 5.22 have been measured without a cavity at a later time.

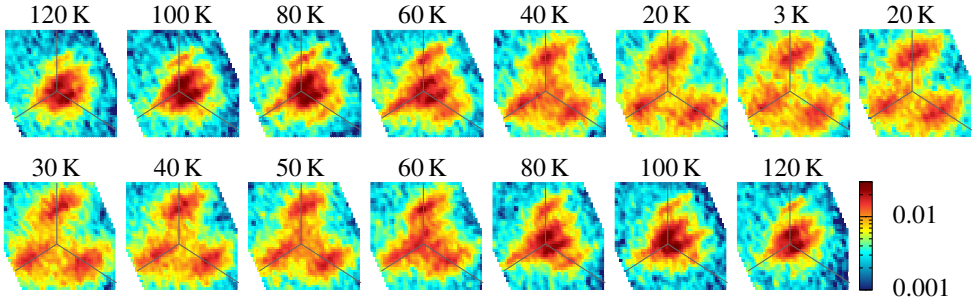

Figure 5.23: Temperature dependence observed on the magnetic peak $(2/3\ 2/3\ 0)$ in the total magnetic scattering measured at MIRA (sorted by the order of each measurement). The small crystal reveals a continuous change between two spin structures with different propagation vectors.

For the investigation of the temperature dependence the magnetic peaks $(2/3\ 2/3\ 0)$, $(4/3\ 1/3\ 0)$ and $(2/3\ \overline{1/3}\ 2)$ have been selected, as they provide the highest intensity and differ regarding their symmetry relation. The magnetic peak $(2/3\ 2/3\ 0)$ is symmetrical transverse to **Q** in the total magnetic scattering, while the peak $(4/3\ 1/3\ 0)$ allows for intensity variation over all three satellite peaks and the $(2/3\ \overline{1/3}\ 2)$ peak is of a different scattering plane. Still all peaks show a similar temperature dependence. Figure 5.23 displays exemplarily the variation of the total

magnetic scattering with temperature for the magnetic peak $(2/3\ 2/3\ 0)$. Upon cooling from 150 to 80 K, the overall scattering increases while the main peak is significantly stronger, compared to the satellite peaks. Below 80 K the main peak's intensity decreases with the satellite peaks increasing in intensity. Between 40 and 20 K the intensity at the K-point vanishes below the measurable statistics. The peaks have been mapped along heating as well. Here the main peak reappears between 40 and 50 K. The slight hysteresis can be attributed to phase stability of the magnetic structure related to the satellite peaks against temperature. The chiral scattering is calculated using the same channels and exhibits a transverse asymmetry regarding to **Q** for all peaks and temperatures (cf. Fig. B.5 top row). Due to its definition the background is subtracted, therefore the structure is visible more clearly. It is only along two arms of the BZ boundary, that peaks are visible in the chiral scattering. At each of them two peaks can be observed, shifted by the same distance to the K-point, respectively. The two peaks further away are at the position of the satellite peaks, whereas the others are even closer to the K-point. The latter ones vanish below 60 K, while chiral scattering is observed at the satellite peaks position for all temperatures, yet is most prominent below 20 K. Comparing the scattering for the channels z spin-flip $I_{z\bar{z}}$ (cf. Fig. B.5 middle row) and z non spin-flip I_{zz} (cf. Fig. B.5 bottom row), at the K-point higher intensity is observed in $I_{z\bar{z}}$ at all temperatures. This means that the moments of the spin structure related to the main peak have a smaller component parallel to the c-axis than to the ab-plane. At the same temperature, where the intensity in the z spin-flip channel vanishes at the K-point, intensity arises at the satellite positions, where chiral scattering is observed. The intensity in the non-spin flip z channel increases together with the satellite peaks at all three positions, but is most prominent on the satellite peak, which does not exhibit chiral scattering. On the hand this indicates a structure with moments more strongly canted out of ab-plane, but on the other hand the variation in intensity in both scattering contributions is intriguing and will be discussed further in Section 6.3.

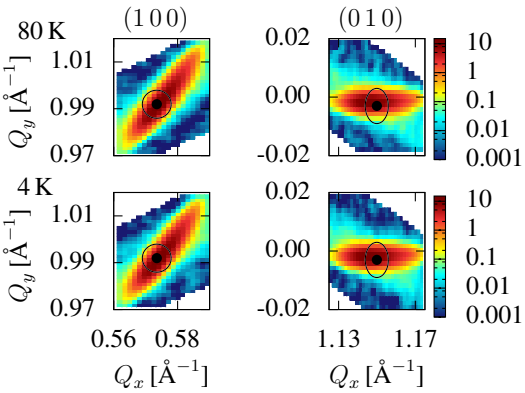

Figure 5.24: Selected crystal structure peaks measured at MIRA on the large crystal, structural invariance between 80 and 4 K is seen as well as an elongation of the resolution ellipsoid along **Q**. Black dots mark the BZ centre, which was defined during the experiment to a precision of $\Delta Q \approx 0.012\,\text{Å}^{-1} \cdot (|h| + |k|)$, indicated by the black circle.

In order to compare the magnetic order observed on the small crystal and the large crystal with $(h\,k\,0)$ orientation, the large one has also been measured at MIRA. The measurement times have been reduced to 10 seconds per detector image, as the large crystal holds around 100 times the volume of the smaller one. The measurement plan had to be shortened due to a lack of beamtime. At the same time by increasing the sample volume, the achievable resolution of the

data is expected to decrease. Looking at single detector images, the crystal length determines obviously the resolution along this direction projected on the detector. Comparing the crystal structure peaks in the $(h\,k\,0)$ scattering plane measured on both crystals, the ones taken from the large crystal feature a larger half-width half-maximum, which implies a resolution ellipsoid with greater semi-axis along these directions as well. Like for the small crystal, the crystal Bragg peaks do no change between 4 and 80 K (cf. Fig. 5.24).
The observed magnetic peaks at 80 K appear rather broad without the detailed structure ob-

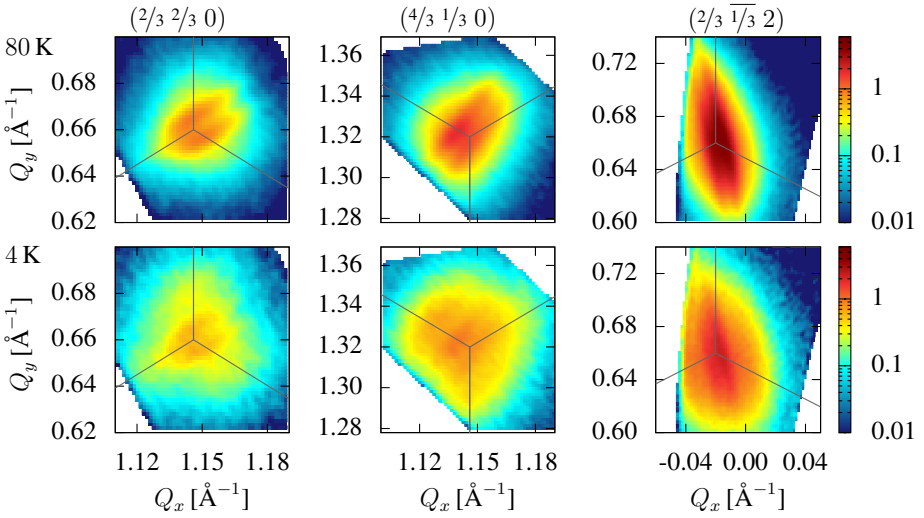

Figure 5.25: Peak structure close to the K-point of the BZ in the total magnetic scattering measured at MIRA on the large crystal shows relatively high diffuse scattering and a structured peak at the K-point at 80 K. At 4 K a slight additional structure is visible at the satellite peak positions.

served on the small crystal (cf. Fig. 5.25 upper row). Each peak seems to be split at the K-point, transverse to the **Q** vector, which is most likely related to two peaks very close to the K-point convoluted with the resolution ellipsoid. However, the peaks are not symmetric radially along the **Q** vector. Taking the crystal symmetry as well as the resolution ellipsoid into account, it can be assumed, that the elongation from the K-point to the origin or radially away from it stems from a third magnetic peak positioned along this direction. The observation indicates, that the slight structuring of the main peak observed on the small crystal is actually inherent to the compound. Additionally, diffuse scattering is more pronounced close to the BZ boundary, however, without specific structure in comparison to the small crystal.
Cooling the crystal down to 4 K, the diffuse scattering increases strongly and spreads further away from the K-point, while the intensity at the K-point itself decreases. In principle, this is a similar behaviour to the one observed on the small crystal, however, a distinct splitting could not be observed and the main peak remains more intense compared to what is related to the previously observed satellite peaks (cf. Fig. 5.25 lower row). Still, an additional structure arises at the same position in **Q** as observed on the small crystal (cf. Fig. 5.26). Due to the resolution ellipsoid's shape, this is visible best for peaks symmetric to **Q**, on $[h\,h\,l]$ or its equivalents, e.g. $(\overline{1/3}\ 2/3\ 0)$ and $(2/3\ 2/3\ 0)$.
Thus, the temperature dependence of the side structure is best visible on these peaks. In Fig. 5.27 the decrease of the diffuse scattering upon heating from 20 to 80 K is clearly visible and

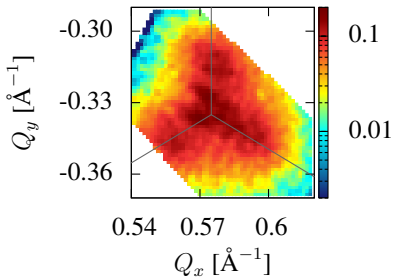

Figure 5.26: The magnetic scattering close to the magnetic peak $(\overline{1/3}\ 2/3\ 0)$ measured on the large crystal at 4 K. Here satellite peaks are visible with the scattering at the K-point being still prominent.

at the same time the increase in intensity at the K-point. Also the slight indications of satellite peaks vanish between 60 and 80 K. The temperature dependence for the other scattering contributions is in regards to their structure similar to the ones observed on the small crystal. Of course, these are only similar under the premise of the intensity close to the K-point, being dominant in all contributions and at all temperatures.

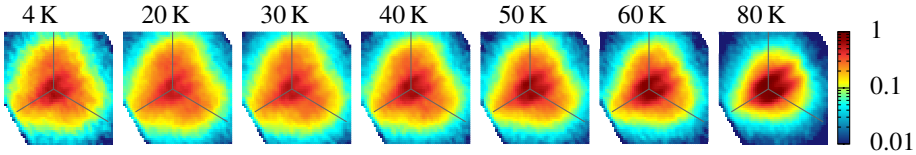

Figure 5.27: Magnetic peak structure of the peak $(2/3\ 2/3\ 0)$ measured at MIRA at several temperatures on the large crystal, sorted by the order of each measurement. These maps have been measured in-between the measurements of the large peak sets at 4 and 80 K, whereas the maps at 4 and 80 K are from the respective set.

In order to compare the temperature dependence of the scattering intensity measured on both crystals with the observations made on DNS, the integrated scattering of the **Q**-space mapped for a single magnetic peak was determined for each different channel. The scattering background can assumed to be temperature independent, judging from the scattering maps. Then the background can been corrected under the assumption of constant background for all channels and using the fact that the total magnetic scattering can be calculated in two different ways:

$$I_{x\bar{x}} + I_{\bar{x}x} = |\mathbf{M}_\perp|^2 \approx I_{z\bar{z}} + I_{zz}. \tag{5.6}$$

The part of the resulting temperature dependence measured on the large crystal is similar to one observed at DNS. However, here no decrease in the total magnetic scattering is present below 80 K (cf. Fig. 5.28 right), which was already questioned in Subsection 5.1.2. The temperature dependence for the small crystal reveals an even higher intensity of the scattering from moments parallel to c-axis and chiral scattering compared to the scattering from moments parallel to ab-plane (cf. Fig. 5.28 left). The intensity of the magnetic scattering from moments parallel to the ab-plane reaches its maximum again at around 80 K, but the intensity of the chiral scattering is already higher at 60 K. As in the scattering maps the small crystal, a faster reorientation to the structure related to the satellite peaks is observed. The hysteresis visible for the scattering maps

is absent from the total magnetic scattering and only slightly apparent in the chiral scattering, as well as the scattering from moments parallel to the c-axis. The temperature dependence for the other two peaks shows a similar behaviour.

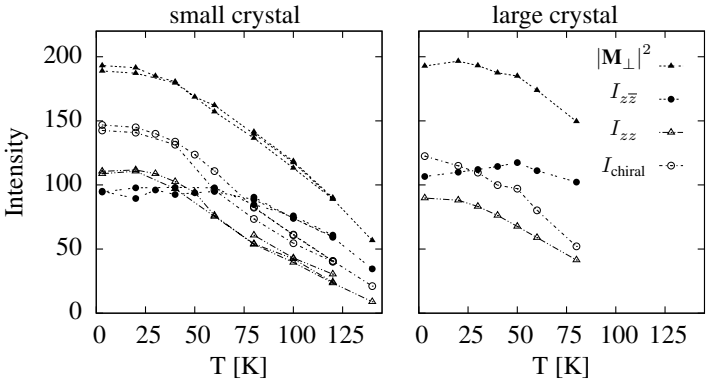

Figure 5.28: Temperature dependence of integrated intensities for the $(4/3\ 1/3\ 0)$ peak, which resembles the one measured at DNS (cf. Fig. 5.3). Comparing both crystals, in the case of the small one, the scattering from moments out of plane and chiral scattering is even more pronounced. The background was subtracted using Equation 5.6.

5.6 Spin dynamics

The results on the magnetic order have revealed a quite complex structure, but using polarization analysis some of its complexity has been elucidated. The investigation of the spin dynamics can even go beyond that. Even though the excitations are measured, important conclusions can also be drawn for the magnetic order. Furthermore, the dynamics are a very useful tool to study the interactions of a system. With only the elastic scattering at hand the possible insight would be rather limited. The spin dynamics in $CaBaCo_2Fe_2O_7$ have been previously investigated in [Rei11] using a triple-axis and a time-of-flight spectrometer. Still two major questions remained open. Especially the lower part of the excitations in energy could not be explored sufficiently and the comparison to the dispersions from LSWT (cf. Section 4.2) was inconclusive.

5.6.1 The overall spin wave excitation spectrum

The experiment itself has been performed prior to this thesis and has been described in [Rei11]. The combined data sets measured at ARCS (SNS, Oak Ridge, USA) cover a huge part in **Q**-space and energy, from which one can extract approximately the excitation spectra along certain directions, by integrating over the perpendicular directions. The measurement was conducted on the two large crystals with $(h\,k\,0)$ and $(h\,h\,l)$ orientation. In the case of the $(h\,h\,l)$-orientated sample, the excitations are integrated along a rectangular grid. As the excitations follow the same symmetry, the integration enhances the statistics. But in the case of the crystal with $(h\,k\,0)$ orientation, an integration over the hexagonal symmetry will blur the excitations and

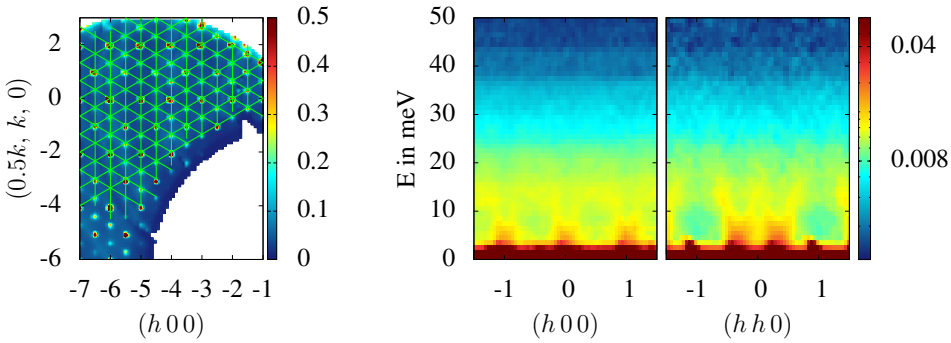

Figure 5.29: Extracting cuts along symmetry directions from the measurement taken at 4 K on the crystal with $(h\,k\,0)$-orientation on ARCS. Possible cuts along directions symmetrically equivalent to $[1\,1\,0]$ (left). The resulting E versus **Q**-cuts after adding the extracted cuts (right).

cuts with a small integration volume do not provide enough statistics.

During this thesis the evaluation of the data has been pushed further, aiming to enable exploration of the excitations along the high symmetry directions in the $\{h\,k\,0\}$ scattering planes. The measured **Q**-space spans over a huge number of magnetic Brillouin zones. In theory the dispersions within each BZ are the same, but their spectral weight will differ. Superimposing the excitations of all BZs can increase the statistics by several magnitudes, but the software Horace [Hor] used for the evaluation does not allow for such a method. Another possibility is to sum up symmetrically equivalent cuts. The single data sets add up to a 60° angular segment of the **Q**-space. This allows for cuts with three different yet symmetrically equivalent directions, for each high symmetry direction (cf. Figure 5.29 left). The cuts from all $\{h\,k\,0\}$-scattering planes and their translations along the direction of the cuts have been superimposed. For the used incident energy this method increases the statistics by a factor of 1000 on average. In the resulting cuts spin wave dispersions are visible up to 18 meV in energy (cf. Fig. 5.29 right). At around 22 meV a sudden drop in intensity is present, which can be assumed to be the limit in energy of the excitation in the $(h\,k\,0)$-scattering plane. In-between the excitation branches, lower intensity is observed, which shows that the excitation cones do not exhibit an excitation continuum. Two-magnon processes apparently do not play a major role. Even though the statistics have been increased, the limited resolution in energy and **Q** cannot be overcome. Within this resolution the excitations do not show a gap in energy close to the elastic line.

Integrating the combined data sets, measured on the crystal with $(h\,h\,l)$-orientation, perpendicular to the $[0\,0\,1]$ direction, an excitation spectrum has been observed, which reveals dispersions along $\langle 0\,0\,1\rangle$ to be present up to 68 meV [Rei11]. However, in contrast to the dispersions calculated with LSWT (cf. Fig. 4.3) no gap in energy is observed. Instead the observed excitation appear more closely related to the dispersions of a linear antiferromagnetically coupled spin chain (cf. Fig. 5.30 left) with half its period stretching over $4 \cdot c^*$. This implies that the magnetic unit cell along the c-axis for these dispersions is a quarter of the structural unit cell, which is a single kagome or triangular layer. This is a contradiction in itself, as an antiferromagnetic linear spin chain has a unit cell consisting of two spins of opposite orientation. In correspondence with the results from the LSWT (Subsection 4.2) a better approximation is a combination

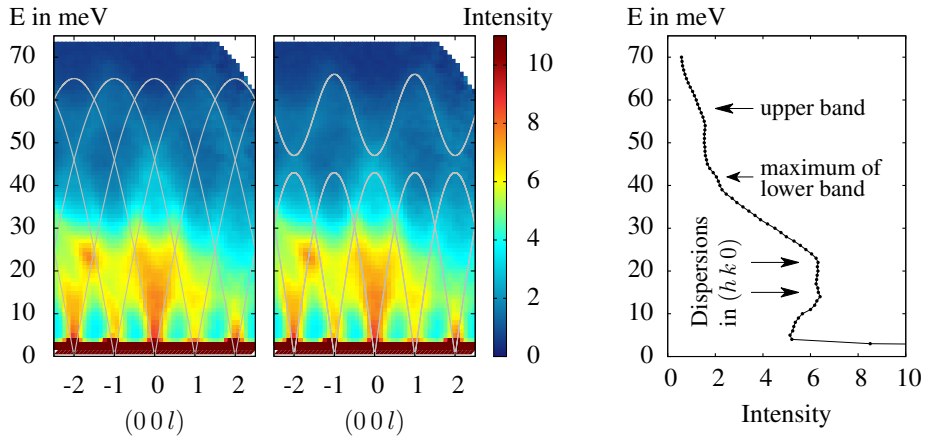

Figure 5.30: Excitations along $[0\,0\,1]$ measured on ARCS at 4 K. Dispersions for a linear antiferromagnetic (left) and pseudo-ferrimagnetic (middle) spin chain (gray line) are added for comparison. Full integration along the spatial directions close to the origin (± 5 Å^{-1}) reveals intensity levels (right), corresponding to the dispersions of a pseudo-ferrimagnetic chain.

of an antiferromagnetic linear spin chain for the lower band and a ferrimagnetic linear spin chain for the upper band. In this model dispersions of both the lower and upper band span with half its period over $2 \cdot c^*$ (cf. Fig. 5.30 middle). In contrast to the dispersions of a linear antiferromagnetically coupled spin chain, the slopes of the observed excitations can be modelled while remaining physically meaningful. In this model the unit cell along c holds an effective spin of the triangular layer as well as that of the kagome layer. The plotted dispersions for the lower band reach up to 43 meV and for the upper band from 47 meV up to 66 meV. The approximation of the excitations along $[0\,0\,1]$-direction with a linear antiferro-ferrimagnetic spin chain is not only in correspondence with the model, but can also be supported by levels in intensity visible when all directions except the one along energy are integrated (cf. Fig 5.30). At very low energies up to 3 meV the intensity is overshadowed by the resolution in energy, but apart from that the first level is visible up to 25 meV. This level relates to the numerous dispersions in the $(h\,k\,0)$-scattering plane, which only span up to 25 meV in energy (cf. Figure 5.29). Following, the next level is visible up to 42 meV, which stems from the excitations along the $\langle 0\,0\,1\rangle$-directions belonging to the lower band. The level at energies up to 68 meV consists of the excitations of the upper band. Dispersions like the ones of the linear antiferromagnetic spin chain, which span continuously up to the highest energies, cannot explain the different slopes in intensity from 30 to 60 meV.

In contrast to the Heisenberg nearest neighbour model, the actual compound $CaBaCo_2Fe_2O_7$ features Co^{2+} and Fe^{3+} ions with different spins statistically distributed over the magnetic sites, which cannot be implemented in a simple model. Analogue to the gap in the dispersions of a ferrimagnetic chain it can be assumed, that in present model a decrease of the effective kagome spin will also decrease the gap between the upper and lower band. The comparison with the measurement shows that the disorder due to the statistically distributed spins and due to finite temperature can lead to a decrease in the difference between the effective kagome spin and triangular spin. This reveals the influence of the actual compound in contrast to the model and the amount of disorder still present at 4 K.

5.6.2 Investigating spin wave excitations with resolution adapted cuts

The time-of-flight spectrometer 4Seasons offers the use of four different incident energies at the same time. Apart from that it is similar in design to the time-of-flight spectrometer ARCS. Since the same crystal was used for the measurement (large crystal with $(h\,h\,l)$ orientation) the overall results for the high incident energies ($E_i = 90$ meV) are comparable. But the smaller incident energies ($E_i = 10$ and 17 meV) provide a significantly better resolution in **Q** and energy, which allows one to resolve the dispersions at lower energies.
As discussed in Section 2.4, for a given incident energy the scattering can be measured at the

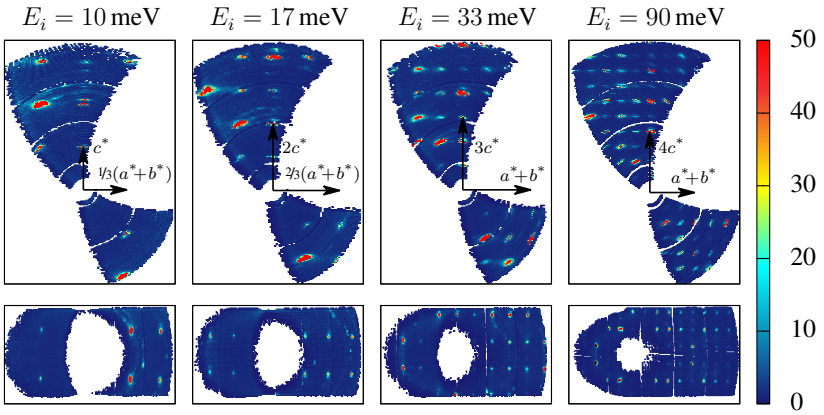

Figure 5.31: Slim cuts of the elastic part of the scattering planes $(h\,h\,l)$ (upper row) and $(h{+}1/6,\ -h{+}1/6,\ l)$ (lower row) extracted from the combined data sets measured with several incident energies at 4 K. Regular pattern of the magnetic and crystal structure peaks are visible.

same time only at specific points in **Q** and energy, but using several different incident energies the covered volume increases and the resulting data sets complement each other in **Q** and energy. This allows one to to cover a larger part of the **Q** and energy space at the same time. In this experiment we have measured the excitations using two sets of incident energies at 4 K and one set at 80 K. In Figure 5.31 the coverage of the **Q**-space using one set of incident energies ($E_i = 10$, 17, 33 and 90 meV) is displayed. Since these are slim cuts along the respective scattering planes, rings of zero intensity are visible, which stem from small gaps between two detector banks. The shape of the covered **Q**-space is the same for all energies, yet according to the incident wave vector k_i this results in different parts, which can be combined to a total coverage. The displayed scattering planes clearly show a regular Bragg peak pattern, which is a combination of the magnetic and crystal structure peaks. Additional diffuse scattering or even low intense peaks are most likely to be attributed to a textured powder scattering from the aluminium components in the neutron beam. An elongation of the magnetic peaks has been observed in the $(h\,h\,l)$-scattering plane on DNS as well (cf. Fig. 5.2 right), but here especially at incident energies $E_i \geq 33$ meV this is due to the orientation of the resolution ellipsoid (long semi-axis along the direction of the sample rotation).
With the different incident energies at hand and the coverage of a huge part of the space in **Q** and energy the excitations can be investigated along various directions. Yet for a K-type

antiferromagnetic order, as discussed in 5.1.2, only a few directions are actually necessary for the comprehension of the overall excitations. Here, we focus on a few important results, which have been gained thanks to the increased resolution and statistics. This allows for slimmer cuts reducing the effects from integration. In the following, two dimensional cuts are considered, which means there are two directions spanning the cut and the other two being integrated over. From the orientation of the crystal, four perpendicular directions are defined: $[1\,1\,0]$, $[0\,0\,1]$, $[1\,\bar{1}\,0]$ and E. The widths of a cut or rather the integration ranges in the spatial directions are determined from the full width half maxima of the crystal Bragg peaks along these directions. The resolution along the remaining direction is set to half the width. The cut's width along the energy dimension is selected by the instrumental resolution (about 5% of the incident energy) and the resolution for the cut as half the width.

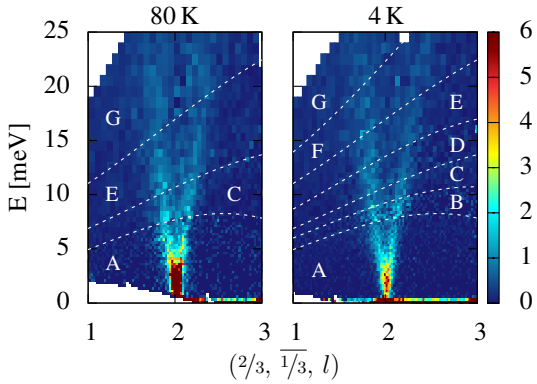

Figure 5.32: Combined extracted cuts along the $[0\,0\,1]$-direction through $(2/3,\ \overline{1/3},\ 0)$ from the data sets measured using different incident energies E_i (A: 10 meV, B: 14 meV, C: 17 meV, D: 24 meV, E: 33 meV, F: 53 meV and G: 90 meV). No excitation continuum is present in between the excitation branches. At 4 K an anisotropy gap is indicated by a local intensity minimum below 2 meV.

Such cuts are extracted from the excitations along different directions through the Γ-point of the magnetic Brillouin zone (cf. inset of Fig. 4.3), which is the K-point in the BZ. In Figure 5.32 the spatial direction of the cut ($[0\,0\,1]$) corresponds to $\Gamma \leftrightarrow$ A and in Figure 5.33 ($[1\,\bar{1}\,0]$) to $\Gamma \leftrightarrow M$. The latter ones are similar to the excitations along $[1\,1\,0]$ and accordingly $\Gamma \leftrightarrow$ K, but due to the orientation of the crystal these are covered incompletely within a single cut. The cuts along both directions are taken from the data sets of the different incident energies and combined in such a way, that the cut with the best resolution is used where available. This reveals the huge benefit of a multi-incident energy time-of-flight spectrometer, allowing one to follow the excitations in energy with adapted resolution. In the resulting figures the observed excitations show a linear dependence close to the Γ-point which descend to the elastic line. Especially at 80 K there is a significant increase in intensity around 2 meV. The same is also true at 4 K, but according to the Bose-Einstein statistics (cf. Eq. 2.38) the intensity is reduced. As the cuts are quite slim, the excitation cone arising from the Γ-point is sliced. Especially along the direction $[0\,0\,1]$ (cf. Fig. 5.32) the borders of the cone are visible as maxima in intensity, which means no excitation continuum is prominent down to at least 5 meV. Below 5 meV the excitation branches are not distinguishable any more with the available resolution. Along the $[1\,\bar{1}\,0]$-direction (cf. Fig. 5.33) the intensity on the branches decreases faster and is more blurred. This observation can be confirmed with the constant energy cuts in $\{h\,h\,l\}$-

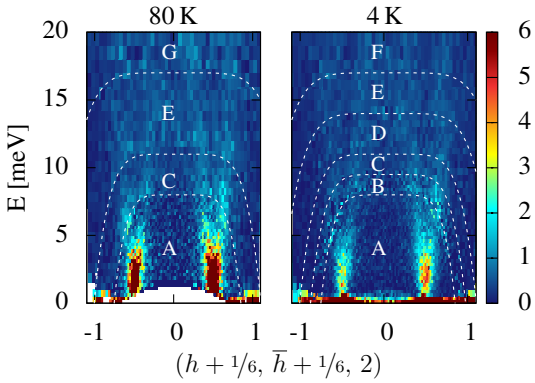

Figure 5.33: Combined extracted cuts along the $[1\,\overline{1}\,0]$-direction through $(1/6,\ 1/6,\ 2)$ from the data sets measured using different incident energies E_i (A: 10 meV, B: 14 meV, C: 17 meV, D: 24 meV, E: 33 meV, F: 53 meV and G: 90 meV). No excitation continuum is present inbetween the excitation branches. At 4 K an anisotropy gap is indicated by a local intensity minimum below 2 meV.

scattering planes (cf. Fig. 5.34). When cut at a specific energy the surface of the excitation cone becomes a circle or in this case, where the directions are not symmetrically equivalent, an ellipse elongated along $[1\,1\,0]$. Such an ellipse is adumbrated already at 5 meV, but clearly visible at higher energies in both planes and at both temperatures. Furthermore, a directional dependence can be observed in the intensity on the ellipse. Similar to the branches along $[1\,\overline{1}\,0]$ (cf. Fig. 5.33), here the intensity is decreased along $[1\,1\,0]$, which is in correspondence with previous measurements on ARCS [Rei11] (also cf. Subsection 5.6.1). Only along the $\langle 0\,0\,1\rangle$-directions, distinct excitations have been found. The absence of an excitation continuum implies that two magnon processes, which are also neglected in the linear spin wave theory, are less relevant. For a geometrically frustrated compound, which also does not exhibit a unique ground state, two magnon processes are usually expected. In addition, another observation can be made at low energies. Even though the excitations exhibit no distinct gap, still at 4 K a maximum in intensity is present at around 2 meV along both directions. The drop in intensity between this maximum and the intensity at the elastic line indicates the existence of an anisotropy gap. The gap is small compared to the total width of the inelastic spectrum and hence small compared to J_{in} and J_{out}, which relates to a similarly small anisotropy.

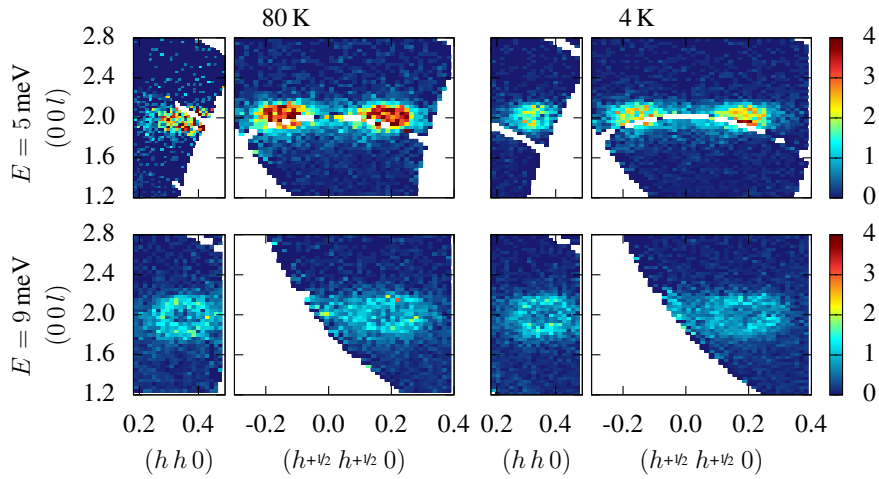

Figure 5.34: Constant energy cuts at 5 and 9 meV taken at two different planes from data sets with incident energy $E_i = 17$ meV. At both temperatures the ellipse of the excitation cone is unfilled above 5 meV. In addition the intensity on the ellipse is lower from the centre along the $[1\,1\,0]$-direction. The x and y-axes are scaled to fit regarding Å^{-1}.

6 Discussion

In Chapter 4 the results on the compound family Swedenborgites in general have been presented, together with the new spin dynamics simulations. In the following Chapter 5 the results on $CaBaCo_2Fe_2O_7$ from several methods have been discussed. In order to understand the full scope of the observed phenomena the results will be combined in the following sections. In Section 6.1 the results on the average magnetic order are collected for a conclusion on its spin structure. Followingly, the long-periodic order is discussed in Section 6.2 regarding its characteristics and how such an order can arise. The other interesting problem regarding the long-periodic order is its spin structure, which will be answered in Section 6.3. Finally in Section 6.4, the question is approached how the measured spin wave excitations relate to the results from LSWT (cf. Section 4.2) and the numerical spin dynamics (cf. Section 4.3).

6.1 Average and commensurate magnetic order

From the experimental results two different structures have been distinguished; a commensurate and a long-periodic structure. However, the additional structure observed close to the K-point of the BZ is shifted only slightly in the $\{h\,k\,0\}$-scattering planes by $\delta \approx 0.017\,\text{Å}^{-1}$. Therefore, the neutron scattering instruments without the necessary resolution are unable to resolve it. On these experiments only the average magnetic order is observed. This obviously also applies for macroscopic experiments. Still, these results give insight to the general spin structure. As the structure of the long-periodic order is related to the average order it is also very interesting to study.

From the measurements of the $(h\,k\,0)$- and $(h\,h\,l)$-scattering plane conducted at DNS (cf. Fig. 5.2), the correlation length along all three axes for the magnetic peaks can be observed. From this, it is apparent that the spin system exhibits a three dimensional order at 4 K. Using polarization analysis the total magnetic scattering has been extracted. Apart from the peaks located at the K-points of the BZ no further magnetic scattering has been observed. Therefore, the scattering is related to a $\sqrt{3} \times \sqrt{3}$ antiferromagnetic order and a propagation vector $(1/3\ 1/3\ 0)$. The temperature dependence of the integrated intensities reveals a phase transition at around 160 K, which is consistent with magnetization and specific heat measurements [RRS$^+$14]. In magnetization measurements a second yet broad local extremum is visible at around 80 K (cf. Fig. 5.4). In conjunction with the observations in Monte Carlo simulations, at this temperature the component of the moments on the kagome sites parallel to the c-axis start to align more

strongly. This is followed by a continuous spin reorientation between 80 and 4 K, visible in the magnetometry (cf. Fig. 5.4) as well as in the different scattering contributions (cf. Fig. 5.3). Thus, two spin structures are discernible. At 80 K, the spins are primarily oriented parallel to the ab-plane. At around 4 K the spin structure converges into a state with the spins canted more out of the ab-plane. Concerning the results from magnetometry the out-of-plane component is fixed, whereas the in-plane component is now able to vary.
In order to determine these spin structures integrated intensities of a set of magnetic peaks has been measured at both temperatures on Morpheus (cf. Section 5.3.2). Refinements of the intensities for the possible magnetic space groups have been most conclusive within the trigonal magnetic space groups. Both space groups are in agreement with the spin structure of the ground state from Monte Carlo simulation, which is of the same space groups. The solution in magnetic space group $P31m'$ (cf. Table. D.9) can exhibit a net magnetization along the c-direction. Such a net magnetization cannot be excluded, since a slight loop is present in field dependent hysteresis measurements [RRS$^+$14] and small peaks are visible at the crystal Bragg peak positions in the total magnetic scattering (cf. Fig. 5.2). The solution in $P31m$ is in better agreement with constraints calculated using the proposed model. Surprisingly, the goodness for the refinement at 4 K is worse compared to the one at 80 K. This means that the magnetic ordering at 80 K can be described better with a commensurate model, while the spin structure at 4 K deviates stronger from the commensurate order. The model within both magnetic space groups $P31m'$ and $P31m$ can be used to refine the powder diffractograms measured at POWGEN. By design, this is only successful for the peaks at the commensurate positions and due to the overlap between satellite and central peaks, the quantitative results are not reliable. Still, the commensurate part of the magnetic scattering is in correspondence with the model at all temperatures.
At 80 K the scattering maps measured at Morpheus, Biodiff and MIRA all show peaks at the K-point of the BZ, but also diffuse scattering in a triangular shape elongated along the BZ boundary. The distinct peaks at the K-points correspond to the commensurate order, but the diffuse scattering indicates disorder present in the spin structure. As the diffuse scattering is confined close to the K-points, the deviations from the commensurate structure are small, which is why the refinement of an average order at 80 K is reasonable. The elastic part of the dynamic structure factor from the spin dynamics simulation shows similar shaped diffuse scattering, which depends strongly on temperature and ratio $J_{\text{out}}/J_{\text{in}}$ (cf. Fig. 4.4). Increasing temperature increases the disorder in the structure and thus the diffuse scattering becomes more pronounced. However, increasing the ratio decreases the diffuse scattering, which is related to the decrease in freedom provided by the sum rule. As the measured diffuse scattering is present down to 4 K (cf. Fig. 5.2), it can be concluded that the ratio modelling the observed order in $CaBaCo_2Fe_2O_7$ best is below $\tau = 1.5$. The resulting freedom allows for the long-periodic structure to establish with a period length so constituted that its satellite peaks arise within the triangular shaped diffuse scattering.

6.2 Long-periodic order due to a spin spiral state

Comparing the measurements, the deviations from the average magnetic order differ for the various experiments. Some of the difference can be attributed to material variations between samples despite using the same recipe, which apparently influences the arising magnetic order. Furthermore, the resolution ellipsoid of the measurements depends not only on the instrumentation, but also on the investigated crystal. This determines if said magnetic order can be discerned. Here measurements on the large crystal with $(h\,k\,0)$-orientation and the small one (8mm^3) are of major interest. The latter one offers a better resolution at the disadvantage of a significant drop in intensity.
At DNS only the average magnetic order has been observed, still two different spin structures have been identified from the scattering contributions. Using other instruments with higher resolution a more complex structure has been resolved. The resolution limited magnetic peaks at the K-point of the BZ at DNS have been resolved to feature a smaller peak at the centre, but additionally structured scattering close by (cf. Fig. 5.7). The structure of the additional scattering intensity varies from diffuse scattering to specific peaks depending on instrument, temperature and sample. Yet, in all cases additional scattering structure was observed in the $\{h\,k\,0\}$-scattering planes only. Along $\langle 0\,0\,1\rangle$ the magnetic peaks are not elongated. Thus the structure stems from a variation parallel to the ab-plane of the spin structure. The peaks at the K-points relate to a commensurate magnetic order, similar to the average order discussed in Section 6.1. The temperature dependence of the integrated intensity extracted from the diffractograms measured at POWGEN shows, that the commensurate peaks exhibit the highest intensity at 80 K and decreases at low temperature below the intensity of the satellite peaks, while the intensity of the latter ones increase. Comparing these gradients with the ones observed on DNS, a similar trend has been observed for the intensity of the main peak and the scattering from moments in the plane and accordingly, a similar trend for the intensity of the satellite peaks and the chiral scattering as well as the scattering from moments parallel to the c-axis. Thus the scattering contribution from moments in the plane can be attributed mainly to the commensurate order and the scattering from moments parallel to the c-axis mainly to the long-periodic order, which indicates a more canted spin structure in case of the long-periodic order. As the peak pattern could be fit using a temperature independent peak splitting, this is a transition between two distinct types of ordering. However, the temperature dependent measurements of the integrated intensities at DNS (cf. Fig. 5.3), the magnetometry (cf. Fig. 5.4) and the extracted intensities from the powder diffractograms at POWGEN (cf. Fig. 5.9), all evidence a distinct Néel-transition at 160 K, but instead of an additional phase transition a continuous spin reorientation. The fit of different models to the powder diffraction data (cf. Subsection 5.3.1) and also the structure of the magnetic observed at MIRA (cf. Fig. 5.23) reveals the commensurate and long-periodic order to exist combined over a large range in temperature and to arise simultaneously at 160 K, which explains the absence of a second phase transition. In the measurements of the magnetic peak structure at 80 K also the commensurate peaks show a slight splitting at the limit of the instrumental resolution (cf. Figs. 5.22 and 5.25). If this observation is to be trusted, the spin reorientation takes place between a long-periodic order with a significantly longer period length of about 150 nm and the long-periodic order discussed here.
The measurement at Biodiff has been performed on the small single crystal and shows a clear splitting of three satellite peaks along the BZ boundary for each magnetic peak at 4 K (cf. Fig. 5.18). The observed splitting corresponds to the assumed model used for fitting the powder data (cf. Fig. 5.7). The commensurate peaks, which are present at 80 K, vanish completely. Com-

paring the intensity variation over each triplet, the satellite of $\{4/3\ 1/3\ 0\}$ and $\{4/3\ 1/3\ 1\}$, which overlaps with the main peak in the measurement at POWGEN, is actually the most intense one. Thus the integrated intensity of the commensurate peak might decrease in the powder data even stronger. Changing from the commensurate order to a long-periodic one is similar to the change between the crystal structure and the antiferromagnetic order (cf. Section 2.2). In both cases the new unit cell increases by the periodicity and the reciprocal cell decreases, but the shape of both cells is derived from the commensurate or rather the crystallographic one, which is determined by the symmetry. This is naturally only valid if the crystal structure symmetry is maintained upon the phase transition, as it is the case for $CaBaCo_2Fe_2O_7$. Thus, according to the magnetic space group determined for the average magnetic order, a splitting in the $\{h\,k\,0\}$-scattering planes on top of the antiferromagnetic order would result in six satellite peaks close to the K-point, but only three have been observed. Therefore the splitting has to stem from a long-periodic magnetic structure on top of the crystal structure and consequently a completely independent structure with a propagation vector

$$\mathbf{k}_1 = (1/3 + \delta,\ 1/3 + \delta,\ 0) \ \text{ with } \ \delta \approx 0.009 \tag{6.1}$$

noted in the crystallographic unit cell and its symmetrically equivalents

$$\begin{aligned} \mathbf{k}_2 &= (2/3 + 2\delta,\ -1/3 - \delta,\ 0) = -\mathbf{k}_5, \\ \mathbf{k}_3 &= (1/3 + \delta,\ -2/3 - 2\delta,\ 0) = -\mathbf{k}_6, \\ \mathbf{k}_4 &= -\mathbf{k}_1, \end{aligned}$$

resulting in a multi-q structure. The parameter δ is defined as the distance between the K-point and a satellite peak (cf. Fig. 5.7). Within the mapped **Q**-space the scattering pattern observed in total magnetic scattering (cf. Figs. 5.18 and B.2) still fulfils the symmetry of the same magnetic space group, e.g. the six-fold rotation symmetry around c^* and mirror planes symmetrically equivalents of $(h\,h\,l)$. In this sense the long-periodic order is related to the commensurate order. The usage of the polarization analysis at MIRA clearly proves the conclusion the long-periodic order to be stronger canted out of the ab-plane as correct, since the connection between the satellite peaks and scattering from moments parallel to the c-axis is directly visible (cf. Fig. B.5).

Still such a transition remains unusual, as this is not a slight reorientation, but a complete change of the whole structure. Apparently, this transition can be partly suppressed due to slight material variations. Only the small crystal exhibits a complete transition, where the commensurate magnetic peaks completely vanish at 4 K. The theoretical possibility of the transition from a long-range antiferromagnetic order to a long-range long-periodic order can be understood with the help of the Heisenberg nearest neighbour model. The rules derived from minimizing the energy for each double tetrahedron result in a unique solution for the triangular spins while the solution for the kagome spins is degenerate for ratios $\tau < 1.5$. This leads to the kagome layers to vary from each other within ranges determined by the ratio, which is the so-called spin liquid phase. The elastic part of the dynamic structure factor calculated from such a spin structure shows diffuse scattering close to the peak at the K-point of the BZ (cf. Fig. 4.4). The diffuse scattering is elongated along the same direction as the satellite peak positions. Thus the long-periodic order is part of the spin system's phase space, and the disorder plays an important role if a system can manage to undergo the transition. In a system with a unique solution for all kagome layers already at the Néel transition, all spins start to anneal to this solution and a transition to a different long-range order will be suppressed. However, in a spin liquid structure the energy barrier for this transition is smaller. This is the same reason why the nematic

phase exists for very small temperature fluctuations at $T/J_{\text{in}} \ll 0.01$. Yet the transition as it was observed in the measurements has not been found in the simulation. On the one hand, the transition might be suppressed by the periodic boundary conditions, which do not fit to the period of the order, on the other hand the necessary mechanism is missing from the model. The broken inversion symmetry on the bonds between nearest neighbour magnetic sites allows for the Dzyaloshinskii-Moriya (DM) interactions to be present. Based on the crystal structure the allowed DM vectors can be determined using the Moriya rules [Mor60]. As discussed in Section 4.1 four different bonds exist, with Oxygen ions shifted away from the bond breaking the inversion symmetry (first rule). In the case of the bonds connecting kagome and kagome sites a mirror plane of the structural symmetry is located on the middle of the bond perpendicular to this bond, the DM vectors ($\mathbf{D}$ and $\mathbf{D}'''$) are therefore constraint to be perpendicular to the bond (second rule). On the bonds between kagome and triangular site, there a mirror plane exists spanned by the bond and the Oxygen ion, which constraints the DM vector ($\mathbf{D}'$ and $\mathbf{D}''$) on these bond perpendicular to this mirror plane (third rule). The fourth and fifth Moriya rule are not fulfilled as no rotation axis exist neither perpendicular nor parallel to the bond. This results in the allowed DM vectors depicted in Figure 6.1. The DM interaction for two spins $\mathbf{S}_i,\ \mathbf{S}_j$ is

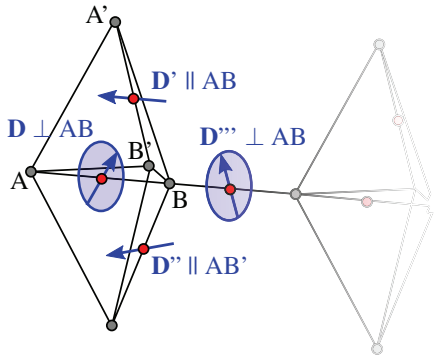

Figure 6.1: Possible Dzyaloshinskii-Moriya interactions determined from the crystal structure using the Moriya rules [Mor60]. From symmetry the DM vectors on the bonds between a kagome and triangular are fixed parallel to the opposite bond of the tetrahedron, while the vectors on kagome-kagome bonds can vary in the plane perpendicular to the bond.

defined as

$$H_{\text{DM}} = \mathbf{D}_{ij} \cdot (\mathbf{S}_i \times \mathbf{S}_j) \tag{6.2}$$

with $\mathbf{D}_{ij}$ as the vectors noted in Fig. 6.1. As the crossproduct is maximal for perpendicular spins the energy can be minimized for the crossproduct antiparallel to the Dzyaloshinskii-Moriya vector. Depending on the orientation of the DM vector in regards to the bond this either leads to a helical (parallel) or cycloidal (perpendicular) spin structure. As determined by the Moriya rules the DM vectors allowed by the structure are perpendicular to the bond and, thus, induces a cycloidal spin structure. However the combination of all possible DM vectors is still vast. In the conducted experiments the long-periodic order is only observed in the $\{h\,k\,0\}$-planes, which indicates that the DM vectors $\mathbf{D}'$ and $\mathbf{D}''$ must compensate each other to suppress a cycloidal structure along c-direction. In addition, the part of the DM vectors $\mathbf{D}$ and $\mathbf{D}'''$ parallel to the c-axis just leads to a canting of the kagome spins parallel to the ab-plane. As a simplification, we just consider DM vectors $\mathbf{D}$ and $\mathbf{D}'''$ parallel to ab-plane. Introducing such DM vectors on

the nearest neighbour bonds (as allowed in Fig. 6.1) favours a canting of the spins out of the ab-plane. Already a weak interaction can have a significant impact on the ordering due to the high degeneracy. Considering the experimental results the DM interaction has to be weak regarding temperature fluctuations above 80 K leading to the magnetic order closer related to the commensurate ordering. But upon cooling the interaction is strong enough to select a solution of the phase space and followingly initiate a spin reorientation.

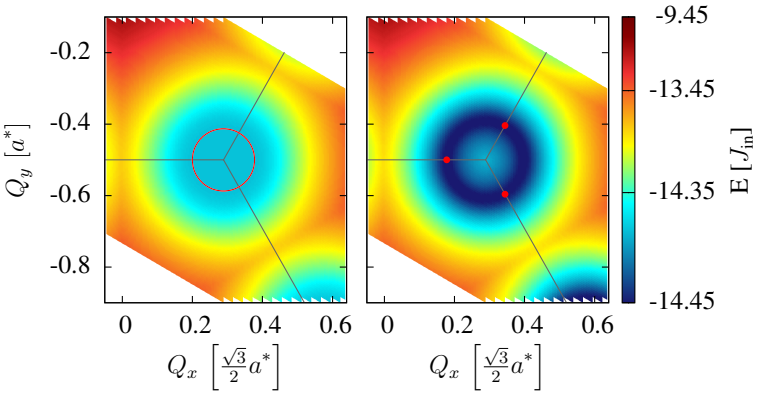

Figure 6.2: Configurational energy close to the magnetic peak $(1/3,\ 1/3,\ 0)$. The BZ boundary is indicated as grey lines. (Left) calculation is based on the Heisenberg nearest neighbour model for a ratio of $J_{out}/J_{in} = 1.45$ and $\mathbf{D}_{ij} = 0$ resulting in a region flat in energy close to the K-point (marked by the red circle). (Right) Dzyaloshinskii-Moriya exchange interaction ($D_{||ab} = 0.02$ and $D'''_{||ab} = 0.01$) is introduced making the commensurate order energetically less favourable. The new minima in energy are marked as red dots. The source code used for the calculation is courtesy of Maxim Mostovoy.

In cooperation with Maxim Mostovoy the energy landscape close to the K-point has been explored using spin structures with different propagation vectors. Here preliminary results are presented, which are courtesy of Maxim Mostovoy. He has developed an algorithm, which determines a spin configuration on a double tetrahedron minimizing the energy for Heisenberg nearest neighbour model including H_{DM} and propagation vector. Subsequently, the whole lattice is created from this double tetrahedra and the configurational energy is calculated using the respective model. This is repeated for many propagation vectors covering the $(h\,k\,0)$-scattering plane of the reciprocal space in the vicinity of the magnetic peak $(1/3,\ 1/3,\ 0)$, where the satellite peaks have been observed experimentally. For the Heisenberg nearest neighbour model without DM terms the energy close to the K-point is flat or rather varies by less than $10^{-6}J_{in}$ from the absolute minimum in energy $E = -14.41J_{in}$. This corresponds to the observation of the diffuse scattering enhanced close to the K-point in MCS even at very low temperatures (cf. Fig. 4.4). The size of the flat area decreases with increasing ratio J_{out}/J_{in} and vanishes for $J_{out}/J_{in} \geq 1.5$, similarly to the diffuse scattering. But introducing a DM exchange interaction ($D_{||ab} = 0.02$ and $D'''_{||ab} = 0.01$) to the Heisenberg model creates a local maximum in the configurational energy at the K-point, the commensurate spin structure with the propagation vector $(1/3,\ 1/3,\ 0)$ becomes unfavourable. At the same time a ring flat in energy develops just outside the previously flat area with an even lowered energy. The radius of the ring increases with decreasing ratio. The absolute minima in energy are situated in the ring along the BZ boundary, which vary by less than $10^{-6}J_{in}$ from the absolute minimum in energy $E \approx -14.45J_{in}$. While the

shift is larger than the one observed for the satellites in measurements, the direction of the shift corresponds exactly to the observed splitting. As a specific spin structure is selected due to the DM exchange interactions, the overall diffuse scattering is expected to decrease compared to previous results from Monte Carlo simulations (cf. Fig. 4.4). The investigation will be pursued further in order to determine the combination of exchange interactions J_{in}, J_{out} and DM vectors, where the resulting model yields energy minima in **Q**-space at the observed satellite positions. From the results up to now, it can be concluded that the introduction of DM interaction has proven to result in a mechanism, which can change the spin structure from a commensurate to a long-periodic order for sufficiently low temperature fluctuations and most likely a ratio of $J_{\text{out}}/J_{\text{in}}$ slightly smaller than 1.5 with appropriate DM terms is suitable to model the magnetic order in $CaBaCo_2Fe_2O_7$. The addition of the DM terms also suppresses the transition to the nematic phase, which explains why the nematic phase (cf. Fig. 4.2a) is not expected to be observed in magnetometry (cf. Fig. 5.4) and the integrated intensities at DNS (cf. Fig. 5.3).
Since the long-periodic order is closely connected with the DM interaction, small changes in the DM terms can have a significant impact. The DM terms again are related to the position of the oxygen ions breaking the inversion symmetry on the bonds between the magnetic ions. There have been several studies on the oxygen stoichiometry in compounds of the Swedenborgite family and it was shown that deviations in the stoichiometry influence the magnetic order [SDP+11, ACZ+13]. Thus, it can be assumed that the difference observed in the magnetic order at 4 K on the small crystal (cf. Fig. 5.22 lower row) and the large crystal with $(h\,k\,0)$-orientation (cf. Fig. 5.25 lower row) stems from a variation in the oxygen stoichiometry, the position of the oxygen ions, or both.

6.3 Cycloidal spin structure and skyrmion lattice

The spin structure for the long-periodic order cannot be determined using Monte Carlo simulation, even if the appropriate Dzyaloshinskii-Moriya exchange interactions are included, because the periodic boundary conditions most likely suppress any transition to this order. Therefore, the results of the various scattering experiments have to be used to determine a spin structure, which exhibits a similar structure factor. The spin structure must fulfil the following observations:

- A splitting of each magnetic peak into three satellite peaks within the respective $(h\,k\,0)$-scattering plane (cf. Figs. 5.8, 5.18 left and 5.22 lower row).
- The satellite peaks exhibit similar scattering intensity for the contribution from moments parallel to the c-axis as well as the contribution from moments parallel to the ab-plane (cf. Figs. B.5).
- An anti-symmetrical chiral scattering transverse with regards to the **Q**-vector of the commensurate magnetic Bragg peak position.
- Each scattering contribution has to obey the symmetry relations of the trigonal magnetic space groups.

A long-periodic order, which also exhibits chiral magnetic scattering, relates to a spin structure with a handedness. Such a handedness exists in helical (spiral with constant diameter, also known as proper screw) or cycloidal structures. They can be discerned by the difference in chiral scattering I_{chiral} (cf. Eq. 2.31). As the splitting only occurs within the $\{h\,k\,0\}$ planes,

the propagation vector has to be in ab-plane. In the case of the peaks in $(h\,k\,0)$-scattering plane the **Q**-vector has a component only in x and y. In case of a helical structure there is always an effective contribution perpendicular to **Q**, which means for each **Q** with non vanishing magnetic scattering the chiral scattering is non zero as well. As satellite peaks, which are along the **Q**-vector to the commensurate peak position, vanish in the chiral scattering a helical spin structure can be excluded. This is different for cycloidal spin structures. If the propagation vector of the cycloid is parallel to the **Q**-vector there is no effective contribution from perpendicular spins perpendicular to **Q**. Thus the chiral scattering as it was observed, is only possible to model using cycloidal spin structures. The same peak vanishes also in the scattering from moments parallel to ab-plane (cf. Fig. B.5 middle), which leads to the same conclusion. In cycloidal structures the rotation vector is perpendicular to the propagation vector. It has been discussed already that the observed splitting can only arise for a propagation vector $(0.342,\, 0.342,\, 0)$ in the notation of the crystallographic unit cell. This translates to the real space in the sense that the same spin in neighbouring columns is rotated by less than 120°. The starting configuration in itself has to fulfil the space group symmetries, otherwise the created structure cannot satisfy it either. Therefore a collinear spin configuration along the c-axis is used as the starting configuration, $\mathbf{S}_i^0 \in \{\mathbf{S}_{\text{tri}} = \mathbf{e}_z\,,\ \mathbf{S}_{\text{kag}} = -\mathbf{e}_z\}$. Since the scattering contributions from moments in the ab-plane and parallel to c-axis are similar in intensity the rotation vector for the cycloids can be chosen to be in ab-plane as well. From the rotation, both scattering contributions will arise. In order to obtain the 120° rotation symmetry around the c-axis, three planar waves j are created with appropriate propagation vectors in the ab-plane $\mathbf{p}_j = p \cdot \hat{\mathbf{p}}_j$ at 120° to one another and rotation vectors $\mathbf{R}_j$, where $\mathbf{p}_j * \mathbf{R}_j = 0$ and p being the period of the planar waves. In order to keep the antiferromagnetic order, the three different columns have a different phase $\phi_i \in \{0°, 120°, 240°\}$. The spins $\mathbf{S}_{i,j}$ for each of the planar waves j are determined by

$$\mathbf{S}_{i,j} = \underline{\mathbf{M}}_{\mathbf{R}_j,\phi_i-\alpha} \cdot \mathbf{S}_i^0, \quad \text{with } \alpha = \frac{\mathbf{r}_i \cdot \mathbf{R}_j}{2\pi \cdot p}, \tag{6.3}$$

where $\underline{\mathbf{M}}_{\mathbf{R},\alpha}$ is the rotation matrix for a rotation axis $\mathbf{R}_j$ and an angle α and $\mathbf{r}_i$ is the position of the spin $\mathbf{S}_i$. Adding up the planar waves results in a spin structures like the ones displayed in Figures 6.4a and B.10. The actual source code is provided in Appendix Chapter E.
This method is not the only one to create such a spin structure. A similar one has also been tested, which uses a collinear spin configuration along the y-axis as the starting configuration. However, since the y-axis is special, this has to be compensated using two additional starting configurations rotated by 120° for three planar waves each. Furthermore, the rotation vectors for the planar waves can be rotated out of plane, which results in a different ratio between the scattering contributions from moments in-plane and those out-of-plane. This can be used to optimize the agreement between the model and the measured data.
The period length can be calculated for the measured splitting of $\delta \approx 0.017\,\text{Å}^{-1}$ and a lattice parameter $a = 6.36\,\text{Å}$ with

$$p = \left\lfloor \frac{2\pi}{\delta} \cdot \frac{1}{\sqrt{3}a} \right\rfloor = 33\ [\text{mag. u.c.}]. \tag{6.4}$$

The resulting spin structure is displayed for a decreased period of 6 magnetic unit cells in Fig. 6.4a and for the correct period of 33 magnetic unit cells (mag. u.c.) in Fig. B.10. The starting configuration is repeated according to the period with a three-fold symmetry. In between considering only the spins with the same offset in their phase, these rotate continuously. At specific symmetry positions of the periodic spin structure the ground state of the antiferromagnetic

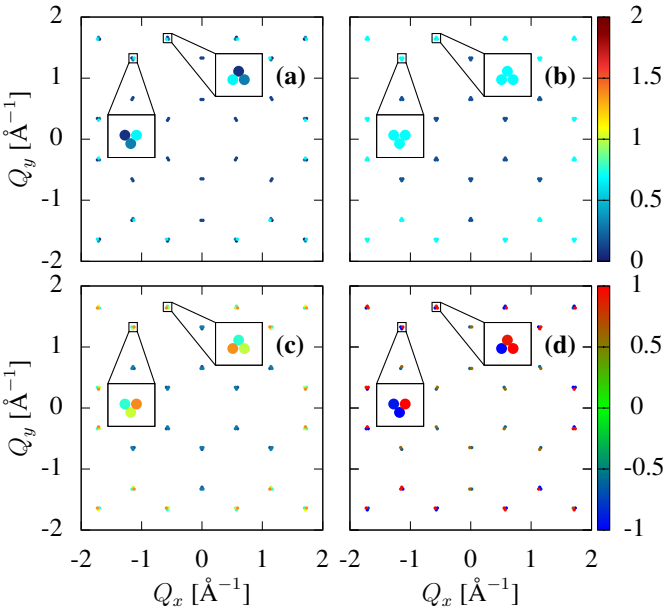

Figure 6.3: Structure factor calculated from the long-periodic spin structure. Background has been removed. **(a)** Scattering from moments in the ab-plane. **(b)** Scattering from moments parallel to the c-axis. **(c)** Total magnetic scattering. Insets display intensity distribution over satellite peaks similar to data measured at 4 K (cf. Fig. 5.18a). **(d)** Chiral magnetic scattering, shows the same antisymmetry as data from Morpheus (cf. Fig. 5.20 lower row) and MIRA (cf. Fig. B.3).

order can be recognized. By design the conditions to the scattering are fulfilled successfully, moreover the intensity variation from one triplet to another is similar to the observed scattering. The intensity for the satellites close to the magnetic peak $(1/3\ 1/3\ 0)$ or its equivalent peaks is the lowest. The satellites' intensity close to around $(2/3\ 2/3\ 0)$ is slightly higher and the satellites close to $(4/3\ 1/3\ 0)$ exhibit the highest intensity. The intensity for the satellites of magnetic peak $(5/3\ 2/3\ 0)$ is slightly lower compared to $(4/3\ 1/3\ 0)$. This corresponds to measurements on Biodiff (cf. Fig. 5.18 left) and results from using the antiferromagnetic ground state as a reference, which featured the same intensity variation. It is even more intriguing, that the variation in intensity over the satellite peaks for each triplet observed on Biodiff (cf. insets of Fig. 5.18 left) are reproduced, which probably results from the symmetry imposed on the created spin structure.

Yet, deviations between the model and measurement are present as well. In both scattering contributions from moments in ab-plane and parallel to the c-axis a variation in intensity over the three satellites is visible in the experimental data (cf. Figs. B.4 and B.5), at least where allowed by symmetry. The model spin structure exhibits such a variation for the contribution from moments in the ab-plane but it is missing in the contribution from moments parallel to the c-axis. Furthermore the scattering intensity of the latter contribution is smaller than the one from moments in the ab-plane for all triplets. In the measurements at MIRA the intensity of both contributions is similar below 20 K though the respective intensity for each satellite is

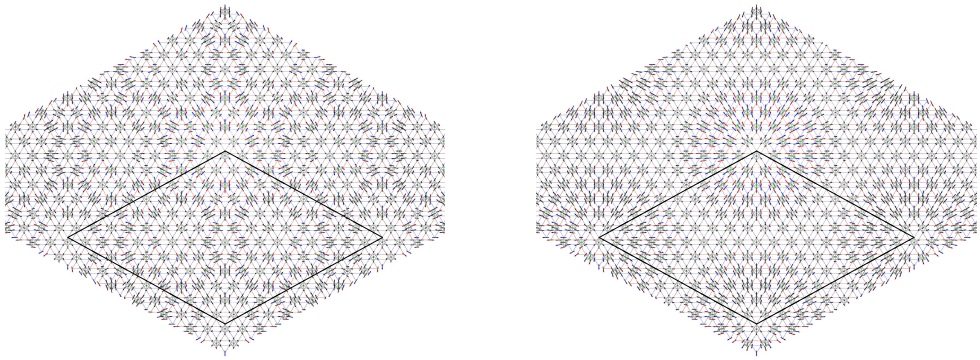

(a) **(b)**

Figure 6.4: Long-periodic spin structure created with cycloids propagating in ab-plane viewed along the c-axis. The rotation angle has been increased or rather the length of the period length has been decreased to 6 magnetic unit cells in order to highlight the symmetry of the arising spin structure. Compare Figure B.10 for the spin structure with the correct period length of 33 magnetic unit cells. The unit cell of the long-periodic order is marked with black lines.
(a) Spin structure is related by its creation principle to the scattering in Fig. 6.3. **(b)** During the creation the antiferromagnetic modulation was removed for comparison. The spin structure shows a clear translation symmetry and link to the hedgehog type skyrmion.

different. This can be corrected by tilting the rotation vectors $\mathbf{R}_j$ of the planar waves against the ab-plane.
The starting configuration is repeated on a triangular lattice throughout the spin structure. A similar pattern is observed in the skyrmion lattices of MnSi [MBJ+09] and Cu_2OSeO_3 [SKI+12], where the skyrmion is repeated on a triangular lattice. In [BF13] the skyrmion phase was successfully modelled with a spin structure created in a similar way like here superimposing three helical waves. However in contrast to these lattices here the spin structure is created from cycloids. From these analogues, we assume this spin structure to be a skyrmion lattice as well, which is called a hedgehog in the case of cycloids. Neglecting the antiferromagnetic modulation (cf. Fig 6.4b), the triangular lattice becomes even more obvious. Furthermore, the resulting structure resembles the planar projection of said hedgehog illustrating the connection to this skyrmion type. The winding number (cf. e.g. [Bra12]) generally defined as

$$w = \frac{1}{4\pi} \iint \mathrm{d}x\, \mathrm{d}y\ \mathbf{m} * (\partial_x \mathbf{m} \times \partial_y \mathbf{m}) \tag{6.5}$$

denotes if a spin structure is topological protected. In the case of a skyrmion lattice the winding number counts the number of skyrmions in the lattice. Here we are dealing with stacked discrete and limited lattices. Therefore an approximation valid for large lattices is better suited to calculate the winding number for each sublattice l of the spin structure separately via the solid angle [VS83, Buh15] using:

$$w_l = \frac{1}{A} \sum_{ijk} \hat{\mathbf{S}}_{l,i} * (\hat{\mathbf{S}}_{l,j} \times \hat{\mathbf{S}}_{l,k}). \tag{6.6}$$

Here ijk denotes a triangle of three neighboured spins i, j, k sorted anticlockwise belonging to the same sublattice l. The result is normed depending on the coverage with triangles, triangular

layer $A = 8\pi$ and kagome layer $A = 2\pi$. The spin structure was created in the way that along both directions a and b it holds two periods of the order, which results in four unit cells of the long-periodic order independent from the period length. Thus a winding number of ± 4 is expected for the whole lattice with one skyrmion per unit cell [MBJ+09, ACW+12]. The winding number was calculated for several spin structures different in their period length denoted in commensurate magnetic unit cells, both with and without the antiferromagnetic modulation (cf. Fig. 6.5). The winding number varies with the period, since the size of the triangles has

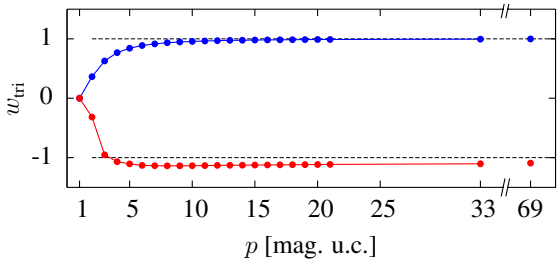

Figure 6.5: Winding number per unit cell of the long-periodic order calculated for a triangular layer of the spin structure, which was created with (red) and without (blue) the antiferromagnetic modulation using a period length of p commensurate magnetic unit cells (mag. u.c.).

to be small compared to the size of the skyrmion for Equation 6.6. However, as required the winding number per long-periodic unit cell is independent from the number of this unit cell per spin structure. For the triangular layer the winding number per unit cell of the long-periodic order converges to $w_{\mathrm{tri,\,ferro}} = 1$ without the antiferromagnetic modulation. For the long-periodic order including the antiferromagnetic modulation the winding number does not converge to -1 within the performed computational effort. Yet, the winding number is expected to converge to $w_{\mathrm{tri,\,af}} \approx -1$ for sufficiently large periods. The additional modulation requires an even larger skyrmion for the winding number to converge. Nevertheless, as expected each unit cell of the long-periodic order holds a single topological charge.
Furthermore the length of the spins has been checked (cf. Fig. 6.6), whether they vary down

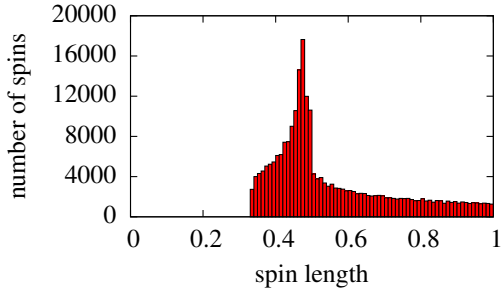

Figure 6.6: Spin length distribution of the calculated spin structure with the periodicity $p = 33$ [mag. u.c.]. Apparently the spins can vary within a certain range, but all spins have a non zero length required for a valid spin structure.

to a spin length of zero, which would indicate the calculated spin structure to be invalid. Here all spins have a non-zero length. It might be possible to reduce the variation of the spin length

without changing the scattering pattern. By design the spin structure does not properly fulfil the sum rule (cf. Eq. 4.4). For a ratio of $\tau = 1.45$ the sum rule offers some freedom for the spins on double tetrahedra or rather requires those spins to cant. Through the canting not only the 120° between the columns can be complied and the spin length can be increased while maintaining the effective spin length.
In the ferromagnetic compounds, where the skyrmion lattice was observed, the phase was stabilized using an external magnetic field. However in an antiferromagnetically coupled material this is not that obvious. In the refinement of the magnetic structure the solution within the $P31m'$ allows for a net magnetisation along the c-direction (cf. Subsection 5.3.2), so this mechanism is not excluded just from to the coupling. Yet, in the experiments at POWGEN and BioDiff a splitting was observed, although no external magnetic field was applied at all. Whether a different stabilizing mechanism plays an important role or no external stabilization is necessary, this is under ongoing research.

6.4 Spin dynamics under strong frustration

The magnetic order revealed a quite complex nature, which of course also influences the spin dynamics. Yet, the neutron scattering instruments used for investigation do not offer sufficient resolution as they are not designed that way. On the other hand combining the inelastic neutron scattering with a polarization option could allow for separating some contributions but also reduces the low statistics in the inelastic scattering even further, which is why only unpolarised neutrons are used here. In [Rei11] the excitations of $CaBaCo_2Fe_2O_7$ have been measured at low energies using the triple-axis spectrometer PANDA and at high energies the time-of-flight spectrometer ARCS. Here, the multi incident energy time-of-flight spectrometer 4Seasons was used to investigate the excitations with an adapted resolution (cf. Subsection 5.6.2). For a theoretical comparison dispersions have been calculated using linear spin wave theory for ratios $J_{\text{out}}/J_{\text{in}} \geq 1.5$ in [Rei11]. Additionally within this study, the dynamic structure factor has been determined also for ratios $J_{\text{out}}/J_{\text{in}} < 1.5$ using spin dynamics simulations, which can be used to study the magnetic order as well as the magnetic excitations (cf. Section 4.3).

The results from linear spin wave theory and the spin dynamics simulations at $T = 0.01 J_{\text{in}}$ do correspond perfectly for $J_{\text{out}}/J_{\text{in}} = 1.5$, but in the latter case the spectral weight as well as the dispersions width could be determined in addition. In both cases the dispersions along the $\langle 0\,0\,1 \rangle$-directions stick out most as they are linear at the Γ-point and stretch over a large range in energy, while the dispersions along the other directions are comparably flat. Furthermore these dispersions are gapped at non zero energy split in an acoustic and optical excitation band. The direction $[0\,0\,1]$ corresponds to the c-direction in real space, thus the spins along the double tetrahedra column are relevant. Based on a single double tetrahedra column the dispersions have been calculated using LSWT, which are similar to the ones observed for the whole structure (cf. Fig. 6.7). Therefore we limit the discussion of the dispersions to the spin waves along the double tetrahedra column.
Then the energy dependency can be described by assuming two kinds of spin chains. In the case of the lower band the interactions between single spins along the directions are considered, which results in an antiferromagnetic coupled linear spin chain along the c-axis. The dispersion of such a spin chain is in accordance with the lower band. However if one regards the effective spin of each layer this results in a linear ferrimagnetic spin chain, whose upper band

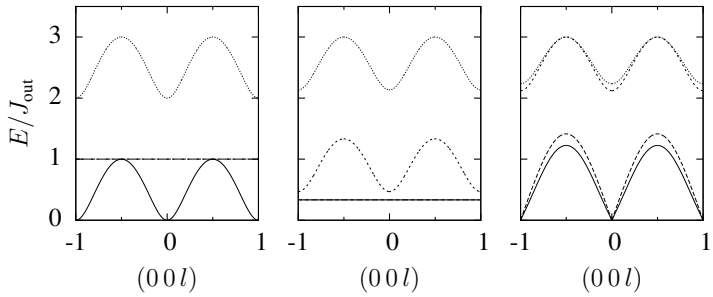

Figure 6.7: Dispersions along $[0\,0\,1]$-direction calculated with LSWT for a single double tetrahedra column along c-direction. Note, that here the energy scale is divided by J_{out}. Based on the Heisenberg nearest neighbour model two situations are compared: decoupled kagome spins for exchange interactions $J_{\text{out}} = 1.5$ and $J_{\text{in}} = 0.0$ (left) and coupled kagome spins for $J_{\text{out}} = 1.5$ and $J_{\text{in}} = 1.0$ (middle). The dispersions along $[0\,0\,1]$-direction for the whole structure with $J_{\text{out}} = 1.5$ and $J_{\text{in}} = 1.0$ are displayed for comparison (right), here the magnetic unit cell was reduced to two layers, one kagome and one triangular.

corresponds to the upper band of the calculated dispersions. In the spin dynamics simulations the dependence on the ratio $J_{\text{in}}/J_{\text{out}}$ is investigated, which is different for the lower and upper excitation band. The upper one increases faster in energy with the ratio, because additionally to the usual ratio dependence of the upper band of a ferrimagnetic spin chain, the effective moment of the kagome spins increases with ratio according to the sum rule (cf. Eq. 4.5). Combining these results the dynamics along the c-direction can be described by a pseudo-ferrimagnetic spin chain. In Subsection 4.3.2 the ratio dependence of the upper and lower excitation band was discussed qualitatively. Here, a more quantitative approach is taken determining the limits of the excitation bands depending on the ratio.

		$\tau = J_{\text{out}}/J_{\text{in}}$						
		1.0	1.1	1.2	1.3	1.4	1.5	mean
lower	upper	1.46(8)	1.62(5)	1.76(2)	1.89(2)	2.01(2)	2.13(2)	-
band	upper/τ	1.46(8)	1.48(4)	1.47(2)	1.45(1)	1.44(1)	1.42(1)	1.44(1)
	upper	2.00(7)	2.41(2)	2.88(2)	3.38(3)	3.93(3)	4.39(2)	-
upper	upper/τ^2	2.00(7)	2.00(2)	2.00(1)	2.01(1)	1.98(1)	1.95(1)	1.99(1)
band	width	0.55(8)	0.74(7)	0.92(4)	1.07(4)	1.21(4)	1.32(3)	-
	width/τ^2	0.55(8)	0.61(6)	0.64(3)	0.63(2)	0.62(2)	0.59(1)	0.61(1)

Table 6.1: Limits of the excitation bands in energy noted in units of J_{in}. In the lower band a linear dependence on τ is present and in the upper band a quadratic one.

Taking constant **Q**-scans from the excitations along $[0\,0\,1]$-direction at $T/J_{\text{in}} = 0.01$ (cf. Fig. 4.5 bottom row) the limits of the observed dispersions have been extracted using Gaussian fits (cf. Table 6.1). From these results it follows for the ratio $\tau = J_{\text{out}}/J_{\text{in}}$ that the upper limit of the upper band and its width both scale with τ^2, but the upper limit of the lower band scales with τ confirming the qualitative discussion. Using error weighted means the excitations can

be approximated for the ratios $1.0 \leq \tau \leq 1.5$ with the following dispersions:

$$\frac{\hbar\omega(k)}{J_{\text{in}}} = \begin{cases} 1.44\tau \cdot \sin\left(\frac{\pi l}{2}\right) & \text{lower band} \\ 1.99\tau^2(1 - \frac{0.61}{4} \cdot (1 + \cos(\pi l))) & \text{upper band,} \end{cases} \tag{6.7}$$

with l being the reciprocal lattice unit along c^*. The goodness of this approximation decreases for the ratios $\tau \leq 1.0$ and the sum rule holds only for ratios up to $\tau = 1.5$. Similar to the ferrimagnetic chain two separated excitation bands exist and the limit of the lower one scales with the exchange interaction. For the discussed reasons the upper limit of the upper band scales with the square of τ instead linearly with τ. However, in contrast both excitation bands of the ferrimagnetic dispersions have the same width, and they are proportional to the smaller spin length (cf. Fig. 2.7), which is not the case here. It is quite intriguing that the width of the upper band scales with the square of τ and it is smaller than the lower band's width. Thus the spins responsible for the lower and upper band are are different one. While the spin for the lower band has constant length, the length of the spin for the upper band scales with τ.

In order to understand the origin of these excitations the dispersions have been calculated for a single double tetrahedra column using LSWT considering two different cases (cf. Fig. 6.7). Of course these calculations are only valid within the restrictions of LSWT as discussed before. Calculating the dispersions for a single double tetrahedra allows us to distinguish between the influence of the columns and the interaction between those. In the first case (cf. Fig. 6.7 left) $J_{\text{out}} = 1.5$ and $J_{\text{in}} = 0$ were chosen in order to study the influence of the in-plane exchange interaction on the dispersions, propagating out of plane. Yet, in the second case the exchange interactions have been set to $J_{\text{out}} = 1.5$ and $J_{\text{in}} = 1.0$, according to the previous studies. Both cases consist of four different spins, which results in four dispersions each, and here the non-dispersive modes are actually degenerate. Apart from these modes the dispersions for the first case are exactly those of a linear ferrimagnetic spin chain, with a small spin $S_B = 1$ and a large spin $S_A = 3$ (cf. Fig. 2.7 right). Increasing J_{in} continuously results in dispersions with the dispersive modes rising in energy and at the same time the flat modes being lowered in energy until $J_{\text{in}} = 1.0$ (cf. Fig. 6.7 middle). This leads to an excitation gap in energy, which has to be overcome for any spin wave to occur. Additionally, the lower limit of both bands appears to shift slightly to higher energies and simultaneously decreasing both bands' width. Those calculated with LSWT for the whole structure are additionally split, but aside from that the limits nicely coincide. Therefore we can deduce the following indications. The upper limit of the upper band definitely scales with the effective kagome spin independent from J_{in}. The width of the upper band is slightly influenced by the ratio, which is beyond the assumption of a linear chain. Finally comparing the dispersion for the full structure with the latter case shows, that the coupling of the double tetrahedra columns leads to the linear dispersions close to Γ-point.

In the experimental data the excitations along the $\langle 0\,0\,1 \rangle$ are also the most distinct and span continuously from the elastic line to 66 meV. In the case of the model, the gap between the bands vanishes for ratios $J_{\text{out}}/J_{\text{in}} \leq 1.1$. Taking into account the width of the dispersions a ratio slightly above 1.1 is still possible. However in the elastic structure factor simulated for this ratio the diffuse scattering is of higher intensity compared to the experimental data. In the model all spins are set to unity length, which is in strong difference to the actual material $CaBaCo_2Fe_2O_7$. From the oxidation states Co^{2+} and Fe^{3+}, spins of lengths $S_{\text{Co}} = 3/2$ and $S_{\text{Fe}} = 5/2$ exist. In principle the model is not restricted to unity spin lengths. Because if all kagome spins and and triangular spins have the same length respectively, their length can be

absorbed into the exchange interaction ($J'_{\text{in}} = S^2_{\text{kag}} \cdot J_{\text{in}}$ and $J'_{\text{out}} = S_{\text{kag}} S_{\text{tri}} \cdot J_{\text{out}}$). However here the ions are statistically distributed over the magnetic sites favouring Fe on the triangular and Co on the kagome sites. Considering this distribution this results in an average spin of length of $S_{\text{kag}} \approx 1.89$ on the kagome sites and $S_{\text{tri}} \approx 2.35$ on the triangular sites, which reduces the effective spin of the kagome triangle (cf. Eq. 4.5). Though in order to explain the observed gapless excitations within the model the effective spin has to be even smaller, which means that there is still considerable disorder present on the kagome sites. This corresponds very nicely with results from Monte Carlo simulation and spin structure refinement. Still within the model of a pseudo-ferrimagnetic chain relations can be extracted based on the comparison between the dispersions and the measured excitation spectrum along the $\langle 0\,0\,1 \rangle$-directions (cf. Fig. 5.30).

Using the transition temperature T_N determined experimentally and those in simulations as a fixed-point, than the temperature at which the excitations have been measured (4 K) is similar to $T/J_{\text{in}} = 0.01$ for ratios close to $\tau = 1.5$ [Rei11]. Comparing the results from the model to the experimental results, it can be assumed that the upper limit of the excitations observed in $CaBaCo_2Fe_2O_7$ scales with the effective kagome spin, as the largest spin matters, and the ratio τ. In order to compare to the model of the linear spin chain only the effective component parallel to the quantization axis is considered, thus S_{kag} and S_{tri} are expected to be decreased. This also simplifies the equation of the sum rule (cf. Eq. 4.5) to

$$2\tau S_{\text{tri}} = \sum_i S_{\text{kag},i} = S_{\text{kag, eff}}. \tag{6.8}$$

Here, the limits determined from the dispersions of the antiferro-ferrimagnetic spin chain (cf. Fig. 5.30 middle) are used here, since these are only estimations this also applies to the following calculations. Then the relation can be derived from the previously determined dispersions (cf. Eq. 6.7):

$$\begin{aligned} 66\,\text{meV} &= E = J_{\text{in}} \cdot 2\tau^2 S_{\text{tri}} \\ \xrightarrow{\text{Eq. 6.8}} \quad &= J_{\text{in}} \cdot \tau S_{\text{kag, eff}} \\ &= J_{\text{out}} S_{\text{kag, eff}}. \end{aligned} \tag{6.9}$$

Since the width of the upper band is related to the length of the triangular spin S_{tri} and varies only slightly taking the whole spin structure into account (cf. Fig. 6.7), the observed width can be approximated with

$$\begin{aligned} (66-47)\,\text{meV} &= J_{\text{in}} \cdot 0.61\tau^2 S_{\text{tri}} \\ \xrightarrow{\text{Eq. 6.8}} \quad 19\,\text{meV} &= J_{\text{in}} \cdot 0.3\tau S_{\text{kag, eff}} \\ 63\,\text{meV} &\approx J_{\text{out}} S_{\text{kag, eff}}, \end{aligned}$$

which corresponds relatively well to the previous result. This agreement shows, that the application of the model is apparently suited for the measured excitations. The upper limit of the lower band is defined as

$$\begin{aligned} 43\,\text{meV} &= J_{\text{in}} \cdot 1.44\tau S_{\text{tri}} \\ 30\,\text{meV} &= J_{\text{out}} S_{\text{tri}}. \end{aligned} \tag{6.10}$$

Furthermore, the whole range of the dispersions can be defined via the upper limit of the lower band, the gap of 4 meV and the width of the upper band:

$$\begin{aligned} 66\,\text{meV} &= J_{\text{in}} \cdot 1.44\tau S_{\text{tri}} + 4\,\text{meV} + 0.3 \cdot 66\,\text{meV} \\ 42\,\text{meV} &\approx 1.44 J_{\text{out}} S_{\text{tri}} \\ 29\,\text{meV} &\approx J_{\text{out}} S_{\text{tri}}, \end{aligned}$$

which again nicely corresponds to the previous result. From the Equations 6.9 and 6.10 the ratio between effective kagome spin and the triangular spin can be calculated:

$$\frac{S_{\text{kag, eff}}}{S_{\text{tri}}} \approx \frac{66\,\text{meV}}{30\,\text{meV}} = 2.2, \tag{6.11}$$

which is definitely plausible especially considering $S_{\text{kag}} < S_{\text{tri}}$. With the sum rule (cf. Eq. 6.8) the ratio τ can be calculated from the same Equations:

$$\tau = \frac{1}{2}\frac{S_{\text{kag, eff}}}{S_{\text{tri}}} \approx 1.1, \tag{6.12}$$

which is exactly, what was expected from the comparison to the spin dynamics simulation results (cf. Fig. 4.5). However, for the calculation of the ratio also the highest possible ratio has to be considered:

$$\tau_{\text{max}} = \frac{3S_{\text{kag}}}{2S_{\text{tri}}} \approx 1.21. \tag{6.13}$$

Therefore, the corrected ratio is actually

$$\tau_{\text{cor}} = \frac{\tau}{\tau_{\text{max}}} \cdot 1.5 \approx 1.37. \tag{6.14}$$

This means, that the observed excitations along the $[0\,0\,1]$-direction can be described with a model considering spins of non unity length, which closes the gap visible in the spin dynamics simulations. However, regarding the resulting order and the dispersions' full width half maximum, the ratio is related more closely to the ratio $\tau_{\text{cor}} \approx 1.37$. Furthermore, the result for the out-of plane exchange interaction in combination with the spin lengths $J_{\text{out}} S_{\text{tri}}$ (cf. Eq. 6.10) is in agreement with previous results ($J'_{\text{out}} \approx 41$ meV for $\tau = 1.5$ calculated in [Rei11]). Following the same calculation for the determined ratio of $\tau_{\text{cor}} \approx 1.37$, the exchange interaction is $J'_{\text{out}} \approx 44$ meV, which allows to estimate the spin length on the kagome sites:

$$\begin{aligned} & 44\,\text{meV} \approx J'_{\text{out}} = J_{\text{out}} S_{\text{tri}} S_{\text{kag}} = 30\,\text{meV} \cdot S_{\text{kag}} \\ \Rightarrow \quad & S_{\text{kag}} \approx 1.46. \end{aligned} \tag{6.15}$$

Since the component along the quantization axis is considered, the length of the moments on triangular sites and the interaction can be calculated with Equations 6.8 and 6.11:

$$S_{\text{tri}} \approx \frac{3S_{\text{kag}}}{2.2} \approx 2.00 \Rightarrow J_{\text{out}} \approx 15\,\text{meV} \ \wedge \ J_{\text{in}} \approx 11\,\text{meV}. \tag{6.16}$$

As expected both spin lengths along the quantization axis are decreased with the one for the kagome sites even further and the value for the exchange interaction J_{out} matches with the transition temperature $T_N \approx 160\,\text{K}$. Despite the strong simplification of the excitations, the derived conclusion are self-contained and consistent with observations from other experiments,

which confirms the simple Heisenberg nearest neighbour model to be valid also for the spin wave excitations in $CaBaCo_2Fe_2O_7$ and probably other Swedenborgites as well.

Within this discussion additional small anisotropies can be disregarded, since they have only a influence at low energy. Here, the anisotropy gap observed below 2 meV at 4 K on 4Seasons (cf. Fig. 5.33), which is only a very slight shift δE compared to J_{in} and J_{out}. Observation from polarization analysis suggest that the spin orientation is not isotropic but a preference is seen for spin components in ab-plane. The magnetic structure refinement suggests a solution in magnetic space groups $P31m'$ or $P31m$ both feature a preferred in-plane anisotropy. In Section 6.3 the DM exchange interactions have been discussed as a mechanism leading to the formation of the long-periodic order. The DM interactions arise by their nature from spin-orbit coupling (and coupling of space and spin space causes anisotropy). Their contribution to a gap depends on the specific model and is quantitatively less obvious related to δE than a simple single site anisotropy term. When the exact DM terms have been determined from the study of the magnetic order, they can be added to the Heisenberg nearest neighbour model, which can be used for a more detailed spin wave modelling.

7

Summary and Outlook

In the present thesis we have presented the conducted research on the magnetic order and spin dynamics in the extended kagome structure, which has been observed in Swedenborgite compounds. One family member, the compound $CaBaCo_2Fe_2O_7$, was investigated in further detail using primarily neutron scattering and spin dynamics calculations. The findings from both approaches have been compared for a deeper understanding. The observations have been differentiated into main topics: commensurate and long-periodic magnetic order, spin structure of the long-periodic order and spin dynamics.

The Heisenberg nearest neighbour model discerning only between the in-plane J_{in} and out-of-plane J_{out} exchange interactions was already shown to model the scattering observed on $YBaCo_4O_7$ successfully in [MCR$^+$09] and further elaborated in [KMMC10]. Studying the magnetic order using numerical methods namely Monte Carlo simulations, the calculated scattering from the model is comparable to the scattering measured using neutron scattering (cf. Fig. 5.2) for a ratio of $\tau = J_{\text{out}}/J_{\text{in}} \approx 1.5$. However, since the periodic boundary conditions are used to stabilize the magnetic order, the simulation is generally limited to the commensurate order. Still in the 3d spin liquid phase (cf. Fig. 4.2a), the influence of the sum rule for the double tetrahedra (cf. Eq. 4.4) is visible in the shape and dependence on the ratio τ of the diffuse scattering, which is enhanced close to the commensurate peaks, elongated along the BZ and becomes broader for lower ratios. With increasing temperature the diffuse scattering increases as well. Therefore the diffuse scattering basically describes the possible variation between the spin structures of different kagome lattices.

In the macroscopic data a Néel transition was found at 160 K. This transition was also observed in neutron powder as well as single crystal data. Separating the scattering contributions for the single crystal data reveals a more complex temperature dependence. A spin reorientation is present between 80 K and 4 K from a more coplanar to a more canted structure regarding the ab-plane, also visible in magnetometry (cf. Fig. 5.4). The extracted intensities from the neutron powder diffractograms show two different structures to exist, a commensurate one prominent at 80 K and a long-periodic one, at 4 K. Comparing the temperature dependences of the integrated intensities to the scattering contributions, the commensurate order relates to the coplanar structure and the long-periodic order to the canted structure.

In the neutron scattering experiments conducted on instruments with limited resolution the observed magnetic peaks relate to the average over the commensurate and long-periodic peaks. Based on the crystal structure and the commensurate antiferromagnetic order with a $\sqrt{3} \times \sqrt{3}$ larger unit cell, the possible magnetic space groups have been determined. Then the data set

of integrated intensities has been refined within these space groups. The best agreement has been found for descending to the trigonal space groups $P31m'$ and $P31m$, which are also valid for the ground state determined with MCS. In correspondence with the sum rule and MCS the refined ordered-moment on the kagome sites is less then on the triangular sites. Comparing the refinement at 80 and 4 K the refinement's goodness-of-fit and the ordered moment lengths decrease at the lower temperature.
On neutron scattering instruments with sufficient resolution, the commensurate peak can be separated from the satellite peaks. Fitting the satellite peaks in the powder diffractograms reveals the splitting of $\delta \approx 0.017\,\text{Å}^{-1}$ between satellite peak and K-point to be temperature independent and just the fraction of the two structures changes with temperature. On the neutron single crystal diffractometers a difference has been observed between the two measured single crystals of $CaBaCo_2Fe_2O_7$. The overall dependence and the splitting is similar, but only for one of them the commensurate peaks vanish completely. This indicates that the temperature dependence is quite sensitive to material variations. From the single crystal data the periodicity is observed in the ab-plane, while the spin structure remains commensurate along the c-direction. Since only three satellite peaks are present close the K-point of the BZ along its boundary, the structure can be described with the propagation vector $(0.342,\ 0.342,\ 0)$ and its multi-q equivalents. In comparison with the model, the peaks arise within the range of variation allowed by the sum rule. Therefore already small additional Dzyaloshinskii-Moriya terms are suited to select the specific canted structure. Calculating the energy for spin structures with various propagation vectors the DM terms change the energy landscape in a way disfavouring the commensurate order and favouring the long-periodic order.
With the different scattering contributions from the polarization analysis at hand, there have been relatively strong constraints to the underlying spin structure. Considering the chiral magnetic scattering, which is anti-symmetrical with respect to the **Q**-vector, and scattered intensity from moments parallel to the ab-plane and parallel to the c-axis, the spins were calculated as a superposition of three cycloidal waves with the appropriate periodicity and an antiferromagnetic modulation. The calculated scattering from such a spin structure is comparable with the measured scattering, as the splitting, the symmetry of the scattering contributions and even a relative intensity distribution within a satellite triplet are reproduced correctly. Still one cannot exclude the possibility of another spin structure created using a different construction yielding the same scattering pattern. But since all the constraints have to be satisfied this is unlikely. In real space the spin structure can be described as a repetition of the starting configuration, on a triangular lattice and in between the spins rotate continuously, which also results in intermediate structures similar to the commensurate antiferromagnetic one. This is similar to the skyrmion-lattice observed on MnSi. However, whether this spin structure is actually a skyrmion lattice, has not yet been elucidated.
The spin dynamics has been investigated using both simulations and inelastic neutron scattering, revealing a strong dependence on the symmetry direction. The spin waves propagating in the kagome layers are rather flat and broad. This is to be expected, as these spins are coupled less strongly and suffer from the geometric frustration. But along the c-axis or rather the double tetrahedra the spins are ordered more strongly, which leads to more distinct excitations also reaching over a larger range in energy up to 66 meV in the experiment. It was shown, that these can be described using the Heisenberg nearest neighbour model, if non unity spin lengths are assumed. The derived moments lengths projected to the quantization axis and also the exchange interactions agree with the results from other measurements. The spin lengths indicate a spin structure with imperfectly aligned spins, which fits with the calculated ratio $\tau_{\text{cor}} \approx 1.37$. In

MCS a long-range 3d magnetic order is still observed at this ratio. In the data from a high resolution time-of-flight spectrometer a small anisotropy of 2 meV is visible, corresponding to a small anisotropy like the before mentioned DM interaction.

The investigation of the Swedenborgite magnetic structure has unravelled very interesting observations, which are mostly related to its building block the double tetrahedron and the ratio of the exchange interactions J_{in} and J_{out}. As both interactions cannot be fulfilled at the same time, for ratios $J_{\text{out}}/J_{\text{in}} < 1.5$ the resulting freedom and variation due to the geometric frustration leads to rather complex but intriguing mechanisms.
Nonetheless, some interesting questions remain for further investigations. In the present study it was shown, that the introduction of DM interactions reduces the degeneracy and selects a specific spin structure. After determining the exact DM terms suited to establish the observed long-periodic order, these can be added to Heisenberg model for Monte Carlo simulations. With the periodic boundary conditions tuned to the periodicity of the long-periodic structure, it should be possible to model the temperature dependence of the long-periodic structure (cf. Figs. 5.9 and 5.23) and the scattering contributions (cf. Fig. 5.3). In $CaBaCo_2Fe_2O_7$, a skyrmion-like lattice has been found at low temperatures, but the additional complexity due to the antiferromagnetic coupling requires further investigation. In cooperation with Maxim Mostovoy, it is planned to determine whether antiferromagnetically coupled sykrmions can arise and if the observed order is related to such a lattice. Furthermore, in future studies it is of interest to compare the results from spin dynamics simulations to the spin wave excitations measured in other compounds of the Swedenborgite family. Similarly to the presented evaluation in Section 6.4, moment lengths and interactions can be deduced from the comparison.

Acknowledgement

At this point, I would like to sincerely thank all the coworkers of JCNS-2 and PGI-4, which have been ready to help at all times. This work would not have been possible in this way without the help and support from several people. I would like to thank everyone, who contributed to this work:

Werner Schweika for his great support, mentoring and discussions, but especially for allowing me to perform the research self-determined.

Prof. Thomas Brückel for enabling me to take part in current research, regarding both conducting up to date experiments and presenting the results on international conferences.

Prof. Stefan Weßel for agreeing to take the second revision of this work.

Prof. Maxim Mostovoy for his collaboration on introducing the Dzyaloshinskii-Moriya interaction and understanding the skyrmion lattice.

Lars Fritz and Stefan Buhrandt for discussions on the theoretical model, especially the sum rule.

Martin Valldor for the sample preparation and discussions.

Instrument responsibles for on-site user support and subsequent evaluation:
Olivier Gourdon and Shibarati Nandi (Powgen, SNS)
Oksana Zaharko (Morpheus, PSI) also for support on the single crystal refinement
Yixi Su and Kirill Nemkovski (DNS, MLZ)
Tobias Schrader and Andreas Ostermann (Biodiff, MLZ)
Robert Georgii and Georg Brandl (MIRA, MLZ) providing some evaluation subroutines
Mitsutaka Nakamura and Kazuki Iida (4Seasons, MLF)

Artur Glavic for his help regarding all sorts of programming issues and providing the software suite plot.py used for the evaluation of the data measured at DNS.

Yinguo Xiao for the preparation of magnetometry measurements.

Jörg Persson for preparing the small sample for neutron experiments.

Benedikt Klobes, Paul Hering, Abdelfattah Mahmoud for supporting me conduct additional experiments (Resonant ultrasound spectroscopy, X-ray powder diffraction and magnetometry), which did not make it into the thesis.

IT-department at FZ-Jülich for the help reorienting the data set measured at 4Seasons.

Hailey Williamson for reviewing my thesis drafts.

Rebecca Sohn for enduring all the stress and exercising the patience for getting through it.

My family for unwavering support all these years.

Office mates Markus Schmitz and Ronnie Simon, thank you for lightening up the mood.

A

Bibliography

[AB33] G. Aminoff and R. Blix, "On the structure and chemical composition of swedenborgite", *Kunglia Svenska Vetenskaps Akademiens Handlingar* **11**, 4 (1933).

[ABY11] V. N. Antonov, L. V. Bekenov, and A. N. Yaresko, "Electronic Structure of Strongly Correlated Systems", *Advances In Condensed Matter Physics* **2011** (2011).

[ACW+12] T. Adams, A. Chacon, M. Wagner, A. Bauer, G. Brandl, B. Pedersen, H. Berger, P. Lemmens, and C. Pfleiderer, "Long-Wavelength Helimagnetic Order and Skyrmion Lattice Phase in Cu_2OSeO_3", *Physical Review Letters* **108**, 23 (2012).

[ACZ+13] S. Avci, O. Chmaissem, H. Zheng, A. Huq, P. Manuel, and J. F. Mitchell, "Oxygen stoichiometry in the geometrically frustrated kagome system $YBaCo_4O_{7+\delta}$: Impact on phase behavior and magnetism", *Chemistry of Materials* **25**, 21 (2013).

[APMO+11] M. I. Aroyo, J. M. Perez-Mato, D. Orobengoa, E. Tasci, G. de la Flor, and A. Kirov, "Crystallography online: Bilbao Crystallographic Server", *Bulgarian Chemical Communications* **43**, 2 (2011).

[BF13] S. Buhrandt and L. Fritz, "Skyrmion lattice phase in three-dimensional chiral magnets from Monte Carlo simulations", *Physical Review B* **88**, 19 (2013).

[BF14] S. Buhrandt and L. Fritz, "Spin-liquid phase and order by disorder of classical Heisenberg spins on the swedenborgite lattice", *Physical Review B* **90**, 2 (2014).

[Blu63] M. Blume, "Polarization effects In magnetic elastic scattering of slow neutrons", *Physical Review* **130**, 5 (1963).

[Bra12] H.-B. Braun, "Topological effects in nanomagnetism: From superparamagnetism to chiral quantum solitons", *Advances In Physics* **61**, 1 (2012).

[Buh15] S. Buhrandt: *Magnetic monopoles in chiral magnets & frustrated magnetism on the swedenborgite lattice*, Universität zu Köln, Diss., (2015), `http://dspace.library.uu.nl/handle/1874/305850`.

[CHS92] J. T. Chalker, P. C. W. Holdsworth, and E. F. Shender, "Hidden order in a frustrated system: Properties of the Heisenberg kagome antiferromagnet", *Physical Review Letters* **68**, 6 (1992).

[CPH+10] V. Caignaert, V. Pralong, V. Hardy, C. Ritter, and B. Raveau, "Magnetic structure of $CaBaCo_4O_7$: Lifting of geometrical frustration towards ferrimagnetism", *Physical Review B* **81**, 9 (2010).

[CRZM06] L. C. Chapon, P. G. Radaelli, H. Zheng, and J. F. Mitchell, "Competing magnetic interactions in the extended Kagome system $YBaCo_4O_7$", *Physical Review B* **74**, 17 (2006).

[CZ09] A. L. Chernyshev and M. E. Zhitomirsky, "Spin waves in a triangular lattice antiferromagnet: Decays, spectrum renormalization, and singularities", *Physical Review B* **79**, 14 (2009).

[FTS+06] V. Fritsch, J. D. Thompson, J. L. Sarrao, H. A. K. von Nidda, R. M. Eremina, and A. Loidl, "Correlation between magnetic frustration and electrical conductivity in RInCu$_4$ compounds (R=Gd-Tm)", *Physical Review B* **73**, 9 (2006).

[GBJ+07] R. Georgii, P. Boeni, M. Janoschek, C. Schanzer, and S. Valloppilly, "MIRA - A flexible instrument for VCN", *Physica B-condensed Matter* **397**, 1-2 (2007).

[GBP03] R. Georgii, P. Boni, and N. Pleshanov, "Polarised reflectometry with MIRA at the FRM-II", *Physica B-condensed Matter* **335**, 1-4 (2003).

[GGG10] J. S. Gardner, M. J. P. Gingras, and J. E. Greedan, "Magnetic pyrochlore oxides", *Reviews of Modern Physics* **82**, 1 (2010).

[Hah06] T. Hahn, *International Tables for Crystallography (2006). Vol. A, Space-group symmetry*, 1st online ed., Chester: International Union of Crystallography, (2006).

[Hel88] K.-H. Hellwege, *Einführung in die Festkörperphysik*, 3rd ed., Berlin, Heidelberg: Springer, (1988).

[HHGH11] A. Huq, J. P. Hodges, O. Gourdon, and L. Heroux, "Powgen: A third-generation high-resolution high-throughput powder diffraction instrument at the Spallation Neutron Source", *Zeitschrift für Kristallographie Proceedings* **43**, 1 (2011).

[HJ39] O. Halpern and M. H. Johnson, "On the magnetic scattering of neutrons", *Physical Review* **55**, 10 (1939).

[HMZ+06] A. Huq, J. Mitchell, H. Zheng, L. Chapon, P. Radaelli, K. Knight, and P. Stephens, "Structural and magnetic properties of the Kagomé antiferromagnet $YbBaCo_4O_7$", *Journal of Solid State Chemistry* **179**, 4 (2006).

[Hor] *Homepage of the software suite Horace*, `http://horace.isis.rl.ac.uk/Main_Page`, [Online] (Accessed: 21/5/2015).

[Hov54] L. van Hove, "Correlations in space and time and Born approximation scattering In systems of interacting particles", *Physical Review* **95**, 1 (1954).

[KCR+09] D. D. Khalyavin, L. C. Chapon, P. G. Radaelli, H. Zheng, and J. F. Mitchell, "Structural behavior of the kagome antiferromagnet $TmBaCo_4O_7$: Neutron diffraction study and group-theoretical consideration", *Physical Review B* **80**, 14 (2009).

[KMMC10] D. D. Khalyavin, P. Manuel, J. F. Mitchell, and L. C. Chapon, "Spin correlations in the geometrically frustrated $RBaCo_4O_7$ antiferromagnets: Mean-field approach and Monte Carlo simulations", *Physical Review B* **82**, 9 (2010).

[KNI+13] R. Kajimoto, M. Nakamura, Y. Inamura, K. Ikeuchi, S. Ji, K. Nakajima, S. Ohira-Kawamura, W. Kambara, M. Sawabe, A. Kamiya, K. Inoue, T. Futagami, M. Kobayashi, A. Kishi, K. Satou, K. Aizawa, and M. Arai, "Recent Improvement of the Signal-to-Noise Ratio on the Fermi Chopper Spectrometer 4SEASONS", *Journal of the Physical Society of Japan* **82** (2013).

[KNN+09] R. Kajimoto, K. Nakajima, M. Nakamura, K. Soyama, T. Yokoo, K. Oikawa, and M. Arai, "Study of the neutron guide design of the 4SEASONS spectrometer at J-PARC", *Nuclear Instruments & Methods In Physics Research Section A-accelerators Spectrometers Detectors and Associated Equipment* **600**, 1 (2009).

[KOA+11] N. Kanazawa, Y. Onose, T. Arima, D. Okuyama, K. Ohoyama, S. Wakimoto, K. Kakurai, S. Ishiwata, and Y. Tokura, "Large topological Hall effect in a short-period helimagnet MnGe", *Physical Review Letters* **106**, 15 (2011).

[LCF+08] D. Lebeugle, D. Colson, A. Forget, M. Viret, A. M. Bataille, and A. Gukasov, "Electric-field-induced spin flop in $BiFeO_3$ single crystals at room temperature", *Physical Review Letters* **100**, 22 (2008).

[Lit08] D. B. Litvin, "Tables of crystallographic properties of magnetic space groups", *Acta Crystallographica Section A* **64** (2008).

[Lit13] D. B. Litvin, *Magnetic Group Tables - 1-, 2- and 3-Dimensional Magnetic Subperiodic Groups and Magnetic Space Groups*, IUCr, (2013).

[LSM08] K. Lefmann, H. Schober, and F. Mezei, "Simulation of a multiple-wavelength time-of-flight neutron spectrometer for a long-pulsed spallation source", *Measurement Science & Technology* **19**, 3 (2008).

[MA11] K. J. Millman and M. Aivazis, "Python for scientists and engineers", *Computing In Science & Engineering* **13**, 2 (2011).

[Mal02] S. V. Maleev: "General theory of polarised neutrons in magnetic materials", In: T. Brückel and W. Schweika: *Polarized Neutron Scattering*, Forschungszentrum Jülich, (2002) (Matter and Materials).

[MBJ+09] S. Mühlbauer, B. Binz, F. Jonietz, C. Pfleiderer, A. Rosch, A. Neubauer, R. Georgii, and P. Boeni, "Skyrmion Lattice in a Chiral Magnet", *Science* **323**, 5916 (2009).

[MBS63] S. V. Maleev, V. G. Baryakhtar, and R. A. Suris, "The scattering of slow neutrons by complex magnetic structures", *Soviet Physics-solid State* **4**, 12 (1963).

[MCR+09] P. Manuel, L. C. Chapon, P. G. Radaelli, H. Zheng, and J. F. Mitchell, "Magnetic correlations in the extended Kagome $YBaCo_4O_7$ probed by single-crystal neutron scattering", *Physical Review Letters* **103**, 3 (2009).

[MGN+06] K. Matan, D. Grohol, D. G. Nocera, T. Yildirim, A. B. Harris, S. H. Lee, S. E. Nagler, and Y. S. Lee, "Spin waves in the frustrated kagome lattice antiferromagnet $KFe_3(OH)_6(SO_4)_2$", *Physical Review Letters* **96**, 24 (2006).

[Mor60] T. Moriya, "Anisotropic superexchange interaction and weak ferromagnetism", *Physical Review* **120**, 1 (1960).

[MR06] R. Moessner and A. R. Ramirez, "Geometrical frustration", *Physics Today* **59**, 2 (2006).

[MRK69] R. M. Moon, T. Riste, and W. C. Koehler, "Polarization analysis of thermal-neutron scattering", *Physical Review* **181**, 2 (1969).

[NT12] N. Nagaosa and Y. Tokura, "Emergent electromagnetism in solids", *Physica Scripta* **T146** (2012).

[Ope86] W. Opechowski, *Crystallographic and Metacrystallographic Groups*, Northern California, (1986).

[PKW35] L. Pauling, H. P. King, and A. N. Winchell, "The crystal structure of swedenborgite, NaBe4SbO7", *American Mineralogist* **20**, 7 (1935).

[PTVF92] W. Press, S. Teukolsky, W. Vetterling, and B. Flannery, *Numerical recipes in C: The art of scientific computing*, Second Edition, Cambridge University Press, (1992).

[Pyt] Python Software Foundation: *Python Language Reference, version 2.7. Available at*, `http://www.python.org`, [Online] (Accessed: 21/5/2015).

[Qua] Quantum Design, Inc.: *PPMS® DynaCool™*, `https://www.qdusa.com/products/dynacool.html`, [Online] (Accessed: 21/5/2015).

[Ram94] A. P. Ramirez, "Strongly geometrically frustrated magnets", *Annual Review of Materials Science* **24** (1994).

[RC93] J. Rodríguez-Carvajal, "Recent advances In magnetic-structure determination by neutron powder diffraction", *Physica B* **192**, 1-2 (1993).

[RC11] J. Rodríguez-Carvajal: *Short reference guide of the program FullProf*, (2011).

[RCSB08] J. Robert, B. Canals, V. Simonet, and R. Ballou, "Propagation and ghosts in the classical kagome antiferromagnet", *Physical Review Letters* **101**, 11 (2008).

[Rei11] J. Reim: *Spindynamik im Schwedenborgit $CaBaCo_2Fe_2O_7$: Untersuchung mit Neutronenstreuung und Spinwellentheorie*, Rheinisch-Westfälischen Technischen Hochschule Aachen, Diplomarbeit, (2011), `http://www.fz-juelich.de/SharedDocs/Downloads/PGI/PGI-4/DE/DipDoc/Diplomarbeit_Reim_pdf`.

[Rhi14] F. Rhiem: *Visualisierung eines Skalarfelds auf einem dünn besetzten, n-dimensionalen Punktgitter*, Fachhochschule Aachen, Campus Jülich, Diplomarbeit, (2014).

[Rob07] J. Robert: *Systèmes magnétiques frustration géométrique : approches expérimentale et théorique*, l'Université Joseph Fourier – Grenoble 1, Diss., october (2007), `https://tel.archives-ouvertes.fr/tel-00257237`.

[Ros11] E. Rosén: *Magnetische Eigenschaften und Spinkorrelationen in Co- und Fe-basierten Swedenborgiten*, Rheinisch-Westfälischen Technischen Hochschule Aachen, Diplomarbeit, (2011), `http://www.fz-juelich.de/SharedDocs/Downloads/PGI/PGI-4/DE/DipDoc/DiplomarbeitErikRosen_pdf`.

[RPCM11] B. Raveau, V. Pralong, V. Caignaert, and A. Maignan, "Swedenborgite-type cobaltites and ferrites: Tetrahedral frameworks with exceptional magnetic properties", *Zeitschrift für Anorganische und Allgemeine Chemie* **637**, 9 (2011).

[RRS+14] J. D. Reim, E. Rosen, W. Schweika, M. Meven, N. R. Leo, D. Meier, M. Fiebig, M. Schmidt, C.-Y. Kuo, T.-W. Pi, Z. Hu, and M. Valldor, "Structural invariance upon antiferromagnetic ordering in geometrically frustrated swedenborgite, $CaBaCo_2Fe_2O_7$", *Journal of Applied Crystallography* **47** (2014).

[Sac92] S. Sachdev, "Kagome-lattice and triangular-lattice Heisenberg antiferromagnets: Ordering from quantum fluctuations and quantum-disordered ground-states with unconfined bosonic spinons", *Physical Review B* **45**, 21 (1992).

[SC93] O. Schärpf and H. Capellmann, "The XYZ-difference method with polarized neutrons and the separation of coherent, spin incoherent, and magnetic scattering cross-sections in a multidetector", *Physica Status Solidi A-applied Research* **135**, 2 (1993).

[Sch10] W. Schweika, "XYZ-polarisation analysis of diffuse magnetic neutron scattering from single crystals", *Polarized Neutrons and Synchrotron X-rays For Magnetism Conference 2009* **211**, 1 (2010).

[SDP+11] T. Sarkar, V. Duffort, V. Pralong, V. Caignaert, and B. Raveau, "Oxygen hyperstoichiometric hexagonal ferrite $CaBaFe_4O_{7+\delta}$ ($\delta \approx 0.14$): Coexistence of ferrimagnetism and spin glass behavior", *Physical Review B* **83**, 9 (2011).

[SKI+12] S. Seki, J. . H. Kim, D. S. Inosov, R. Georgii, B. Keimer, S. Ishiwata, and Y. Tokura, "Formation and rotation of skyrmion crystal in the chiral-lattice insulator Cu_2OSeO_3", *Physical Review B* **85**, 22 (2012).

[SOL+11] T. E. Schrader, A. Ostermann, B. Laatsch, P. Jüttner, F. Suxdorf, L. Fleischhauer-Fuß, M. Wagener, H. Kleines, M. Monkenbusch, W. Petry, and D. Richter: "First test of detectors at the instrument BIODIFF" / MLZ, 2011. – Technical report.

[Squ78] G. L. Squires, *Introduction to the theory of thermal neutron scattering*, Cambridge University Press, (1978).

[SVL07] W. Schweika, M. Valldor, and P. Lemmens, "Approaching the ground state of the kagome antiferromagnet", *Physical Review Letters* **98**, 6 (2007).

[SYM+06] M. Soda, Y. Yasui, T. Moyoshi, M. Sato, N. Igawa, and K. Kakurai, "Magnetic structure of $YBaCo_4O_7$ with kagome and triangular lattices", *Journal of the Physical Society of Japan* **75**, 5 (2006).

[TFO+12] E. S. Tasci, G. de la Flor, D. Orobengoa, C. Capillas, J. M. Perez-Mato, and M. I. Aroyo, "An introduction to the tools hosted in the Bilbao Crystallographic Server", *Contribution of Symmetries In Condensed Matter* **22** (2012).

[Tou77] G. Toulouse, "Theory of frustration effect in spin-glasses", *Communications On Physics* **2**, 4 (1977).

[TRH+14] M. Taillefumier, J. Robert, C. L. Henley, R. Moessner, and B. Canals, "Semiclassical spin dynamics of the antiferromagnetic Heisenberg model on the kagome lattice", *Physical Review B* **90**, 6 (2014).

[VA02] M. Valldor and M. Andersson, "The structure of the new compound $YBaCo_4O_7$ with a magnetic feature", *Solid State Sciences* **4**, 7 (2002).

[Val04a] M. Valldor, "Disordered magnetism in the homologue series $YBaCo_{4-x}Zn_xO_7$ (x=0, 1, 2, 3)", *Journal of Physics: Condensed Matter* **16**, 50 (2004).

[Val04b] M. Valldor, "Syntheses and structures of compounds with $YBaCo_4O_7$-type structure", *Solid State Sciences* **6**, 3 (2004).

[Val05a] M. Valldor, "Magnetic investigations on six compounds with the general formula (Ca,Y)Ba(Co,Fe,Al,Zn)$_4$O$_7$ and the structures of $YBaCoFeZn_2O_7$ and $YBaCO_2FeZnO_7$", *Solid State Sciences* **7**, 10 (2005).

[Val05b] M. Valldor, "Magnetic properties of compounds in the system $CaBaCo_{4-x-y}Zn_xAl_yO_7$ ($x = 0, 1, 2,\ y = 0, 1$)", *Journal of Physics and Chemistry of Solids* **66**, 6 (2005).

[VS83] A. Vanoosterom and J. Strackee, "The solid angle of a plane triangle", *IEE Transactions On Biomedical Engineering* **30**, 2 (1983).

[VSS09] M. Valldor, Y. Sanders, and W. Schweika, "High spin frustration in Co based Swedenborgites", *Journal of Physics: Conference Series* **145**, 1 (2009).

[Wan50] G. H. Wannier, "Antiferromagnetism. The triangular Ising net", *Physical Review* **79**, 2 (1950).

[WCV11] S. van der Walt, S. C. Colbert, and G. Varoquaux, "The NumPy Array: A Structure for Efficient Numerical Computation", *Computing In Science & Engineering* **13**, 2 (2011).

[Wol14] Wolfram Research, Inc.: "Mathematica", 2014 (Version 10.0). – Technical report.

[YOK+10] X. Z. Yu, Y. Onose, N. Kanazawa, J. H. Park, J. H. Han, Y. Matsui, N. Nagaosa, and Y. Tokura, "Real-space observation of a two-dimensional skyrmion crystal", *Nature* **465**, 7300 (2010).

[Zhi08] M. E. Zhitomirsky, "Octupolar ordering of classical kagome antiferromagnets in two and three dimensions", *Physical Review B* **78**, 9 (2008).

B

Additional Figures

In this chapters additional figures are displayed, which complete the presented data in the respective chapters.

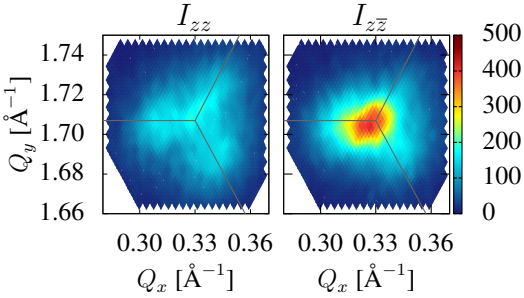

Figure B.1: Additional polarization channels measured at 4 K around the magnetic peak $(4/3\ 1/3\ 0)$ on the large crystal on Morpheus, which reveal the spin structure related to the commensurate scattering to be less canted than the long-periodic spin structure.

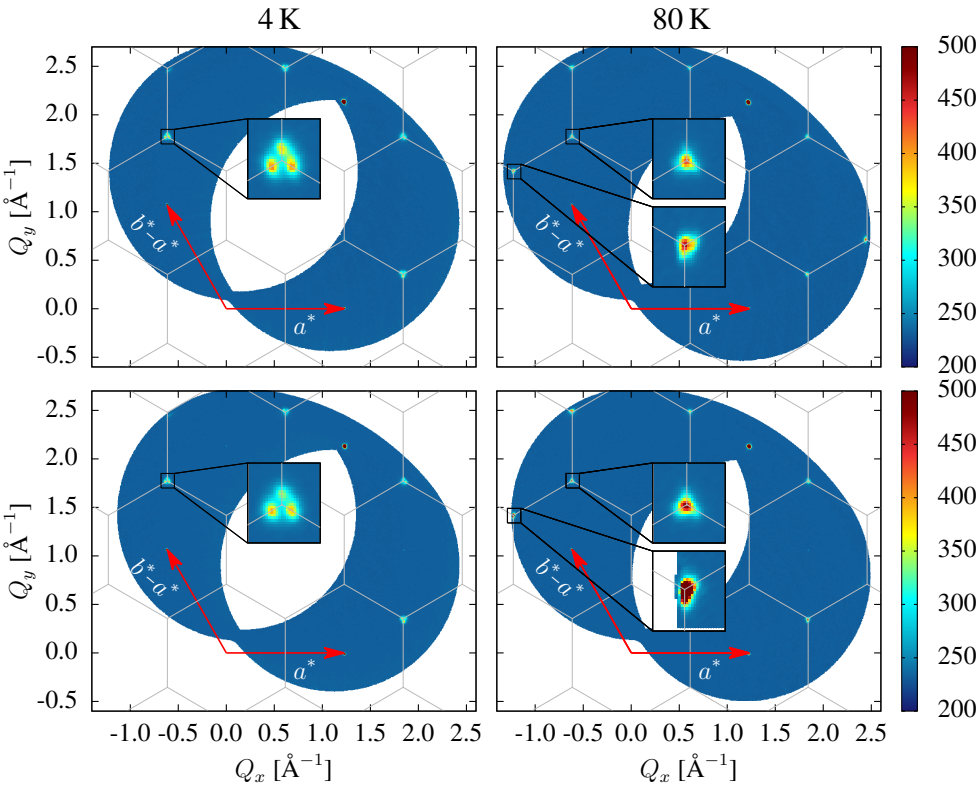

Figure B.2: Extracted cuts of the $(h\,k\,1)$ (upper row) and $(h\,k\,\overline{1})$ (lower row) scattering plane from the measurements at Biodiff at 4 K (left) and 80 K (right). The BZ boundary is marked in grey. The magnetic Bragg peaks $(\overline{5/3}\ 4/3\ 0)$ and $(\overline{4/3}\ 5/3\ 0)$ (symmetrically equivalents to $(4/3\ 1/3\ 0)$) are highlighted in insets. The data of $(h\,k\,1)$ was shifted by $\Delta Q_x = -0.025$Å^{-1} and in the case of $(h\,k\,\overline{1})$ by $\Delta\mathbf{Q} = (0.018,\ 0.005,\ 0)$Å^{-1} compensating the misalignment of the sample. The commensurate peak shape at 80 K and peak splitting at 4 K observed in $(h\,k\,0)$-scattering plane (cf. Fig. 5.18) is present in parallel planes as well. Thus the change in spin structure is restricted to within the ab-plane.

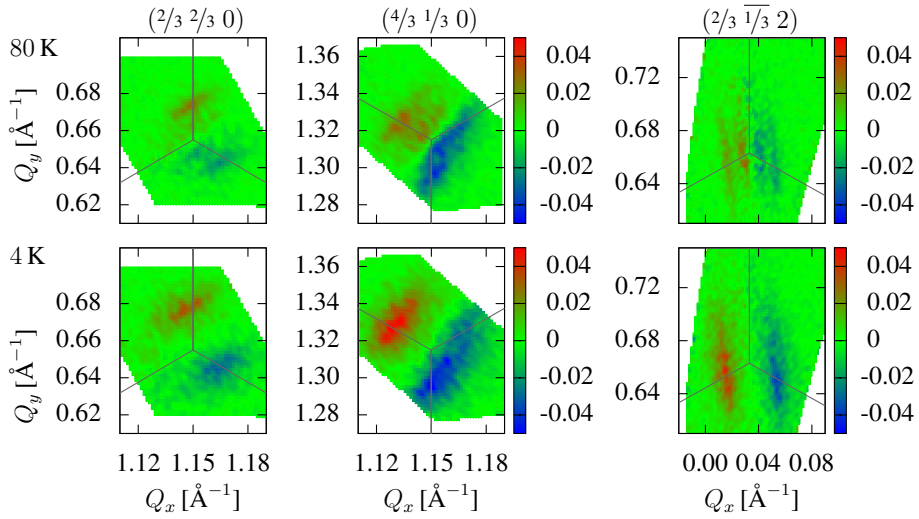

Figure B.3: Magnetic peak structure in the chiral scattering measured at MIRA on the small crystal. At both temperatures and all peaks the chiral scattering is anti-symmetric transverse to **Q**. This scattering contribution is observed even close to the commensurate magnetic peaks positions.

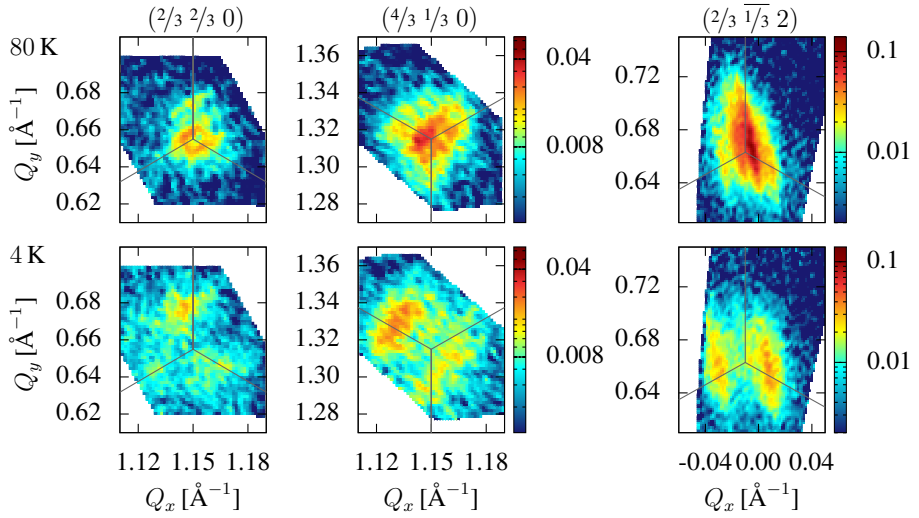

Figure B.4: Magnetic peak structure in the scattering from moments parallel to the ab-plane measured at MIRA on the small crystal. In case of the magnetic peak (2/3 1/3 2) the third satellite peak is obstructed by the cavity, which is necessary to separate this channel.

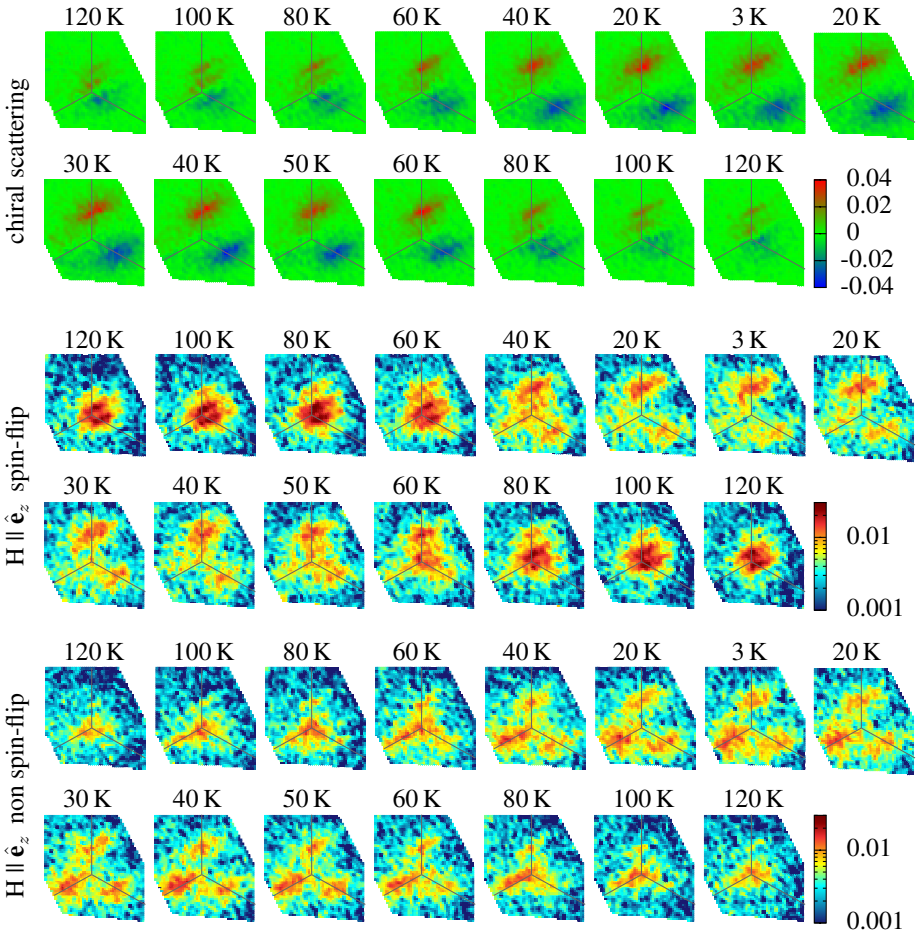

Figure B.5: Temperature dependence in scattering contributions measured around the magnetic peak $(2/3\ 2/3\ 0)$ at MIRA on the small crystal (sorted by the order of each measurement).

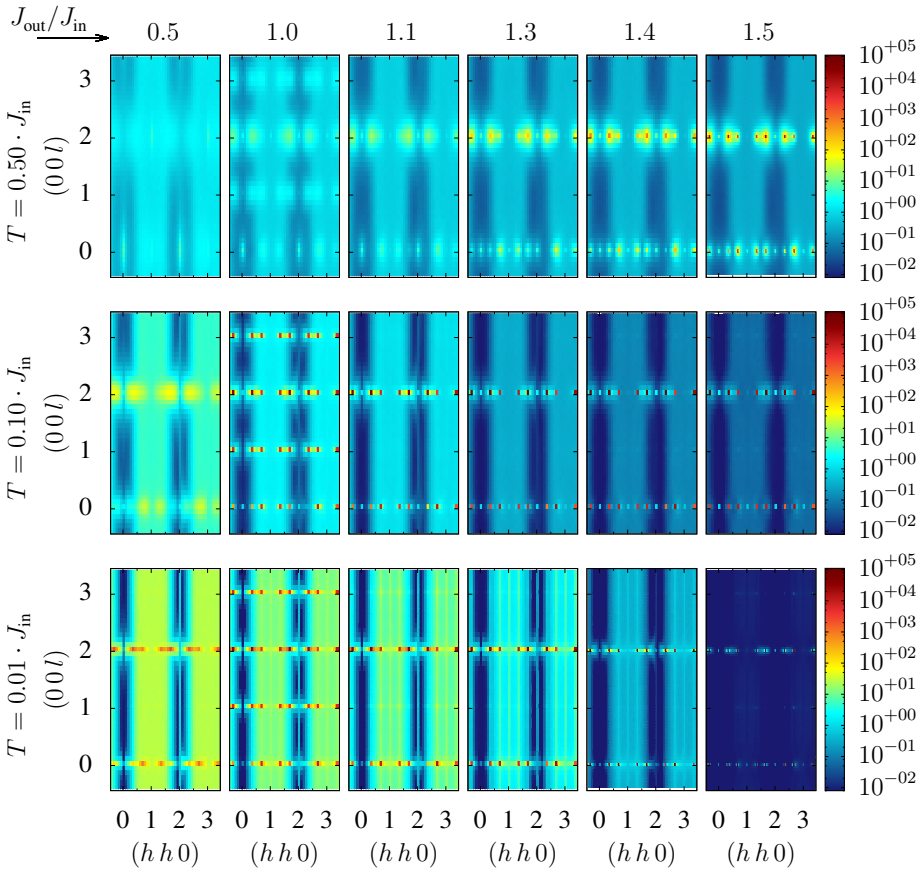

Figure B.6: Extracted $(h\,h\,l)$ scattering plane from structure factor, calculated using the spin dynamics simulation for $-0.021J_{\text{in}} < E < 0.021J_{\text{in}}$. Aside from the prominent magnetic Bragg peaks diffuse scattering without additional structure along $\langle 0\,0\,1 \rangle$ at all temperatures and ratios, which only disappears for $\tau = 1.5$ and $T = 0.01 \cdot J_{\text{in}}$. This indicates the present disorder to have no correlation along the c-axis at all. The colour scale denotes the value of $S(\mathbf{Q}, \omega)$ per $(\delta Q)^3 \cdot \delta E$.

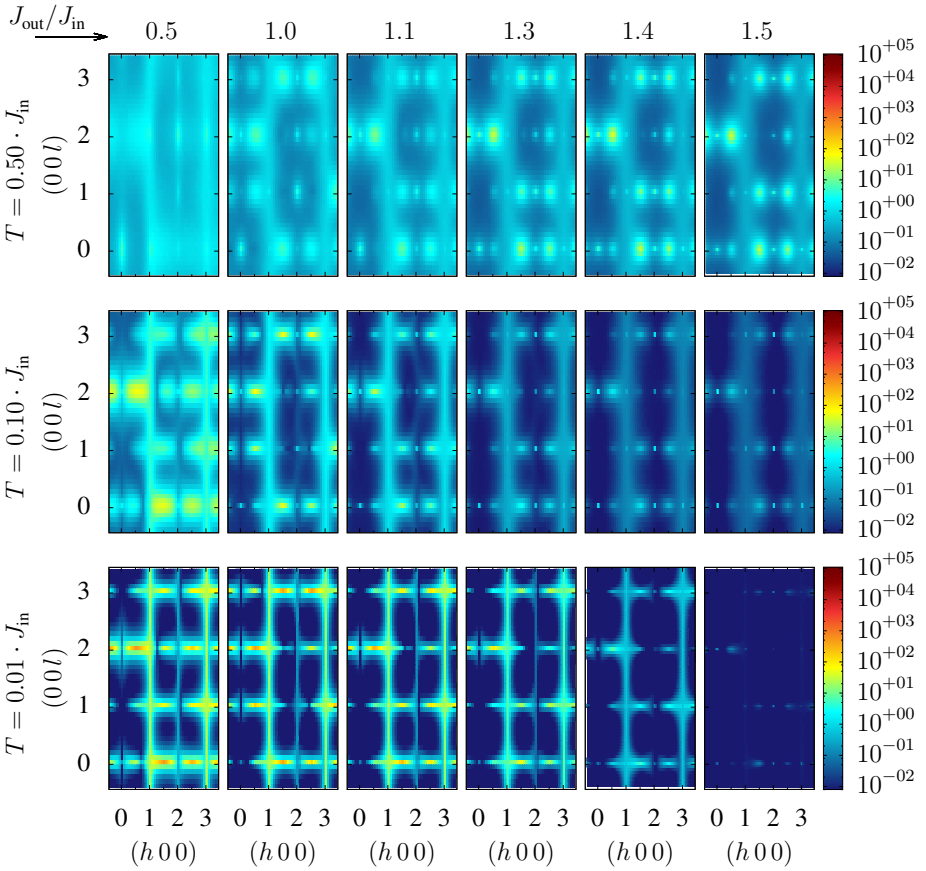

Figure B.7: Extracted $(h\,0\,l)$ scattering plane from structure factor, calculated using the spin dynamics simulation for $-0.021 J_{in} < E < 0.021 J_{in}$.The colour scale denotes the value of $S(\mathbf{Q}, \omega)$ per $(\delta Q)^3 \cdot \delta E$.

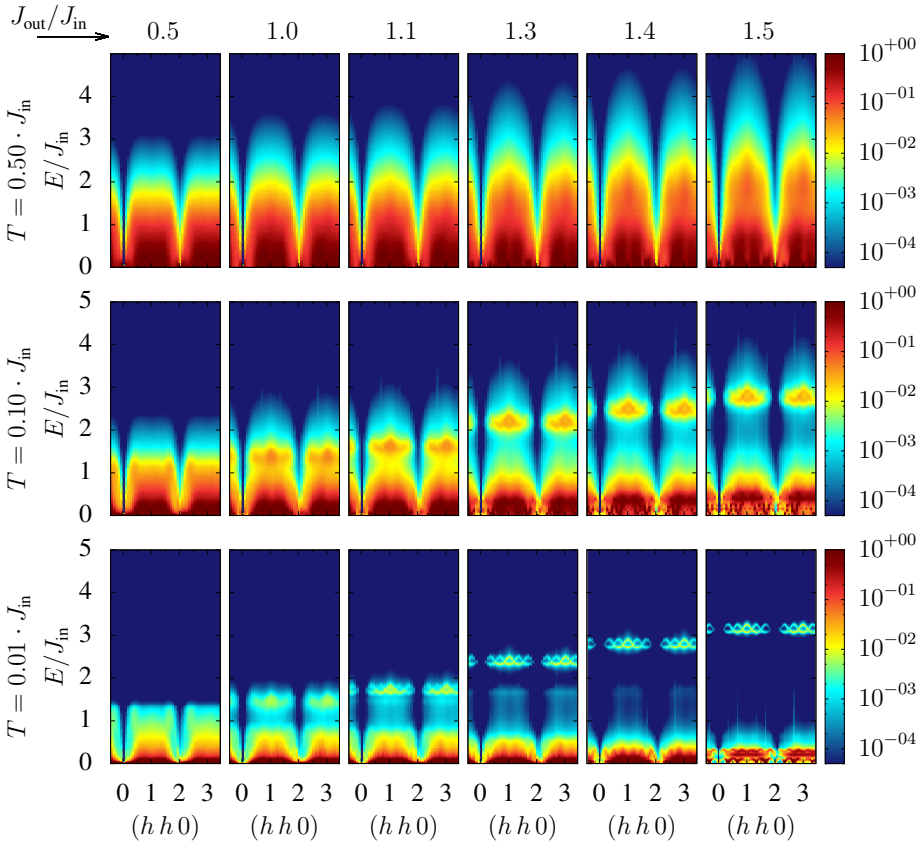

Figure B.8: Simulated excitations along $[1\,1\,0]$-direction. In contrast to the dispersions along $[0\,0\,1]$-direction (cf. Fig. 4.5) here for most ratios and temperatures a broad excitation response is present. For temperatures $T \leq 0.1 \cdot J_{\text{in}}$ two excitation bands are visible separated in energy. The colour scale denotes the value of $S(\mathbf{Q}, \omega)$ per $(\delta Q)^3 \cdot \delta E$.

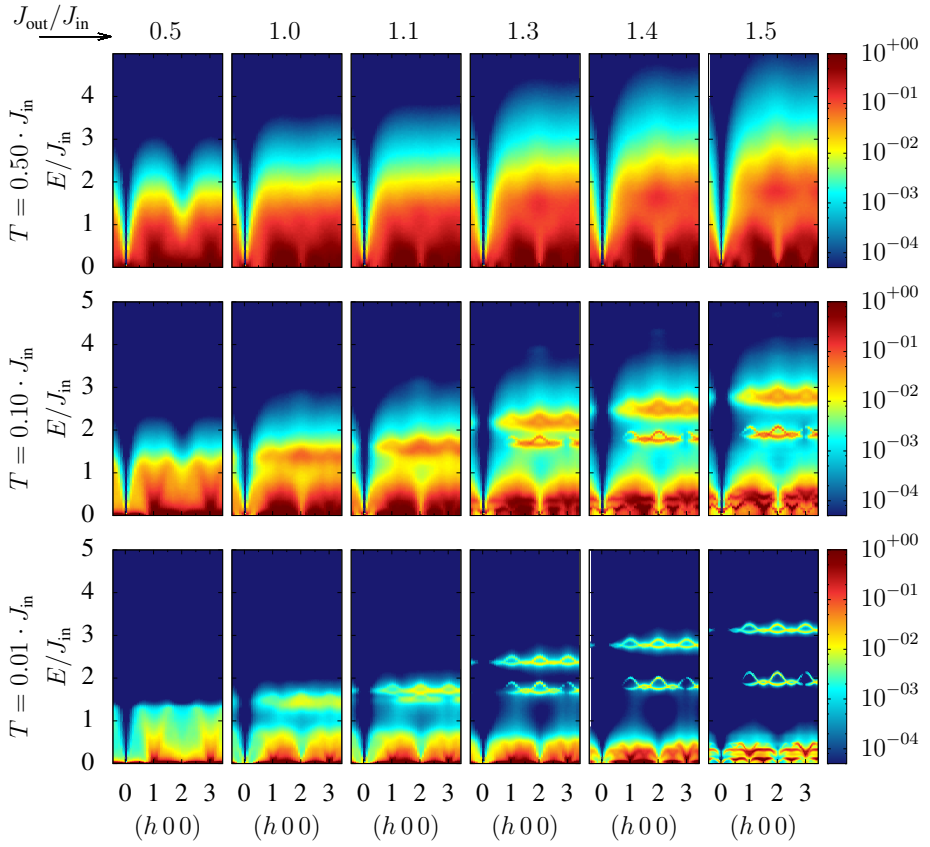

Figure B.9: Simulated excitations along $[1\,0\,0]$-direction. Somewhat similar to the dispersions along $[1\,1\,0]$-direction, but since the absolute length is smaller the dispersions are resolved more clearly. For $T \leq 0.1 \cdot J_{in}$ three excitation bands are visible separated in energy. The colour scale denotes the value of $S(\mathbf{Q}, \omega)$ per $(\delta Q)^3 \cdot \delta E$.

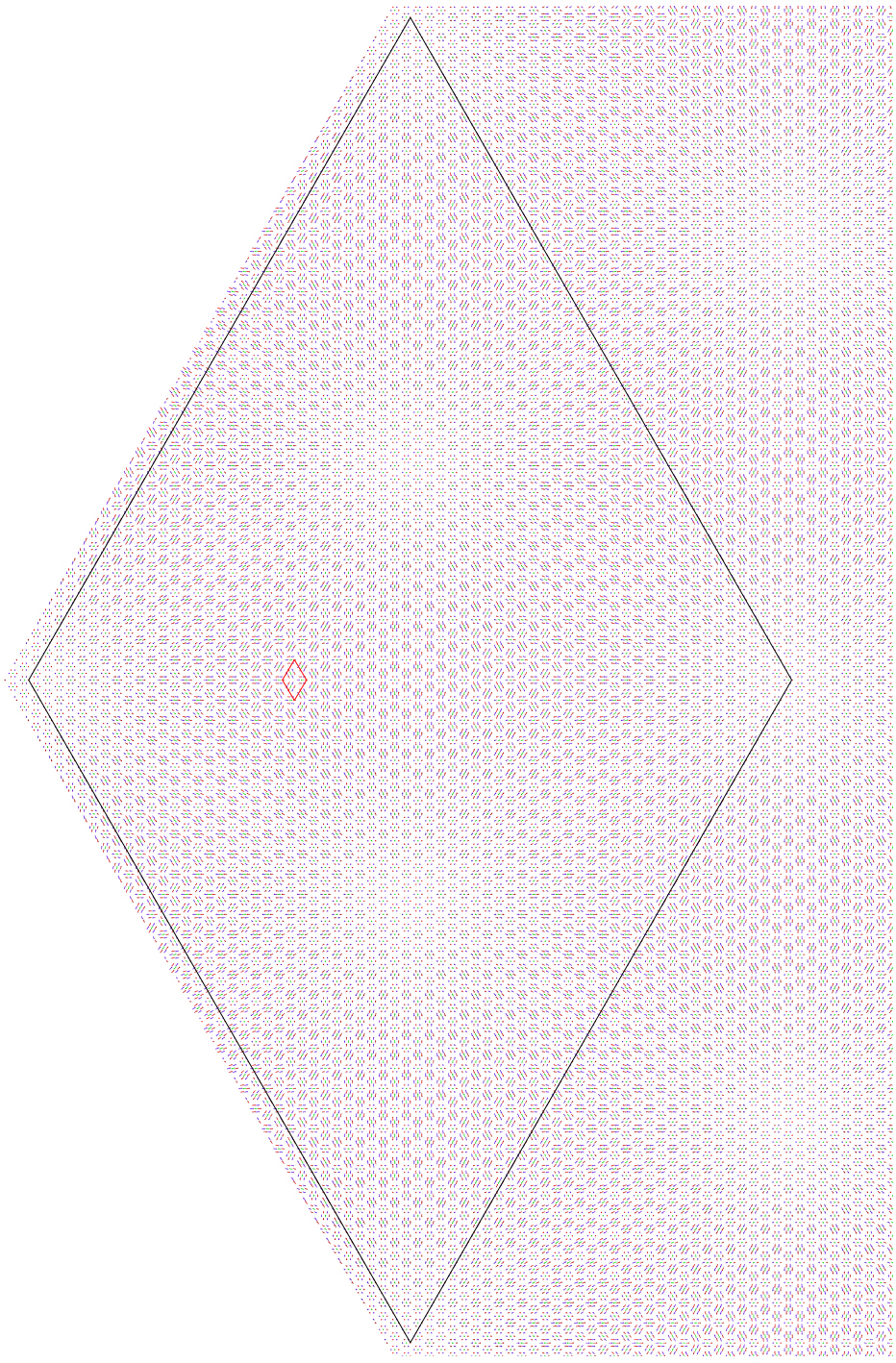

Figure B.10: Spin structure calculated by the instructions in Section 6.3 and particular in Eq. 6.3 with a period length of $p = 33$ corresponding to the splitting observed in measurements. The long-periodic unit cell is marked by the black lines and the commensurate antiferromagnetic one in red. Picture was rotated 90° clockwise.

C

List of Figures

2.1 Construction of the Ewald sphere in two dimensions. Bragg reflections are marked in red. 7
2.2 Illustration of a ferromagnetic order on a linear chain of ions. 9
2.3 Illustration of an antiferromagnetic order on a linear chain of ions. 10
2.4 Illustration of an ferrimagnetic order on a linear chain of ions. 10
2.5 Illustration of a long periodic order with a period of n unit cells for a prominent ferromagnetic coupling on a linear chain of ions 10
2.6 Cases of frustration in two and three dimensions relevant for the present study, with exchange interactions $J_{\text{ex}},\ J_{\text{in}},\ J_{\text{out}} < 0$. **(a)** Antiferromagnetically coupled spins order in a 120° structure due to geometric frustration. **(b)** The interaction J_{in} connecting neighbouring blue spins and J_{out} connecting blue and green spins compete with each other. For a ratio of $J_{\text{out}}/J_{\text{in}} \geq 1.5$ the interaction J_{out} forces the blue spins to align parallel. For lower ratios the order on the double tetrahedron becomes more complex. 11
2.7 Dispersions calculated for linear spin chains, for ferromagnetically (left), antiferromagnetically (middle) and ferrimagnetically coupled spins (right). In the case of the ferrimagnetic spin chain $S_B = 1/3 \cdot S$ and $S_A = S$. 16

3.1 Small crystal with its c-axis oriented parallel to the normal vector of the paper. . 19
3.2 Instrumental setup at Biodiff. Sample is mounted inside an aluminium can. The cylindrical image plate was moved to the bottom for mounting the can. The CCD camera is to the back and the incident beam to the right. 20
3.3 Schematics regarding the evaluation of the detector images taken at BioDiff. **(a)** The Ewald sphere of the scattered beam is projected onto the cylindrically shaped detector plate. **(b)** Horizontal cut through the Ewald sphere displaying the method of interpolation between two detector images of neighbouring rotation steps. 21
3.4 Schematic drawing of the polarization analysis setup at the neutron diffractometer Morpheus for the polarization channel H parallel to **Q**. The inset shows the Eulerian cradle and inside the metal plates held together with the permanent magnets, as well as in the middle the permanent magnets for the guide field and to the right the analyser. 23
3.5 Close up of the cage of hand-wound coils at the sample position. 24

3.6 Schematic of the configuration for the polarization channel H parallel to **Q** setup at the neutron diffractometer MIRA (cf. Fig. 3.5). 25
3.7 After applying a slight reorientation the magnetic and crystal structure peaks of the $\{h\,h\,l\}$-scattering planes superimpose perfectly. 26

4.1 Crystal structure of the mineral $NaBe_4SbO_7$ called Swedenborgite [PKW35]. . 27
4.2 Ground state in the antiferromagnetically ordered phase [KMMC10, Ros11, BF14], view along c-axis. Triangular spins in green and kagome spins in red/blue. Figure adapted from [Rei11]. Kagome spins with the same colour are of the same layer. 29
4.3 Spin wave dispersions determined with LSWT for $J_{\text{out}}/J_{\text{in}} = 1.5$, based on the Heisenberg nearest neighbour model [Rei11]. The inset shows the high symmetry points of the hexagonal Brillouin zone. The dispersion in $\{h\,k\,0\}$-scattering planes are rather flat, compared to the steep dispersions along $\langle 0\,0\,1\rangle$-directions. Furthermore, a large gap in energy is present. 30
4.4 Extracted $(h\,k\,0)$ scattering plane from the dynamic structure factor for $-0.021J_{\text{in}} < E < 0.021J_{\text{in}}$, calculated using the spin dynamics simulation. The magnetic order increases with increasing ratio and decreasing temperature, while the diffuse scattering is mostly localized along the crystal stucture Brillouin zone boundary. The colour scale denotes the value of $S(\mathbf{Q},\omega)$ per $(\delta Q)^3 \cdot \delta E$. 33
4.5 Excitations along $[0\,0\,1]$-direction. Cuts are taken from the dynamic structure factor of the spin dynamics calculations. Two excitation bands are present. The lower excitation band appears to be only loosely related with the ratio of the exchange interactions and temperature, while the upper one raises significantly with decreasing temperature and increasing ratio. The colour scale denotes the value of $S(\mathbf{Q},\omega)$ per $(\delta Q)^3 \cdot \delta E$. 35
4.6 Cuts of the high symmetry scattering planes for $-0.021J_{\text{in}} < E < 0.021J_{\text{in}}$ through the dynamic structure factor simulated at $T/J_{\text{in}} = 0.001$ for a ratio of $J_{\text{out}}/J_{\text{in}} = 1.3$. In the nematic phase the diffuse scattering is located close to the K-points in the $(h\,k\,0)$ scattering plane. The scattering planes $(h\,h\,l)$ and $(h\,0\,l)$ show a significant decrease of the intensity variation along $\langle 0\,0\,1\rangle$ indicating a shorter correlation length along c. The colour scale denotes the value of $S(\mathbf{Q},\omega)$ per $(\delta Q)^3 \cdot \delta E$. 37
4.7 Possible spin configurations on a double tetrahedron for $J_{\text{out}}/J_{\text{in}} = 1.3$ in the nematic phase with kagome spins in blue and triangular spins in green. View is along c-axis. Due to the coplanarity, the kagome spins deviate more strongly from the antiferromagnetic ground state according to the sum rule. **(a)** Symmetrically tilted kagome spins. **(b)** Antisymmetrically tilted kagome spins. . . . 38
4.8 Cuts in energy and along the high symmetry directions through the dynamic structure factor simulated at $T/J_{\text{in}} = 0.001$ for a ratio of $J_{\text{out}}/J_{\text{in}} = 1.3$. In the nematic phase the dispersions become more distinct along all directions. The colour scale denotes the value of $S(\mathbf{Q},\omega)$ per $(\delta Q)^3 \cdot \delta E$. 39

5.1 Crystal structure of $CaBaCo_2Fe_2O_7$ [RRS$^+$14]. The statistical distribution of Co and Fe over the magnetic sites is displayed as pie charts. The bonds show nearest neighbour connections between magnetic sites. The double tetrahedra forming columns along c are highlighted in cyan. 42

5.2 The $(h\,k\,0)$ and $(h\,h\,l)$ scattering plane measured at DNS at 4 K on the large single crystals, from [Ros11]. The BZ is marked in grey. Only at the K-points magnetic peaks are observed indicating a commensurate antiferromagnetic order. The corresponding spin structure is similar to the antiferromagnetic ground state (cf. Fig. 4.2b). 43

5.3 Temperature dependence of the different scattering contributions for the magnetic peak $(4/3\ 1/3\ 0)$ measured at DNS and normalized to the total magnetic scattering at 80 K, from [Ros11]. Integrated intensity was calculated from the absolute of the intensity map at the peak position. Below the phase transition at 160 K, between 80 K and 4 K a spin reorientation is visible. 44

5.4 Magnetic moment from FC (red curves) and ZFC (blue curves) measurements converted to moment in μ_B per ion (cf. Eq. 5.1). For easier viewing each curve is divided by the external field. Below the phase transition a reorientation is visible between the states at 80 K and 10 K. 45

5.5 Powder diffractograms measured above and below the magnetic phase transition at 160 K at the time-of-flight diffractometer Powgen. The pattern at 190 K is fitted with the structural model (cf. Fig. 5.1), difference between fit and data as blue line. Indicators for crystal structure peaks in red and magnetic ones in blue. The shape of the crystal structure peaks does not change upon transitioning, indicating a structural invariance. Figure adapted from [RRS$^+$14]. 47

5.6 Powder diffraction pattern measured at Powgen (SNS) with the low-Q wavelength band. The refinement of the crystal structure using FullProf is marked as blue lines. The difference can be attributed to the magnetic contribution, but the single peaks show a more complex structure. 48

5.7 Model used for the extraction of the integrated intensities from powder diffraction data. **(a)** The three satellites are assumed to be shifted away from the K-point along the BZ boundary by the distance δ. **(b)** Visualization of the fit results in two dimensions of the peak $(4/3\ 1/3\ 0)$ at 4 K. 48

5.8 Fit (blue line) of the diffraction pattern around the magnetic peaks $\{4/3\ 1/3\ 0\}$, $\{2/3\ 2/3\ 2\}$ and $\{4/3\ 1/3\ 1\}$ with a main and three satellite peaks each (cf. Fig. 5.7a). The splitting δ is kept constant and was refined initially from the data at 12 K. The contribution from the satellite peaks (green line) includes the fitted background. 49

5.9 Temperature dependence of extracted intensities from the magnetic peak $\{4/3\ 1/3\ 0\}$ and its satellite peaks from powder diffraction data measured at POWGEN. The main peak includes the satellite peak. Intensities have been normalized to the total magnetic scattering at 80 K. A trade of in intensity between the main peak and the satellite peaks are visible with the main peak most prominent at 80 K. . 50

5.10 Spin structure refined in magnetic space group $P6_3c'm'$. 51

5.11 Spin structure refined in magnetic space group $P6'_3cm'$. 52

5.12 Spin structure refined in magnetic space group $P6'_3c'm$. 52

5.13 Spin structure refined in magnetic space group $P6_3cm$. 52

5.14 Spin structure refined in magnetic space group $P31m'$. 53

5.15 Spin structure refined in magnetic space group $P31m$. 53

5.16 Integrated intensities of the scattering planes $(h\,k\,0)$ and $(h\,k\,\overline{2})$ measured on Morpheus at 80 K, plotted in the respective scattering plane. Left: Original intensities show a deviation between symmetrically equivalent peaks. Right: The deviation has been corrected by applying an angular dependent factor f_{angular} (cf. Equation 5.4). 54
5.17 Spin structure was rotated by 90° around the c-axis and comparing it with magnetic space group $P31m$. 57
5.18 Extracted cuts of the hk0 scattering plane from the measurements at Biodiff at 4 K (left) and 80 K (right). The BZ boundary is marked in grey. The magnetic Bragg peaks $(\overline{5/3},\ 4/3,\ 0)$ and $(\overline{4/3},\ 5/3,\ 0)$ (symmetrical equivalents to $(4/3,\ 1/3,\ 0)$) are highlighted in insets. The commensurate magnetic peaks at 80 K vanish upon cooling to 4 K with only split peaks remaining. The splitting corresponds to the model in Fig. 5.7 for $\delta \approx 0.017\,\text{Å}^{-1}$. 60
5.19 A cut through the magnetic peak $(\overline{4/3}\ 5/3\ 0)$ along $\hat{\mathbf{e}}_x$ as defined in Fig. 5.18, extracted from the data set measured on BiodDiff at 80 K. Shift in Q_z stems from a misalignment of the sample. Judging from the peak width the spin structure has a long correlation length along $\langle 0\,0\,1\rangle$-direction. 61
5.20 Structure of selected magnetic peaks calculated from polarization channels measured at 4 K on Morpheus. In the total magnetic scattering (upper row) the peaks reveal additional structure along the Brillouin zone boundary (grey). The chiral scattering (lower row) is anti-symmetrical transverse to the **Q**-vector for all peaks. 62
5.21 Selected crystal peak structure measured at MIRA on the small crystal show structural invariance between 80 and 4 K and an elongation of the resolution ellipsoid along **Q**. Black dots mark the BZ centre, which was defined during the experiment to a precision of $\Delta Q \approx 0.012\,\text{Å}^{-1} \cdot (|h| + |k|)$, indicated by the black circle. 63
5.22 Peak structure close to the K-point of the BZ in the total magnetic scattering measured at MIRA on the small crystal. Satellite peaks with the same splitting are observable at 80 and 4 K, while the intensity at the K-point vanishes completely at 4 K. 64
5.23 Temperature dependence observed on the magnetic peak $(2/3\ 2/3\ 0)$ in the total magnetic scattering measured at MIRA (sorted by the order of each measurement). The small crystal reveals a continuous change between two spin structures with different propagation vectors. 64
5.24 Selected crystal structure peaks measured at MIRA on the large crystal, structural invariance between 80 and 4 K is seen as well as an elongation of the resolution ellipsoid along **Q**. Black dots mark the BZ centre, which was defined during the experiment to a precision of $\Delta Q \approx 0.012\,\text{Å}^{-1} \cdot (|h| + |k|)$, indicated by the black circle. 65
5.25 Peak structure close to the K-point of the BZ in the total magnetic scattering measured at MIRA on the large crystal shows relatively high diffuse scattering and a structured peak at the K-point at 80 K. At 4 K a slight additional structure is visible at the satellite peak positions. 66
5.26 The magnetic scattering close to the magnetic peak $(\overline{1/3}\ 2/3\ 0)$ measured on the large crystal at 4 K. Here satellite peaks are visible with the scattering at the K-point being still prominent. 67

5.27 Magnetic peak structure of the peak $(2/3\ 2/3\ 0)$ measured at MIRA at several temperatures on the large crystal, sorted by the order of each measurement. These maps have been measured in-between the measurements of the large peak sets at 4 and 80 K, whereas the maps at 4 and 80 K are from the respective set. . 67

5.28 Temperature dependence of integrated intensities for the $(4/3\ 1/3\ 0)$ peak, which resembles the one measured at DNS (cf. Fig. 5.3). Comparing both crystals, in the case of the small one, the scattering from moments out of plane and chiral scattering is even more pronounced. The background was subtracted using Equation 5.6. 68

5.29 Extracting cuts along symmetry directions from the measurement taken at 4 K on the crystal with $(h\,k\,0)$-orientation on ARCS. Possible cuts along directions symmetrically equivalent to $[1\,1\,0]$ (left). The resulting E versus **Q**-cuts after adding the extracted cuts (right). 69

5.30 Excitations along $[0\,0\,1]$ measured on ARCS at 4 K. Dispersions for a linear antiferromagnetic (left) and pseudo-ferrimagnetic (middle) spin chain (gray line) are added for comparison. Full integration along the spatial directions close to the origin (± 5 Å^{-1}) reveals intensity levels (right), corresponding to the dispersions of a pseudo-ferrimagnetic chain. 70

5.31 Slim cuts of the elastic part of the scattering planes $(h\,h\,l)$ (upper row) and $(h{+}1/6,\ -h{+}1/6,\ l)$ (lower row) extracted from the combined data sets measured with several incident energies at 4 K. Regular pattern of the magnetic and crystal structure peaks are visible. 71

5.32 Combined extracted cuts along the $[0\,0\,1]$-direction through $(2/3,\ \overline{1/3},\ 0)$ from the data sets measured using different incident energies E_i (A: 10 meV, B: 14 meV, C: 17 meV, D: 24 meV, E: 33 meV, F: 53 meV and G: 90 meV). No excitation continuum is present in between the excitation branches. At 4 K an anisotropy gap is indicated by a local intensity minimum below 2 meV. 72

5.33 Combined extracted cuts along the $[1\,\overline{1}\,0]$-direction through $(1/6,\ 1/6,\ 2)$ from the data sets measured using different incident energies E_i (A: 10 meV, B: 14 meV, C: 17 meV, D: 24 meV, E: 33 meV, F: 53 meV and G: 90 meV). No excitation continuum is present inbetween the excitation branches. At 4 K an anisotropy gap is indicated by a local intensity minimum below 2 meV. 73

5.34 Constant energy cuts at 5 and 9 meV taken at two different planes from data sets with incident energy $E_i = 17$ meV. At both temperatures the ellipse of the excitation cone is unfilled above 5 meV. In addition the intensity on the ellipse is lower from the centre along the $[1\,1\,0]$-direction. The x and y-axes are scaled to fit regarding Å^{-1}. 74

6.1 Possible Dzyaloshinskii-Moriya interactions determined from the crystal structure using the Moriya rules [Mor60]. From symmetry the DM vectors on the bonds between a kagome and triangular are fixed parallel to the opposite bond of the tetrahedron, while the vectors on kagome-kagome bonds can vary in the plane perpendicular to the bond. 79

6.2 Configurational energy close to the magnetic peak ($1/3$, $1/3$, 0). The BZ boundary is indicated as grey lines. (Left) calculation is based on the Heisenberg nearest neighbour model for a ratio of $J_{\text{out}}/J_{\text{in}} = 1.45$ and $\mathbf{D}_{ij} = 0$ resulting in a region flat in energy close to the K-point (marked by the red circle). (Right) Dzyaloshinskii-Moriya exchange interaction ($D_{||ab} = 0.02$ and $D'''_{||ab} = 0.01$) is introduced making the commensurate order energeticly less favourable. The new minima in energy are marked as red dots. The source code used for the calculation is courtesy of Maxim Mostovoy. 80

6.3 Structure factor calculated from the long-periodic spin structure. Background has been removed. **(a)** Scattering from moments in the ab-plane. **(b)** Scattering from moments parallel to the c-axis. **(c)** Total magnetic scattering. Insets display intensity distribution over satellite peaks similar to data measured at 4 K (cf. Fig. 5.18a). **(d)** Chiral magnetic scattering, shows the same antisymmetry as data from Morpheus (cf. Fig. 5.20 lower row) and MIRA (cf. Fig. B.3). . . . 83

6.4 During the creation the antiferromagnetic modulation was removed for comparison. The spin structure shows a clear translation symmetry and link to the hedgehog type skyrmion. 84

6.5 Winding number per unit cell of the long-periodic order calculated for a triangular layer of the spin structure, which was created with (red) and without (blue) the antiferromagnetic modulation using a period length of p commensurate magnetic unit cells (mag. u.c.). 85

6.6 Spin length distribution of the calculated spin structure with the periodicity $p = 33$ [mag. u.c.]. Apparently the spins can vary within a certain range, but all spins have a non zero length required for a valid spin structure. 85

6.7 Dispersions along $[0\,0\,1]$-direction calculated with LSWT for a single double tetrahedra column along c-direction. Note, that here the energy scale is divided by J_{out}. Based on the Heisenberg nearest neighbour model two situations are compared: decoupled kagome spins for exchange interactions $J_{\text{out}} = 1.5$ and $J_{\text{in}} = 0.0$ (left) and coupled kagome spins for $J_{\text{out}} = 1.5$ and $J_{\text{in}} = 1.0$ (middle). The dispersions along $[0\,0\,1]$-direction for the whole structure with $J_{\text{out}} = 1.5$ and $J_{\text{in}} = 1.0$ are displayed for comparison (right), here the magnetic unit cell was reduced to two layers, one kagome and one triangular. 87

B.1 Additional polarization channels measured at 4 K around the magnetic peak ($4/3$ $1/3$ 0) on the large crystal on Morpheus, which reveal the spin structure related to the commensurate scattering to be less canted than the long-periodic spin structure. 105

B.2 Extracted cuts of the $(h\,k\,1)$ (upper row) and $(h\,k\,\overline{1})$ (lower row) scattering plane from the measurements at Biodiff at 4 K (left) and 80 K (right). The BZ boundary is marked in grey. The magnetic Bragg peaks ($\overline{5/3}$ $4/3$ 0) and ($\overline{4/3}$ $5/3$ 0) (symmetrically equivalents to ($4/3$ $1/3$ 0)) are highlighted in insets. The data of $(h\,k\,1)$ was shifted by $\Delta Q_x = -0.025\text{Å}^{-1}$ and in the case of $(h\,k\,\overline{1})$ by $\Delta\mathbf{Q} = (0.018,\, 0.005,\, 0)\text{Å}^{-1}$ compensating the misalignment of the sample. The commensurate peak shape at 80 K and peak splitting at 4 K observed in $(h\,k\,0)$-scattering plane (cf. Fig. 5.18) is present in parallel planes as well. Thus the change in spin structure is restricted to within the ab-plane. 106

B.3 Magnetic peak structure in the chiral scattering measured at MIRA on the small crystal. At both temperatures and all peaks the chiral scattering is anti-symmetric transverse to **Q**. This scattering contribution is observed even close to the commensurate magnetic peaks positions. 107
B.4 Magnetic peak structure in the scattering from moments parallel to the ab-plane measured at MIRA on the small crystal. In case of the magnetic peak $(2/3\ \overline{1/3}\ 2)$ the third satellite peak is obstructed by the cavity, which is necessary to separate this channel. 107
B.5 Temperature dependence in scattering contributions measured around the magnetic peak $(2/3\ 2/3\ 0)$ at MIRA on the small crystal (sorted by the order of each measurement). 108
B.6 Extracted $(h\,h\,l)$ scattering plane from structure factor, calculated using the spin dynamics simulation for $-0.021J_{\text{in}} < E < 0.021J_{\text{in}}$. Aside from the prominent magnetic Bragg peaks diffuse scattering without additional structure along $\langle 0\,0\,1\rangle$ at all temperatures and ratios, which only disappears for $\tau = 1.5$ and $T = 0.01 \cdot J_{\text{in}}$. This indicates the present disorder to have no correlation along the c-axis at all. The colour scale denotes the value of $S(\mathbf{Q},\omega)$ per $(\delta Q)^3 \cdot \delta E$. . 109
B.7 Extracted $(h\,0\,l)$ scattering plane from structure factor, calculated using the spin dynamics simulation for $-0.021J_{\text{in}} < E < 0.021J_{\text{in}}$.The colour scale denotes the value of $S(\mathbf{Q},\omega)$ per $(\delta Q)^3 \cdot \delta E$. 110
B.8 Simulated excitations along $[1\,1\,0]$-direction. In contrast to the dispersions along $[0\,0\,1]$-direction (cf. Fig. 4.5) here for most ratios and temperatures a broad excitation response is present. For temperatures $T \leq 0.1 \cdot J_{\text{in}}$ two excitation bands are visible separated in energy. The colour scale denotes the value of $S(\mathbf{Q},\omega)$ per $(\delta Q)^3 \cdot \delta E$. 111
B.9 Simulated excitations along $[1\,0\,0]$-direction. Somewhat similar to the dispersions along $[1\,1\,0]$-direction, but since the absolute length is smaller the dispersions are resolved more clearly. For $T \leq 0.1 \cdot J_{\text{in}}$ three excitation bands are visible separated in energy. The colour scale denotes the value of $S(\mathbf{Q},\omega)$ per $(\delta Q)^3 \cdot \delta E$. 112
B.10 Spin structure calculated by the instructions in Section 6.3 and particular in Eq. 6.3 with a period length of $p = 33$ corresponding to the splitting observed in measurements. The long-periodic unit cell is marked by the black lines and the commensurate antiferromagnetic one in red. Picture was rotated 90° clockwise. 113

D

Single crystal refinement results

In Subsection 5.3.2 the magnetic structure has been refined from integrated intensities measured on the large single crystal with $(h\,h\,l)$-orientation at the 4-circle diffractometer Morpheus (PSI, Villigen, Switzerland). Assuming a commensurate K-type antiferromagnetic order as observed at DNS (cf. Fig. 5.2) six possible magnetic space groups ($P6_3c'm'$, $P6'_3cm'$, $P6'_3c'm$, $P6_3cm$, $P31m'$ and $P31m$) have been derived from the crystallographic space group $P6_3mc$ of $CaBaCo_2Fe_2O_7$. The accessible crystal Bragg peaks (cf. Table D.1) have been reduced in the crystallographic space group resulting in the unique reflections in Table D.2, which will be used as a intensity reference for the refinement of the magnetic structure. The total set of integrated magnetic peaks (cf. Table D.3) is reduced within each magnetic space group separately resulting in a set of unique reflections for the hexagonal and trigonal space groups each (cf. Tables D.4 and D.5). In Subsection 5.3.2 five different models for the refinement are discussed. In Table D.8 the results from simulated annealing are listed for the model **D** applied to the magnetic space groups with hexagonal symmetry. The results for the trigonal space groups are given in the case of simulated annealing for the models **D** and **E** in Table D.9 and in the case of Rietveld refinement for model **E** in Table D.10.

	80 K					4 K				
No.	h	k	l	Int. (cts)	σ	h	k	l	Int. (cts)	σ
1	-1	1	0	5319.24	16.82	-1	1	0	5441.46	16.93
2	1	-1	0	6261.70	18.19	1	-1	0	5790.31	17.37
3	-1	0	0	4900.79	16.07	-1	0	0	5047.58	16.26
4	0	-1	0	5537.82	17.14	0	-1	0	5289.18	16.59
5	0	1	0	6210.19	18.08	0	1	0	5984.74	17.71
6	1	0	0	6520.39	18.49	1	0	0	6063.36	17.77
7	-1	1	-1	1640.13	9.76	-1	1	-1	1701.51	9.93
8	-1	1	1	1597.44	9.57	-1	1	1	1676.09	9.81
9	1	-1	-1	1890.33	10.40	1	-1	-1	1644.87	9.71
10	1	-1	1	1823.82	10.22	1	-1	1	1719.92	9.92
11	-1	0	1	1437.11	9.06	-1	0	1	1502.57	9.25
12	0	-1	1	1626.52	9.66	0	-1	1	1609.34	9.59
13						0	1	-1	1885.69	10.44
14						1	0	-1	1714.75	9.91
15						-1	0	-1	1451.40	9.12
16						0	-1	-1	1572.11	9.49

17		0	1	1	1656.15	9.73
18		1	0	1	1675.10	9.78
19		-1	0	2	2283.58	12.42
20		0	-1	2	2632.67	13.27
21		0	1	-2	2981.96	14.24
22		1	0	-2	2364.77	12.63
23		-1	1	-2	2831.28	13.88
24		-1	1	2	2088.53	11.93
25		1	-1	-2	1770.58	10.96
26		1	-1	2	2746.19	13.56
27		0	-1	-2	2030.45	11.73
28		0	1	2	2227.61	12.30
29		-1	0	-2	2511.04	13.01
30		1	0	2	2546.76	13.11
31		-1	2	0	3375.64	16.58
32		1	-2	0	3289.58	16.43
33		-2	1	0	2723.90	14.95
34		2	-1	0	3694.62	17.38
35		-1	-1	0	2591.58	14.56
36		1	1	0	3635.04	17.23
37		-2	1	1	4.54	5.20
38		-1	2	-1	6.23	6.17
39		1	-2	1	4.87	5.17
40		2	-1	-1	4.55	5.17
41		-1	2	1	7.96	8.25
42		1	-2	-1	5.36	5.53
43		-2	1	-1	6.53	6.63
44		2	-1	1	2.46	3.19
45		-1	-1	1	5.92	6.19
46		1	1	-1	5.31	5.24
47		-1	-1	-1	6.02	6.18
48		1	1	1	5.43	5.22
49		0	1	-3	6182.32	22.98
50		1	0	-3	4617.23	19.64
51		-1	1	-3	7120.65	24.85
52		1	-1	-3	6440.43	23.26
53		-1	0	-3	7350.52	24.92
54		0	-1	-3	7402.26	24.94
55		-2	2	0	6413.95	22.96
56		2	-2	0	7271.40	24.40
57		-2	0	0	5466.01	21.06
58		0	-2	0	6124.00	22.21
59		0	2	0	7220.65	24.28
60		2	0	0	7428.51	24.67

Table D.1: Integrated intensities of crystal structure peaks measured at Morpheus. Notation of $(h\,k\,l)$ in the crystallographic unit cell.

	80 K					4 K				
No.	h	k	l	Int. (cts)	σ	h	k	l	Int. (cts)	σ
1	1	0	0	5733.5728	584.5475	1	0	0	5578.2705	372.5243
2	1	0	1	1655.7567	149.4647	1	0	1	1643.5691	106.7580
3						1	0	2	2367.8884	346.1510
4						1	1	0	3160.0854	431.0378
5						1	0	3	6341.7876	1045.2333
6						2	0	0	6570.2788	729.1144

Table D.2: Unique reflections resulting from the reduction of the crystal structure peaks measured at Morpheus (cf. Table D.1) within crystallographic space group $P6_3mc$. Notation of $(h\,k\,l)$ in the crystallographic unit cell.

	80 K					4 K				
No.	h	k	l	Int. (cts)	σ	h	k	l	Int. (cts)	σ
1	1/3	1/3	0	381	5	1/3	1/3	0	500	6
2	-1/3	-1/3	0	363	4	-1/3	-1/3	0	469	6
3	-2/3	1/3	0	325	5	-2/3	1/3	0	433	6
4	1/3	-2/3	0	526	5	1/3	-2/3	0	645	6
5	-1/3	2/3	0	533	5	-1/3	2/3	0	667	6
6	2/3	-1/3	0	352	5	2/3	-1/3	0	579	7
7	1/3	1/3	-1	23	2	2/3	-1/3	0	579	7
8	-1/3	-1/3	1	22	2	1/3	1/3	-1	27	2
9	-1/3	-1/3	-1	19	2	-1/3	-1/3	1	37	2
10	1/3	1/3	1	13	2	-1/3	-1/3	-1	21	2
11	-2/3	1/3	1	9	2	1/3	1/3	1	16	2
12	1/3	-2/3	1	38	2	-2/3	1/3	1	19	2
13	-1/3	2/3	-1	47	2	1/3	-2/3	1	40	2
14	2/3	-1/3	-1	9	2	-1/3	2/3	-1	49	2
15	-2/3	1/3	-1	13	2	2/3	-1/3	-1	19	2
16	1/3	-2/3	-1	48	2	1/3	-2/3	-1	45	2
17	-1/3	2/3	1	50	2	-1/3	2/3	1	48	2
18	2/3	-1/3	1	13	2	2/3	-1/3	1	19	2
19	-2/3	4/3	0	1449	9	-2/3	4/3	0	1617	11
20	-4/3	2/3	0	1252	8	-4/3	2/3	0	1314	10
21	4/3	-2/3	0	1646	10	4/3	-2/3	0	1723	12
22	2/3	-4/3	0	1500	9	2/3	-4/3	0	1615	12
23	-2/3	-2/3	0	1267	9	-2/3	-2/3	0	1340	10
24	2/3	2/3	0	1671	10	2/3	2/3	0	1757	12
25	1/3	1/3	-2	7139	21	1/3	1/3	-2	6577	22
26	2/3	-1/3	-2	6229	20	2/3	-1/3	-2	5602	21
27	-2/3	4/3	-1	55	2	-2/3	4/3	-1	62	3
28	-4/3	2/3	1	35	2	-4/3	2/3	1	45	3
29	4/3	-2/3	-1	49	2	4/3	-2/3	-1	61	3
30	2/3	-4/3	1	52	2	2/3	-4/3	1	68	3
31	-4/3	2/3	-1	39	2	-4/3	2/3	-1	44	3
32	-2/3	4/3	1	46	2	-2/3	4/3	1	58	3
33	2/3	-4/3	-1	50	2	2/3	-4/3	-1	59	3
34	4/3	-2/3	1	48	2	4/3	-2/3	1	60	3

35	-2/3	-2/3	1	40	2	-2/3	-2/3	1	46	3
36	2/3	2/3	-1	52	2	2/3	2/3	-1	62	3
37	-2/3	-2/3	-1	44	2	-2/3	-2/3	-1	49	3
38	2/3	2/3	1	51	2	2/3	2/3	1	55	3
39	-4/3	-1/3	0	2441	12	-4/3	-1/3	0	2616	15
40	-1/3	-4/3	0	2660	12	-1/3	-4/3	0	2844	16
41	1/3	4/3	0	3470	14	1/3	4/3	0	3785	18
42	4/3	1/3	0	3573	14	4/3	1/3	0	3885	18
43	-4/3	5/3	0	2924	13	-4/3	5/3	0	3200	17
44	4/3	-5/3	0	3198	13	4/3	-5/3	0	3479	17
45	-5/3	4/3	0	2675	12	-5/3	4/3	0	2988	16
46	5/3	-4/3	0	3349	14	5/3	-4/3	0	3673	18
47	1/3	-5/3	0	2863	13	-1/3	5/3	0	3582	18
48	-1/3	5/3	0	3269	13	-5/3	1/3	0	2584	15
49	-5/3	1/3	0	2442	12	5/3	-1/3	0	3793	18
50	5/3	-1/3	0	3556	14	-2/3	4/3	-2	953	9
51	-2/3	4/3	-2	1037	8	-4/3	2/3	2	728	8
52	-4/3	2/3	2	655	6	4/3	-2/3	-2	853	8
53	4/3	-2/3	-2	867	7	2/3	-4/3	2	787	8
54	2/3	-4/3	2	732	7	-4/3	2/3	-2	753	8
55	-4/3	2/3	-2	864	7	-2/3	4/3	2	783	8
56	-2/3	4/3	2	730	6	2/3	-4/3	-2	890	8
57	2/3	-4/3	-2	978	7	4/3	-2/3	2	761	8
58	4/3	-2/3	2	768	7	-2/3	-2/3	2	700	8
59	-2/3	-2/3	2	641	6	2/3	2/3	-2	985	9
60	2/3	2/3	-2	1000	8	-2/3	-2/3	-2	753	8
61	-2/3	-2/3	-2	845	7	2/3	2/3	2	801	8
62	2/3	2/3	2	817	7	-4/3	-1/3	1	1579	11
63	-4/3	-1/3	1	1369	9	-1/3	-4/3	1	1827	12
64	-1/3	-4/3	1	1602	10	1/3	4/3	-1	2352	13
65	1/3	4/3	-1	2172	11	4/3	1/3	-1	2292	13
66	4/3	1/3	-1	2044	11	-1/3	-4/3	-1	1822	12
67	-1/3	-4/3	-1	1695	10	1/3	4/3	1	2255	13
68	1/3	4/3	1	1966	10	-4/3	-1/3	-1	1661	11
69	-4/3	-1/3	-1	1576	9	4/3	1/3	1	2291	13
70	4/3	1/3	1	2039	11	-4/3	5/3	-1	2070	13
71	-4/3	5/3	-1	1935	11	4/3	-5/3	1	2328	13
72	4/3	-5/3	1	1999	11	-5/3	4/3	1	1807	12
73	-5/3	4/3	1	1573	10	5/3	-4/3	-1	2332	13
74	5/3	-4/3	-1	2088	11	-4/3	5/3	1	1927	12
75	-4/3	5/3	1	1668	10	4/3	-5/3	-1	2133	13
76	4/3	-5/3	-1	1968	11	-5/3	4/3	-1	1791	12
77	-5/3	4/3	-1	1686	10	5/3	-4/3	1	2275	13
78	5/3	-4/3	1	1939	11	1/3	-5/3	1	1958	12
79	1/3	-5/3	1	1678	10	-1/3	5/3	-1	2182	13
80	-1/3	5/3	-1	2025	11	-5/3	1/3	1	1586	11
81	-5/3	1/3	1	1358	9	5/3	-1/3	-1	229	13
82	5/3	-1/3	-1	1992	11	1/3	-5/3	-1	2048	13
83	1/3	-5/3	-1	1945	11	-1/3	5/3	1	2244	13
84	-1/3	5/3	1	1994	11	-5/3	1/3	-1	1654	11

85	-5/3	1/3	-1	1519	9	5/3	-1/3	1	2314	13
86	5/3	-1/3	1	2022	11	-1/3	-4/3	2	63	3
87	-1/3	-4/3	2	57	2	1/3	4/3	-2	82	3
88	1/3	4/3	-2	85	2	-4/3	-1/3	2	67	3
89	-4/3	-1/3	2	60	2	4/3	1/3	-2	115	3
90	4/3	1/3	-2	113	3	-1/3	-4/3	-2	71	3
91	-1/3	-4/3	-2	80	2	1/3	4/3	2	70	3
92	1/3	4/3	2	76	2	-4/3	-1/3	-2	80	3
93	-4/3	-1/3	-2	93	3	4/3	1/3	2	113	3
94	4/3	1/3	2	114	3	-4/3	5/3	-2	73	3
95	-4/3	5/3	-2	80	2	4/3	-5/3	2	70	3
96	4/3	-5/3	2	74	2	-5/3	4/3	2	73	3
97	-5/3	4/3	2	65	2	5/3	-4/3	-2	66	3
98	5/3	-4/3	-2	76	2	-4/3	5/3	2	66	3
99	-4/3	5/3	2	74	2	4/3	-5/3	-2	82	3
100	4/3	-5/3	-2	80	2	-5/3	4/3	-2	76	3
101	-5/3	4/3	-2	78	2	5/3	-4/3	2	76	3
102	5/3	-4/3	2	81	2	1/3	-5/3	2	76	3
103	1/3	-5/3	2	79	2	-1/3	5/3	-2	84	3
104	-1/3	5/3	-2	86	3	-5/3	1/3	2	99	3
105	-5/3	1/3	2	95	3	5/3	-1/3	-2	124	4
106	5/3	-1/3	-2	116	3	1/3	-5/3	-2	65	3
107	1/3	-5/3	-2	75	2	-1/3	5/3	2	74	3
108	-1/3	5/3	2	73	2	-5/3	1/3	-2	99	3
109	-5/3	1/3	-2	108	3	5/3	-1/3	2	95	3
110	5/3	-1/3	2	102	3	4/3	-2/3	-3	1355	12
111	-2/3	4/3	-3	1168	8	-4/3	2/3	-3	1519	12
112	4/3	-2/3	-3	1061	8	2/3	-4/3	-3	1789	13
113	-4/3	2/3	-3	1375	9	2/3	2/3	-3	1242	11
114	2/3	-4/3	-3	1368	9	-2/3	-2/3	-3	1479	12
115	2/3	2/3	-3	1133	8					
116	-2/3	-2/3	-3	1481	9					

Table D.3: Integrated intensities of magnetic peaks measured at Morpheus. Notation of $(h\,k\,l)$ in the crystallographic unit cell.

				80 K		4 K	
No.	h	k	l	Int. (cts)	σ	Int. (cts)	σ
1	-2/3	1/3	0	409.02	83.82	541.97	87.72
2	1/3	-2/3	-1	25.33	15.27	28.41	12.35
3	2/3	-4/3	0	1442.04	163.93	1541.64	173.43
4	2/3	-1/3	-2	6661.82	455.00	6049.76	487.35
5	-2/3	-2/3	1	46.75	5.85	55.20	7.49
6	-1/3	-4/3	0	2987.01	402.77	3245.20	463.64
7	2/3	-4/3	2	807.65	124.60	802.84	85.86
8	1/3	4/3	1	1793.36	233.27	2007.51	261.24
9	-5/3	1/3	2	79.80	16.05	79.71	16.73
10	-2/3	-2/3	-3	1247.49	151.55	1456.24	183.92

Table D.4: Unique reflections resulting from the reduction of the magnetic peaks measured at Morpheus (cf. Table D.3) within the hexagonal magnetic space groups. The reduction within the four different space groups yields the same result. Notation of $(h\,k\,l)$ in the crystallographic unit cell.

				80 K		4 K	
No.	h	k	l	Int. (cts)	σ	Int. (cts)	σ
1	-2/3	1/3	0	409.02	83.82	541.97	87.72
2	-2/3	1/3	1	25.33	15.27	28.41	12.35
3	-4/3	2/3	0	1442.04	163.93	1541.64	173.43
4	1/3	1/3	-2	6661.82	455.00	6049.76	487.35
5	-4/3	2/3	1	46.75	5.85	55.20	7.49
6	5/3	-1/3	0	2987.01	402.77	3245.20	463.64
7	-4/3	2/3	-2	807.65	124.60	802.84	85.86
8	-5/3	1/3	1	1791.17	233.86	2009.47	270.22
9	5/3	-1/3	1	1795.52	232.68	2005.55	251.82
10	1/3	-5/3	2	80.19	16.26	80.28	14.06
11	-4/3	5/3	-2	79.45	15.81	79.15	19.03
12	-2/3	-2/3	-3	1247.49	151.55	1456.24	183.92

Table D.5: Unique reflections resulting from the reduction of the magnetic peaks measured at Morpheus (cf. Table D.3) within the trigonal magnetic space group. The reduction within the two different space groups yields the same result. Notation of $(h\,k\,l)$ in the crystallographic unit cell.

	$\mathbf{S}_{\mathrm{tri},1}$	$\mathbf{S}_{\mathrm{tri},2}$	$\mathbf{S}_{\mathrm{kag},1}$	$\mathbf{S}_{\mathrm{kag},2}$
x $[3a]$	0.0000	0.0000	0.0573	0.0573
y $[3b]$	0.0000	0.3333	0.9427	0.2760
z $[c]$	0.5612	0.5612	0.3135	0.3135

Table D.6: Unique magnetic sites of the hexagonal magnetic space groups noted as relative coordinates in the large unit cell $(3a, 3b, c)$. The other sites are created from the symmetry operations of the respective space group.

	$\mathbf{S}_{\mathrm{tri},1}$	$\mathbf{S}_{\mathrm{tri},2}$	$\mathbf{S}_{\mathrm{kag},1}$	$\mathbf{S}_{\mathrm{kag},2}$	$\mathbf{S}_{\mathrm{kag},3}$	$\mathbf{S}_{\mathrm{kag},4}$
x $[3a]$	0.0000	0.0000	0.0573	0.8853	0.9427	0.1147
y $[3b]$	0.0000	0.0000	0.9427	0.9427	0.0573	0.0573
z $[c]$	0.5612	0.0612	0.3135	0.3135	0.8135	0.8135

Table D.7: Unique magnetic sites of the trigonal magnetic space groups noted as relative coordinates in the large unit cell $(3a, 3b, c)$. The other sites are created from the symmetry operations of the respective space group.

			$P6_3c'm'$		$P6'_3cm'$		$P6'_3c'm$		$P6_3cm$	
			80 K	4 K	80 K	4 K	80 K	4 K	80 K	4 K
$\mathbf{S}_{\text{tri},1}$	r	[μ_B]	2.43^{1}	2.48^{1}	0.88^{1}	0.72^{1}	0^{*}	0^{*}	0^{*}	0^{*}
	ϕ	[°]	0^{*}	0^{*}	0^{*}	0^{*}	0^{*}	0^{*}	0^{*}	0^{*}
	θ	[°]	0^{*}	0^{*}	0^{*}	0^{*}	0^{*}	0^{*}	0^{*}	0^{*}
$\mathbf{S}_{\text{tri},2}$	r	[μ_B]	2.43^{1}	2.48^{1}	0.88^{1}	0.72^{1}	3.43	3.56	0.00	0.00
	ϕ	[°]	0^{*}	0^{*}	0^{*}	0^{*}	0^{*}	0^{*}	0^{*}	0^{*}
	θ	[°]	180^{*}	180^{*}	180^{*}	180^{*}	180^{*}	180^{*}	180^{*}	180^{*}
$\mathbf{S}_{\text{kag},1}$	r	[μ_B]	1.50^{2}	1.57^{2}	1.99^{2}	2.04^{2}	0.97^{1}	0.90^{1}	1.21^{1}	1.23^{1}
	ϕ	[°]	330^{*}	330^{*}	330^{*}	330^{*}	60^{*}	60^{*}	60^{*}	60^{*}
	θ	[°]	155.72	158.37	15.58	166.30	90^{*}	90^{*}	90^{*}	90^{*}
$\mathbf{S}_{\text{kag},2}$	r	[μ_B]	1.50^{2}	1.57^{2}	1.99^{2}	2.04^{2}	0.97^{1}	0.90^{1}	1.21^{1}	1.23^{1}
	ϕ	[°]	122.64	123.62	221.18	230.54	223.21	206.10	255.60	258.10
	θ	[°]	28.12	26.59	130.18	53.18	24.48	24.12	95.34	80.37
R_{Bragg}			46.4	41.1	80.8	79.8	70.1	67.5	80.5	78.6

Table D.8: Refinement results from simulated annealing applied to the reduced peak set (cf. Table D.4) for the hexagonal magnetic space groups and model **D**. Only the independent spins are listed. The others are calculated from the symmetry operations of the respective magnetic space group. Parameters fixed by symmetry are marked with * and those linked by the model with same number ^{n}. The spins on the triangular (tri) sites are on the special Wyckoff position $2a$ and the kagome (kag) sites on $6c$.

			$P31m'$				$P31m$			
			model **D**		model **E**		model **D**		model **E**	
			80 K	4 K	80 K	4 K	80 K	4 K	80 K	4 K
$\mathbf{S}_{\text{tri},1}$	r	[μ_B]	2.73^{1}	2.63^{1}	2.73^{1}	2.58^{1}	3.05^{1}	2.97^{1}	2.96^{1}	2.89^{1}
	ϕ	[°]	210^{*}	210^{*}	210^{*}	210^{*}	300^{*}	300^{*}	300^{*}	300^{*}
	θ	[°]	89.82	90.34	90.34^{3}	90.33^{3}	90^{*}	90^{*}	90^{*}	90^{*}
$\mathbf{S}_{\text{tri},2}$	r	[μ_B]	2.43^{1}	2.63^{1}	2.73^{1}	2.58^{1}	3.05^{1}	2.97^{1}	2.96^{1}	2.89^{1}
	ϕ	[°]	210^{*}	210^{*}	210^{*}	210^{*}	300^{*}	300^{*}	300^{*}	300^{*}
	θ	[°]	89.99	89.88	$89.66^{\overline{3}}$	$89.66^{\overline{3}}$	90^{*}	90^{*}	90^{*}	90^{*}
$\mathbf{S}_{\text{kag},1}$	r	[μ_B]	2.19^{2}	2.15^{2}	2.23^{2}	2.23^{2}	2.37^{2}	2.35^{2}	2.40^{2}	2.39^{1}
	ϕ	[°]	30.45	32.01	36.77^{4}	38.4^{4}	92.23	88.70	103.78^{3}	97.48^{3}
	θ	[°]	78.81	74.16	102.12^{5}	75.92	96.92	82.64	84.98	82.74
$\mathbf{S}_{\text{kag},2}$	r	[μ_B]	2.19^{2}	2.15^{2}	2.23^{2}	2.23^{2}	2.37^{2}	2.35^{2}	2.40^{2}	2.39^{1}
	ϕ	[°]	30^{*}	30^{*}	30^{*}	30^{*}	120^{*}	120^{*}	120^{*}	120^{*}
	θ	[°]	128.60	134.50	49.08^{6}	137.97^{6}	90^{*}	90^{*}	90^{*}	90^{*}
$\mathbf{S}_{\text{kag},3}$	r	[μ_B]	2.19^{2}	2.15^{2}	2.23^{2}	2.23^{2}	2.37^{2}	2.35^{2}	2.40^{2}	2.39^{1}
	ϕ	[°]	39.73	41.89	36.77^{4}	38.4^{4}	106.41	100.30	103.78^{3}	97.48^{3}
	θ	[°]	102.08	102.01	$77.88^{\overline{5}}$	$104.08^{\overline{5}}$	47.97	140.63	132.42	140.79
$\mathbf{S}_{\text{kag},4}$	r	[μ_B]	2.19^{2}	2.15^{2}	2.23^{2}	2.23^{2}	2.37^{2}	2.35^{2}	2.40^{2}	2.39^{1}
	ϕ	[°]	30^{*}	30^{*}	30^{*}	30^{*}	120^{*}	120^{*}	120^{*}	120^{*}
	θ	[°]	48.54	44.60	$130.92^{\overline{6}}$	$42.03^{\overline{6}}$	90^{*}	90^{*}	90^{*}	90^{*}
R_{Bragg}			17.4	22.8	17.6	23.2	17.2	22.7	17.3	22.9

Table D.9: Refinement results from simulated annealing applied to the reduced peak set (cf. Table D.5) for the trigonal magnetic space groups. Only the independent spins are listed. The others are calculated from the symmetry operations of the respective magnetic space group. Parameters fixed by symmetry are marked with * and those linked by the model used in the refinement with same number ^{n}, whereas $^{\overline{n}}$ denotes an inversely proportional link. The spins on the triangular (tri) sites are on the special Wyckoff position $2a$ and the kagome (kag) sites on $6c$.

			$P31m'$				$P31m$			
			80 K		4 K		80 K		4 K	
			p	σ_p	p	σ_p	p	σ_p	p	σ_p
$\mathbf{S}_{\text{tri},1}$	r	[μ_B]	2.15^{1}	0.34	2.12^{1}	0.28	1.97^{1}	0.50	1.85^{1}	0.38
	ϕ	[°]	210^{*}		210^{*}		300^{*}		300^{*}	
	θ	[°]	89.58^{3}	2.72	90.08^{3}	2.74	90^{*}		90^{*}	
$\mathbf{S}_{\text{tri},2}$	r	[μ_B]	2.15^{1}	0.34	2.12^{1}	0.28	1.97^{1}	0.50	1.85^{1}	0.38
	ϕ	[°]	210^{*}		210^{*}		300^{*}		300^{*}	
	θ	[°]	$90.42^{\overline{3}}$	2.72	$89.91^{\overline{3}}$	2.74	90^{*}		90^{*}	
$\mathbf{S}_{\text{kag},1}$	r	[μ_B]	1.18^{2}	0.25	1.11^{2}	0.20	1.37^{2}	0.51	0.91^{2}	0.32
	ϕ	[°]	26.56^{4}	5.02	29.36^{4}	4.97	93.89^{3}	51.47	78.16^{3}	22.52
	θ	[°]	105.51^{5}	7.01	72.48^{5}	6.97	82.13	34.63	77.28	47.22
$\mathbf{S}_{\text{kag},2}$	r	[μ_B]	1.18^{2}	0.25	1.11^{2}	0.20	1.37^{2}	0.51	0.91^{2}	0.32
	ϕ	[°]	30^{*}		30^{*}		120^{*}		120^{*}	
	θ	[°]	65.12^{6}	9.66	120.53^{6}	8.94	90^{*}		90^{*}	
$\mathbf{S}_{\text{kag},3}$	r	[μ_B]	1.18^{2}	0.25	1.11^{2}	0.20	1.37^{2}	0.51	0.91^{2}	0.32
	ϕ	[°]	26.56^{4}	5.02	29.36^{4}	4.97	93.89^{3}	51.47	78.16^{3}	22.52
	θ	[°]	$74.49^{\overline{5}}$	7.01	$102.01^{\overline{5}}$	6.97	144.02	9.03	147.36	11.05
$\mathbf{S}_{\text{kag},4}$	r	[μ_B]	1.18^{2}	0.25	1.11^{2}	0.20	1.37^{2}	0.51	0.91^{2}	0.32
	ϕ	[°]	30^{*}		30^{*}		120^{*}		120^{*}	
	θ	[°]	$114.88^{\overline{6}}$	9.66	$59.47^{\overline{6}}$	8.94	90^{*}		90^{*}	
R_{Bragg}			67.3		67.9		91.0		76.6	

Table D.10: Results from Rietveld refinement applied to the reduced peak set (cf. Table D.5) for the trigonal magnetic space groups. Only the independent spins are listed. The others are calculated from the symmetry operations of the respective magnetic space group. Parameters fixed by symmetry are marked with * and those linked by the model **E** used in the refinement with same number ^{n}, whereas $^{\overline{n}}$ denotes an inversely proportional link. The spins on the triangular (tri) sites are on the special Wyckoff position $2a$ and the kagome (kag) sites on $6c$.

E

Source code for creating a skyrmion-like lattice

The following source code is written in the programming language Python [Pyt, MA11]. In order to speed up the calculation the module NumPy [WCV11] was used extensively. It creates a skyrmion-like lattice using three cycloidal spin structures, whose propagation directions are rotated 120° against each other. The mathematical formula and the evaluation of the structure has been described in Section 6.3.

```
# -*- coding: utf-8 -*-
"""
Created on Thu Nov  7 12:44:13 2013

@author: reim
"""

import spin_gui as sg
import numpy as np
import math
import time
import sys
import periodictable
import collections as col

from mpl_toolkits.mplot3d import Axes3D
import matplotlib.pyplot as plt
from itertools import product, combinations


triSites = [4,8]
kagSites = [1,2,3,5,6,7]


def rotation_matrix(axis,theta):
  axis = axis/np.sqrt(np.dot(axis,axis))
  a = np.cos(theta/2)
  b,c,d = -axis*np.sin(theta/2)
  return np.array([[a*a+b*b-c*c-d*d, 2*(b*c-a*d), 2*(b*d+a*c)],
      [2*(b*c+a*d), a*a+c*c-b*b-d*d, 2*(c*d-a*b)],
      [2*(b*d-a*c), 2*(c*d+a*b), a*a+d*d-b*b-c*c]])


# Propagation vectors
R1 = np.array([1.,0.,0.])
R1 = R1/np.linalg.norm(R1)
R2 = np.array([-1.,np.sqrt(3.),0.])
R2 = R2/np.linalg.norm(R2)
R3 = np.array([-1.,-np.sqrt(3.),0.])
R3 = R3/np.linalg.norm(R3)

# Rotation vectors
```

```
# cycloidal out of plane
rotaxisForR1_ooP = np.dot(rotation_matrix(np.array([0.,0.,1.]),np.pi/2.),R1)
rotaxisForR2_ooP = np.dot(rotation_matrix(np.array([0.,0.,1.]),np.pi/2.),R2)
rotaxisForR3_ooP = np.dot(rotation_matrix(np.array([0.,0.,1.]),np.pi/2.),R3)

# cycloidal in plane
rotaxisForR1_inP = np.array([0.,0.,1.])
rotaxisForR2_inP = np.array([0.,0.,1.])
rotaxisForR3_inP = np.array([0.,0.,1.])




class predefinedConfig(object):

  def __init__(self, UnitCellFilename,CellParam,UcR1,UcR2,UcR3,ExportType,NumberCells):
    self.unitCellFilename = UnitCellFilename
    self.cellParam = CellParam
    self.a = UcR1
    self.b = UcR2
    self.c = UcR3

    if self.a[1] == -1.73205:
      self.a[1] = -np.sqrt(3)
    if self.b[1] == -1.73205:
      self.b[1] = -np.sqrt(3)

    self.aStar = 2*np.pi *np.cross(self.b,self.c)/(np.dot(self.a,np.cross(self.b,self.c)))
    self.bStar = 2*np.pi *np.cross(self.c,self.a)/(np.dot(self.a,np.cross(self.b,self.c)))
    self.cStar = 2*np.pi *np.cross(self.a,self.b)/(np.dot(self.a,np.cross(self.b,self.c)))

    self.exportType = ExportType
    self.numberCells = NumberCells

    self.aStarRed = self.aStar/self.numberCells['R1']
    self.bStarRed = self.bStar/self.numberCells['R2']
    self.cStarRed = self.cStar/self.numberCells['R3']

    self.unitCell = sg.InputFile(UnitCellFilename).get_data()
    print 'Unit cell loaded with %i spins.' %len(self.unitCell)

    # check if unit cell has to be scaled
    if np.linalg.norm(self.a) != self.cellParam[0] or np.linalg.norm(self.b) != self.
        cellParam[1] or np.linalg.norm(self.c) != self.cellParam[2]:

      self.ratioR1 = self.cellParam[0]/np.linalg.norm(self.a)
      self.ratioR2 = self.cellParam[1]/np.linalg.norm(self.b)
      self.ratioR3 = self.cellParam[2]/np.linalg.norm(self.c)
      print 'Cell parameter do not fit with vectors,\n   unitCell will be scaled
          appropriately! %f %f %f' %(self.ratioR1,self.ratioR2,self.ratioR3)
      self.scaleUnitCell(self.ratioR1,self.ratioR2,self.ratioR3)

    else:
      self.ratioR1 = 1.
      self.ratioR2 = 1.
      self.ratioR3 = 1.

    self.aNucStar = 2*self.aStar - self.bStar
    self.bNucStar =   self.aStar + self.bStar
    self.cNucStar =   self.cStar


  def scaleUnitCell(self,ratioR1,ratioR2,ratioR3):

    self.a = self.a*ratioR1
    self.b = self.b*ratioR2
    self.c = self.c*ratioR3
    self.aStar = 2*np.pi *np.cross(self.b,self.c)/(np.dot(self.a,np.cross(self.b,self.c)))
    self.bStar = 2*np.pi *np.cross(self.c,self.a)/(np.dot(self.a,np.cross(self.b,self.c)))
    self.cStar = 2*np.pi *np.cross(self.a,self.b)/(np.dot(self.a,np.cross(self.b,self.c)))
    print 'ReciCell',np.linalg.norm(self.aStar),np.linalg.norm(self.bStar),np.linalg.norm(
        self.cStar)
```

```
112       self.aStarRed = self.aStar/self.numberCells['R1']
113       self.bStarRed = self.bStar/self.numberCells['R2']
114       self.cStarRed = self.cStar/self.numberCells['R3']
115
116       newCell = []
117       for spin in self.unitCell:
118         newCell.append([spin[0]*ratioR1,spin[1]*ratioR2,spin[2]*ratioR3,spin[3],spin[4],spin
              [5],spin[6]])
119
120       self.unitCell = newCell
121
122     def getUnitCell(self):
123       return self.unitCell
124
125     def getCellParam(self):
126       return self.cellParam
127
128     def getExportType(self):
129       return self.exportType
130
131     def getReciCell(self):
132       return [self.aStar,self.bStar,self.cStar]
133
134     def getRedReciCell(self):
135       return [self.aStarRed,self.bStarRed,self.cStarRed]
136
137
138     def __str__(self):
139       return 'Config:\n\tfilename: %s\n\tcellParam: %s\n\ta: %s\n\tb: %s\n\tc: %s\n\
              tnumberCells: %i,%i,%i\n\texportType: %s' %(
140           self.unitCellFilename,toStr(self.cellParam),toStr(self.a),toStr(self.b),toStr(self
                .c),self.numberCells['R1'],self.numberCells['R2'],self.numberCells['R3'],self
                .exportType)
141
142
143 class Spin():
144
145     def __init__(self,Coord,Direc,Num,CellNum):
146       self.coord = Coord
147       self.direc = Direc
148       self.num = Num
149       self.cellNum = CellNum
150
151     def getDis(self,otherSpin):
152       return np.linalg.norm(self.coord - otherSpin.coord)
153
154     def getWriteString(self):
155       return '  %f  %f  %f  %f  %f  %f  %i' %(self.coord[0],self.coord[1],self.coord[2],self
              .direc[0],self.direc[1],self.direc[2],self.num)
156
157
158
159 def readConfigFile(filename = 'config.txt'):
160     '''
161
162     reads predefined configuration from file
163
164     '''
165     #Tags
166     tagUnitCellFile = '@UnitCellFile'
167     tagCellParam    = '@CellParam'
168     tagVectorR1     = '@R1'
169     tagVectorR2     = '@R2'
170     tagVectorR3     = '@R3'
171     tagNumberCells  = '@NumberCells'
172     tagType         = '@Type'
173
174     unitCellFilename = 'standardSmall.uc'
175     angle = 0.
176
177     numberCells = None
178     propVec     = None
```

```
  precision   = None

  configFile = open(filename,'r')
  for line in configFile.readlines():
    lineStrip = line.strip()
    if len(lineStrip)==0:
      pass
    elif lineStrip.startswith('#'):
      pass
    elif lineStrip.startswith(tagUnitCellFile):
      unitCellFilename = lineStrip.split(':')[1].strip()
    elif lineStrip.startswith(tagCellParam):
      cellParam = np.array(lineStrip.split(':')[1].strip().split(','),dtype =float)
    elif lineStrip.startswith(tagVectorR1):
      ucR1 = np.array(lineStrip.split(':')[1].strip().split(','),dtype =float)
    elif lineStrip.startswith(tagVectorR2):
      ucR2 = np.array(lineStrip.split(':')[1].strip().split(','),dtype =float)
    elif lineStrip.startswith(tagVectorR3):
      ucR3 = np.array(lineStrip.split(':')[1].strip().split(','),dtype =float)
    elif lineStrip.startswith(tagNumberCells):
      temp = lineStrip.split(':')[1].strip().split(',')
      numberCells = {'R1': int(temp[0]), 'R2': int(temp[1]), 'R3': int(temp[2])}
    elif lineStrip.startswith(tagType):
      exportType = lineStrip.split(':')[1].strip()

  return predefinedConfig(unitCellFilename,cellParam,ucR1,ucR2,ucR3,exportType,numberCells
      )



def createSpinlattice(Config):
  '''
  from the read configfile the skyrmions along R1 and R2 are created
  first create the necessary number of cells along R2 and then at all places along R1
  '''
  numberCellInR1=Config.numberCells['R1']
  numberCellInR2=Config.numberCells['R2']
  numberCellInR3=Config.numberCells['R3']

  Spins = []

  numberCells = numberCellInR1 * numberCellInR2 * numberCellInR3
  print 'Due to the propagation vector %i cells get calculated' %numberCells
  cellNum = 0
  # create magnetic unit cells for two periods along a and b
  rangeR1 = np.arange(-int(numberCellInR1),int(numberCellInR1))
  rangeR2 = np.arange(-int(numberCellInR2),int(numberCellInR2))
  rangeR3 = np.arange(1)

  for i in rangeR1:
    for j in rangeR2:
      for k in rangeR3:
        for ucNum,spin in enumerate(Config.getUnitCell()):
          koord = np.array(spin[0:3]) + i*Config.a + j*Config.b + k*Config.c
          direc = np.array(spin[3:6])
          num = int(spin[6])
          if ucNum in range(0,8):
            towerNum = cellNum*3+0
          elif ucNum in range(8,16):
            towerNum = cellNum*3+1
          elif ucNum in range(16,24):
            towerNum = cellNum*3+2
          Spins.append(Spin(np.array([koord[0],koord[1],koord[2]]),np.array([direc[0],
              direc[1],direc[2]]),num,towerNum))

        cellNum +=1

  # add additional spins to create periodic boundary or rather complete all triangles
  fullTriangleSpins = []
  xmax = ((rangeR1.max())*Config.a + (rangeR2.min()+1)*Config.b)[0]
  xmin = ((rangeR1.min()+1)*Config.a + (rangeR2.max())*Config.b)[0]
  ymax = ((rangeR1.max())*Config.a + (rangeR2.max())*Config.b)[1]
```

```
  ymin = ((rangeR1.min()+1)*Config.a + (rangeR2.min()+1)*Config.b)[1]

  addedSpins = 0
  triSpins = 0
  for spin in Spins:
    fullTriangleSpins.append(spin)
    if (spin.num == 1 or spin.num == 2 or spin.num == 3 or spin.num == 5 or spin.num == 6
        or spin.num == 7):
      if spin.coord[0]<xmin-spin.coord[1]/ymax*xmin+0.1:
        fullTriangleSpins.append(Spin(spin.coord-Config.b*len(rangeR2),spin.direc,spin.num
            ,spin.cellNum))
        addedSpins +=1
      if spin.coord[0]<xmin-spin.coord[1]/ymin*xmin-35:
        fullTriangleSpins.append(Spin(spin.coord+Config.a*len(rangeR2),spin.direc,spin.num
            ,spin.cellNum))
        addedSpins +=1
      if spin.coord[0]>xmax-spin.coord[1]/ymax*xmax-0.1:
        fullTriangleSpins.append(Spin(spin.coord-Config.a*len(rangeR2),spin.direc,spin.num
            ,spin.cellNum))
        addedSpins +=1
      if spin.coord[0]>xmax-spin.coord[1]/ymin*xmax+35:
        fullTriangleSpins.append(Spin(spin.coord+Config.b*len(rangeR2),spin.direc,spin.num
            ,spin.cellNum))
        addedSpins +=1
      if spin.coord[0]<0.01 and spin.coord[0]>-0.01 and spin.coord[1] > ymax-0.1:
        fullTriangleSpins.append(Spin(spin.coord-Config.a*len(rangeR1)-Config.b*len(
            rangeR2),spin.direc,spin.num,spin.cellNum))
        addedSpins +=1
    elif (spin.num == 4 or spin.num == 8):
      triSpins +=1
      if spin.coord[0]<xmin-spin.coord[1]/ymax*xmin+5.0:
        fullTriangleSpins.append(Spin(spin.coord-Config.b*len(rangeR2),spin.direc,spin.num
            ,spin.cellNum))
        addedSpins +=1
      if spin.coord[0]<xmin-spin.coord[1]/ymin*xmin-30:
        fullTriangleSpins.append(Spin(spin.coord+Config.a*len(rangeR2),spin.direc,spin.num
            ,spin.cellNum))
        addedSpins +=1
      if spin.coord[0]>xmax-spin.coord[1]/ymax*xmax-5.0:
        fullTriangleSpins.append(Spin(spin.coord-Config.a*len(rangeR2),spin.direc,spin.num
            ,spin.cellNum))
        addedSpins +=1
      if spin.coord[0]>xmax-spin.coord[1]/ymin*xmax+30:
        fullTriangleSpins.append(Spin(spin.coord+Config.b*len(rangeR2),spin.direc,spin.num
            ,spin.cellNum))
        addedSpins +=1
      if spin.coord[0]<0.01 and spin.coord[0]>-0.01 and spin.coord[1] > ymax-5.1:
        fullTriangleSpins.append(Spin(spin.coord-Config.a*len(rangeR1)-Config.b*len(
            rangeR2),spin.direc,spin.num,spin.cellNum))
        addedSpins +=1
  return fullTriangleSpins

def getRotMatrix(i,Angle):
  if   i == 'R1':
    return rotation_matrix(rotaxisForR1,Angle)
  elif i == 'R2':
    return rotation_matrix(rotaxisForR2,Angle)
  elif i == 'R3':
    return rotation_matrix(rotaxisForR3,Angle)


'''
  creating a Skyrmion lattice starting in a state with spins (anti-)parallel to z-axis
  triSpins +z, kagSpins-z, rotationAxis is in xy-plane
  still compare 0,1,0 vector to commensurate order for additional angle for af order
'''
def createCycloidsWithThreeWaves(Spins,Config):
  '''
  rotation axes: rotated by °+-120 around z-axis
  create a spin wave for each rotation axis
  angle: component perpendicular to rotation axis of the distance to origin + af angle
  '''
```

```
    lengthOfCycloidal = np.sqrt(3)/2.*np.linalg.norm(Config.a)*Config.numberCells['R1']
    cycloidalSpins = []
    R1Spins = []
    R2Spins = []
    R3Spins = []
    triSpins = []

    initialVec = np.array([0.,1.,0.]) # for comparison with af spin structure
    norm = 3.0

    for i,spin in enumerate(Spins):
      offsetAngle = inPlaneAngle(spin.direc,initialVec)
      #offsetAngle = 0 #if antiferro modulation shall be suppressed
      xyCoord = np.array([spin.coord[0],spin.coord[1],0.])
      newSpinDirec = np.array([0.,0.,0.], float)

      if spin.num in triSites:
        startSpin = np.array([0.,0.,1.])
      elif spin.num in kagSites:
        startSpin = np.array([0.,0.,-1.])
      else:
        print 'Spin site %s undefined' %str(spin.num)

      startSpin = np.array([0.,0.,1.])

      # first cycloidal along x
      angle = (spin.coord * R1).sum()/lengthOfCycloidal*2*np.pi
      newDirec = np.dot(rotation_matrix(rotaxisForR1_ooP,-offsetAngle+angle),startSpin)
      R1Spins.append(Spin(spin.coord,newDirec,spin.num,spin.cellNum))
      newSpinDirec += newDirec/norm


      #second cycloidal along -x sqrt(3)y
      angle = (spin.coord * R2).sum()/lengthOfCycloidal*2*np.pi
      newDirec = np.dot(rotation_matrix(rotaxisForR2_ooP,-offsetAngle+angle),startSpin)
      R2Spins.append(Spin(spin.coord,newDirec,spin.num,spin.cellNum))
      newSpinDirec += newDirec/norm


      #third cycloidal along -x -sqrt(3)y
      angle = (spin.coord * R3).sum()/lengthOfCycloidal*2*np.pi
      newDirec = np.dot(rotation_matrix(rotaxisForR3_ooP,-offsetAngle+angle),startSpin)
      R3Spins.append(Spin(spin.coord,newDirec,spin.num,spin.cellNum))
      newSpinDirec += newDirec/norm

      cycloidalSpins.append(Spin(spin.coord,newSpinDirec,spin.num,spin.cellNum))

    return cycloidalSpins

def writeSpinState(filename,Spins):
    fortFile = open(filename,'w')
    fortFile.write("\t%i\n" %(len(Spins)))
    sep = '  '
    for i,spin in enumerate(Spins):
      fortFile.write("%s\n" %spin.getWriteString())

    fortFile.close()


def dft_to_SofQ(SpinKonf, Config):
    global qWerte

    N = len(SpinKonf) #Number of Spins
    scalingFactor = 1000.0

    firstPeakQ = np.sqrt(4.0/np.power(Config.cellParam[0],2))
    reciResR1 = firstPeakQ/Config.numberCells['R1']
    reciResR2 = firstPeakQ/Config.numberCells['R2']

    stepsizeX=reciResR1
    stepsizeY=reciResR2*np.cos(np.pi/6.0)
    stepsizeZ=0.02
```

```
382
383
384   if Config.exportType == 'map':
385     # bounds are in Q
386     lowerboundX=-3
387     upperboundX=+3
388     lowerboundY=-3
389     upperboundY=+3
390     lowerboundZ=+0
391     upperboundZ=+0
392     tempListe = fill_qmatrix(lowerboundX, lowerboundY, lowerboundZ, stepsizeZ, stepsizeX,
          stepsizeY, upperboundZ, upperboundY, upperboundX,Config)
393
394   elif Config.exportType == 'peak':
395     tempListe = createPeaks(Config)
396
397   SofQ=np.zeros((3, len(tempListe)), dtype=np.complex)
398   QMatrix    = np.mat(tempListe)
399
400   qWerte=np.array(np.mat(tempListe).T)
401
402   for i,spin in enumerate(SpinKonf):
403     SkalarQR = QMatrix*np.mat(spin.coord).T
404
405     SofQ -= np.multiply(np.dot(np.mat(spin.direc).T , np.exp(1j * SkalarQR).T))
406
407   return (SofQ/np.sqrt(N),qWerte)
408
409 def fill_qmatrix(lowerboundX, lowerboundY, lowerboundZ, stepsizeZ, stepsizeX, stepsizeY,
      upperboundZ, upperboundY, upperboundX, Config = None):
410     tempListe=[]
411
412   if Config is None:
413     for x in range(int(lowerboundX/stepsizeX),int((upperboundX+stepsizeX)/stepsizeX+
          stepsizeX),1):
414       for y in range(int(lowerboundY/stepsizeY),int((upperboundY+stepsizeY)/stepsizeY+
            stepsizeY),1):
415         for z in range(int(lowerboundZ/stepsizeZ),int((upperboundZ+stepsizeZ)/stepsizeZ+
              stepsizeZ),1):
416           tempListe.append([x*stepsizeX,y*stepsizeY,z*stepsizeZ])
417   else:
418     lbZ = int(lowerboundZ)
419     ubZ = int(upperboundZ)
420
421     for l in range(-1000,1001,1):
422       for m in range(-1000,1001,1):
423         for n in range(lbZ,ubZ+1,1):
424           qPos = l*Config.aStarRed + m*Config.bStarRed + n*Config.cStarRed
425           if qPos[0]>=lowerboundX and qPos[0]<=upperboundX and qPos[1]>=lowerboundY and
                qPos[1]<=upperboundY:
426             tempListe.append(qPos)
427
428
429       return tempListe
430
431 def write_SofQT(filename,numberSpins,SofQ,qWerte,Config):
432   separations = ['chiral','inplane','ooplane','total']
433
434   files = {}
435   intensList = {}
436   qPosLists = {}
437
438   for separation in separations:
439     files[separation]  = open('%s_%s.map'  %(filename,separation),'w')
440     intensList[separation] = []
441
442
443   qxlast=qWerte[0][0]
444
445   qPosList      = []
446
```

```
447   for i,(qx,qy,qz,SofQx,SofQy,SofQz) in enumerate(zip(qWerte[0],qWerte[1],qWerte[2],SofQ
          [0],SofQ[1],SofQ[2])):
448
449
450     intens = {}
451     sofQ = np.array([SofQx,SofQy,SofQz])
452
453     # calculate coordinate system
454     if np.linalg.norm([qx,qy,qz])!=0:
455       eQ = np.array([qx,qy,qz])/np.linalg.norm([qx,qy,qz])
456     else:
457       eQ = np.array([0.,0.,0.])
458     eQy = np.dot(rotation_matrix(np.array([0.,0.,1.]),np.pi/2.),eQ)
459     eQz = np.array([0.,0.,1.])
460
461
462     # chiral magnetic scattering - correct
463     Mperp = np.cross(eQ,np.cross(sofQ,eQ))
464     chiralSofQperpQ = np.dot(2j * (np.cross(Mperp.conj(),Mperp)),eQ).real
465     intens['chiral'] = chiralSofQperpQ/numberSpins
466
467     # magnetic scattering in plane
468     Mperp_y = np.dot(Mperp,eQy)
469     inplaneScattering = (Mperp_y.conj()*Mperp_y).real
470     intens['inplane'] = inplaneScattering/numberSpins
471
472     # magnetic scattering out of plane
473     Mperp_z = np.dot(Mperp,eQz)
474     outofplaneScattering = (Mperp_z.conj()*Mperp_z).real
475     intens['ooplane'] = outofplaneScattering/numberSpins
476
477     # total magnetic scattering
478     totalScattering = np.dot(Mperp.conj(),Mperp).real
479     intens['total'] = (inplaneScattering+outofplaneScattering)/numberSpins
480
481
482     qPosList.append([qx,qy,qz])
483
484     for separation in separations:
485       intensList[separation].append(intens[separation])
486
487
488     qxlast=qx
489
490     sys.stdout.write('\r')
491     sys.stdout.write("calculate maps: \t[%-20s] %3d%%" % ('='*int((i+1.0)/len(qWerte[0])
            *20), int((i+1.0)/len(qWerte[0])*100)))
492     sys.stdout.flush()
493   sys.stdout.write('\n')
494
495   for separation in separations:
496     qPosLists[separation] = np.array(qPosList)
497
498   if Config.exportType == 'map':
499     for separation in separations:
500       idx = np.argsort(np.abs(np.array(intensList[separation])))
501       qPosLists[separation] = qPosLists[separation][idx]
502       intensList[separation] = np.array(intensList[separation])[idx]
503
504   if Config.exportType == 'peak':
505     for separation in separations:
506       qPosLists[separation],intensList[separation] = joinPeaks(qPosLists[separation],
              intensList[separation])
507
508   for separation in separations:
509     for (qx,qy,qz),intens in zip(qPosLists[separation],intensList[separation]):
510
511       files[separation].write("%10f %10f %10f %10f %10f\n" %(qx, qy, qz, np.linalg.norm([
              qx,qy,qz]),intens*100))
512
513   for separation in separations:
514     files[separation].close()
```

```
515
516   return
517
518
519 def createPeaks(Config):
520   nucPeaks = []
521   satPeaks = []
522
523   propVec = (Config.propVec/3.*np.array([Config.aNucStar,Config.bNucStar,Config.cNucStar])
          ).sum(axis=0)
524
525   propVecStar = [ +propVec,
526       -propVec,
527       np.dot(rotation_matrix(np.array([0.,0.,1.]),+1*np.pi/3.),propVec),
528       np.dot(rotation_matrix(np.array([0.,0.,1.]),+2*np.pi/3.),propVec),
529       np.dot(rotation_matrix(np.array([0.,0.,1.]),-1*np.pi/3.),propVec),
530       np.dot(rotation_matrix(np.array([0.,0.,1.]),-2*np.pi/3.),propVec)]
531
532   for l in range(-20,21):
533     for m in range(-20,21):
534       for n in range(-20,21):
535         nucQPos = np.array(l*Config.aNucStar + m*Config.bNucStar + n*Config.cNucStar)
536         nucPeaks.append(nucQPos)
537         for propVec in propVecStar:
538           satQPos = nucQPos + propVec
539           if np.linalg.norm(satQPos)<3.0:
540             satPeaks.append(satQPos)
541
542   return sortPeaks(satPeaks)
543
544 def sortPeaks(PeakList):
545   Qabs = []
546   for peak in PeakList:
547     Qabs.append(np.linalg.norm(peak))
548
549   idx = np.argsort(Qabs)
550   return np.array(PeakList)[idx]
551
552
553 def joinPeaks(PeakList,IntensList):
554   joinedPeakList = []
555   joinedIntensList = []
556   oldQAbs = round(np.linalg.norm(PeakList[0]),4)
557   joinedIntens = 0.
558   for i,(peak,intens) in enumerate(zip(PeakList,IntensList)):
559     qAbs = round(np.linalg.norm(peak),4)
560     if qAbs == oldQAbs:
561       joinedIntens += intens
562     else:
563       joinedPeakList.append(PeakList[i-1])
564       joinedIntensList.append(joinedIntens)
565       joinedIntens = intens
566       oldQAbs = qAbs
567
568   joinedPeakList.append(PeakList[-1])
569   joinedIntensList.append(joinedIntens)
570
571   return joinedPeakList,joinedIntensList
572
573
574
575 def angleVecs(vec1,vec2):
576   return np.arccos(np.dot(vec1,vec2)/(np.linalg.norm(vec1)*np.linalg.norm(vec2)))
577
578 def inPlaneAngle(vec1,vec2):
579   s1 = np.arctan2(*vec1[0:2])
580   s2 = np.arctan2(*vec2[0:2])
581   if s1 < 0:
582     s1 += 2*np.pi
583   if s2 < 0:
584     s2 += 2*np.pi
585   return s2-s1
```

```
586
587
588
589 def calcCommensuratePos(filename,Config):
590   outputFile = open(filename,'w')
591   print Config.aStar,Config.bStar
592   for l in range(0,21):
593     for m in range(0,21):
594       for n in range(0,21):
595         magQPos = np.array(l*Config.aStar + m*Config.bStar + n*Config.cStar)
596         if np.linalg.norm(magQPos)<2.8:
597           outputFile.write('%i\t%i\t%i\t%f\n' %(l,m,n,np.linalg.norm(magQPos)))
598   outputFile.close()
599
600
601
602
603 # Evaluate the Spin structure
604 def evaluateSpinLengths(SpinState,Config):
605
606   spinLengths = []
607   for i,Spin in enumerate(SpinState):
608     spinLengths.append(np.linalg.norm(Spin.direc))
609
610   hist, bins = np.histogram(spinLengths,bins=300,range=(0,3))
611   width = 0.7 * (bins[1] - bins[0])
612   center = (bins[:-1] + bins[1:]) / 2
613   output = open('histo.txt','w')
614   for x,y in zip(center,hist):
615     output.write('%.3f\t%i\n'%(x,y))
616   output.close()
617
618   plt.bar(center, hist, align='center', width=width)
619   plt.show()
620
621
622 def seperateTriSpins(TriSpins):
623   triASpins = []
624   triBSpins = []
625   triCSpins = []
626   triANetMag = np.zeros((1,3))
627   triBNetMag = np.zeros((1,3))
628   triCNetMag = np.zeros((1,3))
629
630   for spin in TriSpins:
631     if spin.cellNum%3  ==0:
632       triASpins.append(spin)
633       triANetMag += spin.direc
634     elif spin.cellNum%3==1:
635       triBSpins.append(spin)
636       triBNetMag += spin.direc
637     elif spin.cellNum%3==2:
638       triCSpins.append(spin)
639       triCNetMag += spin.direc
640
641   writeSpinState('triASpins.txt',triASpins)
642   writeSpinState('triBSpins.txt',triBSpins)
643   writeSpinState('triCSpins.txt',triCSpins)
644
645   print '\tNetMag'
646   print 'triA',triANetMag
647   print 'triB',triBNetMag
648   print 'triC',triCNetMag
649   return triASpins,triBSpins,triCSpins
650
651 def calcNetMag(Spins):
652   absMag = np.zeros((1,3))
653   netMag = np.zeros((1,3))
654   for i,spin in enumerate(Spins):
655     absMag += abs(spin.direc)
656     netMag += spin.direc
657   print 'NetMag:', netMag
```

```
  print 'AbsMag:', absMag


# Winding Number
def calculateWindingNumberTri(NewSpins,Config):
  triSpins = []
  for spinA in NewSpins:
    if spinA.num == 4:
      triSpins.append(spinA)

  greenTriangles=[]
  for spinA in triSpins:
    for spinB in triSpins:
      if spinA.getDis(spinB)<6.6 and not spinA is spinB:
        for spinC in triSpins:
          if spinA.getDis(spinC)<6.6 and spinB.getDis(spinC)<6.6 and not spinA is spinC
              and not spinB is spinC:
            triangleNew = True
            for triangle in greenTriangles:
              if spinA in triangle and spinB in triangle and spinC in triangle:
                triangleNew = False
                break
            if triangleNew:
              greenTriangles.append([spinA,spinB,spinC])


  print 'triSpins',len(triSpins),', greenTriangles',len(greenTriangles)
  greenWinding = 0
  oosterom     = 0
  for triangle in greenTriangles:
    middle = (triangle[0].coord + triangle[1].coord + triangle[2].coord)/3.
    higher = 0
    for spin in triangle:
      if spin.coord[1]>middle[1]+0.1:
        higher +=1

    #sort clockwise
    #upward triangle
    if higher == 1:
      sortedTriangle = [None,None,None]
      for spin in triangle:
        if spin.coord[0] < middle[0]-0.1:
          sortedTriangle[0] = spin
        if spin.coord[0] > middle[0]+0.1:
          sortedTriangle[1] = spin
        if spin.coord[0] > middle[0]-0.1 and spin.coord[0] < middle[0]+0.1:
          sortedTriangle[2] = spin
    #downward triangle
    elif higher == 2:
      sortedTriangle = [None,None,None]
      for spin in triangle:
        if spin.coord[0] < middle[0]-0.1:
          sortedTriangle[0] = spin
        if spin.coord[0] > middle[0]+0.1:
          sortedTriangle[2] = spin
        if spin.coord[0] > middle[0]-0.1 and spin.coord[0] < middle[0]+0.1:
          sortedTriangle[1] = spin

    spin1 = sortedTriangle[0].direc/np.linalg.norm(sortedTriangle[0].direc)
    spin2 = sortedTriangle[1].direc/np.linalg.norm(sortedTriangle[1].direc)
    spin3 = sortedTriangle[2].direc/np.linalg.norm(sortedTriangle[2].direc)
    greenWinding+= np.dot(spin1,np.cross(spin2,spin3))

  print 'gw', greenWinding/(8 *np.pi)/4.
  return greenTriangles


def toStr(Array):
  return '[%f,%f,%f]' %(Array[0],Array[1],Array[2])


def angleVecs(vec1,vec2):
```

```
729     angle = np.arccos(np.dot(vec1,vec2))*180./np.pi
730     if angle<0.:
731       angle += 360.
732     return angle
733
734
735 if __name__ == '__main__':
736     config = readConfigFile('skyrmion.txt')
737
738     # define Spin positions for unit cells in ab direction from configuration
739     spins = createSpinlattice(config)
740
741     # calculate the spin orientation change from the "distance" to the origin:
742     newSpins = createCycloidsWithThreeWaves(spins,config)
743     writeSpinState('test.txt',newSpins)
744
745     #Histogram for spin lengths
746     evaluateSpinLengths(newSpins,config)
747
748     #Net magnetic moment
749     calcNetMag(newSpins)
750
751     #Calculated scattering
752     SofQ,qWerte = dft_to_SofQ(newSpins,config)
753     write_SofQT('test',len(newSpins),SofQ,qWerte,config)
754     calcCommensuratePos('commensuratePos.txt',config)
755
756     #Winding number for triangular sites
757     greenTriangles = calculateWindingNumberTri(newSpins,config)
```

Control file for the previous python script

```
1  # Config file for the python script: createSkyrmion.py
2  # from a predefined unit cell Skyrmions are created along 3 directions
3  #
4  # picture rotate 90 degrees clockwise
5  #
6  #          /\   R2
7  #         /  \
8  #        /    \
9  #        \ UC /
10 #         \  /  R1
11 #          \/
12
13 @UnitCellFile: standardSmallAntiferroEdit.uc
14 @CellParam: 11.00315, 11.00315, 10.264092,90.0,90.0,120.0
15 @R1: +3.000000,+1.73205,0.000000
16 @R2: -3.000000,+1.73205,0.000000
17 @R3: +0.000000,+0.000000,3.2659818
18 @NumberCells: 33,33,1
19 @Type: map
```

Band / Volume 102
Extending the precision and efficiency of the all-electron full-potential linearized augmented plane-wave density-functional theory method
G. Michalicek (2015), 195 pp
ISBN: 978-3-95806-031-9

Band / Volume 103
Metabolic engineering of *Escherichia coli* for the production of plant phenylpropanoid derived compounds
P. V. van Summeren-Wesenhagen (2015), V, 92 pp
ISBN: 978-3-95806-039-5

Band / Volume 104
Spin-reorientation transition in epitaxial Ni_xPd_{1-x} fims on Cu(001): a microscopic analysis
D. Gottlob (2015), x, 134 pp
ISBN: 978-3-95806-049-4

Band / Volume 105
Resonant Magnetic Scattering Studies using Synchrotron Radiation and Laser-Generated Extreme Ultraviolet Light
C. M. Weier (2015), vii, 143 pp
ISBN: 978-3-95806-052-4

Band / Volume 106
Neutron Scattering
Lectures of the JCNS Laboratory Course held at Forschungszentrum Jülich and at the Heinz-Maier-Leibnitz Zentrum Garching
edited by Th. Brückel, D. Richter, G. Roth, A. Wischnewski and R. Zorn (2015), ca 300 pp
ISBN: 978-3-95806-055-5

Band / Volume 107
Neutron Scattering
Experimental Manuals of the JCNS Laboratory Course held at Forschungszentrum Jülich and at the Heinz-Maier-Leibnitz Zentrum Garching
edited by Th. Brückel, D. Richter, G. Roth, A. Wischnewski and R. Zorn (2015), ca 150 pp
ISBN: 978-3-95806-056-2

Band / Volume 108
STM-based quantum transport through molecular wires
N. Fournier (2015), ix, 295 pp
ISBN: 978-3-95806-059-3

Band / Volume 109
Study on the electroforming and resistive switching behaviour of nickel oxide thin fims for non-volatile memory applications
R. Weng (2015), xxi, 159 pp
ISBN: 978-3-95806-062-3

Band / Volume 110
Microswimmers – From Single Particle Motion to Collective Behaviour
Lecture Notes of the DFG SPP Summer School 2015
edited by G. Gompper, C. Bechinger, S. Herminghaus, R. E. Isele-Holder, U.B. Kaupp, H. Löwen, H. Stark, R. G. Winkler (2015)
ISBN: 978-3-95806-083-8

Band / Volume 111
Long range order in 3D nanoparticle assemblies
E. Josten (2015), 238 pp
ISBN: 978-3-95806-087-6

Band / Volume 112
Silicon nanowire structures for neuronal cell interfacing
S. Pud (2015), 153 pp
ISBN: 978-3-95806-089-0

Band / Volume 113
Memristive Phenomena -
From Fundamental Physics to Neuromorphic Computing
Lecture Notes of the 47th IFF Spring School 2016
22 February – 04 March 2016, Jülich, Germany
ed. by R. Waser and M. Wuttig (2016), ca 1000 pp
ISBN: 978-3-95806-091-3

Band / Volume 114
Single-Cell Analysis of Microbial Production Strains in Microfluidic Bioreactors
A. M. Grünberger (2015), XIX, 225 pp
ISBN: 978-3-95806-092-0

Band / Volume 115
Magnetic order and spin dynamics in the extended kagome system $CaBaCo_2Fe_2O_7$
J. Reim (2015), viii, 144 pp
ISBN: 978-3-95806-097-5

Weitere ***Schriften des Verlags im Forschungszentrum Jülich*** unter
http://wwwzb1.fz-juelich.de/verlagextern1/index.asp

Schlüsseltechnologien /
Key Technologies
Band / Volume 115
ISBN 978-3-95806-097-5